Mesh Models of Images, Their Generation, and Their Application in Image Scaling

by

Ali Mostafavian
B.Sc., Iran University of Science and Technology, 2007
M.Sc., Sharif University of Technology, 2009

A Dissertation Submitted in Partial Fulfillment of the
Requirements for the Degree of

DOCTOR OF PHILOSOPHY

in the Department of Electrical and Computer Engineering

Mesh Models of Images, Their Generation, and Their Application in Image Scaling

by

Ali Mostafavian
B.Sc., Iran University of Science and Technology, 2007
M.Sc., Sharif University of Technology, 2009

Supervisory Committee

Dr. Michael D. Adams, Supervisor
(Department of Electrical and Computer Engineering)

Dr. Pan Agathoklis, Departmental Member
(Department of Electrical and Computer Engineering)

Dr. Venkatesh Srinivasan, Outside Member
(Department of Computer Science)

ABSTRACT

Triangle-mesh modeling, as one of the approaches for representing images based on nonuniform sampling, has become quite popular and beneficial in many applications. In this thesis, image representation using triangle-mesh models and its application in image scaling are studied. Consequently, two new methods, namely, the SEMMG and MIS methods are proposed, where each solves a different problem. In particular, the SEMMG method is proposed to address the problem of image representation by producing effective mesh models that are used for representing grayscale images, by minimizing squared error. The MIS method is proposed to address the image-scaling problem for grayscale images that are approximately piecewise-smooth, using triangle-mesh models.

The SEMMG method, which is proposed for addressing the mesh-generation problem, is developed based on an earlier work, which uses a greedy-point-insertion (GPI) approach to generate a mesh model with explicit representation of discontinuities (ERD). After in-depth analyses of two existing methods for generating the ERD models, several weaknesses are identified and specifically addressed to improve the quality of the generated models, leading to the proposal of the SEMMG method. The performance of the SEMMG method is then evaluated by comparing the quality of the meshes it produces with those obtained by eight other competing methods, namely, the error-diffusion (ED) method of Yang, the modified Garland-Heckbert (MGH) method, the ERDED and ERDGPI methods of Tu and Adams, the Garcia-Vintimilla-Sappa (GVS) method, the hybrid wavelet triangulation (HWT) method of Phichet, the binary space partition (BSP) method of Sarkis, and the adaptive triangular meshes (ATM) method of Liu. For this evaluation, the error between the original and reconstructed images, obtained from each method under comparison, is measured in terms of the PSNR. Moreover, in the case of the competing methods whose implementations are available, the subjective quality is compared in addition to the PSNR. Evaluation results show that the reconstructed images obtained from the SEMMG method are better than those obtained by the competing methods in terms of both PSNR and subjective quality. More specifically, in the case of the methods with implementations, the results collected from 350 test cases show that the SEMMG method outperforms the ED, MGH, ERDED, and ERDGPI schemes in approximately 100%, 89%, 99%, and 85% of cases, respectively. Moreover, in the case of the methods without implementations, we show that the PSNR of the reconstructed images produced by the SEMMG method are on average 3.85, 0.75, 2, and 1.10 dB higher than those obtained by the GVS, HWT, BSP, and ATM methods, respectively. Furthermore, for a given PSNR, the SEMMG method is shown to produce much smaller meshes compared to those obtained by the GVS and BSP methods, with approximately 65% to 80% fewer vertices and 10% to 60% fewer triangles, respectively. Therefore, the SEMMG method is shown to be capable of producing triangular meshes of higher quality and smaller sizes (i.e., number of vertices or triangles) which can be effectively used for image representation.

Besides the superior image approximations achieved with the SEMMG method, this work also makes contributions by addressing the problem of image scaling. For this purpose, the application of triangle-mesh mesh models in image scaling is studied. Some of the mesh-based image-scaling approaches proposed to date employ mesh models that are associated with an approximating function that is continuous everywhere, which inevitably yields edge blurring in the process of image scaling. Moreover, other mesh-based image-scaling approaches that employ approximating functions with discontinuities are often based on mesh simplification where the method starts with an extremely large initial mesh, leading to a very slow mesh generation with high memory cost. In this thesis, however, we propose a new mesh-based image-scaling (MIS) method which firstly employs an approximating function with selected discontinuities to better maintain the sharpness at the edges. Secondly, unlike most of the other discontinuity-preserving mesh-based methods, the proposed MIS method is not based on mesh simplification. Instead, our MIS method employs a mesh-refinement scheme, where it starts from a very simple mesh and iteratively refines the mesh to reach a desirable size. For developing the MIS method, the performance of our SEMMG method, which is proposed for image representation, is examined in the application of image scaling. Although the SEMMG method is not designed for solving the problem of image scaling, examining its performance in this application helps to better understand potential shortcomings of using a mesh generator in image scaling. Through this examination, several shortcomings are found and different techniques are devised to address them. By applying these techniques, a new effective mesh-generation method called MISMG is developed that can be used for image scaling. The MISMG method is then combined with a scaling transformation and a subdivision-based model-rasterization algorithm, yielding the proposed MIS method for scaling grayscale images that are approximately piecewise-smooth. The performance of our MIS method is then evaluated by comparing the quality of the scaled images it produces with those obtained from five well-known raster-based methods, namely, bilinear interpolation, bicubic interpolation of Keys, the directional cubic convolution interpolation (DCCI) method of Zhou et al., the new edge-directed image interpolation (NEDI) method of Li and Orchard, and the recent method of super-resolution using convolutional neural networks (SRCNN) by Dong et al.. Since our main goal is to produce scaled images of higher subjective quality with the least amount of edge blurring, the quality of the scaled images are first compared through a subjective evaluation followed by some objective evaluations. The results of the subjective evaluation show that the proposed MIS method was ranked best overall in almost 67% of the cases, with the best average rank of 2 out of 6, among 380 collected rankings with 20 images and 19 participants. Moreover, visual inspections on the scaled images obtained with different methods show that the proposed MIS method produces scaled images of better quality with more accurate and sharper edges. Furthermore, in the case of the mesh-based image-scaling methods, where no implementation is available, the MIS method is conceptually compared, using theoretical analysis, to two mesh-based methods, namely, the subdivision-based image-representation (SBIR) method of Liao et al. and the curvilinear feature driven image-representation (CFDIR) method of Zhou et al..

Contents

List of Tables

List of Figures

List of Acronyms

AMA	adaptive triangular meshes
ARBF	anisotropic radial basis function
ATM	adaptive triangular meshes
BSP	binary space partition
CFDIR	curvilinear feature-driven image representation
dB	decibel
DCCI	directional cubic-convolution interpolation
DDT	data-dependent triangulation
DP	Douglas-Peucker
DT	Delaunay triangulation
ED	error diffusion
ERD	explicit representation of discontinuities
ERDED	ERD using ED
ERDGPI	ERD using GPI
GPI	greedy point insertion
GPR	greedy point removal
GPRFS	GPR from subset
GVS	Garcia-Vintimilla-Sappa
HWT	hybrid wavelet triangulation
MED	modified ED
MGH	modified Garland-Heckbert
MIS	mesh-based image scaling
MISMG	MIS mesh generation
MSE	mean squared error
NEDI	new edge-directed image interpolation
PEE	percentage edge error
PSLG	planar straight line graph
PSNR	peak signal-to-noise ratio
SBIR	subdivision-based image-representation
SEMMG	squared-error minimizing mesh generation
SRCNN	super-resolution using convolutional neural network
SRGAN	super-resolution using generative adversarial network
SSIM	structural similarity
SUSAN	smallest univalue-segment assimilating nucleus
SVD	singular value decomposition
VDSR	very deep super-resolution

ACKNOWLEDGEMENTS

This thesis would have never been written without the help and support from numerous people. I would like to take this opportunity to express my sincere gratitude to certain individuals in particular.

First and foremost, I would like to thank my supervisor, Dr. Michael Adams. It has been an honor to be his first Ph.D. student. I, as a person who had zero knowledge in C++, truly appreciate all he has taught me in C++ programming, from the very basic to advanced concepts. All the efforts he put into preparing C++ materials, exercises, and lectures have significantly helped me to improve my programming skills which will surely help me into my future career. I am also really grateful for all his time and patience to review my writings, including the current dissertation. His thoughtful comments and feedback have greatly improved my writing skills as well as this dissertation. I sincerely appreciate his respectable dedication, commitment, and patience in guiding and supporting me throughout my Ph.D. program.

Next, I would like to express my appreciation to Dr. Pan Agathoklis and Dr. Venkatesh Srinivasan whose insightful comments and feedback in different stages of my Ph.D. program have really helped me to improve the work presented in this dissertation. Moreover, I want to thank my External Examiner, Dr. Ivan Bajić, whose thoughtful recommendations and detailed feedback have significantly improved the quality of this work. Furthermore, I would really like to thank our departmental IT technical support staff, especially Kevin Jones, who always patiently resolved any technical issues with the laboratory machines. Also, I truly thank my dear friend, Ali Sharabiani, for his great help in preparing the survey platform that is used for the subjective evaluation as part of the work in this thesis.

Lastly, I would like to thank my dearest family for all their love, support, and patience. I am thankful to my mom and dad, for being so supportive, understanding, and encouraging. I also thank my brother, Amin, who has always inspired me through this tough Ph.D. journey. And most of all, I am grateful to my beloved, encouraging, supportive, and patient wife, Susan, whose faithful support during the final and toughest stages of this Ph.D. is so appreciated. Thank you.

Success is not final, failure is not fatal: it is the courage to continue that counts.

Winston S. Churchill

DEDICATION

To my beautiful wife, inspiring brother, supportive dad, and caring mom.

Chapter 1

Introduction

1.1 Triangle Meshes for Image Representation

Images are most often represented using uniform sampling. Uniform sampling, however, is almost never optimal because it selects too many sample points in image regions with low variation in pixel intensity and too few sample points in regions with high variation in pixel intensity. Moreover, storing and transmitting uniformly-sampled images often requires large amounts of memory or high bandwidths. On the other hand, nonuniform sampling can choose sample points adaptive to the intensity variations in the image and is able to produce high quality results with a greater compactness which are beneficial in many applications. This is one reason why nonuniform sampling of images has received a considerable amount of attention from researchers recently [84, 13, 85, 46, 54, 96, 77, 74, 42]. Image representations based on nonuniform sampling have proven to be useful for many applications such as: computer vision [73], image filtering [25, 41], tomographic reconstruction [22], image coding [11, 30], feature detection [27], image restoration [21], pattern recognition [71], topography modeling [49], and image interpolation [82, 95, 75].

Among the classes of image representations based on nonuniform sampling, triangle-mesh models have become quite popular (e.g., [46, 95, 80, 60, 102]). An example of how a triangle-mesh model is used for image representation is illustrated in Figure 1.1. An original raster image shown in Figure 1.1(a). This image function can be associated with a surface as shown in Figure 1.1(b), where the height of the surface above the plane corresponds to the intensity of the image. A triangle-mesh model of such an image involves partitioning the image domain by a triangulation into a collection

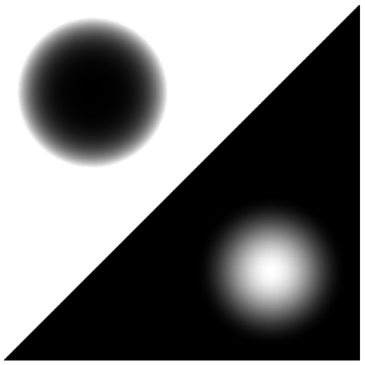

(a)

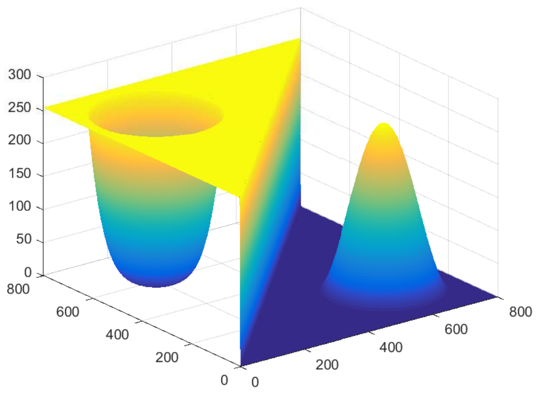

(b)

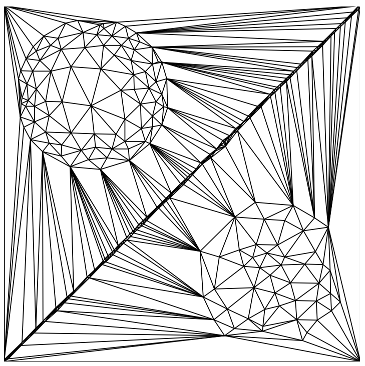

(c)

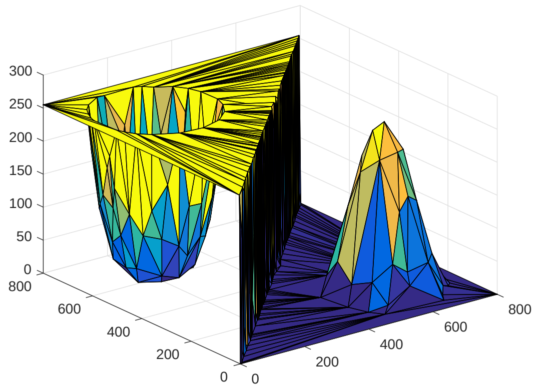

(d)

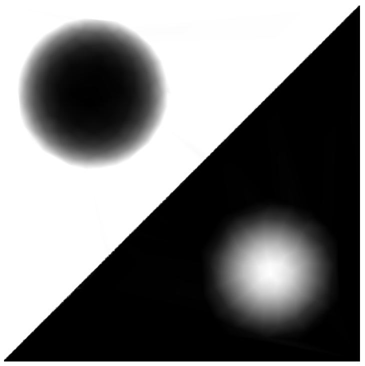

(e)

Figure 1.1: An example of how a triangle-mesh model is used for image representation. The (a) original image and (b) continuous surface associated with the raster image in (a). The (c) triangulation of image domain, (d) triangle-mesh model, and (e) reconstructed image.

of non-overlapping triangles as shown in Figure 1.1(c). The image function is then approximated over each face (i.e., triangle) in the triangulation. Next, by stitching all the approximating functions over faces together, the original image surface is approximated as shown in Figure 1.1(d). Finally, through a rasterization process, the triangulated surface in Figure 1.1(d) is converted to the reconstructed raster image shown in Figure 1.1(e). Using the triangle-mesh models as described above, images can still be represented in high quality, but with many fewer sample points and lower memory cost. Another practical advantage of using triangle-mesh models is that once a mesh model of an image, as the one shown in Figure 1.1(d), is generated, it can be stored and later used for different purposes, such as image editing, or any type of affine transformations, like scaling, rotation, and translation.

1.2 Generation of Mesh Models of Images

In order to use a mesh model, its parameters must first be chosen. The method to select the parameters of the mesh model is known as mesh generation. Given a particular mesh model, various methods are possible to generate that specific model, but each one can employ different parameter-selection techniques. For example, one parameter that is crucial to almost any mesh model is the set of sample points used by the model. Some mesh-generation methods select all the sample points in one step, whereas other methods select them by an iterative process with adding/removing points.

Several factors must be taken into consideration when choosing a mesh-generation method, such as the characteristics of the model, the type of the approximating function (e.g., linear and cubic), and the application in which the model is being used. For example, some methods are designed to only generate mesh models that are associated with continuous functions. As another example, methods that are designed for generating mesh models for a certain application (e.g., image representation) may not be much beneficial to other applications (e.g., image scaling). Therefore, the quality of a mesh-generation method is typically evaluated based on how effective the generated model performs in its specific application.

1.3 Image Scaling

Image scaling, as one of the classical and important problems in digital imaging and computer graphics, has received much attention from researchers. Image scaling refers to the operation of resizing digital images to obtain either a larger or a smaller image. The image-scaling application that is considered in this work is the operation of producing a raster image of larger size (i.e., higher resolution) from a raster image of smaller size (i.e., lower resolution), which is also referred to as upscaling, super-resolution, or resolution enhancement. Although image scaling is generally applicable to both grayscale and color images, the work in this thesis focuses on scaling grayscale images to keep the complexity low. As a future research, however, the work herein can be extended for color images too.

Image scaling is required in many applications such as in producing high-resolution images from the old images taken in the past with low-resolution cameras. Moreover, for printing images on a very large papers/posters, such as on billboards, the image scaling operation is needed to produce images of the size as large as the billboard size. Last, but not least, image scaling is the main operation required by any image zooming tool used in many applications (e.g., medical imaging, satellite imaging, and digital photography).

Image scaling is most commonly performed using an image interpolation method. Many different types of approaches for image interpolation are available. Some are raster based while others are vector based. An interpolation technique is often evaluated based on how well it handles undesired effects that can arise during the scaling process (e.g., edge blurring and ringing) and how well it preserves the qualitative attributes of the input image.

1.4 Historical Perspective

Due to the many advantages of triangle-mesh modeling, various types of triangle-mesh models and numerous mesh-generation schemes have been developed over the years. Similarly, different types of approaches have also been developed to solve the image-scaling problem. Therefore, in what follows, a historical perspective of the related work done in each of the above areas is presented.

1.4.1 Related Work in Mesh Models

Different triangle-mesh models can be categorized based on the type of the approximating functions associated with them. Most of the proposed mesh models are associated with an approximating function that is continuous everywhere, such as the work in [96, 43, 74, 12, 42, 82, 75, 102, 83, 63]. Images, however, usually contain a large number of discontinuities (i.e., image edges). Many types of mesh models have been proposed to consider image-edge information, however, they still use a continuous approximating function. For example, mesh models proposed by Garcia et al. [42] and Zhou et al. [102] employ a technique to represent the image edges using parallel polylines. The mesh model of Phichet et al. [83], however, uses a wavelet-based method to approximate the image-edge directions and then triangle edges are aligned with the image edges. Recently, Liu et al. [63] proposed a feature-preserving mesh model that considers the anisotropicity of feature intensities in an image. For this purpose, they have used anisotropic radial basis functions (ARBFs) to restore the image from its triangulation representation. Their method considers not only the geometrical (Euclidean) distances but also the local feature orientations (anisotropic intensities). Moreover, instead of using the intensities at mesh nodes, which are often ambiguously defined on or near image edges, their method uses intensities at the centers of mesh faces.

Another category of mesh models is the one that is associated with an approximating function which allows for selected discontinuities, such as the models in [72, 49, 90, 60, 84, 66]. For example, Tu and Adams [84] employed an explicitly-represented discontinuities (ERD) mesh model inspired by the model proposed in [72]. The approximating function associated with the ERD model is allowed to have discontinuities across certain triangulation edges. Typically, mesh models, such as the ERD model, that explicitly use image-edge information result in more compact meshes than the models, such as in [74], that do not consider image-edge features.

1.4.2 Related Work in Mesh Generation

In addition to the type of the mesh model itself, the method for generating such a model is of great importance too. Generally, mesh-generation methods can be classified into non-iterative and iterative approaches, based on how the sample points are selected. In non-iterative approaches, all the sample points are selected in one step, such as the methods in [96, 22, 40]. For example, Yang et al. [96] proposed a highly effective technique that uses the classical error-diffusion (ED) algorithm of Floyd and Steinberg [37] to select all the sample points such that their local density is proportional to the maximum magnitude of the second-order directional derivative of the image. Their method is fast with a low computational cost and easy to implement. The ED-based method of [96] was recently adapted by Tu and Adams [84] to generate the ERD model, resulting in the ERD with ED (ERDED) mesh-generation method.

Iterative mesh-generation methods themselves can be categorized into schemes that are based on mesh refinement, mesh simplification, or a combination of both. The mesh-refinement schemes begin with an initial mesh (such as a coarse mesh) and then iteratively refine the mesh by adding more points to the mesh until a desired mesh quality (or a certain number of sample points) is reached, such as the methods of [43, 12, 84, 42, 74, 102, 66]. For example, Garland and Heckbert [43] proposed a technique to iteratively select and insert the points with the highest reconstruction error into the mesh, using a L1-norm error metric. This method was later modified in [12] as called the modified-Garland-Heckbert (MGH) method, where a L2-norm error metric is used. In the MGH method a greedy point-insertion (GPI) scheme is used to make the point-selection process adaptive to the local squared error in the mesh. More specifically, in each iteration in the MGH method, the point with the highest absolute reconstruction error inside the face with largest squared error is inserted into the mesh. Then, the image function is approximated using a continuous function. Recently, Tu and Adams [84] adapted the GPI scheme of [12] to generate the ERD model, resulting in the ERD with GPI (ERDGPI) mesh-generation method.

In contrast, the mesh-simplification schemes start with a refined initial mesh, by selecting all or a portion of all the grid points in the image domain as the vertices in the mesh. Then, one or more vertices/edges are iteratively deleted based on some error metric, until a desired number of vertices is reached, such as the methods of [54, 30, 36, 13, 60]. The mesh-simplification methods, such as the well-known greedy point-removal (GPR) scheme of Demaret and Iske [30] (called “adaptive thinning” in [30]), are very effective in generating meshes of superior quality, but often have large computational and memory costs. This drawback, motivated researchers to propose some techniques to reduce the computational cost of the GPR method. For example, Adams [13] modified the GPR scheme by replacing the initial set of all image points with a subset of the points and introduced a new framework called GPR from subset (GPRFS). Then, the ED and modified ED (MED) schemes were utilized for selecting a subset of the points in the GPRFS framework and two new methods called GPRFS-

ED and GPRFS-MED were proposed, respectively. Both of these methods were shown to have much lower computational and memory complexities than the GPR scheme, but with different tradeoffs between mesh quality and computational/memory complexity.

The third category of iterative mesh-generation methods is the one that combines the mesh-refinement and mesh-simplification schemes. These methods, such as the incremental/decremental techniques of [14, 15, 64] and the wavelet-based approach of [83], take advantage of both point-insertion and point-removal operations. They typically tend to achieve meshes of higher quality than those obtained by mesh-refinement approaches, but such hybrid schemes can sometimes be extremely slow, even slower the the mesh-simplification methods.

In addition to the mesh-generation methods that build a mesh from beginning, another type of work, which has recently become more popular, is based on mesh optimization/adaptation. This type of work focuses on improving the quality of a mesh, which may have been generated from any method, through an iterative process of mesh optimization or adaptation. These mesh optimization/adaptation methods may not be directly considered as mesh-generation schemes essentially because they do not generate the mesh from the beginning. For example, the mesh-optimization methods of Xie et al. in [92, 91] perform both geometry and topology optimizations to strictly reduce the total energy. In their mesh-optimization algorithm, the position of a vertex can be re-adjusted several times, so that the local optimality of that vertex would not be corrupted during later processing of other vertices. In another recent work, Li [58] introduced an anisotropic mesh-adaptation (AMA) method for image representation. The AMA method of Li [58] starts directly with an initial triangular mesh and then iteratively adapts the mesh based on a user-defined metric tensor to represent the image.

1.4.3 Related Work in Image Scaling

In addition to studying the triangle-mesh models for image representation, a significant part of this thesis is focused on the application of mesh models in image scaling. The problem of image scaling, which also goes by the names of image resizing, resolution enhancement, and super-resolution, is essentially ill-posed because much information is lost in the degradation process of going from high to low resolution. Much work has been done on this topic over many years, with some considerable advancements made over the recent years. Each super-resolution method has different advantages and drawbacks. Many image scaling approaches are based on the classical convolution-based interpolation techniques, such as nearest-neighbor, bilinear, bicubic [51], and cubic spline [48] interpolation. Although these methods are fast with very low computational cost, they have the problem of producing blurring (or other artifacts such as blocking and ringing) around image edges. This drawback of the classical methods is mainly because they are not able to recover the high frequency components which provide visual sharpness to an image.

Since the human visual system is particularly drawn to distortions in edges, many edge-directed image interpolation methods have been proposed to reduce the artifacts produced by the classical interpolation methods. Some examples of the effective edge-directed raster-based methods can be found in [59, 99, 24, 44, 17, 101, 98]. In these methods, a crucial step is to explicitly or implicitly estimate the edge directions in the image. For example, the new edge-directed image interpolation (NEDI) method of Li and Orchard [59] uses the local covariances of the image to estimate the edge directions. This method was later improved by Asuni and Giachetti [17] by reducing numerical instability and making the region used to estimate the covariance adaptive. In another work, Giachetti and Asuni [44] proposed an iterative curvature-based interpolation, which is based on a two-step grid filling technique. After each step, the interpolated pixels are iteratively corrected by minimizing an objective function depending on the second-order directional derivatives of the image intensity while trying to preserve strong discontinuities. Moreover, in the directional cubic-convolution interpolation (DCCI) method of Zhou et al. [101], which is an extension of the classical cubic convolution interpolation of Keys [51], local edge direction is explicitly estimated using the ratio of the two orthogonal directional gradients for a missing pixel position. Then, the value at the missing pixel is estimated as the weighted average of the two orthogonal directional cubic-convolution interpolation values. Although these edge-directed super-resolution approaches can improve the subjective quality of the scaled images by tuning the interpolation to preserve the edges of the image, they have high computational complexity. Moreover, although the high-resolution images produced using these methods have sharper edges than those obtained by the classical methods, they often still contain some degree of artifacts like blurring and rippling at the edges.

The most recent advances in the image scaling (also called super-resolution) techniques are based on machine learning. The excellent performance of image scaling methods based on machine learning has recently gained much attention from researchers [89, 33, 62, 52, 78, 86, 57]. In general, learning-based techniques for image super-resolution can be divided into *external* and *internal* methods [89]. External methods, such as [39, 53, 94], learn the mapping between low-resolution and high-resolution image patches, from a large and representative external set of image pairs based on external image samples. Internal methods, however, such as [93, 45, 38], are motivated by the fact that images generally contain a lot of self-similarities. Therefore, internal methods search for example patches from the input image itself, based on the fact that patches often tend to recur within the image or across different image scales. Both external and internal image super-resolution methods have different advantages and disadvantages. For example, external methods perform better for smooth regions as well as some irregular structures that barely recur in the input, but these methods are prone to producing either noise or over-smoothness. Internal methods, however, perform better in reproducing unique and singular features that rarely appear externally but repeat in the input image.

Recently, Wang et al. [89] proposed a joint super-resolution method to adaptively combine the external and internal methods to take advantage of both. Another recent and well-known work is the SRCNN method of Dong et al. [33], which is an image super-resolution (SR) method based on deep convolutional neural networks (CNN). The SRCNN method directly learns an end-to-end mapping between the low/high-resolution images (i.e., it is an external example-based method). The mapping is represented as a deep convolutional neural network that takes the low-resolution image as the input and outputs the high-resolution one. Through experimental results, Dong et al. [33] demonstrated that deep learning is useful in the classical problem of image super-resolution, and can achieve good quality and speed. They designed the SRCNN method based on a three-layer network and concluded that deeper structure does not always lead to better results. Later, Kim et al. [52], however, improved over the SRCNN method and showed that using a deeper structure can achieve better performance. They proposed a very deep super-resolution (VDSR) method that employs a network with depth of 20 layers as apposed to three layers in the SRCNN method. Similar to the most existing super-resolution methods, the SRCNN model is trained for a single scale factor and is supposed to work only with that specified scale. Thus, if a new scale is demanded, a new model has to be trained. In the VDSR model of [52], however, a single network is designed and trained to handle the super-resolution problem with multiple scale factors efficiently. Despite all the advances and breakthroughs in accuracy and speed of image super-resolution using faster and deeper convolutional neural networks, one essential problem has always been how to recover the finer texture details at large upscaling factors. In a very recent work, Ledig et al. [57] proposed an advanced super-resolution (SR) technique using a generative adversarial network (GAN) called SRGAN, which can recover photo-realistic textures from heavily downsampled images. Previous works commonly relied on minimizing the mean squared error (MSE) between the recovered high-resolution image and the ground truth, but minimizing MSE does not necessarily reflect the perceptually better super-resolution result [57]. The SRGAN method, however, relies on a novel perceptual loss function to recover visually more convincing scaled images. Most of the learning-based super-resolution methods, especially those based on deep learning, are very powerful general-purpose methods with excellent performance. They are, however, computationally expensive and need a huge training dataset to be able to perform reasonably well.

Another category of image interpolation techniques, is based on triangle-mesh modeling. Since the triangle-mesh model obtained from an image is resolution-independent, it can be rasterized to an image grid of any arbitrary resolution. This fact has motivated researchers to use triangle-mesh models in the application of image scaling as in [82, 75, 102, 100, 61, 67]. For almost all of these triangulation-based methods to be effective in image scaling, the first essential step is to estimate the edge directions in the image. Then, the second step is to maintain the parallelism of the triangle edges with the image edges. Su and Willis [82], for instance, proposed an edge-directed image interpolation technique by pixel-level data-dependent triangulation (DDT), where the image-edges directions are locally estimated by evaluating the four intensity values at each set of four pixels forming the smallest square in the image grid. Their method, however, only considers the diagonal edge directions. This method was later improved by Shao et al. [75] by considering the horizontal and vertical edge directions in addition to the diagonal direction. Moreover, they defined a threshold for each direction to determine whether it is an edge or not. Later, Zhenjie et al. [100] improved upon the work of Su and Willis [82] by proposing a more effective algorithm to determine the edge direction. More recently, Liu et al. [61] proposed an image interpolation technique using the DDT and a new weighted subdivision scheme. In their method, an image is first converted to a triangular mesh using a DDT. The mesh is then subdivided by controlling the weight coefficients of a rational subdivision. Using the proposed rational subdivision, the image edges are kept sharper during the subdivision process.

As reviewed earlier, most of the mesh-based image interpolation techniques used for image scaling (e.g., [82, 75, 100, 61]) are based on DDTs where all of the grid points in the image are used to generate the mesh. Although using all image points helps to capture details and textures in the image more accurately, this greatly increases the computational and memory cost. In contrast, some methods, such as the curvilinear feature driven technique of Zhou et al. [102], start with a smaller initial mesh and iteratively refine the mesh. In the work of [102], the locations and directions of image edges are first estimated using an edge detector. This edge information is then explicitly used in the triangle-mesh model to preserve the sharpness of the edges in the reconstructed images after scaling. Similar to the work of [61], the proposed method of [102] employs subdivision techniques to produce sufficiently smooth edge curvatures and image functions during scaling. The methods, which do not use all the image points, have much lower computational cost and usually work perfectly for cartoon images. For natural images, however, they have not been widely used because they are not able to capture the complicated textures and details that usually exist in natural images. The mesh-based super-resolution techniques have recently become increasingly popular because, unlike other convolution-based and learning-based methods, they are capable of producing reusable image models that are compact, editable, and scalable. Moreover, they have lower computational and memory cost compared with many state-of-the-art methods based on deep learning that require a huge training dataset.

1.5 Overview and Contribution of the Thesis

In this thesis, image representation using triangle-mesh models and its application in image scaling are explored, resulting in two new methods for solving two different problems. More specifically, a new squared-error minimizing mesh-generation (SEMMG) method is first proposed to address the problem of image representation, by generating ERD mesh models that are effective for grayscale-image representation. Then, to solve the image-scaling problem, the application of the ERD mesh models in image scaling is studied, leading to the proposal of a new mesh-based image scaling (MIS) method for grayscale images that are piecewise-smooth.

The remainder of this thesis consists of six chapters and three appendices. This material is organized as follows.

Chapter 2 provides the background material essential to the understanding of the work presented herein. First, some notation, terminology, and basic geometry concepts are presented, followed by some basic algorithms (e.g., polyline simplification, Otsu method, edge detection, and supersampling). Next, several fundamentals from computational geometry are introduced including Delaunay and constrained Delaunay triangulations. Then, mesh models and mesh-generation methods are formally defined. After that, the ERD mesh model and its mesh-generation methods, namely, the ERDED and ERDGPI methods, on which our work is based, are explained. Then, the image-scaling problem addressed in our work is formally defined. Finally, three metrics, namely, the peak signal-to-noise ratio (PSNR), structural similarity (SSIM) index, and percentage edge error (PEE) that are used herein for image quality assessment are introduced.

In Chapter 3, to solve the mesh-generation problem, the new SEMMG method is proposed for producing ERD triangle-mesh models that are effective for grayscale image representation. First, we present some analysis on two schemes for generating ERD triangle-mesh models, namely, the ERDED and ERDGPI methods. Through this analysis, potential areas for improvement in different steps of the methods are identified. Then, more effective techniques are developed to select the parameters of the ERD mesh model, by applying several key modifications. Finally, all the modifications are integrated into a unified framework to yield the new SEMMG method.

In Chapter 4, the performance of the SEMMG method is evaluated by comparing the quality of the meshes it produces with those obtained by several other competing methods. In the case of the methods with implementations, the proposed SEMMG method is compared with four approaches, namely, the error-diffusion (ED) method of Yang [96], the modified Garland-Heckbert (MGH) method in [12], and the ERDED/ERDGPI methods of Tu and Adams [84]. Moreover, in the case of the methods without available implementations, the SEMMG method is compared with other four approaches, namely, the Garcia-Vintimilla-Sappa (GVS) method [42], the hybrid wavelet triangulation (HWT) method of Phichet [83], the binary space partition (BSP) method of Sarkis [74], and the adaptive triangular meshes (ATM) method of Liu [63]. For this evaluation, errors between the original and reconstructed images, obtained from each method under comparison, are measured in terms of the PSNR. Moreover, in the case of the competing methods whose implementations are available, the subjective quality is compared in addition to PSNR. Evaluation results show that the reconstructed images obtained from the SEMMG method are better than those obtained by the competing methods in terms of both PSNR and subjective quality. More specifically, in the case of the methods with implementations, the results collected from 350 test cases show that the SEMMG method outperforms ED, MGH, ERDED, and ERDGPI schemes in approximately 100%, 89%, 99%, and 85% of cases, respectively. Moreover, in the case of the methods without implementations, we show that the PSNR of the reconstructed images produced by the SEMMG method are on average 3.85, 0.75, 2, and 1.10 dB higher than those obtained by the GVS, HWT, BSP, and ATM methods, respectively. Furthermore, for a given PSNR, the SEMMG method is shown to produce much smaller meshes compared to those obtained by the GVS and BSP methods, with approximately 65 to 80% fewer vertices and 10 to 60% fewer triangles, respectively.

In Chapter 5, for solving the image-scaling problem, the application of triangle-mesh models in image scaling is studied, leading to the development of the proposed MIS method for scaling grayscale images that are approximately piecewise-smooth. Most of the existing mesh-based image-scaling approaches (e.g., [82, 75, 102, 100, 61]) employ mesh models with approximating functions that are continuous everywhere, yielding blurred edges after image scaling. Other mesh-based image-scaling approaches that employ approximating functions with discontinuities (such as [60]) are often based on mesh simplification where the method starts with an extremely large initial mesh, leading to a very slow mesh generation, with high memory cost. The MIS method that is proposed herein, however, firstly, employs an approximating function with selected discontinuities to minimize edge blurring. Secondly, the MIS method in based on mesh refinement which can generally be faster, with lower memory cost, than the approaches employing mesh simplification. For developing the MIS method, the performance of our SEMMG method, which is proposed for image representation, is examined in the application of image scaling. Although the SEMMG method is not designed for image scaling, we study its application in image scaling in order to identify potential shortcomings for this specific application. Through this study, several key techniques are applied to effectively address the shortcomings. Then, by integrating all these techniques, we propose a new method called MISMG that can generate ERD mesh models with the parameters that are more beneficial to the image scaling application. Aside from the mesh generation, several areas in model rasterization are also analyzed and a subdivision-based approach for producing smoother edge contours and image functions is developed. Next, the MISMG mesh-generation method is combined with a scaling transformation and the subdivision-based model-rasterization algorithm, yielding the MIS method.

In Chapter 6, we compare our MIS method with other image scaling methods. For this purpose, the MIS method is compared to five well-known raster-based scaling methods, including bilinear interpolation, bicubic interpolation of Keys [51], the directional cubic-convolution interpolation (DCCI) method of Zhou et al. [101], the new edge-directed image interpolation (NEDI) method of Li and Orchard [59], and the super-resolution with convolutional neural networks (SRCNN) method of Dong et al. [33], using experimental comparisons. Since our main focus is to produce scaled images of better subjective quality with the least amount of edge blurring, the comparison is first performed through a subjective evaluation followed by some objective evaluations. The results of the subjective evaluation show that the proposed MIS method was ranked best overall in almost 67% of the cases, with the best average rank of 2 out of 6, among 380 collected rankings with 20 images and 19 participants. Moreover, visual inspections on the scaled images obtained with different methods show that the proposed MIS method produces scaled images of better quality with more accurate and sharper edges compared to those obtained with other methods which contain blurring or ringing artifacts. In the case of the mesh-based image scaling methods, where an experimental comparison was not possible, the MIS method is compared to the subdivision-based image-representation (SBIR) method of Liao et al. [60] and the curvilinear feature driven image-representation (CFDIR) method of Zhou et al. [102], with a conceptual comparison, highlighting the theoretical differences between the methods.

Chapter 7 concludes the thesis by summarizing the work and key results presented herein and providing some suggestions for future research.

In Appendices A and B, the test images used in this thesis for mesh generation and image scaling are listed, respectively, and a thumbnail of each of them is also provided.

Appendix C represents the full set of experimental results collected for comparing the proposed SEMMG method.

Appendix D describes the software developed for implementing the algorithms and collecting the results presented in this work. This appendix includes a brief description of the programs, their command-line interface as well as data formats employed. For the benefit of the reader, some examples of how to use the software are also provided.

Chapter 2

Preliminaries

2.1 Notation and Terminology

First, a brief digression concerning the notation and terminology used herein is appropriate. Some of the notational conventions employed are as follows. The symbols $\mathbb{Z}$ and $\mathbb{R}$ denote the sets of integers and real numbers, respectively. The cardinality of a set S is denoted by $|S|$. A triangle formed by three vertices A,B, and C is denoted by $\triangle ABC$. An edge (or a line segment) connecting two points A and B is denoted by $\overline{AB}$.

2.2 Basic Geometry Concepts

In this section, we introduce some basic concepts in geometry that are used later. To begin, we introduce the concepts of convex set and convex hull.

Definition 2.1. *(Convex set). A set P of points in $\mathbb{R}^2$ is said to be convex if, for every pair of points $p, q \in P$, the line segment $\overline{pq}$ is completely contained in P.*

An example of a convex set and a nonconvex set is illustrated in Figure 2.1. As can be seen from this figure, for the set P in Figure 2.1(a), any line segment connecting a pair of arbitrary points is completely contained in P, such as the line $\overline{pq}$. Thus, the set P in Figure 2.1(a) is convex. In contrast, for the set P in Figure 2.1(b), a line such as $\overline{pq}$ is not fully contained in P. Therefore, the set P in Figure 2.1(b) is not convex. Having introduced the concept of convex set, in what follows, we provide the definition of a convex hull.

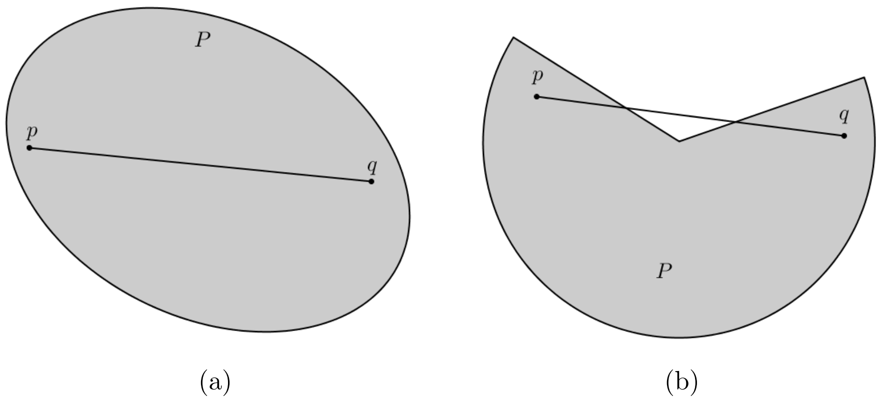

Figure 2.1: Example of a (a) convex set and (b) nonconvex set.

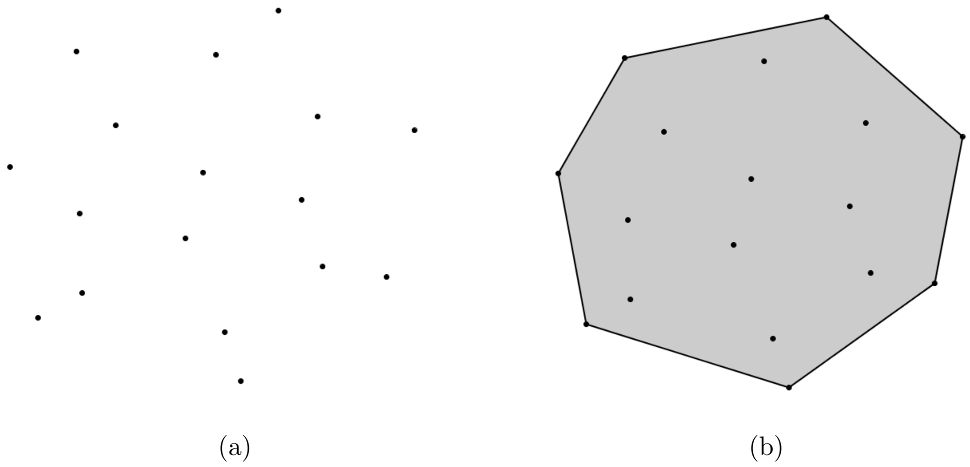

Figure 2.2: Example of a convex hull. (a) A set of points and (b) its convex hull.

Definition 2.2. *(Convex hull). The convex hull of a set P of points in $\mathbb{R}^2$ is the intersection of all convex sets that contain P (i.e., the smallest convex set containing P).*

An example of a convex hull is shown in Figure 2.2. For a set of points illustrated in Figure 2.2(a), its corresponding convex hull is depicted as the shaded area in Figure 2.2(b). Another geometry concept that needs to be introduced is called the planar straight-line graph (PSLG) which is defined next.

Definition 2.3. *(Planar straight line graph (PSLG)). A planar straight line graph is a set P of points in $\mathbb{R}^2$ and a set E of line segments, denoted (P, E), such that:*

1. *each line segment of E must have its endpoints in P, and*

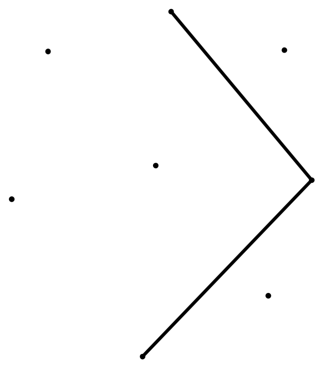

Figure 2.3: Example of a PSLG with eight points and two line segments.

2. *any two line segments of E must either be disjoint or intersect at most at a common endpoint.*

Figure 2.3 shows an example of a PSLG consisting of a set of eight points and a set of two line segments.

The last concept from basic geometry that needs to be introduced is that of a **polyline**. In geometry, a **polyline** is a set of connected consecutive line segments. The general definition of a polyline allows for self intersections. For the purposes of this thesis, however, if a polyline has one or more self-intersections (excluding loops), the polyline is split at each intersection point. In this way, the line segments in a polyline are guaranteed not to have any intersections (excluding loops). Polylines are often used to approximate curves in many applications. Figure 2.4 shows an example of a polyline consisting of seven points and six line segments.

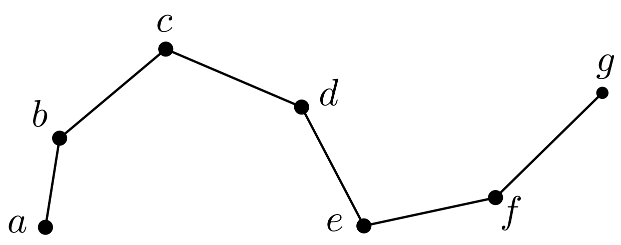

Figure 2.4: Example of a polyline.

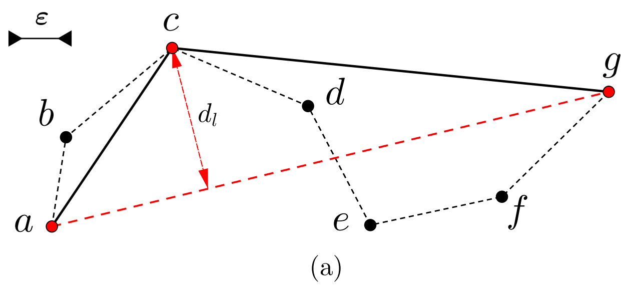

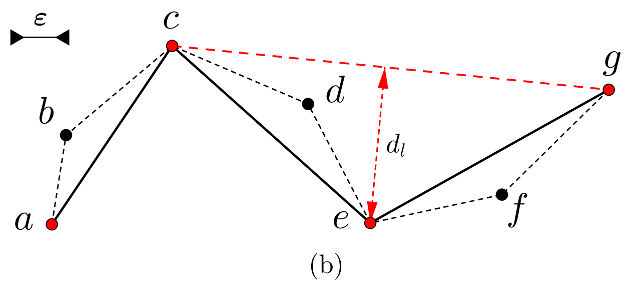

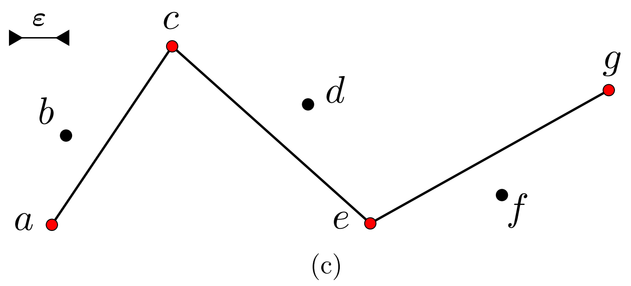

Figure 2.5: An example of the polyline simplification using the DP algorithm. (a) and (b) the procedures of the polyline simplification, and (c) the simplified polyline.

2.3 Polyline Simplification

Polylines may contain too many points for an application. Therefore, for the sake of efficiency, a simplified polyline with fewer points is used to approximate the original polyline. The process of reducing the number of points in a polyline to achieve a new polyline is called **polyline simplification**.

Among the many polyline-simplification methods that have been introduced to date, the Douglas-Peucker (DP) algorithm [34] is one of the classical ones which is widely used. The DP algorithm starts with the two end points of the original polyline and iteratively adds points based on a specific tolerance ε until a satisfactory approximation is achieved as follows. First, the DP algorithm marks the first and the last points of the polyline to be kept. Then, it forms a line segment connecting the first and last points of the polyline, and finds a point p that is furthest from the line segment with a distance d_l . If d_l is larger than ε, the point p is marked to be kept and the algorithm continues. If d_l is smaller than ε, the algorithm stops and all the unmarked points between the first and last points are discarded.

An example of the process of the DP simplification algorithm for the original polyline $abcdefg$ given in Figure 2.4 is illustrated in Figure 2.5, where the tolerance ε is specified in the top-left corner. As Figure 2.5(a) shows, in the DP algorithm, the line segment connecting the first point a and last point g is formed. Then, the distance between each point from b to f and the line segment $\overline{ag}$ is calculated, and the point c is selected as the point with the largest distance d_l. Since d_l is larger than ε, the point c is marked to be kept. So far, three points, namely a, c and g, are marked to be kept. In Figure 2.5(b), similarly, we look for a point between a to c and a point between c to g that is furthest from $\overline{ac}$ and $\overline{cg}$, respectively, with a distance d_l greater than ε. As a result, only the point e as shown in Figure 2.5(b) is marked to be kept, while b is not kept because its distance from $\overline{ac}$ is not larger than d_l. Next, since none of the points b, d, and f, in Figure 2.5(b) are further than ε from $\overline{ac}$, $\overline{ce}$, and $\overline{eg}$, respectively, the simplification process stops. Finally, a simplified polyline consisting of all the points that have been marked as kept (i.e., a, c, e, and g), is generated as shown in Figure 2.5(c). As can be seen from this figure, the simplified polyline $aceg$ is a reasonably good approximation of the original one $abcdefg$, but with three fewer points.

2.4 Otsu Thresholding Technique

In this section, the Otsu thresholding technique, which is used in the work herein, is introduced. In computer vision and image processing, the process of converting a grayscale image to a binary image with respect to a given threshold is referred to as image thresholding (i.e., image binarization). In image thresholding, the pixels whose gray levels are less than a given constant τ (i.e., threshold) are replaced with black pixels (i.e., zero intensity) and those with gray levels greater than τ are replaced with white pixels (i.e., maximum intensity). Figure 2.6 illustrates an example of image thresholding with the lena image from Appendix A. For the grayscale image given in Figure 2.6(a), the corresponding binary image obtained with $\tau = 128$ is shown in Figure 2.6(b).

Among the many image-thresholding approaches proposed to date, the Otsu

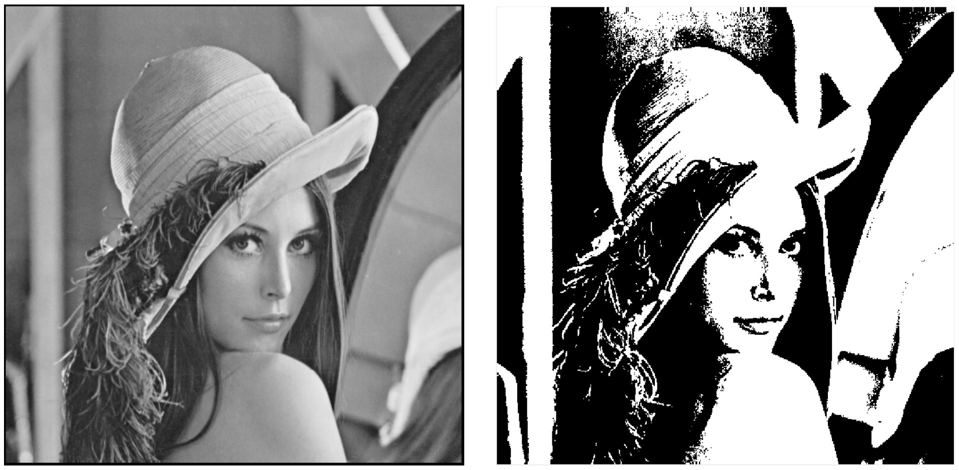

Figure 2.6: An example of image thresholding. The (a) original lena image and (b) the corresponding binary image obtained with $\tau = 128$.

method [68] is a well-known automated clustering-based technique which is used frequently in computer vision and image processing. With the assumption that the image approximately has a bimodal histogram with two classes of pixels, the Otsu algorithm computes the optimum threshold to separate the two classes so that their inter-class variance is maximal (or equivalently, the intra-class variance is minimal). In the context of image thresholding, the input to the Otsu method is a grayscale image and the output is the optimum threshold value. Once the threshold is determined, the binary image can be simply obtained using the threshold.

2.5 Edge Detection

In image processing and computer graphics, edges are one of the most fundamental features of an image since they contain vital information for many applications. Studies have also shown that the human visual system attaches a great importance to edges. An edge can be defined as a contour in an image at which the image function changes abruptly. In other words, edges represent the locations of discontinuities in the image function and the process that estimates the presence and position of edges in an image is known as **edge detection**. The input to the edge detection is a grayscale image and the output is a binary edge map, where each pixel is marked either as an edge point or as a non-edge point. An example of an edge map is illus-

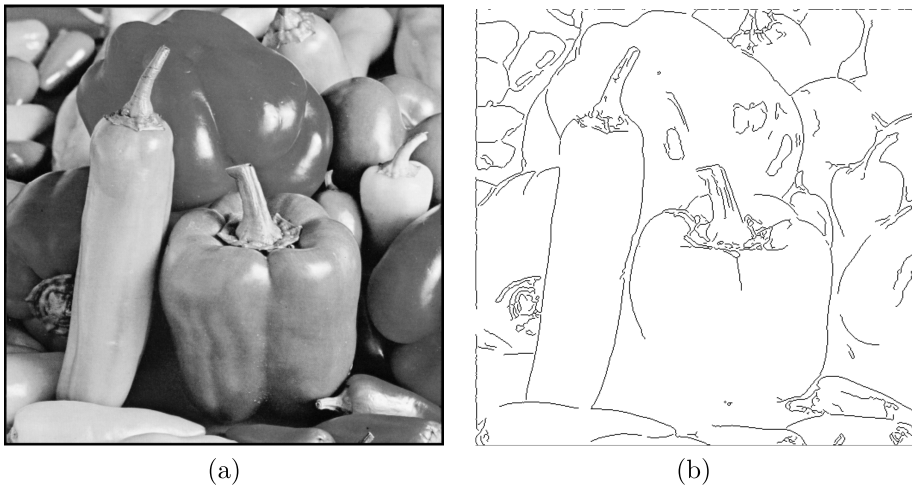

Figure 2.7: An example of an edge detection. (a) The original peppers image and (b) the edge map produced by edge detection.

trated in Figure 2.7 for the peppers image from Appendix A. For the input image shown in Figure 2.7(a), its corresponding edge map is illustrated in Figure 2.7(b), where black pixels represent the estimated edge locations.

Many classes of edge-detection methods have been introduced to date, including edge focusing [19], multi-resolution schemes [55, 103], and anisotropic diffusion methods [70, 20] to name a few. Extensive surveys on edge-detection methods can also be found in [104, 18]. Also, an entirely different approach to low level image processing (including edge detection) was introduced by Smith and Bradly in [79] under the name of the smallest-univalue-segment-assimilating-nucleus (SUSAN) algorithm. Edge detection is of great importance in this thesis since, as will be seen later, it is used as a key step in the mesh-generation process. In particular, the accuracy of the edge detector employed is very important. In what follows, two different edge-detection methods of interest herein, namely the Canny and SUSAN edge detectors, are introduced.

2.5.1 Canny Edge Detection

One of the most extensively used edge detectors is the Canny edge detector which was proposed by Canny [23]. Canny's technique is based on optimizing three criteria desired for any edge-detection filter: good detection, good localization, and only one response to a single edge. The input to the Canny edge detector is a raster image ϕ

which is known only at the points in $\Lambda = \{0, 1, ..., W-1\} \times \{0, 1, ..., H-1\}$ (i.e., a truncated integer lattice of width W and height H). The output of the Canny edge detector is a binary image B defined in Λ. The image B is called the binary edge map as it holds the estimated locations of the edges in the input image. In general, the Canny edge detector consists of four main steps: 1) gradient calculation, 2) local non-maxima suppression, 3) hysteresis thresholding, and 4) edge thinning. In what follows, the detail of each step is presented.

1) Gradient calculation. In the first step, for the input image ϕ defined in Λ, the magnitude and direction of the gradient of each pixel in the original image are calculated (i.e., estimated). To achieve this, the image is first smoothed in the direction (e.g., horizontal and vertical) in which the gradient is calculated. Then, an appropriate convolution mask is used to calculate the values of the first-order partial derivatives in that direction. Assume that the first-order partial derivatives in the horizontal and vertical directions for a pixel are estimated as G_x and G_y, respectively. Then, the gradient magnitude G and the gradient direction θ at that pixel are determined by

$$G = \sqrt{G_x^2 + G_y^2}$$

and

$$\theta = \operatorname{atan2}(G_y, G_x),$$

respectively, where function "atan2" computes the arctangent of G_y/G_x, as defined in the C language standard [1]. The $\operatorname{atan2}(y, x)$ returns tangent inverse of (y/x) in radians which lies between $-\pi$ and π, representing the angle θ between x-axis and the ray from the origin to the (x, y) point, excluding the origin.

2) Non-maxima suppression. After estimating the image gradient magnitude and direction at each pixel location, the Canny edge detector undertakes a search to determine whether the gradient magnitude at each pixel assumes a local maximum in the gradient direction. If the gradient magnitude of the pixel of interest is greater than the gradient magnitudes of the nearby points along the gradient direction, the pixel of interest is considered a local maximum and marked as an edge point. Otherwise, the pixel of interest is suppressed by marking it as a non-edge point. At this step, an edge map f_e is obtained containing a set of non-maxima suppressed edge points.

3) Hysteresis thresholding. The next step is thresholding. Pixels with larger gradient magnitudes are more likely to correspond to actual edges than those with smaller gradient magnitudes. In most cases, however, deciding whether a pixel with a given gradient magnitude corresponds to an edge by specifying only a single threshold is difficult. Therefore, the Canny edge detector uses hysteresis thresholding as follows. Thresholding with hysteresis employs two thresholds, a high threshold τ_h and a low threshold τ_l. If the gradient magnitude of an edge pixel in image f_e (from the previous step) is greater than τ_h, the pixel will be kept as a strong edge point. The pixels whose gradient magnitudes are smaller than τ_l will not be considered as an edge point. In the case of the pixels whose gradient magnitudes are between τ_l and τ_h, the pixels are traced and if they are connected to a strong edge point, they will be kept as an edge point in $f_{\texttt{final}}$. In this way, hysteresis thresholding can help to find weak edges.

4) Edge thinning. Finally, an image processing task called edge thinning is performed on the edge map $f_{\texttt{final}}$ to result in the edge map B with one-pixel-thick edge elements.

Once the above four-step process is complete, we have the output binary edge map B (e.g., Figure 2.7(b)), where each pixel is marked either as an edge point or as a non-edge point. Numerous variations of the Canny edge detector have been introduced to date. The modified Canny edge detector proposed by Ding and Goshtasby in [32] improves the accuracy of the detected edges in the vicinity of intersecting edges, where the original Canny edge detector often performs poorly.

2.5.2 SUSAN Edge Detection

The smallest-univalue-segment-assimilating-nucleus (SUSAN) algorithm [79] is a different approach to low level image processing that can be used for edge and corner detection and structure-preserving noise reduction. A nonlinear filtering is used to define which parts of the image are closely related to each individual pixel. Each pixel is then associated with a local image region that is of similar brightness to that pixel. Same as the Canny edge detector, the input to the SUSAN edge detector is a raster image ϕ which is known only at the points in $\Lambda = \{0, 1, ..., W-1\} \times \{0, 1, ..., H-1\}$ (i.e., a truncated integer lattice of width W and height H). The output of the SUSAN edge detector is a binary edge map B defined in Λ, where each pixel is marked either as an edge point or as a non-edge point.

The SUSAN method employs a circular mask. The basic idea of the SUSAN edge detector is to use a pixel's similarity to its neighbors' gray values as classification criterion. The area of the mask that has the similar brightness as the center pixel (nucleus) is called the univalue-segment-assimilating-nucleus (USAN) area. An example of how the USAN area is defined is illustrated in Figure 2.8. An image of a dark rectangular object on a white background along with three circular masks placed at different regions of the image is shown in Figure 2.8(a). The USAN area corresponding to each circular mask is illustrated in Figure 2.8(b) as a white region inside each mask. The main steps of the SUSAN edge-detection method are as follows:

1. First, a circular mask is placed at each pixel in the input image ϕ and a similarity function c between each pixel p inside the mask and the center pixel p_0 is computed by

$$c(p, p_0) = e^{-\left(\frac{\phi(p)-\phi(p_0)}{t}\right)^6}, \tag{2.1}$$

   where t is a brightness difference threshold (e.g., $t = 27$ in [79]).

2. Next, the USAN area n associated with each center pixel p_0 is calculated by summing all of the similarity values obtained from (2.1) inside each mask as

$$n(p_0) = \sum_p c(p, p_0).$$

3. Next, a thresholding process is applied to find the pixels whose USAN area is less than a specific threshold and to calculate the edge response R for each pixel p_0 as given by

$$R(p_0) = \begin{cases} g - n(p_0) & \text{if } n(p_0) < g \\ 0 & \text{otherwise,} \end{cases} \tag{2.2}$$

   where g is a fixed threshold which is set to $3n_{\max}/4$, and $n_{\max}$ is the maximum value that n can take. Then, an initial edge map is generated, where pixels with non-zero R values are the edge pixels. In (2.2), larger values of R correspond to stronger (i.e., sharper) edges.

4. Once the thresholding step is done, edge direction is determined using the method proposed in [79], which employs moment calculations of the USAN area.

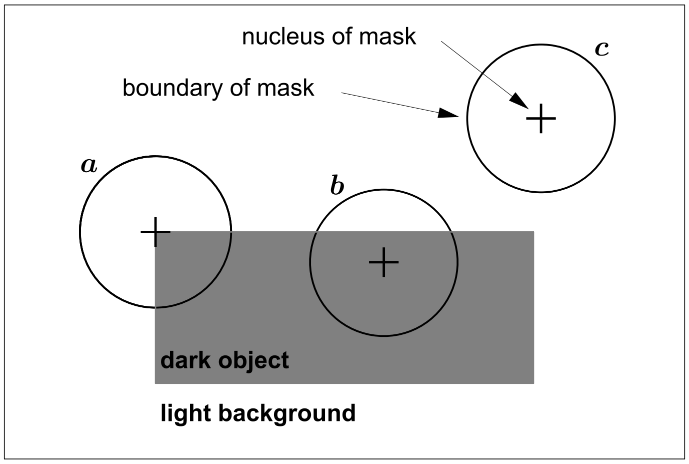

(a)

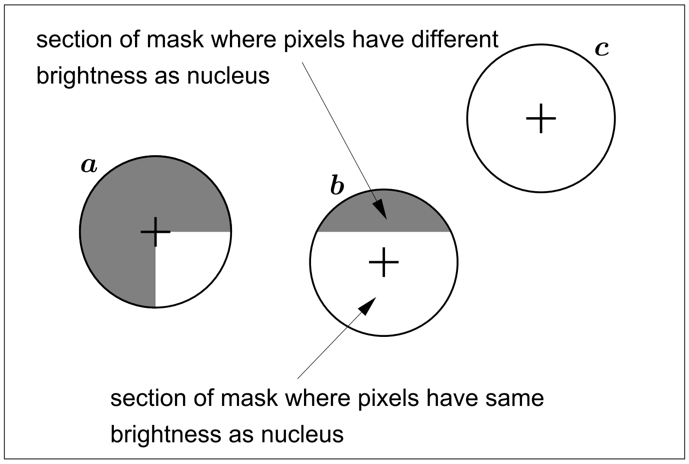
section of mask where pixels have different brightness as nucleus
c
a
b
section of mask where pixels have same brightness as nucleus

(b)

Figure 2.8: An example of USAN area. (a) Original image with three circular masks placed at different regions and (b) the USAN areas as white parts of each mask.

5. Then, non-maxima suppression is performed on the initial edge map in the direction perpendicular to the edge.

6. Finally, the non-maxima-suppressed edge map is thinned to obtain the final binary edge map B with one-pixel-thick edge elements.

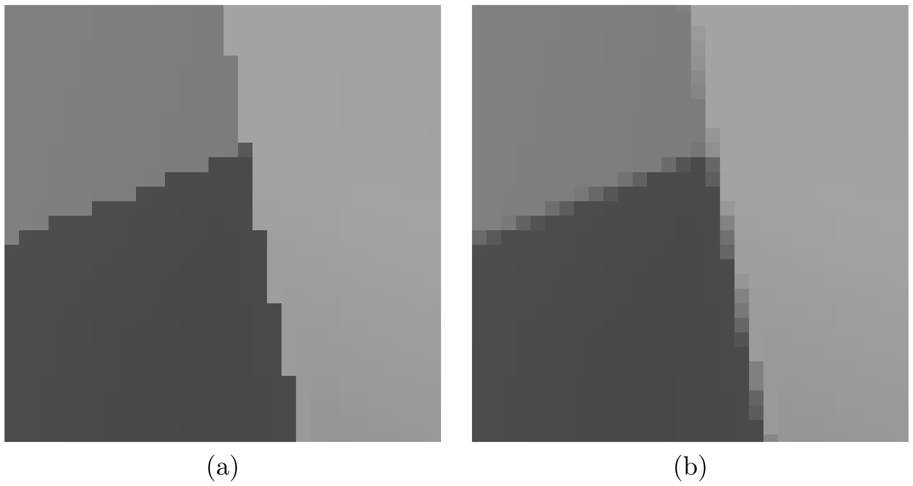

Figure 2.9: Example of anti-aliasing using a small part of the cherry image. (a) The aliased image with jagged edges and (b) the image after anti-aliasing.

2.6 Anti-aliasing and Supersampling

In the context of computer graphics and image rasterization, the jagged and pixelated edges in a rendered image is referred to as **aliasing**. The aliasing distortion often occurs in a region of image where the density of samples points are not sufficiently large to properly represent the high-frequency components of that region. Therefore, to improve the quality of an image, we need to reduce this aliasing distortion (i.e., the jagged edges) in the image.

The technique of minimizing aliasing is known as **anti-aliasing**. An example of the aliasing distortion during image rasterization using the cherry image from Appendix A is illustrated in Figure 2.9. The jagged and pixelated edges that are visible in the aliased image in Figure 2.9(a) are effectively eliminated in the image shown in Figure 2.9(b) where anti-aliasing is used. Therefore, the anti-aliased image in Figure 2.9(b) looks much better than the aliased image in Figure 2.9(a).

One well-known anti-aliasing technique is called **supersampling**. Using supersampling, the image is first rendered at a much higher resolution than the desired resolution. For this purpose, multiple samples are taken inside a pixel. Then, the multiple samples inside a pixel are averaged to compute the single value for that pixel. The result is the anti-aliased image of the desired resolution, where the jagged edges are eliminated with smoother transitions between the pixels along the edges of objects in the image (e.g., Figure 2.9(b)).

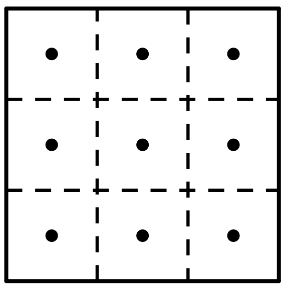

Figure 2.10: Example of splitting a single pixel in supersampling using 3×3 grid algorithm.

Various types of supersampling techniques have been proposed to date. One commonly used type is known as the grid algorithm. The grid algorithm is simple and easy to implement. In the grid algorithm, the pixel is split into $n \times n$ sub-pixels and a sample is taken from the center of each sub-pixel. The final value of the pixel is then computed as the average of the values at all sub-pixel samples. An example of 3×3 grid algorithm for a single pixel is shown in Figure 2.10. As this figure shows, the pixel is divided into a 3×3 array of sub-pixels and total of 9 samples are taken from the center of the sub-pixels (as denoted by black dots in Figure 2.10). The final value of the pixel in Figure 2.10 is then selected as the average of the values of these 9 samples.

2.7 Triangulations

In this section, two types of triangulations are introduced, including the Delaunay and constrained Delaunay triangulations. For this purpose, in what follows, the concept of triangulation is first defined.

Definition 2.4. *(Triangulation). A triangulation of a finite set P of points in $\mathbb{R}^2$ is a set T of (non-degenerate) triangles such that:*

1. *the set of all the vertices of triangles in T is P;*
2. *the interiors of any two triangles in T are disjoint; and*
3. *the union of all triangles in T is the convex hull of P.*

Various classes of triangulations have been introduced over the years. In what follows, one important and popular type of triangulation, which is called the Delaunay triangulation [29], is introduced.

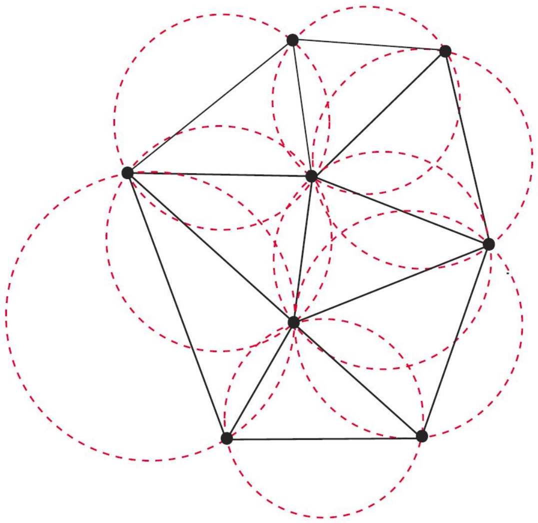

Figure 2.11: An example of a DT.

Definition 2.5. *(Delaunay triangulation (DT)). A triangulation T is said to be Delaunay if each triangle in T is such that the interior of its circumscribed circle (circumcircle) contains no vertices of T.*

Figure 2.11 shows an example of a DT. The circumcircle of each triangle in the triangulation is also illustrated by dashed lines in the figure. As can be seen, each circumcircle in the triangulation contains no vertices of the triangulation in its interior. Therefore, the triangulation shown in Figure 2.11 is Delaunay.

One main property of a DT, which makes it very popular, is the fact that, any DT of set P of points maximizes the minimum interior angle of all triangles over all possible triangulations of P [28]. Consequently, a DT tends to avoid thin and elongated triangles as much as possible.

The DT of a set P of points is not guaranteed to be unique unless no four points in P are co-circular. In the case that a set of points is chosen as a subset of a rectangular lattice (e.g., raster image), many points will typically be co-circular. Therefore, more than one possible DT for such a set of points will exist. Figure 2.12 illustrates two valid DTs for the same set of points. As can be seen from Figure 2.12, the four points v_0, v_1, v_2, and v_3 are co-circular. Figure 2.12(a) shows the DT including the edge $\overline{v_0v_2}$, whereas Figure 2.12(b) shows another DT of the same points including the edge $\overline{v_1v_3}$. The two triangulations in Figure 2.12 are valid DTs but differ. Various methods have been proposed for generating a unique DT, including the symbolic perturbation method [31] and the preferred-directions approach [35].

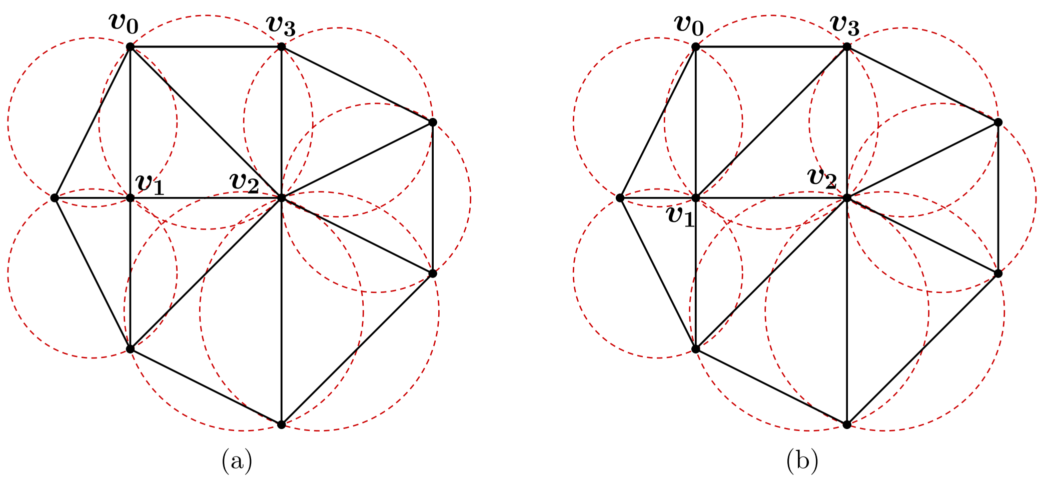

Figure 2.12: Example of two valid DTs for the same set of sample points.

Another special type of triangulation which is useful in some applications is a **constrained triangulation** [26], which must contain certain prescribed edges that are called **constrained edges**. A constrained triangulation can be considered as a triangulation of the point set P of a PSLG (introduced in Section 2.2), where the set E of line segments in the PSLG corresponds to constrained edges.

Having introduced the concepts of Delaunay and constrained triangulations, we now present another type of triangulation known as a constrained DT [26]. Before defining a constrained DT, however, the notation of **visibility** must be first introduced. In a constrained triangulation T with a set V of vertices and a set F of triangles, a vertex $p \in V$ is said to be visible from the interior of a triangle $t \in F$ if and only if for any point q inside t, the line segment $\overline{pq}$ does not intersect any constrained edge in T. To further understand the concept of visibility, two examples are illustrated in Figure 2.13. Figure 2.13(a) gives an example of a point p that is visible from the interior of $\triangle abc$ because for any point q in $\triangle abc$, no line segment $\overline{pq}$ intersects a constrained edge. Figure 2.13(b), however, shows an example of a point p that is not visible from the interior of a triangle $\triangle abc$ because for the interior point q in $\triangle abc$ the line segment $\overline{pq}$, in Figure 2.13(b), intersects with the constrained edge $\overline{ab}$ at point o. Having introduced the concept of visibility, in what follows, we define a constrained DT.

Definition 2.6. *(Constrained DT). A constrained triangulation of set P of points subject to the set E of edge constraints is said to be constrained Delaunay if each*

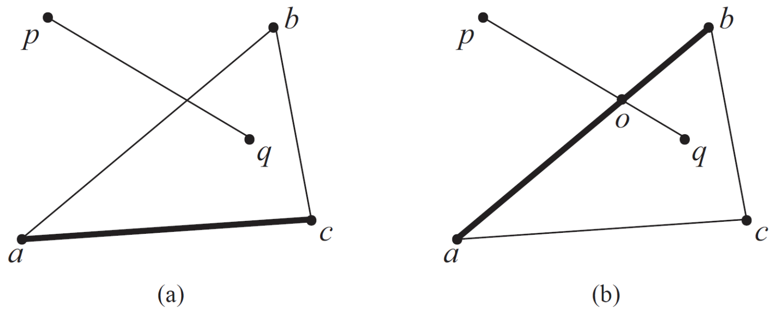

Figure 2.13: Examples of visibility. (a) p is visible from the interior of triangle $\triangle abc$, and (b) p is not visible from the interior of triangle $\triangle abc$.

triangle in the triangulation is such that:

1. *the interior of the triangle does not intersect any constraining line segment in E; and*
2. *no vertex inside the triangle circumcircle is visible from the interior of the triangle.*

An example of a constrained DT is shown in Figure 2.14. For the PSLG shown in Figure 2.14(a), the corresponding constrained DT is shown in Figure 2.14(b), with the triangle circumcircles drawn by dashed lines. As can be seen from Figure 2.14(b), no vertex inside a circumcircle of a triangle is visible from inside that triangle. Therefore, the triangulation in Figure 2.14(b) is constrained Delaunay. Similar to a DT, a constrained DT also tends to avoid long and thin triangles, except those formed by satisfying the edge constraints. Moreover, the constrained DT of a set P of points and a set E of edge constraints is not guaranteed to be unique unless no four points in P are co-circular. Therefore, methods such as the symbolic perturbation method [31] or the preferred-directions approach [35] are used to ensure the generation of a unique constrained DT with a given P and E. In this thesis, the unique constrained DT of P and E, where the preferred-directions approach [35] is used, is denoted by $\mathrm{pcdt}(P, E)$.

2.8 Mesh Models of Images

In the past several years, image representations based on geometric primitives have been receiving an increasing amount of attention. This is mainly due to the fact that, geometric representations of images allow for content-adaptive sampling and are

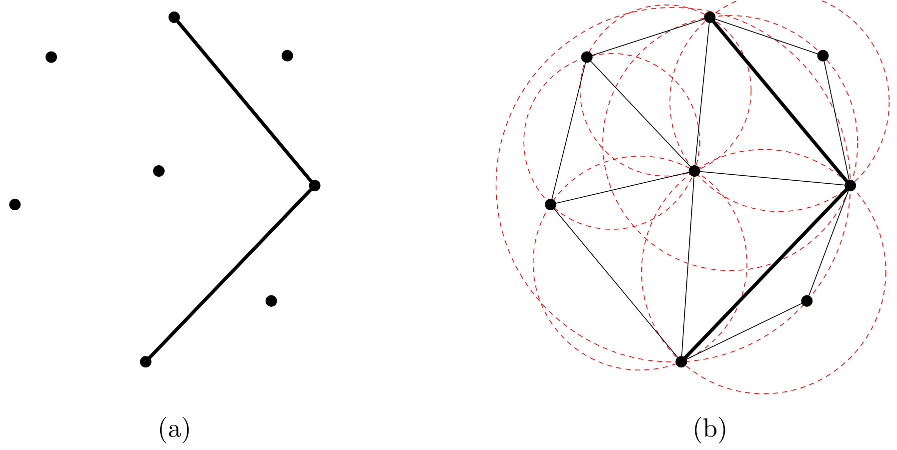

Figure 2.14: Example of a constrained DT. (a) The PSLG and (b) its corresponding constrained DT.

capable of capturing geometric structure in images. In fact, geometric representations can model large regions of images with simple geometric primitives. For example, a large area of an image can be represented by a small number of polygons instead of by hundreds of pixels. Such representations of images are known as **mesh models**. Among the many classes of mesh models for image representations, triangle-mesh models have become quite popular, where the geometric primitives are triangles.

In the context of our work, an image of width W and height H is an integer-valued function ϕ defined on a rectangular region $\Gamma = [0, W-1] \times [0, H-1]$ (i.e., $\Gamma \subset \mathbb{R}^2$) and sampled on the two-dimensional integer lattice $\Lambda = \{0, 1, ..., W-1\} \times \{0, 1, ..., H-1\}$, where the function value corresponds to the brightness. An example of how a triangle-mesh model is used to represent the image ϕ is illustrated in Figure 2.15. As this figure shows, the raster image ϕ sampled on Λ as shown in Figure 2.15(a) can be associated with a bivariate function ϕ defined on the continuous domain Γ as shown in Figure 2.15(b). In fact, the function ϕ in Figure 2.15(b) forms a continuous surface above the xy plane, where the height of the surface at each point corresponds to the brightness value of the image at that point. Mesh modeling of an image involves partitioning the image domain with a triangulation as shown in Figure 2.15(c). Then, the original image function ϕ is approximated over each geometric primitive (i.e., triangle). Next, all of the approximating functions over triangles are stitched together, as shown Figure 2.15(d), to approximate the whole surface of the original image in Figure 2.15(b). Finally, through a rasterization process, the triangulated surface in Figure 2.15(d) is converted to the reconstructed raster image shown in Figure 2.15(e). The process of converting a mesh model to a raster image is called **model rasterization**.

In order to use a mesh model, its parameters must first be chosen. Different types of mesh models may require different sets of parameters to be determined. One parameter that is crucial to almost any mesh model is the set P of sample points used by the model. The quantity $|P|$ is known as the size of the mesh model and the sampling density of the mesh model is defined as $|P|/|\Lambda|$. The method to select the parameters of a mesh model is known as **mesh generation**. For a particular mesh model, many mesh-generation methods are possible, but each one may employ different parameter-selection techniques. Most often, the performance of a mesh-generation method is evaluated by measuring the quality of the reconstructed images it yields. For this purpose the widely-used objective measure, known as the PSNR is employed, as introduced later in Section 2.11.1.

In addition to the PSNR which quantifies the approximation error, an error image is also often used to visualize and locate approximation errors in a reconstructed image. To generate an error image, we proceed as follows. First, the absolute pixel-wise difference between the original and reconstructed images is taken to produce a difference image. Then, the difference image is inverted by replacing the gray level g of each pixel with $(2^\rho - 1) - g$ to obtain the error image. Therefore, in an error image, darker pixels correspond to pixels with higher reconstruction errors. An example of an error image using the bull image from Appendix A is given in Figure 2.16. For the original and reconstructed images shown in Figures 2.16(a) and (b), respectively, the corresponding error image is illustrated in Figure 2.16(c). Darker regions in the error image in Figure 2.16(c) represent the areas of the original image in Figure 2.16(a) that are not reconstructed properly in the image in Figure 2.16(b). Therefore, error images can be used to find the areas where larger approximation errors exist.

2.9 ERD Mesh Model and Mesh-Generation Methods

Having introduced the generality of mesh models and mesh-generation methods, we now introduce the specific type of a triangle-mesh model used in this thesis and some of its associated mesh-generation methods. Recently, Tu and Adams [84] proposed

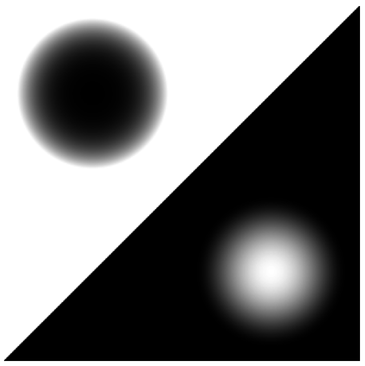
(a)

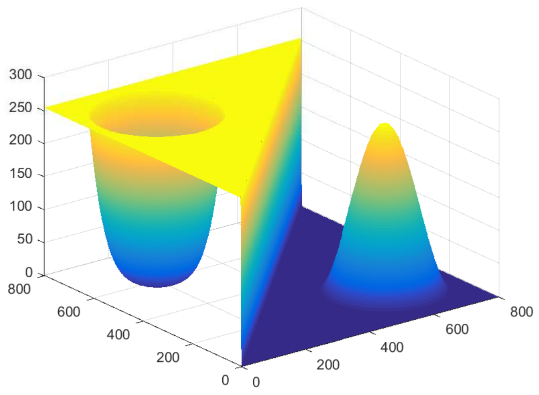

(b)

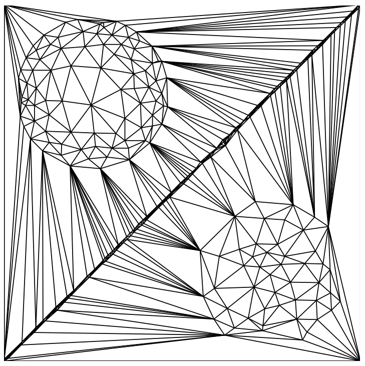
(c)

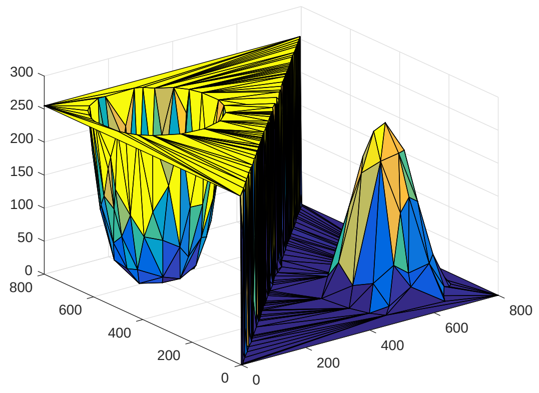

(d)

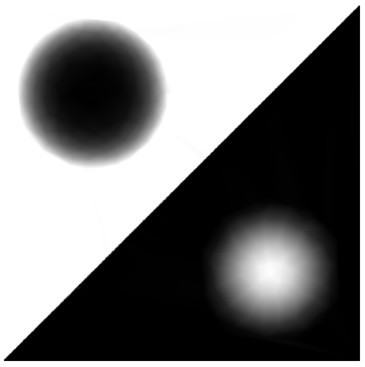
(e)

Figure 2.15: An example of how a triangle-mesh model is used for image representation. The (a) original image and (b) continuous surface associated with the raster image in (a). The (c) triangulation of image domain, (d) triangle-mesh model, and (e) reconstructed image.

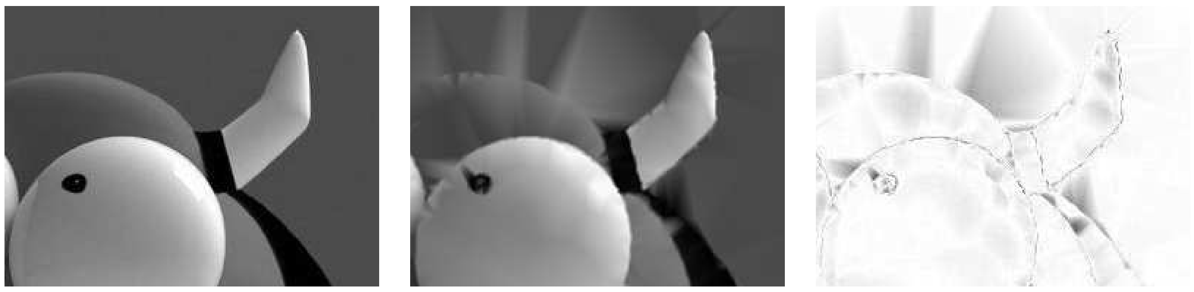

Figure 2.16: Example of an error image using the bull image. Parts of the (a) original, (b) reconstructed, and (c) error images.

a triangle-mesh model for images, called the explicitly-represented discontinuities (ERD) model, that is inspired by the work in [72] and is based on the constrained DT. In [84], two mesh-generation methods, namely, the error-diffusion (ED) scheme of Yang et al. [96] and the MGH method [12] inspired by the greedy point-insertion (GPI) scheme in [43], were adapted to generate the ERD model. Next, two mesh-generation methods, known as ERDED and ERDGPI, were proposed. In what follows, the specifics of the ERD model as well as the ERDED and ERDGPI methods, upon which our work is based, are explained.

Unlike many conventional types of mesh models, the approximating function that is associated with the ERD mesh model is not required to be continuous everywhere. In particular, in the approximating function of an ERD model, discontinuities are permitted across constrained edges in the triangulation. Consider an image function ϕ defined on the rectangular region $\Gamma = [0, W-1] \times [0, H-1]$. An ERD triangle mesh model of ϕ consists of the following parameters:

1. a set $P = \{p_i\} \subset \Gamma$ of sample points,
2. a set E of edge constraints, and
3. a set Z of integers called wedge values (to be explained shortly).

Moreover, the ERD model is associated with the unique constrained DT $\operatorname{pcdt}(P, E)$ and with an approximating function that is not required to be continuous across edge constraints in E. The approximating function is defined over each face in $\operatorname{pcdt}(P, E)$. By combining the functions over all faces, a function $\hat{\phi}$ is obtained that approximates ϕ over the entire image domain Γ. In the ERD model, a set of consecutive faces

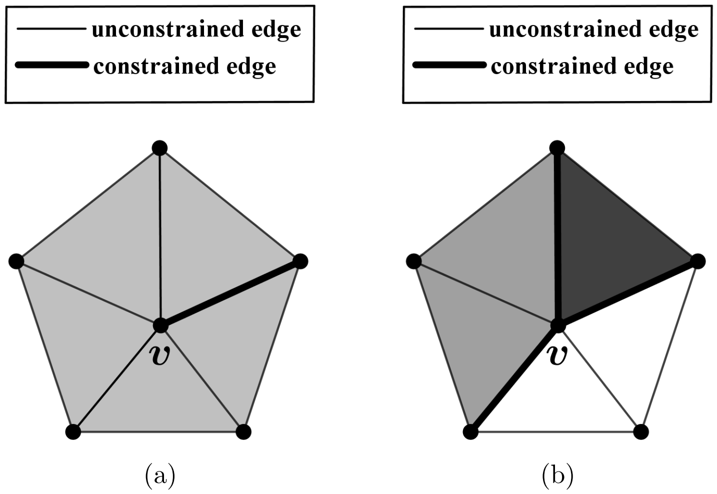

Figure 2.17: The relationship between vertices, constrained edges, and wedges. Each wedge is colored with a different shade of gray. The (a) single-wedge and (b) multiple-wedge cases.

in a loop around a vertex $v \in P$ that are not separated by any constrained edge is called a **wedge**. Figure 2.17 illustrates this definition and the relationship between wedges, vertices, faces, and constrained edges. As this figure shows, the vertex v in Figure 2.17(a) is incident to only one wedge, whereas the vertex v in Figure 2.17(b) is incident to three wedges. Each wedge has associated with it what is called a **wedge value**. The wedge value z of the wedge w belonging to vertex v specifies the limit of $\hat{\phi}(p)$ as p approaches v from points inside the wedge w. The approximating function defined over a given face f in the ERD model is a linear function that interpolates the three wedge values of f corresponding to its three vertices. With the help of the wedge values, $\hat{\phi}$ in the ERD model can represent discontinuities across constrained edges, which are used to represent the image edges.

The ERD mesh model explained above is defined in a continuous domain. In practice, however, digital images are often represented in a discrete domain. Due to the fact that the ERD model explicitly represents discontinuities, image edges could produce undesirable aliasing effects (as explained in Section 2.6) during model rasterization. This aliasing effect results in jagged and pixelated edges that do not look natural to human eyes. Therefore, a supersampling technique such as a 3×3 grid algorithm (as introduced in Section 2.6) can be used to avoid such aliasing effects.

Two mesh-generation methods, called ERDED and ERDGPI, have been proposed in [84] to produce the ERD mesh model explained earlier. Each of these methods selects the parameters of the ERD model (i.e., P, E, and Z) to obtain an approximation $\hat{\phi}$ of the original image ϕ for a given number N of sample points. The inputs to the mesh-generation algorithm are a desired mesh size N and an image function ϕ that is known only at the points in $\Lambda = \{0, 1, ..., W-1\} \times \{0, 1, ..., H-1\}$ (i.e., an integer lattice of width W and height H) and the outputs are the ERD model parameters, including $P \subset \Lambda \subset \Gamma$ (where, $|P| = N$), E, and Z. In what follows, various steps of the ERDED and ERDGPI mesh-generation methods are explained. For this purpose, an example with the test image bull from Appendix A is shown in Figure 2.18 to show the first three steps, which are identical for the ERDED and ERDGPI methods.

1) Locate edges. In the first step, the modified Canny edge detector [32] is used to locate edges in the input image ϕ (at resolution $W \times H$) with half-pixel resolution. To accomplish this, the high-resolution image $\overline{\phi}$ is formed by the bilinear interpolation of ϕ. Then, edge detection is applied to high-resolution image $\overline{\phi}$ (at resolution $(2W-1)\times(2H-1)$). The original image grid is called the coarse grid and the high-resolution interpolated image grid is called the fine grid. Consequently, all operations from now on are applied to the fine grid at resolution $(2W-1)\times(2H-1)$. The output of this step is a binary edge map that is thinned to produce one-pixel thick edges. In the example given in Figure 2.18, for the part of the original image shown in Figure 2.18(a), the corresponding part of edge map is illustrated in Figure 2.18(b).

2) Polyline generation and simplification. After an edge map has been generated, 8-connected edge pixels in the edge map are joined (by line segments) to form polylines. In cases where a polyline has one or more self-intersections (excluding loops), the polyline is split at each intersection point. In this way, the final set of polylines is guaranteed not to have any self-intersections (excluding loops). The Polylines are then simplified using the DP method explained in Section 2.3. In the example given in Figure 2.18, for the part of the edge map shown in Figure 2.18(b), the corresponding sets of polylines and simplified polylines are illustrated in Figures 2.18(c) and (d), respectively. The simplified polylines are then used to select the initial set P_0 of sample points and the set E of constrained edges to be used in the triangulation. The initial set P_0 is chosen as the union of all of the polyline vertices plus the four corner points of the image bounding box. The set E is selected as the union of all line segments from all simplified polylines.

3) Initial triangulation. After selecting the set P_0 of initial sample points and the set E of constrained edges, the initial mesh associated with the triangulation

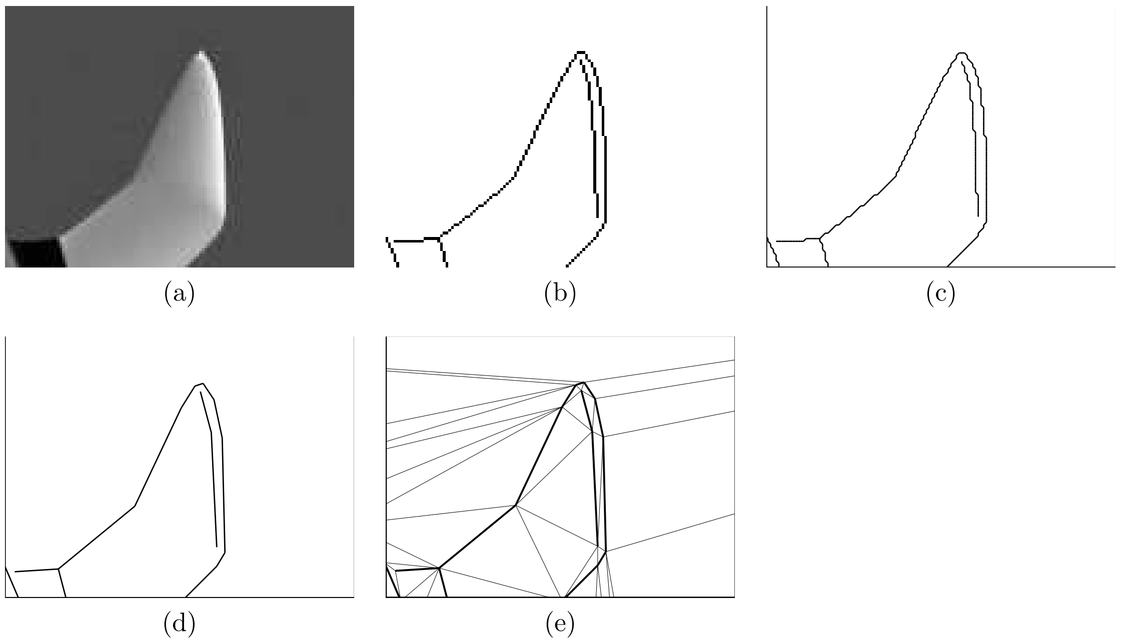

Figure 2.18: Selection of the initial triangulation. (a) Part of the input image bull. The (b) binary edge map of (a). (c) The unsimplified polylines representing image edges in (b). (d) The simplified polylines. (e) The part of the initial triangulation corresponding to (a), with constrained edges denoted by thick lines.

pcdt(P_0, E) is constructed. Let $N_0 = |P_0|$ be the initial mesh size. In the example given in Figure 2.18, for the part of simplified polylines illustrated in Figure 2.18(d), the corresponding part of the initial mesh is shown in Figure 2.18(e).

4) Initial wedge values. Once the initial triangulation is constructed, for each wedge w around each vertex $v \in P_0$, the corresponding wedge value z is selected as follows. If v has zero or one incident constrained edge (e.g., as in Figure 2.17(a)), its single wedge value z is simply chosen as the value of the (bilinear-interpolated) high-resolution image function $\overline{\phi}$ at v (i.e., $z = \overline{\phi}(v)$). Otherwise, if v has more than one incident constrained edge (as shown in Figure 2.17(b)), the wedge value associated with each wedge is calculated using a line-search approach as follows. The grid points along the ray (called the bisecting line) originating from v and bisecting the wedge w are searched. During the line search, the point p whose maximum magnitude second-order directional derivative (MMSODD) is largest is selected. Then, the wedge value z is chosen as the value of $\overline{\phi}$ at p (i.e., $z = \overline{\phi}(p)$). To prevent p from falling far outside of the corresponding triangle face, the line search is restricted to distance $d \in [1, 1.5]$ units in the coarse grid (or, equivalent $d \in [2, 3]$ units in the fine grid) from v. The

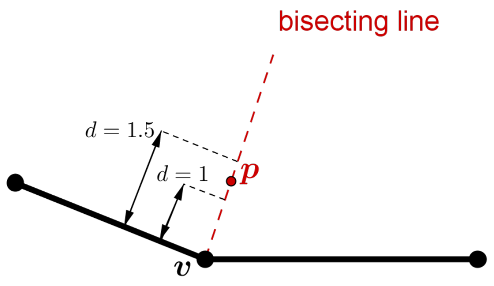

Figure 2.19: The line search process used in the ERDED and ERDGPI methods to calculate the wedge values.

obtained wedge value is then rounded to the nearest integer value. An example of the line-search approach is illustrated in Figure 2.19. As this figure shows, the bisecting line drawn by dashed line is searched and the point p with the highest MMSODD that falls withing the distance range of $[1, 1.5]$ units from v is selected.

5) Point selection. After the initial mesh is constructed, a new sample point $q \in \Lambda$ is selected to be added to the mesh. This is the stage in which new points are to be selected for refining the initial mesh. Since these new points are not selected by the edge detector, they are called non-edge points. This step is performed differently in the ERDED and ERDGPI methods to obtain the set S (where, $|S| = N - N_0$) of new non-edge sample points as follows. In the ERDED method, the points in S are all obtained at once using the error-diffusion technique from the ED method [96] with some modifications. Thus, for the ERDED method, after this step, the output parameter P of the ERD model is already determined. In the ERDGPI method, however, S is generated by an iterative point-selection process as follows. In each iteration, the new non-edge sample point q is chosen in two steps. First, the triangle face f^* with the largest squared error is selected as given by

$$f^* = \underset{f \in F}{\operatorname{argmax}} \sum_{p \in \Omega_f} \left(\hat{\phi}(p) - \phi(p) \right)^2, \tag{2.3}$$

where Ω_f is the set of all points in Λ belonging to face f and F is the set of all triangle faces in the mesh. Next, a point q in f^* for insertion in the mesh is selected as given by

$$q = \underset{p \in \Omega_{f^*}}{\operatorname{argmax}} \left| \hat{\phi}(p) - \phi(p) \right|. \tag{2.4}$$

In short, for the ERDGPI method, the new point q in each iteration is selected as the point with the greatest absolute error inside the face with the highest squared error.

6) Point insertion. Once the new point q is selected, it is inserted in the triangulation. If q is on a constrained edge, the edge is split at q into two constrained edges, and the wedge value is computed for each of the two new wedges around the vertex q using the line-search approach explained in step 4. If, however, q is not on a constrained edge, the wedges remain the same and no wedge values need to be computed. After each point insertion, the set P_{i+1} of sample points for the next iteration is selected as $P_i \cup \{q\}$.

7) Stopping criterion. For the ERDED method, if $|P_{i+1}| < N$, go to step 6 and insert another non-edge point from S that has not yet been inserted. Otherwise, set the output parameter $P = P_{i+1}$ and stop. In the case of the ERDGPI method, however, if $|P_{i+1}| < N$, go to step 5 to select another non-edge point for insertion. Otherwise, set the output parameter $P = P_{i+1}$ and stop.

After completing the above steps, all parameters of the ERD model are determined, including the set P of sample points, set E of constrained edges, and set Z of wedge values.

2.10 Image Scaling

As one of the classical and important problems in image processing and digital photography, image scaling refers to the operation of resizing digital images to obtain a larger or a smaller image. More specifically, if the scaled image is larger than the original image the operation is called upscaling (also super-resolution), and if it is smaller, then the operation is referred to as downscaling. In this thesis, since we are interested in the upscaling operation, the term "scaling" always refers to the upscaling operation, unless otherwise stated.

The image-scaling problem that is being addressed in this thesis can be stated as follows. A low-resolution raster image ϕ_l of width W and height H and an integer scaling factor of $k > 1$ are assumed. The image-scaling problem of interest herein is to find the high-resolution raster image ϕ_h of size $kW \times kH$ as the scaled version of ϕ_l, so that the qualitative attributes of ϕ_l are preserved well in ϕ_h, with the least amount of edge blurring that can arise during image scaling.

As can be perceived from the above problem definition, the scaled raster image ϕ_h has more grid points than the low-resolution raster image ϕ_l (i.e., k times more points in each dimension). Those newly-generated grid points in ϕ_h can be assumed as empty grid points that must be filled with new intensity (i.e., graylevel) values. The missing intensity values at these empty grid points are estimated through certain techniques called image interpolation. A review of the different image-interpolation approaches used for image scaling is provided in Section 1.4. As part of the work presented in this thesis, an improved mesh-based approach to address the image-scaling problem stated earlier is developed later in Chapter 5, using the ERD triangle-mesh models.

2.11 Objective Image Quality Measures

One challenge in digital image processing is image quality assessment. Many image quality measures have been proposed to date. In what follows, three objective image quality measures used for different purposes in this thesis, namely, the peak signal-to-noise ratio (PSNR), structural similarity (SSIM) index, and percentage edge error (PEE), are introduced.

2.11.1 Peak Signal-to-Noise Ratio (PSNR)

The mean squared error (MSE) is probably the most common metric that is widely used for image quality assessment in image processing. The MSE between an original image ϕ of width W and height H, defined a two-dimensional integer lattice $\Lambda = \{0, 1, ..., W-1\} \times \{0, 1, ..., H-1\}$, and its reconstructed image $\hat{\phi}$ defined on Λ is defined

$$\epsilon = \frac{1}{|\Lambda|} \sum_{p \in \Lambda} \left(\hat{\phi}(p) - \phi(p) \right)^2 . \tag{2.5}$$

The MSE is often expressed through the **peak signal-to-noise ratio (PSNR)**. The PSNR is the ratio between the maximum possible power of a signal and the power of corrupting noise. Since signals can have a very wide dynamic range, PSNR is usually expressed in terms of the logarithmic decibel (dB) scale as given by

$$\text{PSNR} = 20 \log_{10} \left(\frac{2^\rho - 1}{\sqrt{\epsilon}} \right), \tag{2.6}$$

where ρ is the number of bits per sample in the image ϕ. In this thesis, the PSNR is used to be able to compare the performance of the proposed SEMMG method with other competing mesh-generation methods. Greater PSNR values correspond to reconstructed images with better quality.

2.11.2 Structural Similarity (SSIM) Index

Although the PSNR metric is still widely used for evaluating many imaging systems, studies (such as the work in [87]) have shown that it does not always reflect the subjective quality of images. Therefore, other metrics based on image perceptual quality have been developed, of which the **structural similarity (SSIM)** index [88] has gained much attention and been widely used. The SSIM index between an original image X of width W and height H, defined a two-dimensional integer lattice $\Lambda = \{0, 1, ..., W-1\} \times \{0, 1, ..., H-1\}$, and its reconstructed image Y defined on Λ is defined as follows.

Let x $= \{x_i | i = 1, 2, ..., N\}$ and y $= \{y_i | i = 1, 2, ..., N\}$ be two image patches of the same size N, extracted from the same spatial location from X and Y, respectively. Given that the mean and variance of x are denoted as μ_x and σ_x^2, mean and variance of y are denoted as μ_y and σ_y^2, and covariance of x and y is denoted as σ_{xy}, the SSIM index between x and y is given by

$$\mathrm{SSIM(x,y)} = \frac{(2\mu_x\mu_y + C_1)(2\sigma_{xy} + C_2)}{\mu_x^2 + \mu_y^2 + C_1)(\sigma_x^2 + \sigma_y^2 + C_2)}, \tag{2.7}$$

where $C_1 = (0.01L)^2$, $C_2 = (0.03L)^2$, and L is the dynamic range of the pixel values (e.g., $L = 255$ for 8-bit grayscale images). The local statistics μ_x, μ_y, σ_x, σ_y, and σ_{xy} are computed within an 11×11 circular window using a symmetric Gaussian weighting function w $= \{w_i | i = 1, 2, ..., N\}$, with a standard deviation of 1.5 samples, normalized to have a unit sum. Then, μ_x, σ_x, and σ_{xy} are estimated by

$$\mu_x = \sum_{i=1}^{N} w_i x_i,$$

$$\sigma_x = \left(\sum_{i=1}^{N} w_i (x_i - \mu_x)^2 \right)^{1/2},$$

and

$$\sigma_{xy} = \sum_{i=1}^{N} w_i (x_i - \mu_x)(y_i - \mu_y).$$

Similarly, μ_y and σ_y can be estimated for the image patch y. The circular window is moved pixel-by-pixel across the whole image space and the SSIM index is calculated within each local window using (2.7). The SSIM index produces a real number in

$[0, 1]$, where higher values correspond to a better image reconstruction. Finally, a mean SSIM index of all windows is calculated as a single overall quality measure between the entire images X and Y.

2.11.3 Percentage Edge Error (PEE)

In the application of image scaling studied in this thesis, our main goal is to produce scaled images of better subjective quality, without losing sharpness of the image edges. For this particular goal, neither the PSNR nor SSIM metrics is designed to measure the sharpness at image edges. Therefore, a metric called **percentage edge error (PEE)** is used for measuring the sharpness of the edges in scaled images.

Between an original image ϕ of width W and height H, defined on a two-dimensional integer lattice $\Lambda = \{0, 1, ..., W-1\} \times \{0, 1, ..., H-1\}$, and its reconstructed image $\hat{\phi}$ defined on Λ, the PEE measures how close the edges in $\hat{\phi}$ are to the original edges in ϕ. The PEE between ϕ and $\hat{\phi}$ is determined by

$$\mathrm{PEE} = \frac{\mathrm{ES}(\phi) - \mathrm{ES}(\hat{\phi})}{\mathrm{ES}(\phi)} \times 100, \tag{2.8}$$

where $\mathrm{ES}(\phi)$ and $\mathrm{ES}(\hat{\phi})$ are the edge strengths of the original and reconstructed images, respectively. The procedure to calculate ES is identical to the one used in [16]. For an image of ϕ, its ES is calculated using the following steps:

1. *Gradient calculation.* Using simple convolution masks, first-order partial derivatives in horizontal and vertical directions at each pixel in ϕ are estimated as g_x and g_y, respectively. Then, the gradient magnitude g at that pixel is determined by $g = \sqrt{g_x^2 + g_y^2}$. Next, a gradient image G is generated in which each pixel holds the value of its estimated gradient magnitude.

2. *Gradient thresholding.* Then, G is passed through a simple thresholding process to obtain the edge intensity image E, as given by

$$E(x, y) = \begin{cases} G(x, y), & G(x, y) \geq \tau \\ 0, & \text{otherwise,} \end{cases}$$

   with threshold $\tau = \overline{G} + \sigma_G$, where $\overline{G}$ and σ_G are the mean value and standard deviation of G.

3. *Edge strength calculation.* Once the edge intensity image E is obtained, the edge strength ES of ϕ is calculated as the total of edge-intensity values in E as given by
$$\mathrm{ES} = \sum_{y} \sum_{x} E(x, y).$$

In (2.8) above, positive PEE values indicate that the reconstructed (i.e., scaled) image is over smoothed, and negative values of PEE are an indication that edges in the reconstructed (i.e., scaled) image have been sharpened. Generally, a decrease in the PEE value is a strong indication of the reduction of blurring effects which is the main purpose of our work in image scaling.

Chapter 3

Proposed SEMMG Method and Its Development

3.1 Overview

In this chapter, a new method called the squared-error minimizing mesh-generation (SEMMG) method is proposed for producing ERD triangle-mesh models for the representation of grayscale images. We start by presenting in-depth analyses of two previously proposed methods for generating ERD models, namely, the ERDED and ERDGPI methods, which were introduced in Section 2.9. Through these analyses, we identify potential areas for improvement in different steps of the methods, including edge detection, wedge-value calculation, and non-edge point selection. Moreover, after identifying problems in each of these steps, solutions are found to address these problems. Then, our SEMMG mesh-generation method is proposed by integrating all the recommended modifications into a unified framework.

3.2 Development of SEMMG Method

Having introduced all of the necessary background material in Chapter 2, we now present how the SEMMG mesh-generation method proposed in this thesis was developed. As mentioned in previous chapters, the work in this thesis focuses on the application of ERD triangle-mesh models, due to their benefit of preserving the image discontinuities. Thus, we first present some in-depth analyses on the existing methods for generating ERD models. Two effective mesh-generation methods for producing

ERD models are the ERDED and ERDGPI methods as proposed in [84]. As we recall from Section 2.9, the general algorithmic framework of each of these methods composed of the following main steps:

1. edge detection,
2. polyline generation and simplification,
3. initial triangulation,
4. initial wedge-value calculation,
5. point selection, and
6. point insertion.

In what follows, through detailed analysis and experimental results, we identify several weaknesses in different approaches employed in above framework. Then, for each weakness, we explore modifying the framework in order to improve upon the weakness. The modifications that result in improvements will later be integrated into the proposed SEMMG method.

3.2.1 Edge Detection Analysis

The primary step in either the ERDED or ERDGPI mesh-generation scheme (and almost any other edge-preserving mesh-generation method) is to locate edges in the input image. The edge-detection step (as we recall from Section 2.9) is performed using the same approach in both the ERDED and ERDGPI methods. Thus, our analysis focuses on one of them, which is the the ERDED method herein. In what follows, two potential areas for improvements in the edge-detection technique used in the ERDED method are analyzed, including junction-point detection and edge-detector parameter selection.

3.2.1.1 Junction-Point Detection

In-depth investigations on the reconstructed images obtained with the ERDED method showed that often some approximation errors exist around the polylines that were broken at junctions (i.e., where three or more image edges meet). Analyses with numerous test cases showed that the root cause of such broken polylines near junctions is due to the edge detector used by the ERDED method. Figure 3.1 illustrates an example of the broken polylines and the approximation error they create using the ERDED method for the wheel image from Appendix A. A part of the wheel image containing a junction area that is marked with a black rectangle and that part under magnification are shown in Figures 3.1(a) and (b), respectively. The corresponding parts in the edge map, triangulation, and reconstructed image are shown in Figures 3.1(c), (d), and (e). The polylines (i.e., constrained edges in mesh) are denoted by thick lines in Figure 3.1(d). As the edge map in Figure 3.1(c) shows, a gap exists near the top of the vertical edge approaching the junction. As a result, this gap also appears in the corresponding polylines, which are generated based on the edge map, near the junction as shown in Figure 3.1(d). As the reconstructed image in Figure 3.1(e) shows, the bottom left side of the image in Figure 3.1(b) is not properly reconstructed. To better locate the approximation error, an image displaying the error between the Figures 3.1(b) and (e) was computed and shown in Figure 3.1(f). As can be seen from Figure 3.1(f), the bottom-left side of the error image is darker and it gradually becomes darker as we approach the junction, which indicates the existence of a larger approximation error.

Careful analysis showed that the reason for missing some edges near a junction (of which an example was given in Figure 3.1) was found to relate to the Canny-based edge detector itself used by the ERDED method. In the non-maxima-suppression step in the Canny edge detector (explained in Section 2.5.1), edge pixels whose gradient magnitudes are not maxima in the direction of the gradient are removed from the edge map. In the case of a junction, as we approach the junction along the weakest edge (i.e., the vertical edge in Figure 3.1(c)), the direction of the gradient becomes increasingly affected by the stronger edge (i.e., the horizontal edge in Figure 3.1(c)) and, at some point, the gradient direction becomes equal to the gradient direction of the stronger edge. This is the point where the non-maxima suppression fails and rejects some parts of the weaker edge, and leaves a gap on the weaker edge near the junction point, such as what happened to the vertical edge in Figure 3.1(c).

As shown through the above observation (as an example of many test cases), the gap in the edge map near junctions can degrade the mesh quality by generating broken polylines at junctions. To further understand why such broken polylines can create a large approximation error near junctions, a simplified example is analyzed through Figure 3.2 as follows. Using the ERD model (introduced in Section 2.9), a junction formed by three constrained edges, like those drawn in Figure 3.2(a), are

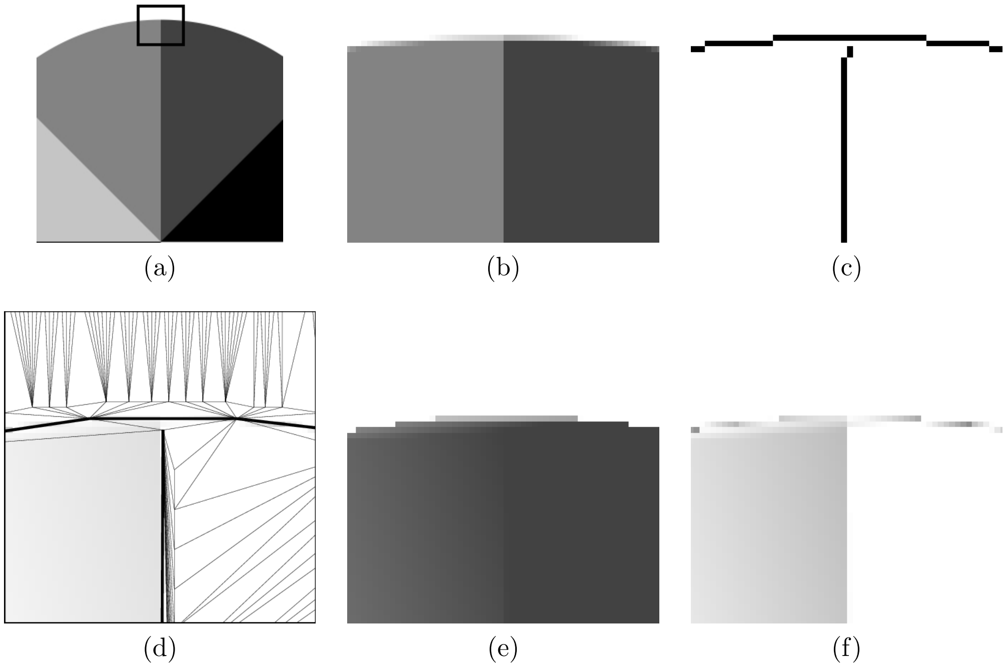

Figure 3.1: An example of how broken polylines at junctions can degrade the mesh quality using the wheel image. The (a) part of the original image containing the junction as marked with the black rectangle, (b) closer view of the junction area, corresponding (c) edge map, (d) triangulation and polylines, (e) reconstructed image, and (f) error image.

modeled with three wedges around the junction point (vertex) with three different wedge values w_0, w_1, and w_2. If, however, the edges approaching the junction are not detected correctly, a gap will be produced in an edge as shown in Figure 3.2(b), and the junction is modeled with two wedges with two new wedge values w_0 and w_1 instead of three. Consequently, the bottom area of the junction in Figure 3.2(b), which should have been reconstructed using two different wedge values, is now reconstructed using a single wedge value (i.e, w_0). Thus, using a single wedge value for the bottom area of the junction in Figure 3.2(b) results in a large approximation error in either the bottom left or right side of the junction. The same analysis explains why we obtain a large approximation error in the bottom left side of the junction previously shown in Figure 3.1(f).

Based on the above observations, one possible solution to the problem of missed edges near junctions is to employ an edge detector that is not based on the Canny

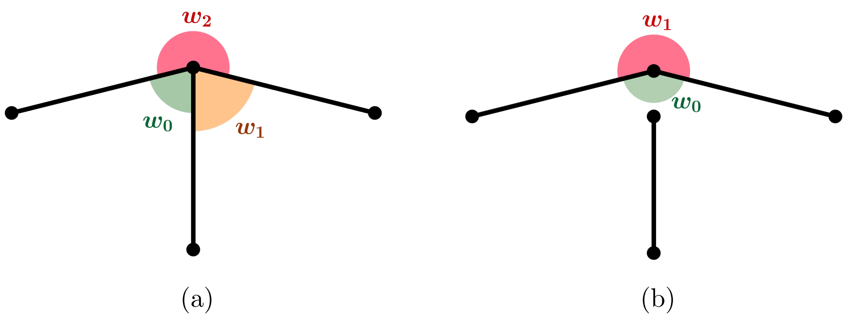

Figure 3.2: (a) A trihedral junction properly modeled with three wedge values. (b) The same junction improperly modeled with two wedge values.

method. For this purpose, the well-known SUSAN edge detector [79] (as introduced in Section 2.5.2) was selected. In particular, in the ERDED method, the Canny-based edge detector was replaced with the SUSAN edge detector to see how it affects the edge maps and reconstructed images. As a result, the edge maps obtained from the SUSAN edge detector showed that the problem of missed edges near junctions are mostly addressed. Therefore, the approximation errors around the missed edges near junctions in the reconstructed images obtained from the ERDED method with the SUSAN edge detector are reduced.

A example to show how using the SUSAN edge detector in the ERDED method affected the results is given in Figure 3.3. Examples shown in Figure 3.3 correspond to the same junction area from the wheel image used in Figure 3.1(b). In Figure 3.3, the top and bottom rows correspond to edge maps, meshes, and error images obtained from the ERDED method with the Canny-based and SUSAN edge detectors, respectively. As Figure 3.3 shows, the missed edges near the junction in the edge map obtained by the Canny-based method in Figure 3.3(a) are recovered in the edge map in Figure 3.3(d) using the SUSAN edge detector. Also, the broken polylines (i.e., thick lines) of the mesh shown in Figure 3.3(b) are connected in the mesh shown Figure 3.3(e) near the junction. Finally, the error image displaying the error between the original image and reconstructed image obtained by the ERDED method with the SUSAN algorithm in Figure 3.3(f) shows smaller approximation errors than the error image obtained by the ERDED method using the Canny-based edge detector in Figure 3.3(c).

Although employing the SUSAN edge detector has improved the quality of the edge maps by recovering the missed edges near junctions, more experiments with

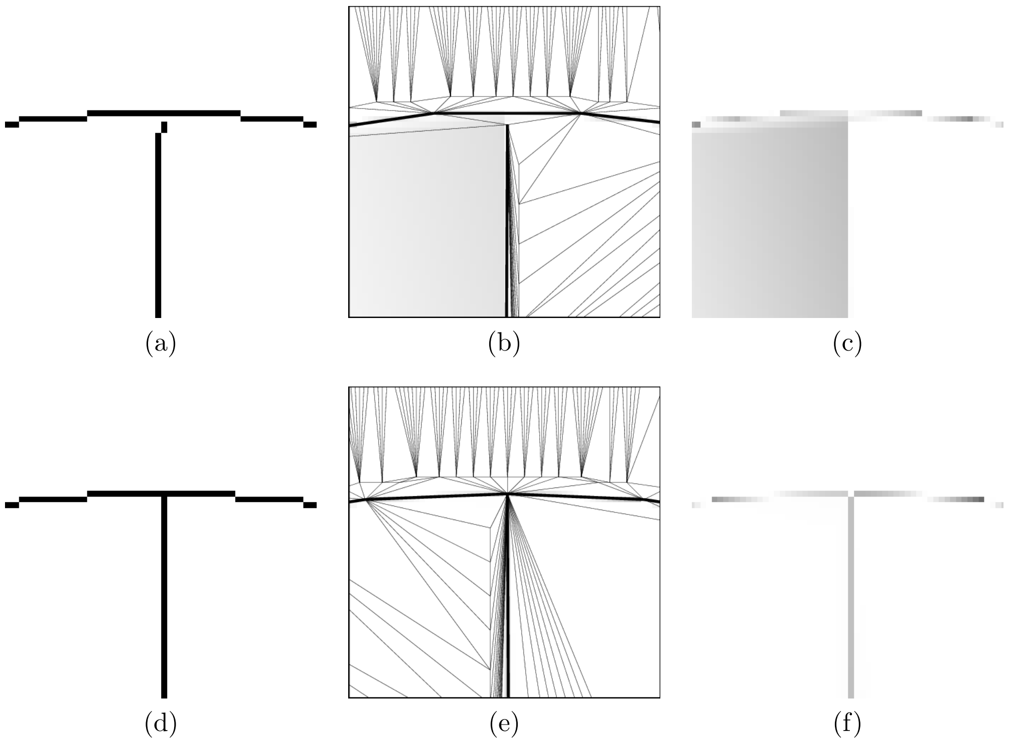

Figure 3.3: A comparison between the meshes obtained with ERDED method using the modified Canny and SUSAN edge detectors for the same junction area shown in Figure 3.1. Top row (a), (b), and (c) are the edge map, triangulations and polylines (i.e., thick lines), and error image obtained by the modified Canny edge detector, respectively. Bottom row (d), (e), and (f) are the edge map, triangulations and polylines (i.e., thick lines), and error image obtained by the SUSAN edge detector, respectively.

different test images showed that the SUSAN edge detector is too sensitive to noise. Some examples with the bull and peppers test images from Appendix A are shown in Figures 3.4 to compare the edge maps obtained from the SUSAN edge detector (i.e., the middle column) with those obtained from the Canny edge detector (i.e., the right column). For example, in the case of the simpler images, such as parts of the bull image shown in Figures 3.4(a) and (d), we can see than the edge maps produced by the Canny edge detector in Figures 3.4(c) and (f) contain much smoother and clearer edge contours than the those obtained from the SUSAN edge detector shown in Figures 3.4(b) and (e), respectively. Moreover, in the case of the more complicated image, such as the part of the bull image shown in Figure 3.4(g), edge contours obtained from the Canny edge detector in Figure 3.4(i) are more accurate than those obtained from the SUSAN edge detector shown in Figure 3.4(h). Similarly, for the

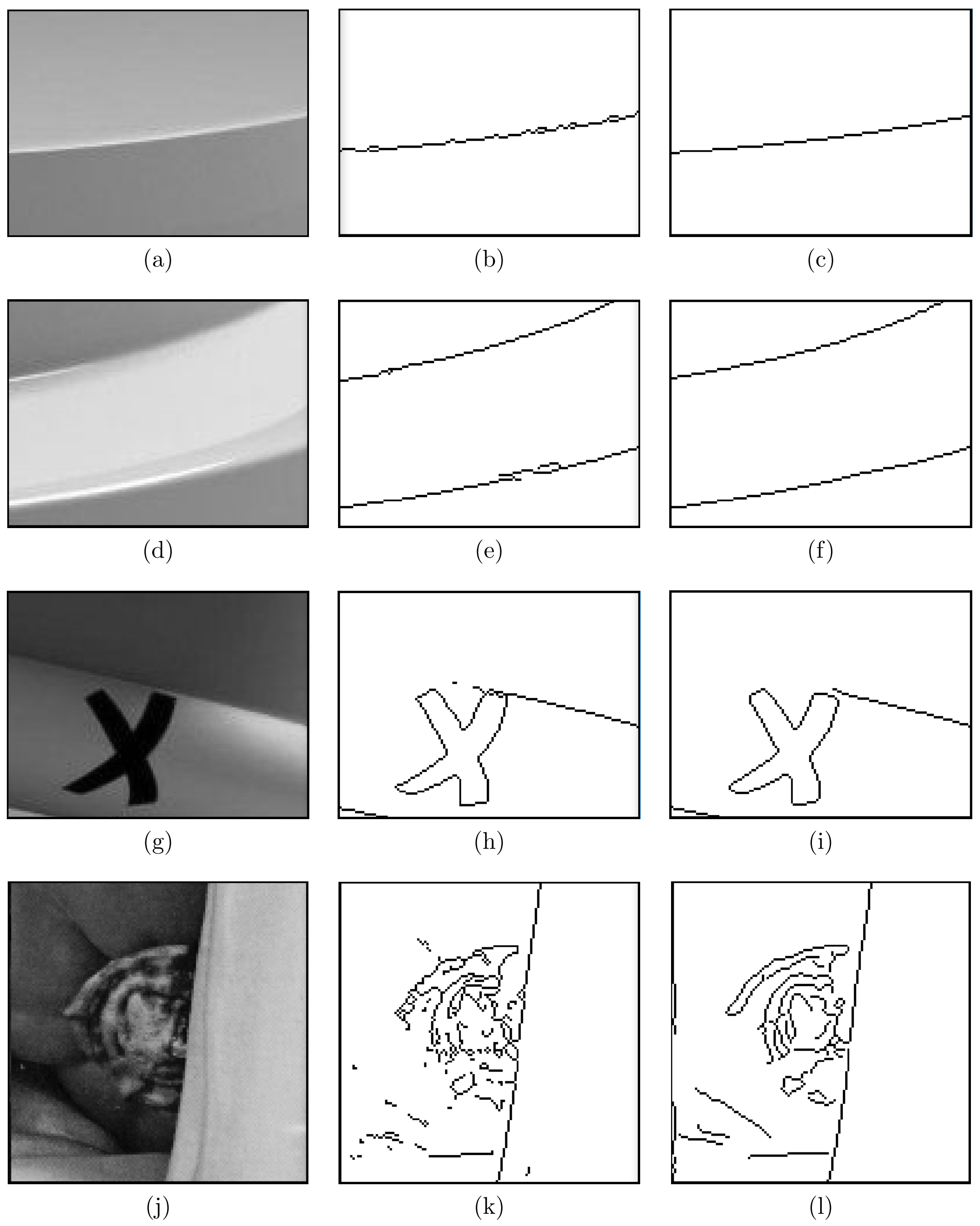

Figure 3.4: Examples showing the inefficiency of the SUSAN edge detector in producing accurate edge contours. The magnified areas of the (a)(d)(g) bull and (j) peppers images. The corresponding edge maps obtained with the (b)(e)(h)(k) SUSAN and (c)(f)(i)(l) Canny edge detectors.

the part of the peppers image shown in Figure 3.4(j), the edge map obtained from the Canny edge detector in Figure 3.4(l) shows more accurate edge contours than those obtained from the SUSAN edge detector shown in Figure 3.4(k).

As seen from the examples in Figure 3.4, the inefficiencies of the SUSAN edge detector lead to inaccurate edge contours in the produced edge maps. These inaccurate edge maps result in polylines that do not effectively represent the image discontinuities. Therefore, the whole process of wedge-value calculation, which is highly affected by the locations of the polylines, produces inaccurate wedge values. Consequently, the overall quality of the mesh is degraded using wedge values that have not been effectively computed, as a result of bad edge localization. Many experiments with different test cases (such as the ones provided in Figure 3.4) have shown that the Canny edge detector is the better choice because it produces more accurate edge maps overall, which are very beneficial to the other steps in mesh generation. Thus, the Canny edge detector of [23] (introduced in Section 2.5.1) has been selected for use in the remainder of the work in this thesis.

3.2.1.2 Edge-Detector Parameter Selection

In the next part of analyzing the edge detector used in the ERDED method, we studied how a poor choice of the edge-detector parameters in the ERDED method can reduce its performance. Our experiments with different test cases showed that the ERDED (or ERDGPI) method undesirably couples the parameters of its edge detector with the sampling density of the mesh. This coupling between the edge-detector parameters and the sampling density of the mesh in the ERDED method results in inaccurate edge maps with too many unnecessary (and false) edges, especially when the mesh sampling density increases. Since the detected edges are then used to generate polylines, more detected edges generally lead to more polylines with more sample points. Therefore, using an edge map with too many false and unnecessary edges results in wasting many sample points in the mesh later and degrading the quality of the final mesh.

In order to show the undesirable dependency of the edge detector parameters to the mesh sampling density in the ERDED method, an example using the bowling image from Appendix A is illustrated in Figure 3.5. For this purpose, the bowling image, as partly shown in Figure 3.5(a), was given to the ERDED method and edge maps obtained at two sampling densities of 1% and 4% are shown in Figures 3.5(b)

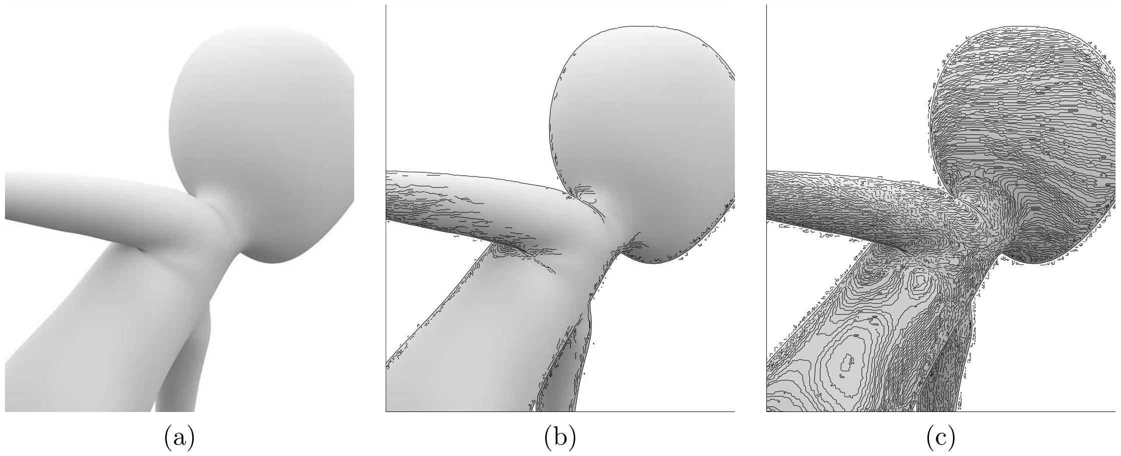

Figure 3.5: An example showing artificial dependency between the edge detector sensitivity and sampling density of the mesh in the edge detector implemented in the ERDED/ERDGPI method. The (a) original image. The (b) and (c) original image superimposed with edge maps obtained with sampling density of 1% and 4%, respectively.

and (c), respectively. As can be seen in Figure 3.5(c), the edge map obtained at the sampling density of 4% is far too dense, unlike the edge map obtained at the sampling density of 1% as shown in Figure 3.5(b). In fact, most of the edges shown in Figure 3.5(c) were falsely detected. The false detection of edges in Figure 3.5(c) is because the edge-detector parameters are improperly selected when the sampling density changes from 1% to 4%. This type of dependency between the edge-detector parameters and the sampling density reduces the performance of the mesh generator, especially at higher sampling densities, by producing too many unnecessary sample points, constrained edges, wedges, and wedge values in the mesh.

To find the root cause of such a dependency between the edge-detector parameters and the sampling density, a short review of the edge detector used by the ERDED method is needed as follows. As explained in Section 2.5.1, one main step in any Canny-based edge detector is hysteresis thresholding. The hysteresis thresholding employs two thresholds, a high threshold τ_h and a low threshold τ_l. The edge pixels whose gradient magnitudes are greater than than τ_h are considered as strong edge points and will be kept in the final edge map, whereas the pixels with gradient magnitudes smaller than τ_l will not. In the case of the pixels whose gradient magnitudes are between τ_l and τ_h, the pixels are scanned and if they are connected to a strong edge point, they will be kept as an edge point. In the ERDED method, first, τ_h

is determined and τ_l is then computed as a fraction of τ_h (e.g., as $0.5\tau_h$) in order to recover the faint edges connected to the strong edges. Therefore, τ_h is the only threshold of the edge detector that the ERDED method needs to determine. Indeed, lower and higher values of τ_h lead to edge maps with more and fewer edges, respectively. Therefore, not only selecting a proper τ_h plays a crucial role in the process of hysteresis thresholding, but it is also of high importance in producing ERD mesh models with accurate selected discontinuities. In the ERDED (or ERDGPI) mesh-generation method, the high threshold τ_h is calculated based on a heuristic process, where the selection of τ_h improperly depends on the sampling density of the mesh. More specifically, in the ERDED (or ERDGPI) method, the τ_h is inversely proportional to the sampling density of the mesh. Consequently, with an increase in the sampling density, τ_h is decreased too much and the edge map will contain too many false edges similar to the example presented in Figure 3.5(c).

As the above observation implies, in the ERDED method, the high threshold τ_h (as the only parameter of the edge detector) is improperly selected, leading to inaccurate edges maps. This motivated the author to look for another way of selecting the threshold τ_h so that it can be determined adaptive to the image content and independent from the sampling density. For this purpose, the Otsu method [68] was considered due to its simplicity and potential to be effective. The Otsu thresholding technique (as introduced in Section 2.4) is primarily used for the purpose of image thresholding, where the input is a grayscale image and the output is a threshold gray value. The threshold τ_h that we want to determine here, however, is not a gray value. Therefore, the Otsu thresholding method needs to be employed in a certain way to serve our purpose of determining τ_h. In what follows, we propose the usage of the Otsu method in the Canny edge detector for finding τ_h.

Canny edge detector using Otsu method. We recall from Section 2.5.1 how the Canny edge-detection method generally works. First, the direction and magnitude of the gradient of each pixel in the input image are estimated, resulting in a gradient map. Then, the gradient map is passed through a non-maxima suppression process. Now, the Otsu method is employed as follows. The non-maxima suppressed gradient map is given as an input to the Otsu method and the output is used as the high threshold τ_h. Then, the τ_l is selected as $\tau_h/2$ and the hysteresis thresholding is performed on the non-maxima suppressed gradient map using τ_l and τ_h. The next steps are the same as the ones in the Canny edge detector explained in Section 2.5.1.

An example of using the Otsu thresholding method, in the way explained above,

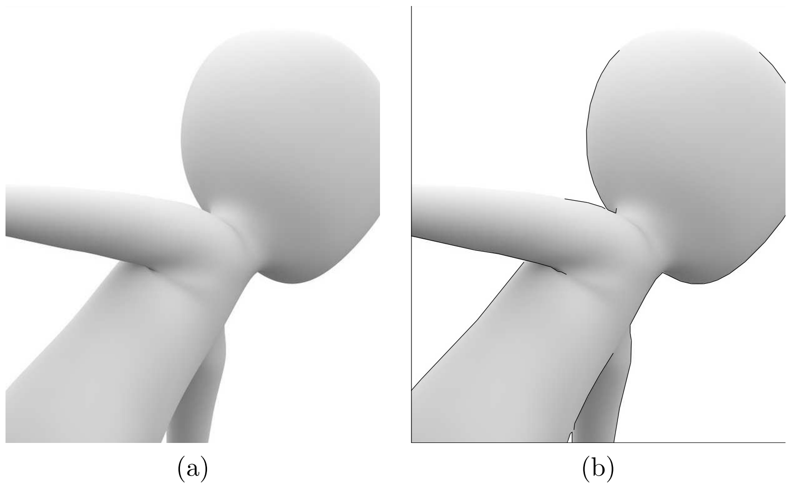

Figure 3.6: An example of using the Otsu thresholding method in the Canny edge detector. The (a) original image and (b) original image superimposed with the edge map obtained with the sampling density of 1% or 4%.

for the same part of the bowling image shown in Figure 3.5(a) is given in Figure 3.6. As can be seen from Figure 3.6, for the part of the original image shown in Figure 3.6(a), the edge maps obtained using the Otsu thresholding method at two sampling densities of 1% and 4% are the same as the one shown in Figure 3.6(b). Moreover, the edge map shown in Figure 3.6(b) looks more accurate than the edge map shown in Figure 3.5(c), which contains too many falsely-detected edges. Thus, using the Otsu method, the undesirable dependency between the edge-detector parameter, τ_h, and the sampling density of the mesh is effectively removed. Consequently, the edge map that is obtained with the help of the Otsu threshold selection is more useful to the polyline generation step in mesh generation, leading to more accurate identifications of the image discontinuities and ERD models of better quality. Therefore, the Otsu threshold selection in the Canny edge detector, as explained above, is considered as one of the modifications that will later be used in the proposed SEMMG mesh-generation method.

3.2.2 Improving Wedge-Value Calculation

Having identified potential areas for improvements in the edge detector used in the ERDED and ERDGPI methods, we now analyze the next area which is the technique used to calculate the wedge values of the ERD mesh model. Many experiments with different test cases showed the reconstructed images obtained by the ERDED (or ERDGPI) method have some particular types of distortions and artifacts near certain edges (i.e., polylines in the mesh). To show this type of distortion herein, the ERDED method was used to generate the reconstructed images. Then, the error between the original and reconstructed images was visualized by an error image (as introduced in Section 2.8) to better locate the distortions. Three examples of the error images obtained by the above process, for the lena and bull images from Appendix A, are illustrated in Figure 3.7. In this figure, the regions of interest marked with rectangles in the parts of the original images in Figures 3.7(a), (b), and (c) are magnified as shown in Figures 3.7(d), (e), and (f), respectively. For the regions of interest shown in Figures 3.7(d), (e), and (f), the corresponding error images generated using the reconstructed images obtained by the ERDED method are shown in Figures 3.7(g), (h), and (i), respectively. As can be seen from the error images in Figures 3.7(g), (h), and (i), some darker shaded areas exist near the edges, indicating the existence of higher reconstruction errors in those regions.

After careful investigation, the root cause of the above type of distortion (of which a few examples shown in Figure 3.7) was found to be in the technique used for calculating the wedge values. The ERDED and ERDGPI methods (as we recall from Section 2.9) both employ a local line search to find the wedge values. For this purpose, the line bisecting the wedge is searched to find the the point whose MMSODD is the greatest. The line search, however, is restricted to a distance in the range [1,1.5] along the bisecting line (as we recall from Figure 2.19). Further careful analysis showed that the line search can lead to inaccurate wedge values because of the fixed distance range of the line search. Then, when the original image function is approximated using the inaccurate wedge values, the errors such as the ones shown in Figure 3.7 are produced.

To better explain why the fixed-range line-search approach is problematic, we consider two edge profiles, one that corresponds to a sharp image edge and one that corresponds to a more blurred image edge. Simplified examples of these types of edge profiles are shown in Figures 3.8 and 3.9. In these figures, parts of triangulations, including the vertex v are shown in Figures 3.8(a) and 3.9(a), where the thicker edges correspond to the constrained edges. The simplified function of the image intensity for each edge profile is drawn in Figures 3.8(b) and 3.9(b). Also, the magnitude of the second-order directional derivatives of the image functions drawn in Figures 3.8(b) and 3.9(b) are shown in Figures 3.8(c) and 3.9(c), respectively. The dotted vertical line passing through the middle of each edge profile corresponds to the image

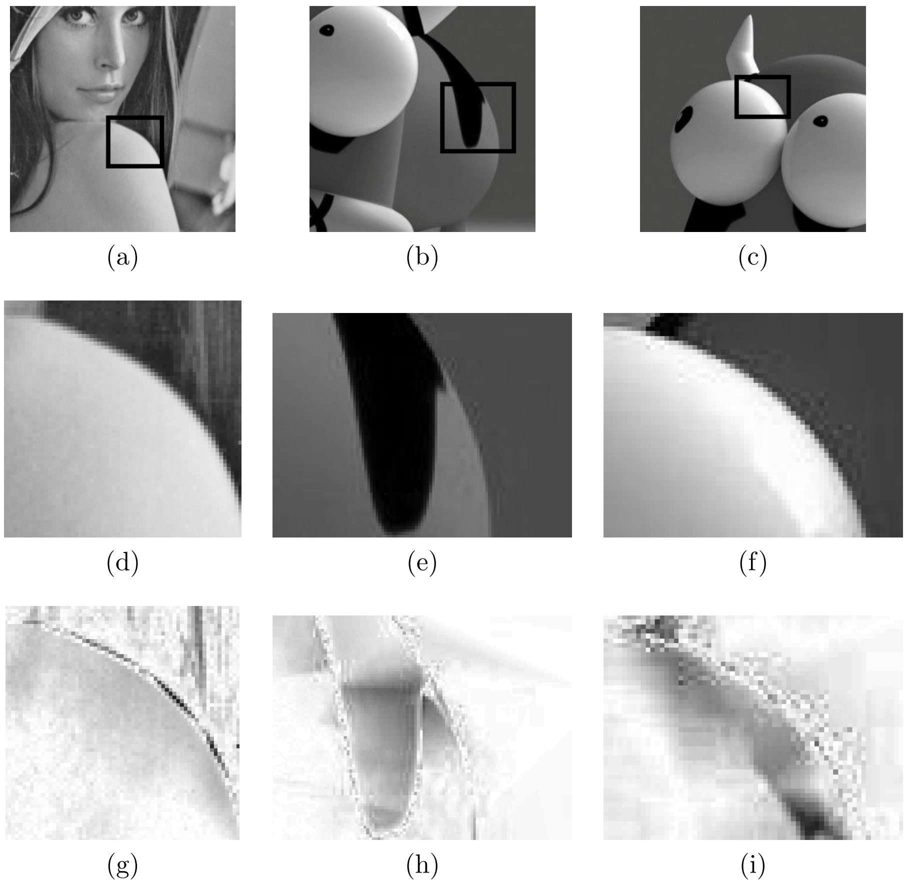

Figure 3.7: Examples of error images obtained by the ERDED method using the lena and bull images. The (a), (b), and (c) parts of original images with regions of interest marked with black rectangles. The (d), (e), and (f) magnified views of the regions of interest in original images. The (g), (h), and (i) error images.

edges detected by the edge detector which are represented with constrained edges. Therefore, in Figures 3.8(a) and 3.9(a), two wedges are formed whose wedge values should be calculated, one on each side of the constrained edge and incident to vertex v. The horizontal dashed line passing through v in Figures 3.8(a) and 3.9(a) is the bisecting line used by the line-search approach. In what follows, we only consider the process of calculating the value of the wedge on the left side of the constrained edges in Figures 3.8 and 3.9. The same analysis applies to the wedge on the right side of the constrained edge.

In the case of the sharp edge in Figure 3.8, the bisecting line (of the left wedge) in Figure 3.8(a) is searched to find the point that has the highest MMSODD and also falls inside the search range of $d \in [1, 1.5]$. As Figure 3.8(c) shows, the point p with

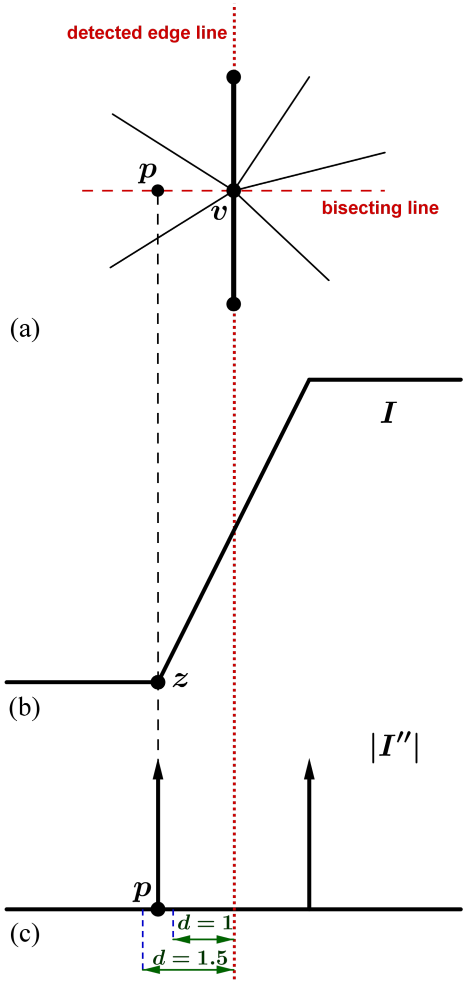

Figure 3.8: Sharp image-edge profile. The (a) top view of the triangulation, (b) cross-section of the image intensity, and (c) magnitude of the second-order directional derivative of the image intensity.

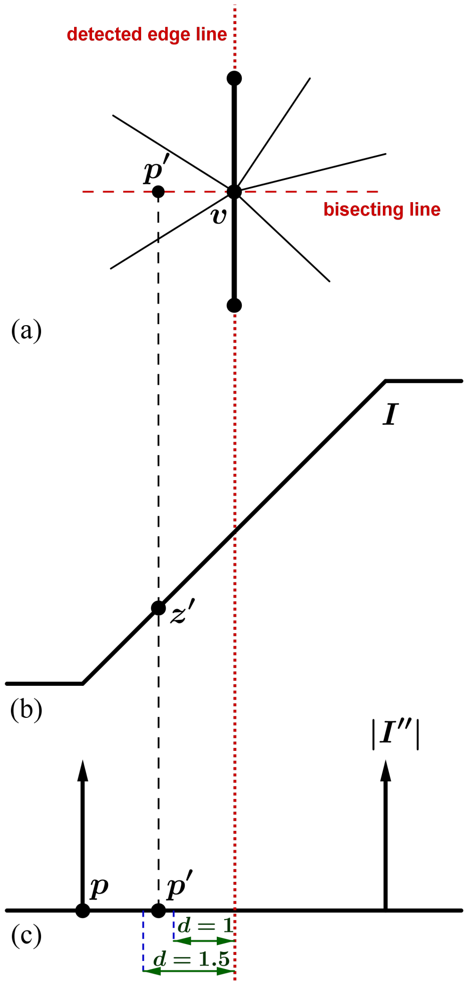

Figure 3.9: Blurred image-edge profile. The (a) top view of the triangulation, (b) cross-section of the image intensity, and (c) magnitude of the second-order directional derivative of the image intensity.

the greatest MMSODD (as denoted by a vertical arrow) falls within the search range of $d \in [1, 1.5]$. Thus, p is selected, which is what we would like to happen. Then, the intensity value z at the point p from the Figure 3.8(b) is selected as the wedge value associated with the wedge on the left side of the edge. Similarly, in the case of the blurred edge profile in Figure 3.9, we would want the algorithm to select point p in Figure 3.9(c) because it is the point with the greatest MMSODD along the bisecting line of the wedge. As the Figure 3.9(c) shows, however, the desired point p falls outside the search range of $d \in [1, 1.5]$. Therefore, the line search fails to detect the

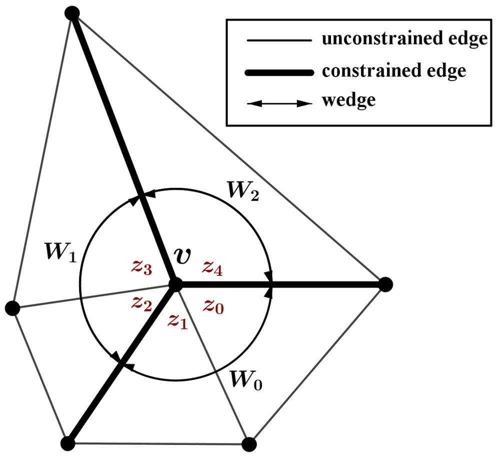

Figure 3.10: The relationship between wedges, corners, and corner values.

point p and, instead, detects another point such as p' within the range of $d \in [1, 1.5]$ as shown in Figure 3.9(c). Consequently, the intensity value z' at the point p' is selected from Figure 3.9(b) as the value of the wedge on the left in Figure 3.9(a). Since an image most often contains different edge profiles with various sharpness levels, no single fixed range of line search can be found that works best for all edge profiles. As a result, high approximation errors are produced on one side of a reconstructed edge, where wedge values are not properly selected. The approximation errors previously shown in the examples in Figure 3.7 can be justified using the above analyses.

The analysis mentioned above motivated us to employ a more effective approach to find more accurate wedge values, which are used to construct the approximating function over the faces. In what follows, a new optimization-based technique to compute the wedge values is proposed.

Optimization-based wedge-value selection. Before introducing our new technique for calculating wedge values, the term *corner z value* that is used by our technique, should be first defined. A wedge (as we recall from Section 2.9), in an ERD model, is a set of triangles surrounded by two constrained edges incident on a vertex v. Also we know that each triangle is composed of three vertices and three angles. In what follows, a pair of a vertex and face in a triangle is referred to as a *triangle corner*. Thus, a wedge incident on v may contain one or more triangle corners incident on v. Each triangle corner of a wedge is associated with a value which is called a *corner z value*.

To better explain the concepts of triangle corners and corner z values, we consider an example of a vertex with three wedges in a triangulation. This example is shown in Figure 3.10. As this figure shows, a part of a triangulation containing a vertex v with three incident constrained edges is displayed. As can be seen in Figure 3.10, vertex v has three wedges denoted by W_0, W_1, and W_2. The wedge W_0 contains two triangle corners associated with the corner z values z_0 and z_1. Similarly, the wedge W_1 contains two triangle corners associated with the corner z values z_2 and z_3, but the wedge W_2 only contains one triangle corner associated with the corner z value z_4.

For an original image function ϕ defined on a truncated rectangle grid $\Lambda = \{0, 1, ..., W-1\} \times \{0, 1, ..., H-1\}$ and the approximating function $\hat{\phi}$, the z value of a triangle corner incident to a vertex v specifies the limit of $\hat{\phi}$ at the point p (i.e., $\hat{\phi}(p)$) as p approaches v from points inside the triangle. In other words, the concept of a corner z value is similar to that of a wedge value (as defined in Section 2.9), but a corner z value is associated with each single triangle corner in a wedge.

Having introduced corner z values, we now describe the proposed optimization-based algorithm for selecting the wedge values in an ERD model, which contains the following steps (in order):

1. corner-value optimization (per each face), and
2. wedge-value calculation (per each vertex).

In the first step above, corner z values associated with triangle corners of each face are optimized with respect to minimizing an error measure. Then, in step 2, the final wedge value associated with each wedge of each vertex is computed using the optimized corner z values inside the wedge. In what follows, the detail of each step is explained.

1) Corner-value optimization. In this step, the corner z values associated with the corners of each face f in triangulation are optimized to minimize the total squared error between the original image function ϕ and approximating function $\hat{\phi}$, which is linear over f. The optimization problem introduced above is given by

$$\underset{C}{\operatorname{argmin}} \sum_{p \in \Omega} \left| \hat{\phi}(p) - \phi(p) \right|^2, \tag{3.1}$$

where Ω is the set of grid points in f and C is the set of corner z values in f that are optimized. The set C for each face f in (3.1) contains only z values of the corners in f that are incident to vertices with more than one constrained edges. In the case

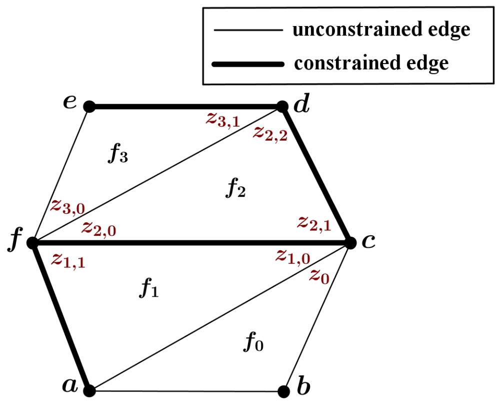

Figure 3.11: An example of a triangulation showing three different optimization cases.

of a vertex with zero or one constrained edge, the z values of the corners incident to that vertex are not optimized and simply selected as the values of the original image function at that vertex position.

To better explain how set C is determined for each face in (3.1), an example with six vertices, four faces, and four constrained edges in a part of a triangulation, as shown in Figure 3.11, is considered. The four faces, in Figure 3.11, are denoted as f_0 to f_3. Also, each corner z value that is optimized is written next to its triangle corner. In this figure, only z values of the corners incident to the vertices c, d, and f are considered for optimization, because these are the only vertices in Figure 3.11 that have only two incident constrained edges. Therefore, in f_0, only the corner z value z_0 is optimized (i.e., $C = \{z_0\}$). Similarly, in f_1, only the two corner z values $z_{1,0}$ and $z_{1,1}$ (i.e., $C = \{z_{1,0}, z_{1,1}\}$) and, in f_3, only $z_{3,0}$ and $z_{3,1}$ (i.e., $C = \{z_{3,0}, z_{3,1}\}$) are optimized. Finally, in f_2, all three corner z values $z_{2,0}$, $z_{2,1}$, and $z_{2,2}$ are considered for optimization (i.e., $C = \{z_{2,0}, z_{2,1}, z_{2,2}\}$). The z values of the corners incident with vertices a, b, and e are not optimized and interpolate the values of the original image function at points a, b, and e, respectively.

The minimization problem (3.1) is solved for every face of the triangulation separately. Moreover, as the minimization (3.1) is a typical least-squares problem, it can be efficiently solved by linear methods. In our work, the well-known gradient descent (also known as steepest descent) method is used to solve (3.1). The corner-value optimization process explained above may yield different corner z values inside the same wedge, introducing discontinuities along the unconstrained edges inside the wedge. In the ERD model, however, discontinuities are only allowed across the constrained edges. So, for the mesh to properly model the discontinuities, all the optimized corner

z values inside the same wedge should be combined to produce a single z value, which is used as the wedge value of that wedge. This process of combining the optimized corner z values in each wedge is performed in the next step.

2) Wedge-value calculation. Once the corner z values in the triangulation are optimized, the wedge value of each wedge is computed as follows. First, weighted average of all corner z values inside the same wedge are computed. For this purpose, the weight associated with each corner z value is the number of grid points inside the face to which the corner z value belongs. The wedge value is then obtained by rounding the averaged value to its nearest integer. In a general case, for a wedge of n triangle faces with n optimized corner z values $\{z_i\}_{i=0}^{n-1}$, the wedge value w is computed by

$$w = \text{round}\left(\frac{\sum\limits_{i=0}^{n-1} |\Omega_i| z_i}{\sum\limits_{i=0}^{n-1} |\Omega_i|}\right), \tag{3.2}$$

where Ω_i is the set of grid points in the face to which z_i belongs and $\sum\limits_{i=0}^{n-1} |\Omega_i| \neq 0$. The operator "round" in (3.2) rounds a real number to its nearest integer value. If, however, $\sum_{i=0}^{n-1} |\Omega_i| = 0$, then wedge value w is simply computed as the mean value of all corner z values $\{z_i\}_{i=0}^{n-1}$. Using the weighted averaging technique in (3.2), the optimized corner z value that belongs to a triangle with a larger area (i.e., $|\Omega|$) receives more weight in the averaging process. Moreover, the effect of (undesirable) corner z values obtained from very thin or tiny triangles is effectively reduced in the averaging process.

In order to perform a preliminary evaluation of the proposed optimization-based wedge-value-selection algorithm, the ERDED mesh-generation scheme was tested with the two old and new approaches for wedge-value selection, namely, the line-search and proposed optimization-based approaches. For this purpose, the two versions of the ERDED method were used to generate the reconstructed images. Then, the error between the original and reconstructed image was visualized by an error image (as introduced in Section 2.8) to better locate the distortions. The error images were then compared to see whether the proposed optimization-based method for wedge-value selection reduced the approximation errors. The results showed that the proposed optimization-based approach effectively reduces those types of artifacts produced by the line-search approach. For the sake of comparison, the same three examples of the

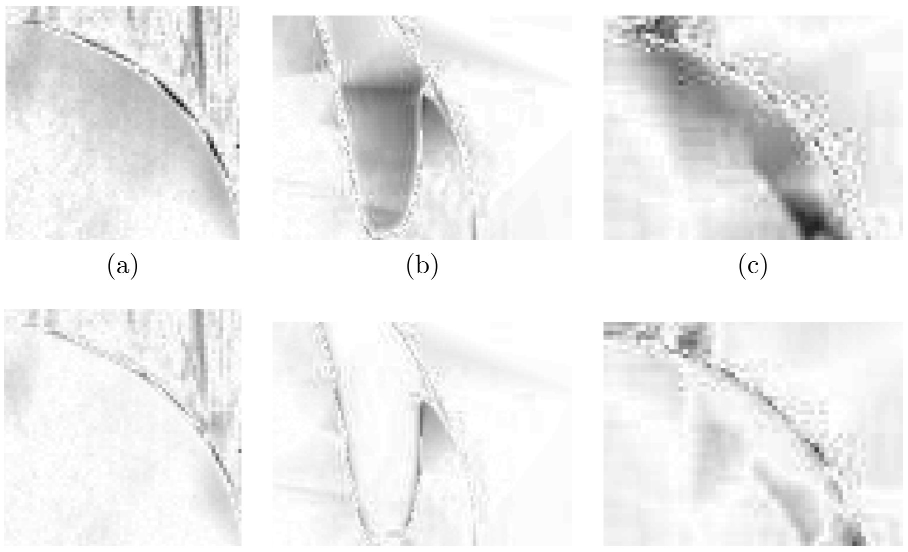
(a) (b) (c)

(d) (e) (f)

Figure 3.12: Examples of error images obtained by the ERDED method with the line-search and optimization-based approaches for the same regions of lena and bull images shown in Figure 3.7. The (a), (b), and (c) error images obtained with the line-search approach. The (d), (e), and (f) error images obtained with the proposed optimization-based approach.

lena and bull images previously used in Figure 3.7 are used here again. The error images obtained by the two versions of the ERDED method for the magnified regions shown in Figures 3.7(d), (e), and (f) are illustrated in Figure 3.12. As this figure shows, the darker areas in the error images obtained using the line-search approach in Figures 3.12(a), (b), and (c) are effectively reduced in the error images obtained using the proposed optimization-based approach of wedge-value selection of which results are shown in Figures 3.7(d), (e), and (f). This reduction of darker areas is an indication of the reduction in the approximation error. Therefore, the reduction of error in the vicinities of the image edges clearly indicates that the wedge values associated with the wedges within those vicinities are computed more accurately using the optimization-based approach.

In addition to the error image comparison, the performance of the proposed optimization-based algorithm in calculating the wedge values in the ERDED method was evaluated using the well-known PSNR metric. For this purpose, the ERDED method with the line-search and proposed optimization-based approaches were used to generate meshes using various images with different sampling densities. Then, for each case, the mean squared error between the original and reconstructed images was measured in terms of PSNR. In what follows, we focus our attention on the set of 20 test cases, including five test images with four sampling densities per image. The images were taken from Appendix A to include photographic, medical, and computer-generated imagery. The obtained PSNR results of the above 20 test cases are summarized in Table 3.1. In Table 3.1, the best result in each test case is highlighted in bold. The sampling densities for which results are presented are chosen to be representative of the range that would typically be used for each image in practice (which differs from image to image depending on image content). From Table 3.1, we can see that the our optimization-based approach outperforms the line-search approach in 18/20 of the test cases by a margin of up to 5.06 dB. Therefore, the results of these preliminary comparisons show that the ERDED method with the optimization-based approach is able to produce meshes of better quality, in terms of PSNR, than the ERDED method with the line-search approach. This improvement in the mesh quality is due to the proposed optimization-based algorithm that produces ERD mesh models with a more effective set of wedge values.

Therefore, in addition to employing the Otsu thresholding method proposed in the previous section, the optimization-based technique proposed for computing wedge values here is another effective modification that will later be incorporated in the newly proposed SEMMG mesh-generation method.

3.2.3 Improving Point Selection

Having analyzed the potential areas for improvements in edge detection and wedge-value selection, we now study the third area which is the criterion used for selecting sample points for mesh refinement. The two previously analyzed tasks (i.e., edge detection and wedge-value calculation) are performed in the same way for both the ERDED and ERDGPI methods. The point-selection criteria (as we recall from Section 2.9), however, are selected differently for the ERDED and ERDGPI methods. In what follows, the point-selection criterion that is employed by the ERDGPI method is analyzed. A detailed study of the reconstructed images obtained by the ERDGPI method with various test cases showed that some distortions were often found near certain smooth vertices (i.e., vertices that do not fall on a constrained edge) in the mesh. An example of such distortions in a reconstructed image obtained by the ERDGPI method using the peppers image from Appendix A is shown in Figure 3.13.

Table 3.1: Comparison of the mesh quality obtained using the ERDED method with the optimization-based and line-search approaches.

Image	Sampling Density (%)	PSNR(dB)	
		Optimization-based approach	Line-search approach
peppers	0.5	**22.49**	22.14
	1	**26.47**	25.97
	2	**29.26**	29.00
	3	**30.37**	30.17
lena	0.5	**20.81**	20.55
	1	**26.14**	25.81
	2	**29.38**	29.28
	3	31.30	**31.31**
ct	0.125	**18.72**	15.63
	0.25	**27.42**	25.97
	0.5	**31.62**	30.06
	1	**36.62**	36.51
bull	0.125	**25.22**	24.68
	0.25	**29.47**	28.86
	0.5	**35.35**	35.15
	1	**39.21**	39.02
wheel	0.0625	**35.75**	30.69
	0.125	**36.54**	34.55
	0.25	**37.24**	35.56
	0.5	37.38	**37.86**

In this figure, a part of the original image is shown in Figure 3.13(a) and the corresponding part in the reconstructed image obtained by the ERDGPI method at a sampling density of 2% is shown in Figure 3.13(b). As the reconstructed image in Figure 3.13(b) shows, several undesirable (triangulated) distortions are clearly visible compared to the original image shown in Figure 3.13(a).

To better identify the root cause of such distortions (for which an example was shown in Figure 3.13), a brief review of the approach used in the ERDGPI method to select the points is required. In the ERDGPI method (as we recall from Section 2.9), once the initial mesh and wedge values are determined, new sample points are selected to be added to the initial mesh. In what follows, these additional points are called non-edge sample points because the they are not selected by the edge detector. In the ERDGPI method, the new non-edge sample points are selected using an iterative process. In each iteration in the ERDGPI method: 1) the face f^* with the highest

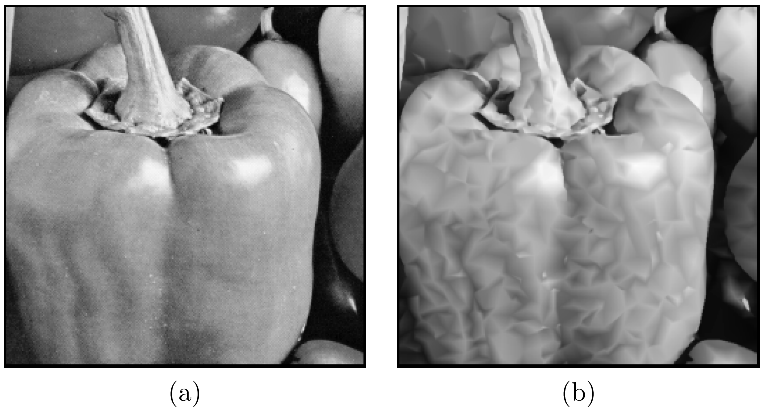

Figure 3.13: An example of the distortions produced by the ERDGPI method using the peppers image. The (a) part of the original image and (b) its corresponding part from the reconstructed image.

squared error is found (using (2.3)); and 2) then the point q with the highest absolute error in f^* is selected (using (2.4)). In what follows, this way of selecting non-edge points in the ERDGPI method is referred to as the "error-based approach".

After in-depth analyses on many reconstructed images obtained with the ERDGPI method, the point q with highest approximation error in f^* was found to often correspond to the noisiest pixel in f^*. Typically, the value of the noisiest pixel significantly differs from the values of the nearby pixels. Thus, in the error-based approach, noisiest pixels are often selected because they often have the largest reconstruction errors among the other nearby pixels in f^*. Also, the approximating function for the ERD model (as we recall from Section 2.9) linearly interpolates the z values at sample points in the original image. Therefore, if the noisiest point q is selected and inserted into the mesh, the approximating function has to interpolate its original z value, which corresponds to the value of the noisiest pixel. Consequently, the noisiest z value in f^* will be used in the approximating function, resulting in undesirable local distortions in the reconstructed images (like that shown in Figure 3.13(b)). Finally, as the above analysis shows, the root cause of such distortions is the criterion used by the error-based approach, which is selecting the point with the highest absolute error in f^*. This problem of the error-based approach motivated the author to consider finding a more effective criterion for selecting the non-edge points. As a solution, in what follows, a centroid-based approach for selecting the non-edge points is proposed.

Centroid-based approach. In the centroid-based approach, once the face f^* with the highest squared error is found, the point q is selected as the point that is

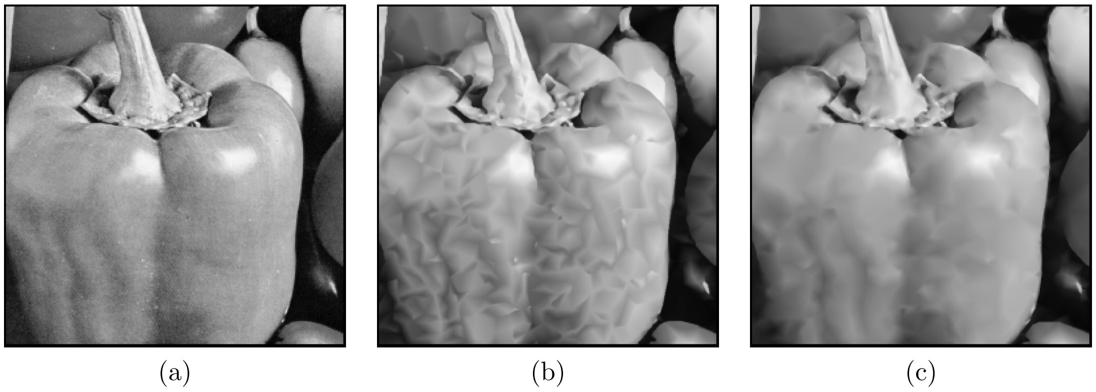

Figure 3.14: An example for comparing the reconstructed images obtained using the error-based and centroid-based approaches for the peppers image. The (a) part of the original image and its corresponding part from the reconstructed images obtained with the (b) error-based and (c) centroid-based approaches.

closest to the centroid of f^*. From a practical point of view, the point that is closest to the centroid is less probable to have the highest noise in f^*. In the error-based approach, however, the point with the highest absolute error is very likely to have the highest noise. Therefore, using the centroid-based approach as proposed above, the probability of selecting q as the noisiest point in f^* is significantly reduced. Moreover, our centroid-based approach increases the minimum interior angle in a triangle mesh, resulting in fewer long and thin triangles, which can often be quite beneficial.

To compare the performance of the centroid-based and error-based approaches, both of them were tested on different images at various sampling densities to generate the reconstructed images. The quality of the reconstructed images were then visually compared. Comparison results clearly showed that using the centroid-based approach effectively reduces the undesirable type of distortion created by the error-based method. To show how our centroid-based approach impacts the reconstructed images, an example with the peppers image from Appendix A is presented in Figure 3.14. For this purpose, the peppers image was reconstructed at a sampling density of 2% using the error-based and centroid based approaches. As Figure 3.14 shows, the distortions in the reconstructed image obtained by the error-based approach in Figure 3.14(b) are considerably reduced in Figure 3.14(c), where the proposed centroid-based approach is used.

As the above comparison indicates, the centroid-based approach selects non-edge sample points more effectively than the error-based approach, leading to reconstructed images of better subjective quality. Thus, the centroid-based approach is considered as the third main modification that will be used later in the SEMMG mesh-generation method (in addition to the Otsu thresholding method and the optimization-based wedge-value selection technique introduced previously).

3.3 Proposed SEMMG Method

In the preceding sections, we identified different potential areas for improvements in the ERDED and ERDGPI methods. Moreover, for each area, we studied how the employed approach affects the quality of the generated ERD mesh model. Also, in each identified area, a specific approach was recommended based on a detailed analysis to improve the performance of the mesh-generation method. With the insight from those analyses, we are now ready to introduce our proposed SEMMG method for producing ERD mesh models.

For an image function ϕ defined on the rectangular region $\Gamma = [0, W-1] \times [0, H-1]$, an ERD mesh model (introduced in Section 2.9) of ϕ consists of: 1) a set $P = \{p_i\} \subset \Gamma$ of sample points, 2) a set E of edge constraints, and 3) a set Z of integer wedge values. The proposed SEMMG mesh-generation method selects the parameters of the ERD model (i.e., P, E, and Z) to obtain an approximation $\hat{\phi}$ of the original image ϕ. The inputs to the SEMMG method are a desired mesh size N (i.e., $N = |P|$) and an image function ϕ that is known only at the points in $\Lambda = \{0, 1, ..., W-1\} \times \{0, 1, ..., H-1\}$ (i.e., a truncated integer lattice of width W and height H). The outputs of the SEMMG method are the ERD model parameters, including $P \subset \Lambda \subset \Gamma$, E, and Z. In what follows, we introduce the general algorithmic framework for the SEMMG method. Then, the specifics of the method are explained. The general algorithmic framework of the SEMMG mesh-generation method consists of the following steps (in order):

1. *Initial triangulation selection.* Select the values for the initial set P_0 of sample points and E. Then, the initial mesh associated with the (unique) preferred constrained Delaunay triangulation $\operatorname{pcdt}(P_0, E)$ (as introduced in Section 2.7) is constructed.

2. *Wedge-value initialization.* For each vertex $v \in P_0$, compute the initial wedge values using the optimization-based technique proposed previously in Section 3.2.2.

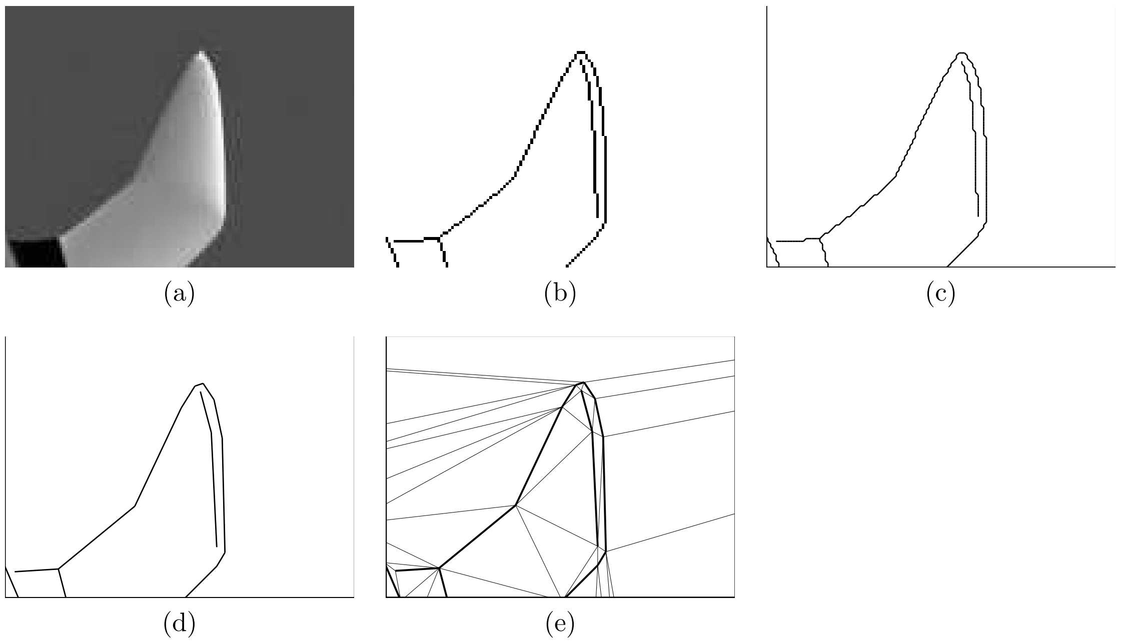

Figure 3.15: Selection of the initial triangulation in step 1 of the SEMMG method. (a) Part of the input image. The (b) binary edge map of (a). The (c) unsimplified polylines representing image edges in (b). The (d) simplified polylines. (e) The initial triangulation corresponding to the part of the image shown in (a), with constrained edges denoted by thick lines.

3. *Point selection.* Select a new sample point $q \in \Lambda$ to add to the mesh using the centroid-based approach proposed previously in Section 3.2.3.

4. *Point insertion.* Insert q in the triangulation. Calculate the wedge values of the affected wedges in the mesh using the same optimization-based technique (proposed in Section 3.2.2) and select the set P_{i+1} of sample points for the next iteration as $P_i \cup \{q\}$.

5. *Stopping criterion.* If $|P_{i+1}| < N$, go to step 3. Otherwise, set the output parameter $P = P_{i+1}$ and stop.

In the framework above, steps 1 and 2 choose an initial coarse mesh of size N_0, where $N_0 = |P_0|$. Then, in steps 3 to 5, the initial mesh is iteratively refined by adding $N - N_0$ sample points to the mesh. In what follows, the selection of P_0 and E in step 1 and point insertion of step 4 will be described in more detail.

Selection of P_0 and E. In step 1 of the SEMMG method, P_0 and E are first selected and then the triangulation $\text{pcdt}(P_0, E)$ is constructed. An example with the test image bull from Appendix A is used in Figure 3.15 to show different stages of selecting P_0, E, and initial triangulation. The sets P_0 and E are selected as follows. First, the Canny edge detector in [23] is applied to the input image ϕ defined on Λ to produce the binary edge map B, in which an entry is one if it corresponds to an edge pixel, and zero otherwise. In the Canny edge detector, the high threshold τ_h is computed using the Ostu-based approach proposed earlier in Section 3.2.1.2. Then the low threshold τ_l is selected as $\tau_l = \tau_h/2$. In the example given in Figure 3.15, for the part of the input image given in Figure 3.15(a), the corresponding binary edge map B is shown in Figure 3.15(b), where edge pixels are shown in black. Then, from B, a collection of polylines is generated to represent edges. To achieve this, edge pixels in B that are 8-connected are joined (by line segments) to form a polyline. If a polyline has one or more self-intersections (excluding loops), the polyline is split at each intersection point. In this way, the final set of polylines are guaranteed to not to have any intersections (excluding loops). In the example given in Figure 3.15, for the edge map shown in Figure 3.15(b), a set of polylines like the one shown in Figure 3.15(c) is constructed. Next, the polylines are simplified. To perform this, polylines with fewer than ℓ points are disregarded. In our method, $\ell = \operatorname{round}(0.01 \max(W, H))$, where the operator "round" rounds a real number to its nearest integer value. Then, from each remaining polyline, we generate another polyline with fewer points that well approximates the original polyline, resulting in a new set of simplified polylines. For this purpose, the well-known Douglas-Peucker (DP) simplification method from [34] (introduced in Section 2.3) is employed, with the tolerance parameter $\varepsilon = 1$. The output of the polyline simplification process is a set D of simplified polylines. In the example given in Figure 3.15, for the polylines given in Figure 3.15(c), a corresponding set D of simplified polylines is illustrated in Figure 3.15(d). Finally, P_0 is chosen as the union of all vertices in D, plus the extreme convex-hull points of Λ (i.e., the four corner points of the bounding box of input image) and E is selected as the union of all line-segments in D.

Once P_0 and E are selected using the above procedure, the $\operatorname{pcdt}(P_0, E)$ is constructed. In the example given in Figure 3.15, for the part of the simplified polylines given in Figure 3.15(d), the corresponding part from the initial triangulation is shown in Figure 3.15(e), where constrained edges are denoted by thick lines.

Point insertion. After the new point q has been selected in step 3 of the above framework, it will be inserted as a new vertex into the mesh and wedge values of the affected wedges should be calculated as follows. If q is on a constrained edge, the

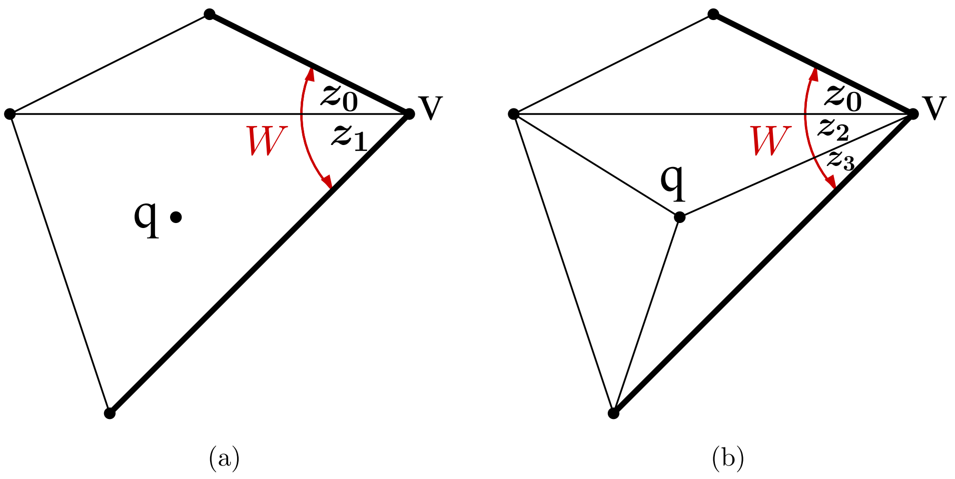

Figure 3.16: An example showing how inserting a new point affects the wedges. The (a) triangulation before inserting new point q. The (b) corresponding triangulation after q has been inserted. Constrained edges are denoted by thick lines.

edge is split at q into two constrained edges. Then, the wedge values for the two new wedges around the vertex q are calculated. If, however, q in not on a constrained edge, the wedge values for the old wedges that are affected by inserting q must be recalculated. In any of the preceding cases, the wedge values are calculated using our optimization-based technique proposed in Section 3.2.2. Figure 3.16 shows a simple example of how inserting a new point q can affect the wedges. The same part of a triangulation before and after point insertion is illustrated in Figures 3.16(a) and (b), respectively, where thick lines denote the constrained edges. The point q in Figure 3.16(a) is the new point that will be added to the mesh (but is not yet added). The wedge W incident to vertex v in Figure 3.16(a) contains only two triangles. Thus, the wedge value associated with W, in Figure 3.16(a), is calculated using two corner z values, z_0 and z_1. After q has been inserted, however, W contains three triangles as shown in Figure 3.16(b). Then, the wedge value of W must be recalculated (with the optimization-based technique) using three corner z values z_0, z_2, and z_3.

After finishing all the steps in the framework explained above, for a desired N number of sample points, the proposed SEMMG method generates an ERD triangle mesh model with all the required parameters, including the set P of sample points (where $|P| = N$), set E of constrained edges, and set Z of wedge values.

Chapter 4

Evaluation and Analysis of the SEMMG Method

4.1 Overview

Having introduced the proposed SEMMG mesh-generation method, we now evaluate its performance by comparing the quality of the meshes obtained from it with those obtained from other mesh-generation schemes. In general, comparing to other mesh-based methods is very difficult because of the following two reasons. Firstly, due to the high complexity of the mesh-based methods, implementing each of them often requires at least several months of work, including coding, testing, and debugging. Secondly, since so much effort is involved in implementing such methods, researchers often do not want to make their code freely available. Thus, finding implementation of other methods is very difficult too. For evaluating our SEMMG method herein, in cases where the implementations of competing methods were available, they were used, but in most cases, no implementation was available. Then, in cases where no implementation was available, the results that could be compared to were used from the publication. With the consideration of the above limitations in comparing to other mesh-based methods, the SEMMG method is compared to eight approaches in total, in two categories of the methods with and without implementations. In particular, the SEMMG method is compared to the following four approaches, where an implementation was available:

- the ED method of Yang et al. [96],
- the MGH method [12], inspired by the work in [43],

- the ERDED method of Tu and Adams [84], and
- the ERDGPI method of Tu and Adams [84].

Moreover, the SEMMG method is compared to the following four schemes, where no implementation was available:

- the GVS method of Garcia et al. [42],
- the HWT method of Phichet [83],
- the BSP method of Sarkis and Diepold [74], and
- the ATM method of Liu et al. [63].

The above eight competing methods are based on mesh-refinement schemes and generate mesh models that are all associated with an approximating function that is piecewise-linear and interpolates the original image function at the sample points (same as the SEMMG method), except the ATM method, which employs a non-linear and non-interpolating approximating function.

For the purpose of comparison, a C++ software implementation of the SEMMG method was developed by the author of this thesis. The details of the software implementation are presented in Appendix D. The performance of the SEMMG method was evaluated by comparing it in terms of mesh quality with each of the above competing methods. The qualities of the meshes obtained by these methods were all measured in terms of the well-known PSNR (as introduced in Section 2.6). The selection of test images was limited by some of the factors mentioned earlier. For example, if the implementation of a method was available, such as the ED, MGH, ERDED and ERDGPI methods, more results were collected with more test images. In the case of the methods without implementations, however, the test images were limited to the only few available ones for which results were reported in the literature. The test images that are used in the following sections are all listed in Appendix A. In what follows, our SEMMG method is compared with each of the previously-listed competing methods. Furthermore, the main differences between the SEMMG method and each of the competing methods are also highlighted. Some of the results presented in this chapter have also been published in the author's paper [66].

4.2 Comparison to Methods With Implementations

Due to the various limitations explained earlier, in the case of the related and comparable mesh-generation methods for which implementations are available, the proposed SEMMG method is compared to the following four methods:

1. the ED method of Yang et al. [96],
2. the MGH method [12], inspired by the work in [43],
3. the ERDED method of Tu and Adams [84], and
4. the ERDGPI method of Tu and Adams [84].

In order to compare the performance of our SEMMG method with the above four methods, the implementation of each method was used to generate meshes. For the ED and MGH methods, their implementations that were developed by the author of [12] were used. For the ERDED and ERDGPI methods, their implementations that were developed by the first author of [84] were used.

It is worth mentioning that the sampling densities that are used here for mesh generation are the input parameters to the methods. Thus, sampling densities are generally defined by the user based on what mesh quality or size is more preferable in an application where a mesh-generation method is used. For example, with a low sampling density of 0.03125% for complicated photographic and small images, such as lena, the SEMMG method yields a very poor image reconstruction (with approximately 17 dB in PSNR). In the case of the larger and simpler images, such as cherry, however, the sampling density of 0.03125% is high enough for the SEMMG method to produce a reconstructed image of satisfactory quality (with approximately 39 dB in PSNR). Therefore, in practice, the range of sampling densities that would be typically used for producing a satisfactory image reconstruction may differ from image to image. In other words, using a fixed range of sampling densities for all images may not always lead to image reconstructions of the same (or even similar) qualities. For consistency, however, in our evaluation, a set of 35 test images was given to each of the five methods (i.e., the ED, MGH, ERDED, ERDGPI, and SEMMG methods) and meshes were generated at 10 sampling densities within a fixed range of 0.0078125% to 3% per image, leading to a test set of 350 cases per method. Then, a reconstructed image from each mesh was produced. Next, for each test case, the mean-squared error between the original image and the reconstructed image was measured in terms of

PSNR. For the comparison here, we focus our attention on a representative subset of 45 test cases per method, including nine images (from Appendix A) with five sampling densities per image. The obtained PSNR results for the above representative subset of test cases for all five methods are shown in Table 4.1, with the best result in each case being highlighted in bold. For the sake of the reader, the full set of 350 test cases is presented in Appendix C.

To be able to fit all the representative evaluation data in a same table, only the results obtained with five representative sampling densities (out of 10) per image are shown in Table 4.1. The nine representative images (out of 35), in Table 4.1, were selected in a way to include three smaller images with mediocre complexities (i.e., lena, peppers, and bull), three larger and more complicated images (i.e., pepper, fruits, and doll), and three simpler and synthetic images (i.e., bowling, cherry, and pig2). Also, the five representative sampling densities per image, in Table 4.1, were selected in way to roughly cover the range that would typically be used for that image. More specifically, for those three simpler and synthetic images, the lowest five, and, for the other more complicated images, the highest five sampling densities in the range are shown. Having explained our evaluation methodology and the process of data collection, we are now ready to compare the proposed SEMMG method with each of the other four methods.

SEMMG versus ED. First, we compare the SEMMG and ED methods. In Table 4.1, from the PSNR results in two columns of the ED and SEMMG methods, we can see that the SEMMG method outperforms the ED scheme in 45/45 (100%) of the test cases, by a margin of 1.75 to 25.95 dB (with a median of 8.58 dB). Similarly, in our full data set of 350 cases, the SEMMG method outperforms the ED scheme in 100% of cases, by a margin of 0.33 to 26.46 dB (with a median of 7.43 dB). Furthermore, subjective image quality was found to correlate reasonably well with PSNR. To compare the subjective qualities of the reconstructed images obtained by the ED and SEMMG methods, an example using the lena image from Appendix A is presented in Figure 4.1. A part of the original image and its corresponding part from the reconstructed images obtained with the ED and SEMMG methods at a sampling density of 2% are illustrated in Figures 4.1(a), (b), and (c), respectively. As Figure 4.1 shows, the reconstructed image obtained with our SEMMG method in Figure 4.1(c) clearly has higher (i.e., 4.5 dB increase in) quality than the one obtained with the ED method shown in Figure 4.1(b).

The improvements achieved by our SEMMG method compared with the ED

Table 4.1: Comparison of the mesh quality obtained with the ED, MGH, ERDED, ERDGPI, and SEMMG methods

		PSNR (dB)				
Images	Sampling Density(%)	ED	MGH	ERDED	ERDGPI	SEMMG
lena	0.25	14.49	21.66	17.96	22.77	**23.08**
	0.5	17.17	24.31	20.55	25.58	**25.75**
	1	21.13	26.91	25.81	**28.35**	28.29
	2	25.83	29.78	29.28	**30.80**	30.39
	3	28.06	31.30	31.31	**32.31**	31.54
peppers	0.25	13.88	21.39	17.66	22.81	**23.00**
	0.5	16.03	24.60	22.14	25.99	**26.30**
	1	21.35	27.45	25.97	28.40	**28.67**
	2	26.09	29.94	29.00	30.42	**30.49**
	3	28.17	31.17	30.17	**31.50**	31.47
bull	0.25	20.59	35.29	28.86	**38.33**	35.91
	0.5	25.89	38.76	35.15	**40.17**	38.47
	1	33.34	41.07	39.02	**41.39**	41.04
	2	37.56	43.07	40.55	42.55	**43.43**
	3	40.36	44.54	41.05	43.35	**44.80**
pepper	0.25	31.91	37.77	34.34	37.57	**40.70**
	0.5	37.34	39.00	36.99	38.80	**41.77**
	1	39.73	40.25	40.13	40.42	**42.61**
	2	41.36	41.64	41.41	41.55	**43.45**
	3	42.15	42.55	40.71	42.66	**44.01**
fruits	0.25	23.95	28.80	27.85	28.58	**31.14**
	0.5	27.00	29.83	29.52	29.71	**32.67**
	1	29.99	30.83	31.80	31.03	**33.42**
	2	31.81	31.88	32.78	32.29	**33.99**
	3	32.57	32.57	33.11	33.06	**34.32**
doll	0.25	28.43	32.33	34.08	32.19	**37.11**
	0.5	33.33	33.50	35.40	33.47	**37.66**
	1	35.22	34.87	36.55	35.11	**38.11**
	2	36.46	36.50	37.61	36.81	**38.68**
	3	37.27	37.63	38.10	37.93	**39.15**
bowling	0.0078125	16.27	22.84	19.70	23.68	**27.27**
	0.015625	16.28	26.64	21.29	33.51	**33.63**
	0.03125	16.96	32.16	26.95	38.70	**38.86**
	0.0625	16.34	37.89	33.89	**42.09**	41.45
	0.125	22.47	43.21	36.35	**45.24**	43.26
cherry	0.0078125	11.76	16.31	11.91	17.01	**34.52**
	0.015625	13.28	17.56	12.10	19.20	**37.77**
	0.03125	13.39	28.10	26.89	31.59	**38.78**
	0.0625	13.92	37.56	41.32	**43.47**	39.87
	0.125	29.24	43.57	41.87	**44.46**	42.25
pig2	0.0078125	17.35	**38.48**	18.22	36.54	37.56
	0.015625	16.43	**42.44**	19.31	39.33	42.22
	0.03125	23.05	44.71	30.93	44.03	**46.22**
	0.0625	27.65	46.08	37.36	45.92	**48.78**
	0.125	35.42	47.02	42.89	46.98	**50.32**

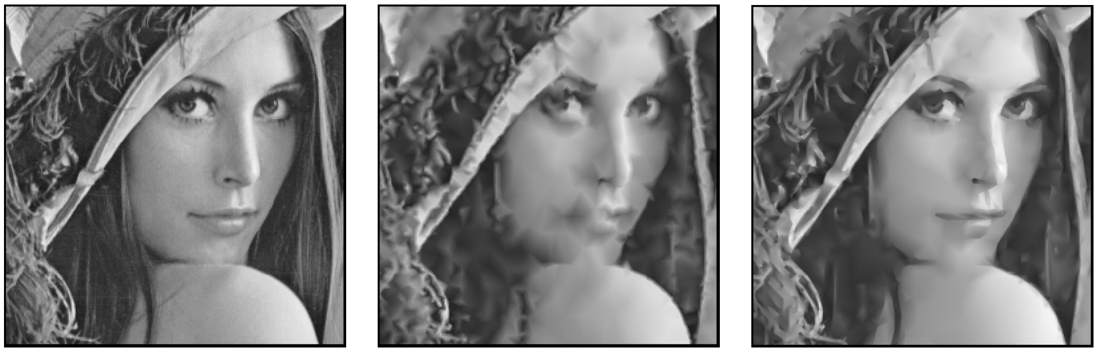
(a) (b) (c)

Figure 4.1: Subjective quality comparison of the ED and SEMMG methods using the lena image. Part of the (a) original image and its corresponding part from the reconstructed images obtained at a sampling density of 2% with the (b) ED (25.83 dB) and (c) SEMMG (30.39 dB) methods.

method, come mainly from the fact that the ED method does not directly take the image discontinuities into account while generating the mesh. Thus, in the meshes resulting from the ED method, many triangle edges cross image edges, leading to poor reconstructions of image edges (e.g., Figure 4.1(b)). Moreover, the ED method is blind to the square error, whereas, in our SEMMG method, some parameters of the model (e.g., corner z values) are computed with respect to minimizing squared errors of the faces in mesh. Consequently, the results obtained with the SEMMG method are superior to those produced with the ED method.

SEMMG versus MGH. Next, we compare the SEMMG and MGH methods. From the PSNR results of two columns for the MGH and SEMMG methods, in Table 4.1, we can see that the SEMMG method outperforms the MGH scheme in 40/45 (89%) of the test cases, by a margin of 0.05 to 20.21 dB (with a median of 2.14 dB). Similarly, in our full data set of 350 cases, the SEMMG method outperforms the MGH scheme in approximately 89% of cases, by a margin of 0.04 to 20.21 dB (with a median of 2.03 dB). Again, subjective quality was found to correlate well with PSNR. To compare the subjective quality of the reconstructed images obtained with the MGH and SEMMG methods, two examples using the bull and cherry images from Appendix A are shown in Figure 4.2. In this figure, a part of each original bull and cherry images is shown in Figures 4.2(a) and (d), respectively. The corresponding parts from the reconstructed bull and cherry images obtained with the MGH method at a sampling density of 0.125% and 0.03125% are shown in Figures 4.2(b) and (e), respectively. Similarly,

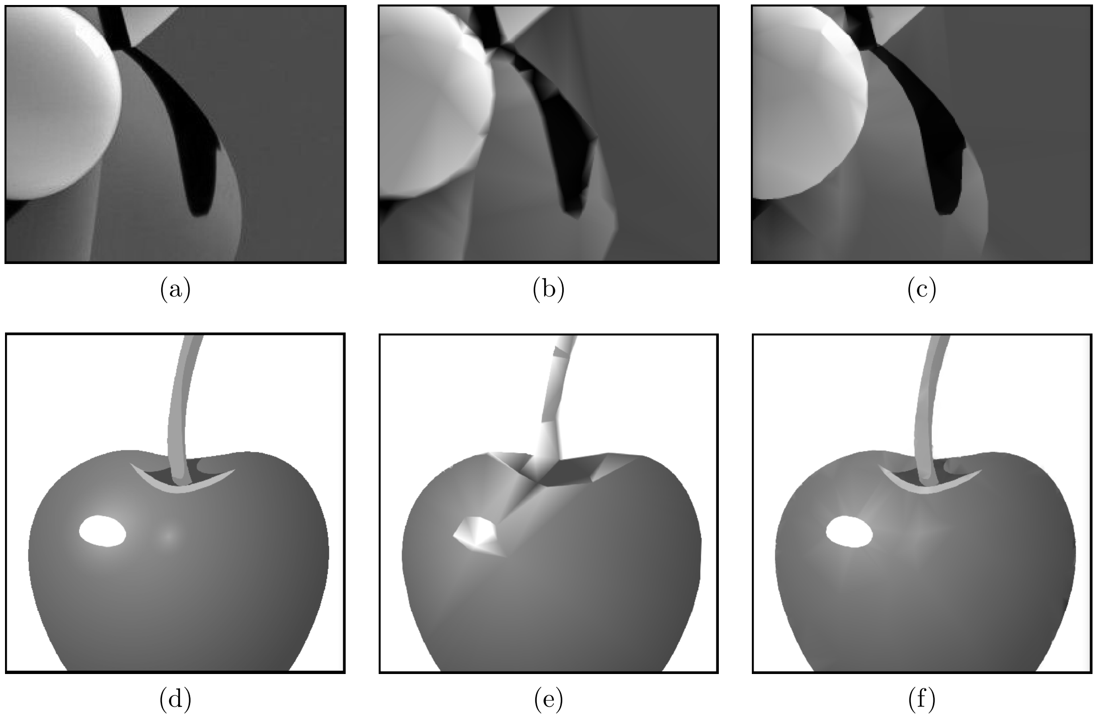

Figure 4.2: Subjective quality comparison of the MGH and SEMMG methods. Part of the original images of (a) bull and (d) cherry. The reconstructed images of bull obtained at a sampling density of 0.125% with the (b) MGH (30.74 dB) and (c) SEMMG (34.10 dB) methods. The reconstructed images of cherry obtained at a sampling density of 0.03125% with the (e) MGH (28.10 dB) and (f) SEMMG (38.78 dB) methods.

the same parts from the reconstructed bull and cherry images obtained with the SEMMG method at a same sampling density of 0.125% and 0.03125% are shown in Figures 4.2(c) and (f), respectively. As can be seen from Figure 4.2, the reconstructed images obtained by the SEMMG method in Figures 4.2(c) and (f) have significantly better qualities than those produced by the MGH method shown in Figures 4.2(b) and (e), respectively. These improvements are mainly due to the fact that the MGH method does not take any image-edge information into account. Thus, the MGH method results in meshes, where the triangle edges cross the image edges, causing high distortions around edges.

SEMMG versus ERDED. Now, we compare the SEMMG and ERDED methods. From the PSNR results of two columns for the ERDED and SEMMG methods in Table 4.1, we can see that the SEMMG method outperforms the ERDED scheme in 44/45 (98%) of the test cases, by a margin of 0.22 to 25.66 dB (with a median of 3.31

dB). Similarly, in our full data set of 350 cases, the SEMMG method outperforms the ERDED scheme in approximately 99% of cases, by a margin of 0.05 to 26.30 dB (with a median of 3.67 dB). The subjective quality was also found to correlate well with PSNR. To compare the subjective quality of the reconstructed images obtained with the ERDED and SEMMG methods, two examples using the pig2 and doll images from Appendix A are shown in Figure 4.3. In this figure, a part of each original pig2 and doll images is shown in Figures 4.3(a) and (d), respectively. The corresponding parts from the reconstructed pig2 and doll images obtained with the ERDED method are shown in Figures 4.3(b) and (e), respectively. Similarly, the same parts from the reconstructed pig2 and doll images obtained with the SEMMG method are shown in Figures 4.3(c) and (f), respectively. As can be seen from Figure 4.3, the reconstructed images obtained by the SEMMG method in Figures 4.3(c) and (f) obviously have better qualities than those produced by the ERDED method shown in Figures 4.3(b) and (e), respectively.

The significant improvements of the SEMMG method over the ERDED scheme can be justified as follows. On one hand, the ERDED method (unlike the ED method) takes image-edge information into account (as explained in Section 2.9) and is able to preserve the image edges. This property of the ERDED method helps to prevent triangle edges from crossing the image edges, leading to better image reconstructions than the ED method. On the other hand, the other drawback of the ED method (as explained previously) still exists in the ERDED method. Similar to the ED scheme, the ERDED method still does not take the squared error into account when selecting the non-edge points, leading to the reconstruction errors, of which examples shown in Figures 4.3(b) and (e). The SEMMG method, however, uses a more effective criterion to select the non-edge points which considers the squared errors of faces and improves the mesh quality, such as the examples shown in Figures 4.3(c) and (f).

SEMMG versus ERDGPI. Finally, we compare the SEMMG and ERDGPI methods. From the PSNR results of two columns for the ERDGPI and SEMMG methods, in Table 4.1, we can see that the SEMMG method outperforms the ERDGPI scheme in 34/45 (76%) of the test cases, by a margin of 0.06 to 18.56 dB (with a median of 2.05 dB). Similarly, in our full data set of 350 cases, the SEMMG method outperforms the ERDGPI scheme in approximately 85% of cases, by a margin of 0.02 to 24.72 dB (with a median of 1.60 dB).

Closer inspection of the PSNR results obtained from the ERDGPI and SEMMG methods, in Table 4.1, show that the ERDGPI method can produce comparable, and

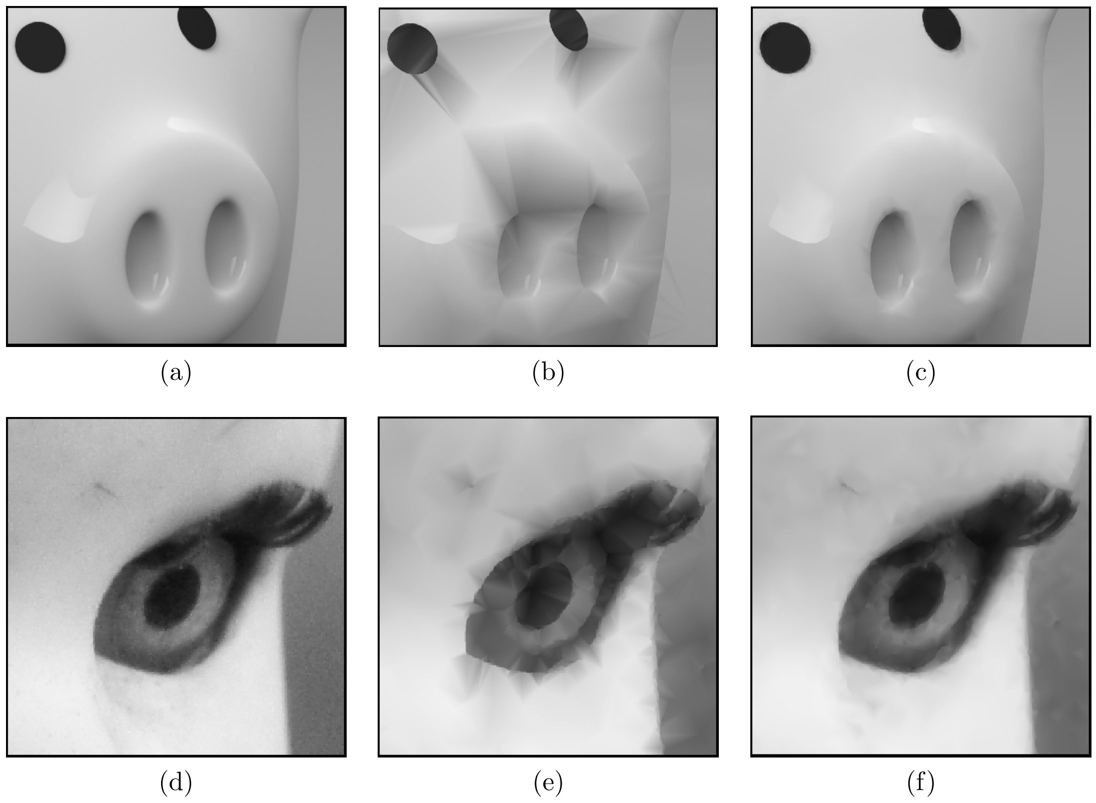

Figure 4.3: Subjective quality comparison of the ERDED and SEMMG methods. Part of the original images of (a) pig2 and (d) doll. The reconstructed images of pig2 obtained at a sampling density of 0.03125% with the (b) ERDED (30.93 dB) and (c) SEMMG (46.22 dB) methods. The reconstructed images of doll obtained at a sampling density of 0.25% with the (e) ERDED (34.08 dB) and (f) SEMMG (37.11 dB) methods.

sometimes better, mesh qualities in the case of the smaller images (e.g., lena, peppers, and bull). This is because the ERDGPI method (as we recall from Section 2.9) uses a high-resolution image grid to locate the edges with half-pixel accuracy. Such a more accurate edge localization is sometimes more beneficial in the case of the smaller images and can lead to meshes with higher qualities. In the case of the larger images in Table 4.1 (e.g., fruits, doll, and pig2), however, the SEMMG method clearly beats the ERDGPI method because employing such an edge detector with higher accuracy is not as advantageous as it was for smaller images.

In order to compare the subjective quality of the reconstructed images obtained with the SEMMG and ERDGPI methods, three examples using the doll, pepper, and fruits images from Appendix A are presented in Figure 4.4. In this figure, a

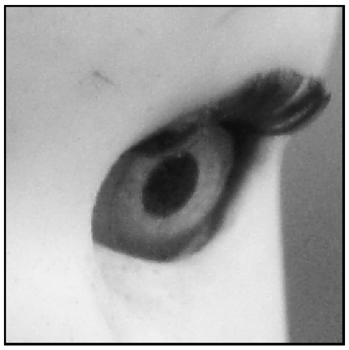
(a)

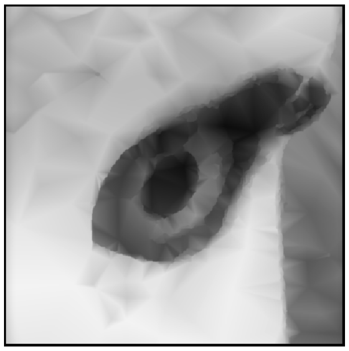
(b)

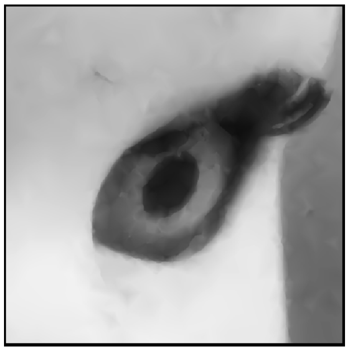
(c)

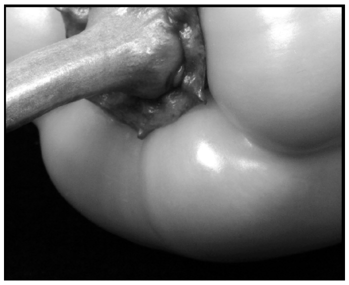
(d)

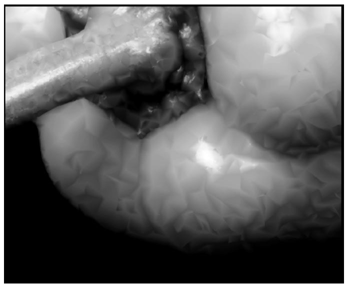
(e)

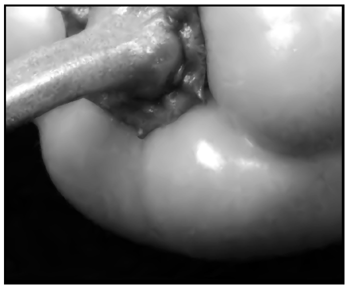
(f)

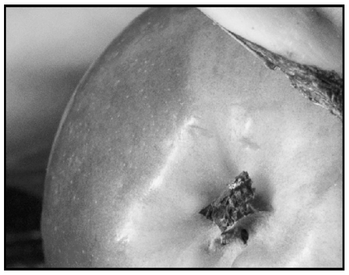
(g)

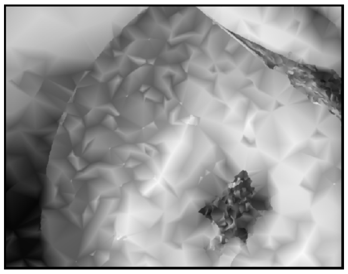
(h)

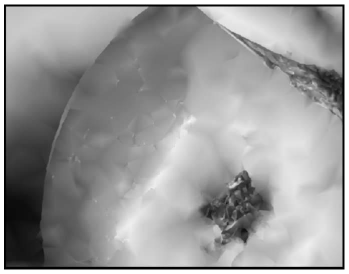
(i)

Figure 4.4: Subjective quality comparison of the ERDGPI and SEMMG methods. Part of original images of (a) doll, (d) pepper, and (g) fruits. The reconstructed images of doll obtained at a sampling density of 0.25% with the (b) ERDGPI (32.19 dB) and (c) SEMMG (37.11 dB) methods. The reconstructed images of pepper obtained at a sampling density of 0.25% with the (e) ERDGPI (37.57 dB) and (f) SEMMG (40.70 dB) methods. The reconstructed images of fruits obtained at a sampling density of 0.25% with the (h) ERDGPI (28.58 dB) and (i) SEMMG (31.14 dB) methods.

part of each original doll, pepper, and fruits images is shown in Figures 4.4(a), (d), and (g), respectively. The corresponding parts from the reconstructed doll, pepper, and fruits images obtained with the ERDGPI method at a sampling density of 0.25% are shown in Figures 4.4(b), (e), and (h), respectively. Similarly, the same parts from the reconstructed doll, pepper, and fruits images obtained with the SEMMG method at the same sampling density of 0.25% are shown in Figures 4.4(c), (f), and (i), respectively. As can be seen from Figure 4.4, the reconstructed images obtained by the SEMMG method in Figures 4.4(c), (f), and (i) have higher qualities than those produced by the ERDGPI method in Figures 4.4(b), (e), and (h), respectively.

4.3 Comparison to Methods Without Implementations

Having compared the SEMMG method with the related mesh-generation schemes of which implementations are available, we now compare it with other schemes for which implementations are not available. As mentioned earlier, one main limitation of comparing against the methods with no implementations is the fact that the comparison is limited to the only test data that was reported in the other researchers' publications. Also, such test data is not necessarily the same among all the publications. Another difficulty of comparing with the methods with no implementations is the fact that they do not always represent their results with respect to the same parameters or metrics. For example, as will be seen later, some publications represent the mesh size in terms of number of vertices, whereas some others represent in terms of the number of triangles. Therefore, due to the above inconsistencies in presenting results between different methods, the comparison to each method herein is performed separately with respect to its own test data and type of parameters. All test images used in these comparisons are listed in Appendix A. With the consideration of the above challenges, in what follows, the SEMMG method is compared with the following schemes:

1. the GVS method of Garcia et al. [42],
2. the HWT method of Phichet [83],
3. the BSP method of Sarkis and Diepold [74], and
4. the ATM method of Liu et al. [63].

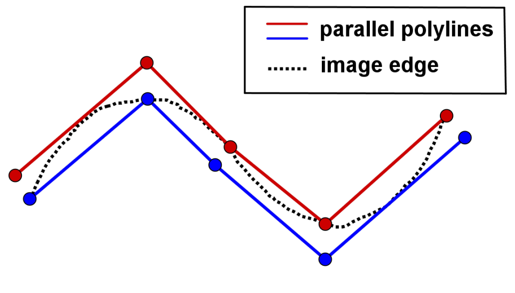

(a)

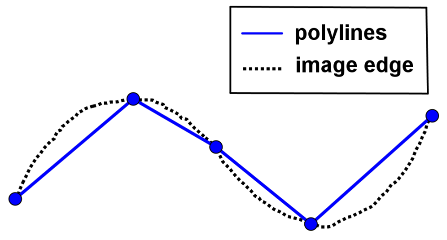

(b)

Figure 4.5: An example of an image-edge feature that is modeled differently in the GVS and SEMMG methods. The edge is modeled with (a) a pair of parallel polylines in the GVS method and (b) one polyline in the SEMMG method.

4.3.1 Comparison With the GVS Method

The GVS method of Garcia et al. [42], as one of the discontinuity-preserving mesh-generation methods, is a good candidate to compare with our proposed SEMMG method. Like our method, the GVS method is based on constrained Delaunay triangulations. Although both the GVS and SEMMG methods generate a mesh model that preserves image discontinuities, each of them employs a different technique to model the image discontinuities. In the GVS method, a pair of parallel polylines is used to model each image discontinuity (i.e., each image-edge feature). In the SEMMG method, however, only one polyline is used to approximate each image discontinuity. An example showing the difference between the discontinuity modeling in the GVS and SEMMG methods is illustrated in Figure 4.5. As this figure shows, the image-edge feature drawn by the dotted line is modeled using a pair of parallel polylines enclosing the edge in the GVS method as shown in Figure 4.5(a). In our SEMMG method, however, using the ERD model, the same edge feature is approximated using a single set of polylines as shown in Figure 4.5(b). Furthermore, the approximating function associated with the GVS mesh model is continuous everywhere, whereas the ERD model is associated with an approximating function that allows for discontinuities across the constrained edges.

To compare our SEMMG method with the GVS method, datasets were limited to only the three used in [42], with test images lena, peppers, and house (as shown in Appendix A). Thus, all those three images were given to our SEMMG method to generate meshes with the same mesh sizes (in terms of number of vertices) as those generated by the GVS method as reported in [42]. Then, from each mesh ob-

Table 4.2: Comparison of the mesh quality obtained with the GVS and SEMMG methods (with the same mesh size)

		PSNR (dB)	
Image	Number of vertices	GVS	SEMMG
lena	7492	28.30	**31.27**
peppers	7224	26.48	**31.09**
house	1649	27.62	**31.55**

tained from the SEMMG method, a reconstructed image was produced. Next, the mean-squared error between the original and reconstructed images was measured and compared with the mean-squared error reported in [42]. The mean-squared errors are represented in terms of the PSNR herein. Since in [42] only one sampling density per each test image was used, our comparison is limited to only three test cases as listed in Table 4.2, with the best result in each case being highlighted in bold. As can be seen from Table 4.2, with the same mesh size (i.e., number of vertices), the SEMMG method clearly outperforms the GVS method by producing better reconstructed images with the PSNR improvements of approximately 3.0, 4.6, and 3.9 dB for the lena, peppers, and house images, respectively.

Furthermore, the sizes of the meshes obtained with the SEMMG and GVS methods were also compared. For this purpose, our SEMMG method was used to generate meshes with the same mean-squared error as reported in [42] for the GVS method. Then, the sizes of the meshes (in terms of the number of vertices) obtained from the SEMMG method were compared to those reported in [42] for the GVS method. The results of this size comparison for all three test cases are presented in Table 4.3, with the best result in each case being highlighted in bold. As can be seen from Table 4.3, for a given PSNR, the SEMMG method generates much smaller meshes with approximately 65%, 80%, and 78% fewer vertices than the GVS method in the case of the lena, peppers, and house images, respectively. Consequently, as both the mesh-quality and size comparisons presented in Tables 4.2 and 4.3 show, our SEMMG method is superior to the GVS method by producing meshes of higher quality with significantly fewer vertices.

4.3.2 Comparison With the HWT Method

The next method that is compared with our SEMMG method is the hybrid wavelet-based triangulation (HWT) method of Phichet in [83]. This method is discontinuity

Table 4.3: Comparison of the mesh sizes obtained with the GVS and SEMMG methods (with the same PSNR)

		Number of vertices	
Image	PSNR (dB)	GVS	SEMMG
lena	28.30	7492	**2622**
peppers	26.48	7224	**1442**
house	27.62	1649	**361**

preserving, where the directions of the image edges are estimated using wavelet analysis. The HWT method employs a combination of both mesh refinement (i.e, point insertion) and simplification (i.e., point/edge removal) to achieve a mesh with a desired number of vertices. Moreover, in different stages of the HWT method, a hybrid technique combining Delaunay and data-dependent triangulations is used for edge swapping to further enhance the mesh quality. Finally, a continuous function is used to approximate the image function.

To compare our SEMMG method with the HWT method, our test data were limited to only the ten cases reported in Table 1 of [83]. These 10 test cases correspond to two test images (i.e., lena and elaine) with five sampling densities per image. For comparison, both lena and elaine images were given to our SEMMG method to generate ten meshes with the same sizes (i.e., number of vertices) reported in Table 1 of [83]. Then, from each mesh a reconstructed image was produced. Next, the mean-squared error between each of the reconstructed and original images was calculated in terms of the PSNR. The PSNR results obtained with all ten test cases from our SEMMG method and those reported in [83] are presented in Table 4.4, with the best result in each case being highlighted in bold. As Table 4.4 shows, the SEMMG method outperforms the HWT method in 10/10 of the test cases, by a PSNR margin of 0.32 to 1.32 dB (with a median of 0.66 dB).

To further understand the technical reason for the above improvement, a short explanation regarding the theory of the HWT method is needed as follows. In the HWT method, the wavelet detail coefficients are used to approximate the directions of the image edges. Then, in the mesh refinement step of the method, each triangle that is selected for further refinement is split in two subtriangles. Although the splitting direction is selected to be as close as possible to the direction of the image edges, it almost never aligns well with them due to a limitation in the HWT method. The splitting line has a limitation such that it always has to start from a vertex in the

Table 4.4: Comparison of the mesh quality obtained with the HWT and SEMMG methods (with the same mesh size)

		PSNR (dB)	
Image	Number of vertices	HWT	SEMMG
lena	4754	28.70	**30.02**
	5215	29.07	**30.38**
	5610	29.62	**30.44**
	6461	30.26	**30.98**
	7454	30.66	**31.26**
elaine	6519	30.41	**31.13**
	7019	30.71	**31.24**
	7510	30.74	**31.32**
	8462	31.02	**31.46**
	9552	31.26	**31.58**

triangle of interest and end at a point on the opposite edge. Consequently, most often, the splitting line is not accurately aligned with the direction of the image edges at early stages of the mesh refinement process. Therefore, more steps of triangle splitting is needed to reach a desired mesh geometry, where triangle edges are aligned well with the directions of the image edges. In the SEMMG method, however, image edges are explicitly represented with constrained edges in the mesh from the beginning. As a result, for the same number of vertices, the SEMMG generates meshes of higher quality than those produced by the HWT method, as shown in Table 4.4.

4.3.3 Comparison With the BSP Method

The next method that is compared with the SEMMG method is the binary space-partitioning (BSP) method of Sarkis and Diepold [74]. The BSP method is very similar to the HWT method discussed earlier in the sense that, in both of them, the triangles with higher errors are split into two subtriangles for further refinement. One main difference between the BSP and HWT methods is how the direction of the splitting line is selected. Three different variations of the BSP method was proposed in [74] based on the approach used for finding the splitting line. First variation of the BSP method uses a simple partitioning approach, where the splitting line is simply selected as the line connecting the middle point on the longest edge of a triangle to the vertex opposite to that edge. This variation is called the BSP-Tritree method. The other two variations are called the BSP-kmeans, which uses kmeans clustering

Table 4.5: Comparison of the mesh quality obtained with the BSP-Tritree and SEMMG methods (with the same mesh size)

		PSNR (dB)	
Image	Number of triangles	BSP-Tritree	SEMMG
lena	25000	30	**32.85**
	70000	35	**36.43**
peppers	25000	30	**32.79**
	75000	35	**35.26**
teddy	33960	30	**32.55**
	70750	35	**36.91**

to find the splitting line, and BSP-SVD, which uses the singular value decomposition (SVD). Based on the results presented in [74], all the above three variants of the BSP method produce meshes of very similar quality, with the BSP-Tritree performing slightly better than the other two variants. Thus, for the sake of comparison with our SEMMG method herein, the results obtained from the BSP-Tritree (i.e., the best results from [74]) are considered.

To compare our SEMMG method with the BSP-Tritree method, our test images were limited to the only three (i.e., lena, peppers, and teddy) used in [74]. For comparison, all three images were given to our SEMMG method to generate meshes with the same sizes (in terms of the number of triangles) reported in Figures 4, 5, and 6 of [74] at two PSNR values of 30 and 35 dB (i.e., total of six test cases). Then, the six meshes (i.e., two meshes per image) obtained form the SEMMG method were used to produce the reconstructed images. Next, the mean squared-error between the original and reconstructed images was computed in terms of the PSNR. The PSNR results obtained using all six test cases are presented in Table 4.5, with the best result in each case being highlighted in bold. As this table shows, the SEMMG method outperforms the BSP-Tritree method in 6/6 of the test cases by producing reconstructed images of better quality with a PSNR improvement of 0.26 to 2.85 dB (with a median of 2.23 dB).

In addition to mesh quality, the sizes of the meshes obtained with the SEMMG and BSP-Tritree methods were also compared. For this purpose, the same three test images (i.e., lena, peppers, and teddy) were given to our SEMMG method to generate meshes with the same PSNR (i.e., 30 and 35 dB) as those reported in [74]. Then, the sizes of the meshes (in terms of the number of triangles) obtained from the SEMMG

Table 4.6: Comparison of the mesh size obtained with the BSP-Tritree and SEMMG methods (with the same PSNR)

		Number of triangles	
Image	PSNR (dB)	BSP-Tritree	SEMMG
lena	30	25000	**9330**
	35	70000	**52183**
peppers	30	25000	**9781**
	35	75000	**67736**
teddy	30	33960	**17464**
	35	70750	**53394**

method were compared to those reported in [74] for the BSP-Tritree method. The results of this size comparison for all six test cases are presented in Table 4.6, with the best result in each case being highlighted in bold. As can be seen from Table 4.6, for a given PSNR, the SEMMG method generates much smaller meshes with approximately 25 to 60%, 10 to 60%, and 25 to 50% fewer triangles than the BSP-Tritree method for the lena, peppers, and teddy images, respectively. Consequently, as both the mesh-quality and size comparisons presented in Tables 4.5 and 4.6 show, our SEMMG method outperforms the BSP-Tritree method by producing meshes of higher quality with many fewer triangles.

To understand the reason for above improvements, the same analysis made earlier in the case of the HWT method applies to all variants of the BSP method as follows. The clustering approaches used in the BSP methods to find the splitting line do not necessarily result in splitting lines that are aligned well with the image edges. Therefore, more steps of triangle splitting are needed to achieve a mesh with higher quality, resulting in many more triangles than our SEMMG method, where the image-edge information is taken into account from the first place.

4.3.4 Comparison With the ATM Method

The last method for comparison is the feature-preserving image restoration method of [63] which is based on adaptive triangular meshes (ATM). Similar to the SEMMG method, the ATM method employs an edge detector to locate the image edges and also employs a constrained Delaunay triangulation for generating the mesh. The ATM method, however, uses a new non-linear approximating function based on anisotropic radial basis functions (ARBFs). Moreover, unlike the SEMMG method, the approx-

Table 4.7: Comparison of the mesh quality obtained with the ATM and SEMMG methods (with the same mesh size)

		PSNR (dB)	
Image (size)	Sampling density (%)	ATM	SEMMG
lena (256×256)	6	28.21	**29.33**

imating function in the ATM method uses the intensities at face centers instead of vertices.

For comparison with the ATM method, our test data was limited to the only four cases reported in [63], for the lena image of size 256×256 and three other biomedical test images. Out of these four images, only the lena image was available to the author of this thesis. A request was also sent to the author of [63] for any chance of providing either the implementation or those three biomedical images, but no reply was received. Therefore, the comparison here is based on only one possible test case. For this purpose, the lena image of size 256×256 was given to the SEMMG method to generate the mesh with the same sampling density of 6% as the one reported in Table 1 in [63]. The mesh obtained from the SEMMG method was then used to produce the reconstructed image. Next, the mean squared-error between the original and reconstructed images was computed in terms of the PSNR. The PSNR obtained from the SEMMG method and the one reported in [63] for the ATM method, for the single test case of lena, are presented in Table 4.7, with the best result being highlighted in bold. As this table shows, the SEMMG method outperforms the ATM method with a PSNR improvement of 1.12 dB for the lena image at a sampling density of 6%. Therefore, although the ATM method employs an improved and more complicated non-linear approximating function based on ARBFs, the SEMMG method is able to produce the mesh with better quality. The lower quality of the mesh obtained from the ATM method can be because of its mandatory step of uniform sampling, where some sample points are uniformly selected to cover the regions with almost constant intensities. This step of uniform sampling in the ATM method may lead to selecting too many sample points in areas with very small variations of intensities, resulting in a mesh with lower quality.

Chapter 5

Proposed MIS Method and Its Development

5.1 Overview

In this chapter, a new mesh-based approach for image scaling, called the MIS method, is proposed for grayscale images that are approximately piecewise-smooth, with no (or minimal) textures or patterns. The inputs to the proposed MIS method are a low-resolution raster image and an integer scaling factor and the output is a high-resolution raster image. In what follows, we first explain how the MIS method was developed. For this purpose, the performance of our SEMMG method, which was previously proposed for image representation in Chapter 3, is examined in the application of image scaling. Having the knowledge that the SEMMG method solves a totally different problem than image scaling, we would not expect it to perform well for this purpose without modification. For example, the polylines used in the SEMMG method to approximate the edges would obviously look rough and jagged if they are scaled. We also would not want to prematurely discard the SEMMG method. Thus, we study how it performs for image scaling in order to better understand potential shortcomings for this application. Through this study, different key techniques are devised to address the shortcomings. By applying these techniques, the mesh-generation method under analysis progressively evolves to a new one called the mesh-based image scaling mesh-generation (MISMG) method that can be effectively used for image scaling. As part of this progression, three intermediate methods, which are called MISMG$_0$, MISMG$_1$, and MISMG$_2$, are also introduced, where each method has an added modification to its predecessor. Aside from the mesh generation, the model rasterization is also analyzed and a subdivision-based approach for producing smoother edge contours and image functions is developed. Finally, the MISMG mesh-generation method is combined with a scaling transformation and the subdivision-based model-rasterization algorithm, yielding the proposed MIS method.

5.2 Development of MIS Method

We now present how the proposed MIS method was gradually developed. The MIS method is designed to solve the image scaling problem, where a low-resolution raster image and an integer scaling factor are the inputs and a high-resolution raster image is the output. The MIS method includes three main stages (in order): 1) mesh generation, 2) mesh transformation, and 3) model rasterization. In stage 1, a mesh-generation method is required to produce a mesh model from the input raster image sampled on a low-resolution grid. Then, in stage 2, an affine transformation is applied to the vertices of of the mesh. Finally, in stage 3, the scaled image is reconstructed by rasterizing the (scaled) mesh model to a high-resolution grid. Although, in the stage 2 above, any combination of affine transformations, such as scaling, rotation, and translation, can be used, this work focuses on the image scaling application. For this purpose, in stage 2, all vertices in the mesh are scaled with respect to k. Once a mesh is generated in stage 1, the process of scaling the vertices and rasterizing the model is almost trivial. Therefore, one may think that any mesh-generation method that is effective for image representation can also be effective in image scaling if used in the stage 1 above. Image representation and scaling, however, are two different problems. Therefore, in this section, we show that, for a mesh-generation method that is initially designed for image representation (at native resolution) to be effective in image scaling, several modifications are required to adapt the method for this specific application. Consequently, another mesh-generation method is required to produce a model with the parameters effectively selected for image scaling. Moreover, we show that, in stage 3 above, a simple model rasterization is not sufficiently effective to produce scaled images of good qualities. Therefore, a more effective model rasterization is also required.

For developing the MIS method, we use the SEMMG method, which is proposed in Section 3.3 for mesh generation, in stage 1 of the above image scaling process. As stated earlier, although we know that the SEMMG method is not designed to solve the image-scaling problem, it is only used (as a guide) to identify potential areas for improvement. The general scaling procedure that is used in the subsequent sections is as follows. An input low-resolution raster image ϕ_l defined on an integer lattice of width W and height H is given to the SEMMG method (or any other intermediate method that is introduced later) and the ERD mesh model is generated. Given an integer scaling factor of $k > 1$, the vertices of the ERD model are first scaled with respect to k, and then, the model is rasterized to an integer lattice of width kW and height kH, resulting in the high-resolution raster image ϕ_h as a scaled version of ϕ_l. As we recall from Section 2.9, the ERD mesh model is rasterized using an approximating function that is piecewise linear and interpolates the values at original sample points.

In what follows, the SEMMG method is used in the scaling procedure described above and various approaches in the method are revisited to identify shortcomings that create artifacts in the scaled images. For this purpose, all the figures presented in the this section are obtained without using any antialiasing (i.e., supersampling) technique, to focus only on the effects generated by image scaling. Then, based on the root causes of each type of artifacts, specific solutions are recommended to gradually adapt the mesh-generation method for the image scaling application. Through this progression, three intermediate mesh-generation methods, which are called MISMG$_0$, MISMG$_1$, and MISMG$_2$, are introduced, where each method has an additional modification to its predecessor. All these modifications will later be combined to form the MISMG mesh-generation method, which is specifically designed for image scaling and is later used in the proposed MIS method. In addition to examining the performance of the mesh generation in image scaling, the model rasterization is also revisited and a subdivision-based approach for producing smoother edge contours and image functions is developed.

5.2.1 Wedge-Value Calculation Revisited

The first approach that is revisited here is the one used for calculating the wedge values. In-depth investigations on several scaled images obtained by the SEMMG method (using the scaling procedure explained before) revealed that some distortions and artifacts exist near some edges in the scaled image. More careful analyses of the scaled images (as will be seen shortly) showed that most of these artifacts are related to the optimization-based approach used in the SEMMG method for computing wedge values. In what follows, two types of these distortions and their root causes are elaborated.

Type 1 – The first type of artifact is the one that is produced because of tiny triangles with zero (or a few) interior grid points. To better display this type of distortion, an example using the bull image from Appendix A is shown through Figure 5.1. In this figure, a part of the input bull image and its corresponding part from the scaled image obtained by the SEMMG method with a scaling factor of 4 is shown in Figures 5.1(a) and (d), respectively, where the region of interest is marked by a rectangle. The closer views of the marked regions in Figures 5.1(a) and (d) are shown in Figures 5.1(b) and (e), respectively. Also, the corresponding part in the triangulation generated by the SEMMG method at a sampling density of 1% is superimposed on Figures 5.1(b) and (e) and shown in Figures 5.1(c) and (f), respectively, with the constrained edges denoted by thick lines. As can be seen from Figure 5.1, the part of the scaled (high-resolution) image shown in Figure 5.1(d) and magnified in Figure 5.1(e) clearly contains some (shading) artifacts along almost all parts of the image edges. To identify the root cause of this type of artifacts, in what follows, we focus on how the wedge values are calculated using the local mesh shown in Figure 5.1(c).

As can be seen from Figure 5.1(c), the lower wedge of vertex a includes three triangles, $\triangle acd$, $\triangle abc$, and $\triangle aeb$, of which three corner z values associated with the corners around a must be computed. Using the optimization-based technique of the SEMMG method (introduced in 3.2.2), the corner z values of each face are selected to minimize the squared error of the face. Now, if the triangle of interest contains no interior grid points such as $\triangle acd$ as labeled in Figure 5.1(c), then the squared error is zero from the beginning. Therefore, the corner z values associated with vertices a and d in $\triangle acd$ are not optimized and remain equal to their initial values, which in this example, are the original image functions at a and d. The same problem also exists in the case of $\triangle abc$ as labeled in Figure 5.1(c). Although $\triangle abc$ contains two grid points along its lower edge $\overline{bc}$, those points do not belong to $\triangle abc$ because of a convention used for implementation. Based on this convention, each grid point should only belong to one triangle in the mesh. As part of this convention, in the case of the points falling on a horizontal edge (such as $\overline{bc}$), which is shared by two triangles, the points are agreed to belong to the triangle below the shared edge. Therefore, the $\triangle abc$ in the example shown in Figure 5.1(c) contains no interior grid points either. Thus, the corner z value associated with vertex a in $\triangle abc$ is not

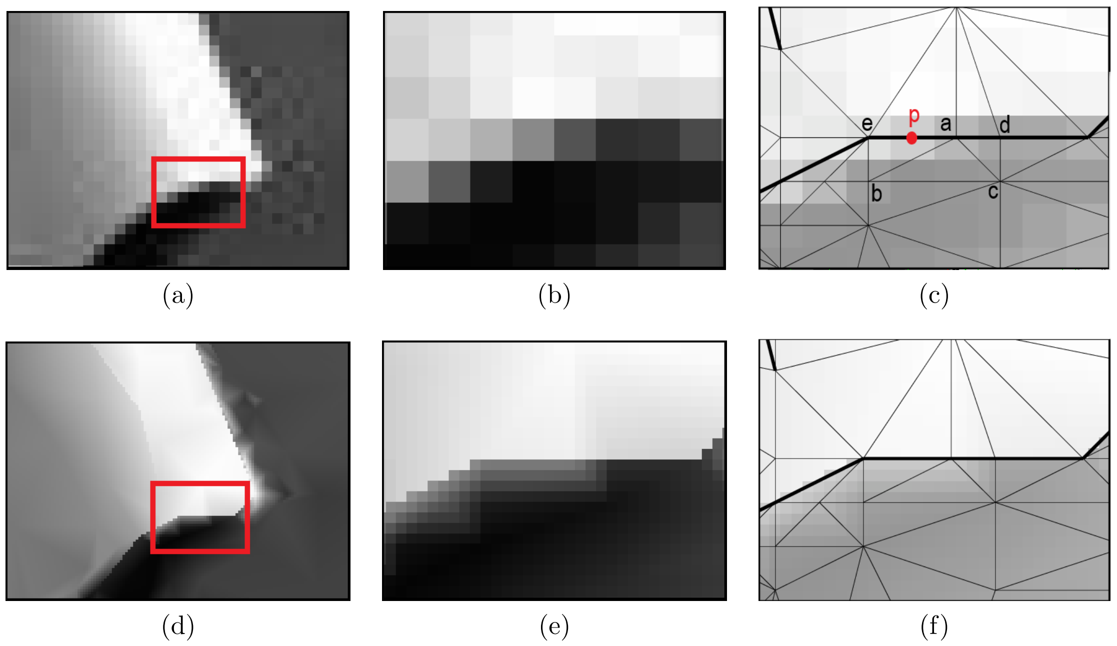

Figure 5.1: An example of the artifacts of type 1 generated by using the SEMMG method in image scaling for the bull image with a scaling factor of $k = 4$. The (a) part of the input low-resolution image and (d) its corresponding part from the scaled image, with the region of interest marked by a rectangle. The magnified view of the regions of interest in (b) low-resolution and (e) scaled images. The corresponding part in the triangulation obtained with the SEMMG method at a sampling density of 1% superimposed on the region of interest in (c) low-resolution and (f) scaled images. The constrained edges are denoted by thick lines in the mesh and the high-resolution image was produced with no antialiasing.

optimized and selected as the value of the original image function at a. Finally, the last corner z of lower wedge of a belongs to $\triangle aeb$, which only contains one grid point p as labeled in Figure 5.1(c). Consequently, the wedge value associated with the lower wedge of vertex a in Figure 5.1(c) is computed using three corner z values, of which only one is optimized with respect to a single grid point p in $\triangle aeb$. Since the points p and a are both parts of the edge pixels in the image, their function values do not distinctly belong to either side of the edge represented by the thick polyline in Figure 5.1(c). Therefore, in the process of image scaling, once the triangles $\triangle acd$, $\triangle abc$, and $\triangle aeb$ are enlarged, new grid points are introduced inside each of them (e.g., Figure 5.1(e)). These new grid points are then approximated using the wedge values that are computed from corner z values that either are never optimized or are optimized using the unreliable values at edge points (as described through the

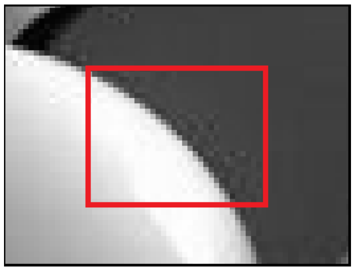
(a)

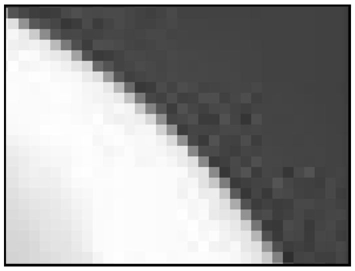
(b)

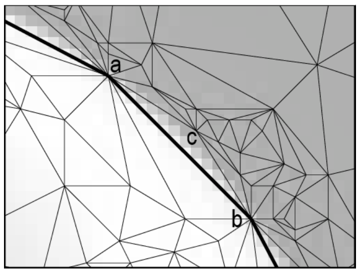

(c)

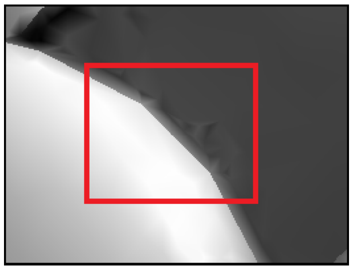
(d)

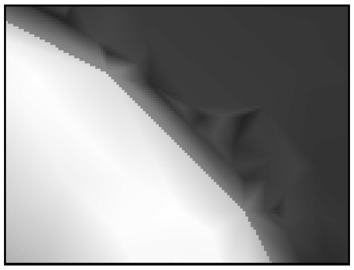
(e)

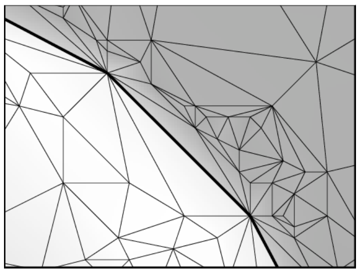
(f)

Figure 5.2: An example of the artifacts of type 2 generated by using the SEMMG method in image scaling for the bull image with a scaling factor of $k = 4$. The (a) part of the input low-resolution image and (d) its corresponding part from the scaled image, with the region of interest marked by a rectangle. The magnified view of the regions of interest in (b) low-resolution and (e) scaled images. The corresponding part in the triangulation obtained with the SEMMG method at a sampling density of 1% superimposed on the region of interest in (c) low-resolution and (f) scaled images. The constrained edges are denoted by thick lines in the mesh and the high-resolution image was produced with no antialiasing.

above example). Consequently, such artifacts (e.g., in Figures 5.1(d) and (e)) will be generated near the reconstructed edges after scaling in the high-resolution image, as a result of using improper wedge values.

Type 2 – The second type of artifact is the one produced because of the long/thin triangles near the constrained edges in the mesh. To better display this type of distortion, an example using the bull image from Appendix A is shown through Figure 5.2. In this figure, a part of the input bull image and its corresponding part from the scaled image obtained by the SEMMG method with a scaling factor of 4 is shown in Figures 5.2(a) and (d), respectively, where the region of interest is marked by a rectangle. The closer views of the marked regions in Figures 5.2(a) and (d) are shown in Figures 5.2(b) and (e), respectively. Also, the corresponding part in the triangulation generated by the SEMMG method at a sampling density of

1% is superimposed on Figures 5.2(b) and (e) and shown in Figures 5.2(c) and (f), respectively, with the constrained edges denoted by thick lines. As can be seen from Figure 5.2, the part of the scaled (high-resolution) image shown in Figure 5.2(d) and magnified in Figure 5.2(e) clearly contains some (shading) artifacts near the image edges. To identify the root cause of this type of artifacts, we focus on the thin triangle $\triangle abc$ as labeled in the mesh shown in Figure 5.2(c). As can be seen from this figure, $\triangle abc$ is a long thin triangle stretched along the image edge contour. Thus, the majority of the grid points inside $\triangle abc$ correspond to the edge pixels in the input image. Therefore, the two corner z values of the two triangle corners at a and b in $\triangle abc$ are optimized with respect to the values of the image function at these edge pixels. Similar to the artifacts of type 1 (explained before), image values at the edge pixels are not reliable because they change rapidly and do not distinctly belong to either side of the edge. As a result, in the process of scaling, newly-introduced grid points in the high-resolution image are approximated using the wedge values that are computed using the corner z values dominated by the unreliable values at edge pixels. Consequently, such improper wedge values produce shading artifacts near the reconstructed edges in the scaled images (e.g., artifacts shown in Figure 5.2(d) and its magnified region in Figure 5.2 (e)).

As the above analyses on the artifacts of type 1 and 2 show, in the application of image scaling, tiny triangles with zero (or few) grid points and long/thin triangles with many edge pixels have negative effects on the corner z values obtained by the optimization-based technique (i.e., from (3.1)). In other words, the root cause of the above two types of artifacts (of which two examples were shown) lies in the optimization-based technique used for computing the wedge values of the ERD model. Consequently, in what follows, another non-optimization based approach for computing the wedge values is proposed that does not rely on the interior points of triangles in the mesh.

5.2.2 Backfilling-Based Approach

In an ERD model (as introduced in Section 2.9), the value z that is associated to a wedge of a vertex v with zero or one incident constrained edge in a triangulation (e.g., Figure 2.17(a)) is simply chosen as the value of the image function ϕ at v (i.e., $z = \phi(v)$). Otherwise, if v has more than one incident constrained edges (e.g., Figure 2.17(b)) we propose to calculate the z value associated with each wedge w

using a backfilling-based approach as follows. First, a set S of vertices is selected, such that each vertex in S: 1) is in the one-ring neighborhood of v from inside w and 2) is not incident on any constrained edges in the mesh. In a special case, where no vertex in the one-ring neighborhood of v satisfies the above conditions, S is selected as the set of points at the midpoint of the unconstrained edges incident to v from inside w. In another special case, where no unconstrained edge is incident to v from inside w, S is selected as the set of points at the midpoint of the only two constrained edges forming the wedge w. After selecting S, the wedge value z associated with w is computed as given by

$$z = \frac{1}{|S|}\sum_{p\in S}\phi(p). \tag{5.1}$$

In the special cases where S is composed of midpoints, if the midpoints do not fall on the integer lattice on which ϕ is defined, the bilinear interpolation technique as in [69] is used to find the values of ϕ at the midpoints.

To further explain how S in (5.1) is chosen, two examples are shown in Figure 5.3. Each example in this figure shows a part of a triangulation containing a vertex v and a wedge w of which the wedge value z must be calculated, where the constrained edges are denoted by thick lines. The set S to calculate the wedge value of w for the example shown in Figure 5.3(a) and (b) is selected as $S = \{b, c\}$ and $S = \{m, n\}$, respectively. Then, the wedge value in each example is calculated by (5.1).

Using the proposed backfilling-base approach above, the set Z of wedge values for the ERD model is calculated without either optimization or any dependencies on the interior grid points of the triangles. Therefore, from now on, the optimization-based technique in the SEMMG method is replaced with the backfilling-based approach. Through this change, the first intermediate method (in the process of developing the final MISMG method) called the MISMG$_0$ is obtained. The MISMG$_0$ method is the same as the SEMMG method with all the same algorithmic steps explained in Section 3.3, except the new backfilling-based approach that is used instead of the optimization-based technique.

5.2.3 Point Selection Revisited

We now continue our analysis with the MISMG$_0$ method introduced in previous section to find other potential areas that need to be addressed for improving the scaled image quality. To achieve this, the MISMG$_0$ method was used in the same

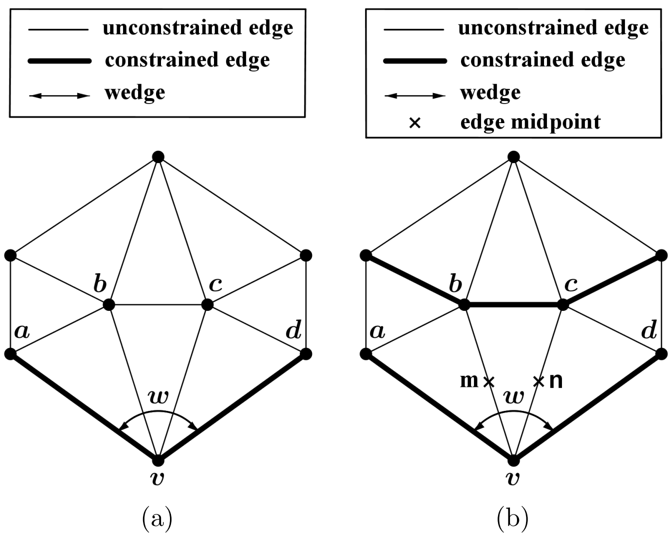

Figure 5.3: Two examples of the set S for calculating the wedge value associated with the wedge w in the backfilling-based approach. The case (a) where $S = \{b, c\}$ and case (b) where $S = \{m, n\}$.

image scaling procedure previously explained and used for the SEMMG method. Several investigations on different scaled images obtained by the MISMG$_0$ method revealed that some other type of shading artifacts are now generated near the image edges. More analyses on the scaled images showed that these artifacts are related to the point-selection approach used in the MISMG$_0$ method. To better describe this type of artifact, an example using the bull image from Appendix A is presented in Figure 5.4. In this figure, a part of the input low-resolution image bull and its corresponding part from the scaled image obtained by the MISMG$_0$ method with a scaling factor of 4 is shown in Figures 5.4(a) and (d), respectively, where a region of interest is marked with a rectangle. The closer views of the regions of interest in the low-resolution and high-resolution (i.e., scaled) images are shown in Figures 5.4(b) and (e), respectively. Also, the corresponding part from the triangulation obtained with the MISMG$_0$ method at a sampling density of 4% is superimposed on the region of interest in the low-resolution image and is shown in Figure 5.4(c), where constrained edges are denoted as thick lines. As can be seen from Figure 5.4, the part of the scaled image shown in Figure 5.4(d) and magnified in Figure 5.4(e) clearly contains some (shading) artifacts near the image edges.

To identify the root cause of this type of artifact, we focus on the part of the triangulation shown in Figure 5.4(c). As this figure shows, many vertices are located

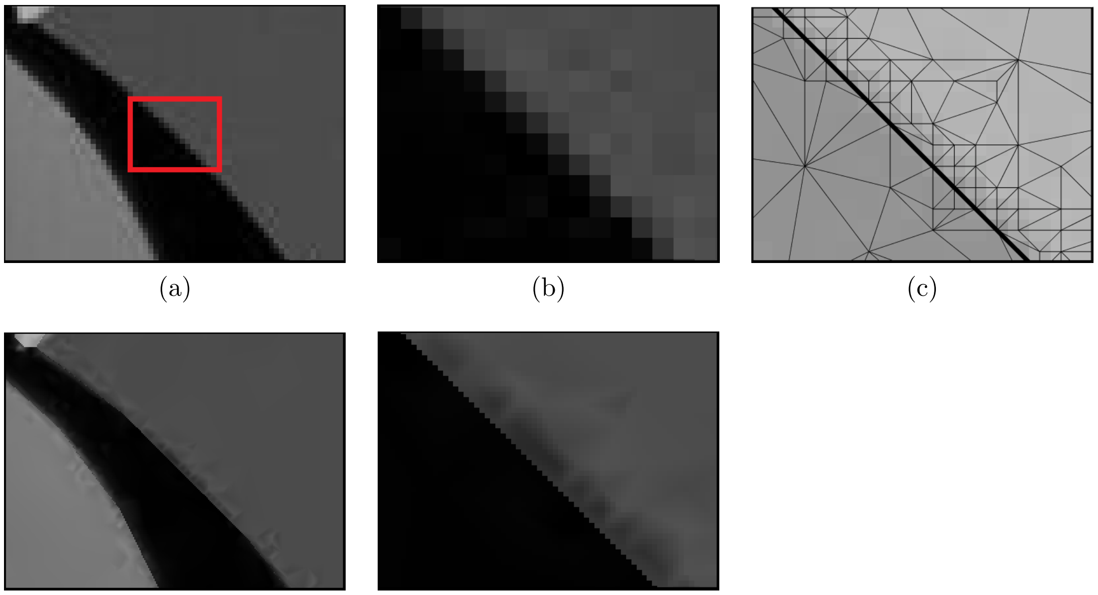
(a) (b) (c) (d) (e)

Figure 5.4: An example showing the shading artifacts produced by the MISMG$_0$ method using the bull image. The (a) part of the input low-resolution image and (d) its corresponding part from the scaled image, with the region of interest marked by a rectangle. The magnified view of the regions of interest in (b) low-resolution and (e) scaled images. The (c) corresponding part in the triangulation obtained with the MISMG$_0$ method at a sampling density of 4% superimposed on the region of interest in the low-resolution image. The constrained edges are denoted by thick lines in the mesh and the high-resolution image was produced with no antialiasing.

at sample points that are too close to the constrained edge. As the constrained edges represent the image edges, any sample points that are selected too close to the constrained edges can easily correspond to some image edges. Thus, the values of the image function at the edge locations are used in (5.1) to compute the wedge values. Since the image function changes rapidly at edges, its values at edges are not reliable to be used for calculating wedge values. Therefore, the effect of these unreliable values at sample points that are inserted too close to image edges will be propagated through newly-generated grid points after scaling. Consequently, some shading artifacts are generated in the vicinity of the edges in the scaled image (e.g., artifacts in Figure 5.4(e)).

As the above analysis shows, the root cause of the shading artifacts around the edges is related to the sample points that are selected and inserted too close to the image edges. Therefore, a potential solution is to use a more effective point-selection approach, where the sample points that are too close to image edges are excluded from being inserted into the mesh. To achieve this, in what follows, a modified point-selection approach is proposed.

5.2.4 Modified Centroid-Based Approach

As mentioned earlier, the general algorithmic framework of the MISMG$_0$ method is the same as the one used in the SEMMG method (introduced in Section 3.3). Therefore, in the mesh refinement process of the MISMG$_0$ method (like the SEMMG method), a new point q required to be iteratively selected and added to the mesh. If ϕ and $\hat{\phi}$ are the original image and its approximating functions, respectively, the modified centroid-based approach selects the new point q in two steps. First, the triangle face f^* with the largest squared error is selected as given by

$$f^* = \operatorname*{argmax}_{f \in F} \sum_{p \in \Omega_f} \left(\hat{\phi}(p) - \phi(p) \right)^2, \tag{5.2}$$

where Ω_f is the set of all the grid points in face f and F is the set of all triangle faces in the mesh. Now, let ω_f be the set of all the interior grid points in f^* that are not 8-connected to any detected edge points. Then, q is selected as the point in ω_f that is closest to the centroid of f^*.

Using the modified centroid-based approach introduced above, the new point q that is selected for insertion is guaranteed to not fall on (or within one-pixel neighborhood of) any detected edges in the image. Thus, in the process of computing wedge values in (5.1), the set S will not contain the vertices that correspond to any points that fall on, or are too close to, the detected image edges. In order to evaluate the modified centroid-based approach, first, the old point-selection technique in the MISMG$_0$ method was replace with the new one (i.e., the modified centroid-based approach). Through this change, the second intermediate method (in the process of developing the final MISMG method) called the MISMG$_1$ method was obtained. Next, the MISMG$_1$ method was used to produce different scaled images (using the same image scaling procedure as before). The scaled images were then compared with those obtained by the MISMG$_0$ method to see if the shading artifacts near the edges are reduced. An example to compare the subjective qualities of the scaled images obtained with the MISMG$_0$ (using the old point-selection approach) and MISMG$_1$ (using the new point-selection approach) methods is presented in Figure 5.5. For generating this figure, the bull image from Appendix A was given to each of the MISMG_0 and MISMG_1 methods and the scaled image at a scaling factor of 4 was generated from each method. In Figure 5.5, parts of the scaled images obtained by the MISMG_0 and MISMG_1 methods are shown in Figures 5.5(a) and (d), respectively. The closer views of the parts shown in Figures 5.5(a) and (d) are displayed in Figures 5.5(b) and (e), respectively. Also, the corresponding parts from the triangulations obtained with the MISMG_0 and MISMG_1 methods at a sampling density of 4% are superimposed on the low-resolution input image and are shown in Figures 5.5(c) and (f), respectively, where constrained edges are denoted by thick lines. In Figure 5.5, as the part of the scaled image obtained from the MISMG_1 in Figure 5.5(d) and its closer view in Figure 5.5(e) show, the shading artifacts near the edges are effectively reduced, resulting in more accurate and visually pleasant image reconstructions around the edges in the scaled image. Furthermore, as the mesh generated by the MISMG_1 method in Figure 5.4(f) shows, with the modified centroid-based approach, the sample points that are too close to edges are not selected as the vertices in the mesh anymore.

As the above comparison shows, the modified centroid-based approach effectively reduces the shading artifacts around the reconstructed edges in the scaled image. Therefore, in addition to the backfilling-based approach, the modified centroid-based approach will also be used later to construct the ultimate MISMG mesh-generation method that is used by the proposed MIS method. In what follows, the MISMG_1 method is studied for detecting further areas for improvements in the application of image scaling.

5.2.5 Model Rasterization Revisited

The next approach that is revisited here is the method used for model rasterization in the image scaling procedure used so far. In the second and third stages of this image scaling procedure (as introduced earlier), the mesh vertices are scaled and the model is simply rasterized to a high-resolution rectangular grid, respectively, to produce the scaled image. Our investigations on the various scaled images obtained with the MISMG_1 method showed that their edge contours are not sufficiently smooth. To better show this such problem of edge contours with low level of smoothness, two examples using the bull image from Appendix A is presented in Figure 5.6. In this figure, two parts of the original bull image containing some edge contours are shown in Figures 5.6(a) and (c). The corresponding edge contours from the scaled

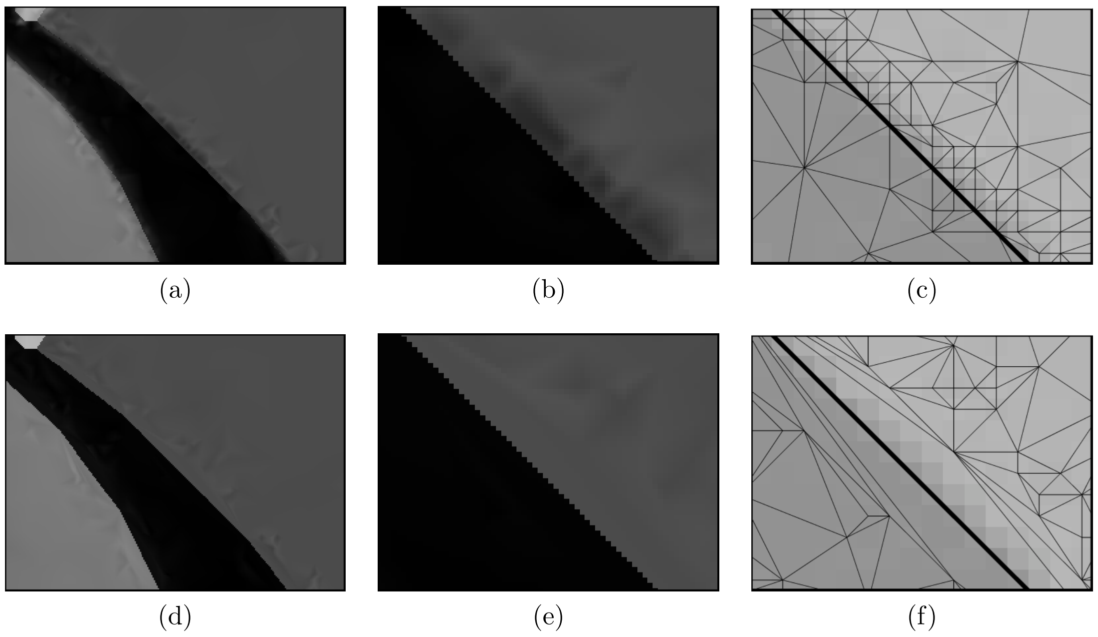

Figure 5.5: Subjective quality comparison between the MISMG$_0$ and MISMG$_1$ methods using the bull image at a scaling factor of $k = 4$. The parts of the scaled images obtained from the (a) MISMG$_0$ and (d) MISMG$_1$ methods. The closer views of the scaled images obtained from the (b) MISMG$_0$ and (e) MISMG$_1$ methods. the corresponding parts from the triangulations obtained at a sampling density of 4% with the (c) MISMG$_0$ and (f) MISMG$_1$ methods superimposed on the low-resolution input image. The constrained edges in the triangulations are denoted by thick lines and the scaled images were produced with no antialiasing.

image obtained with the MISMG$_1$ method with a scaling factor of 4 are shown in Figures 5.6(b) and (d). As can be seen form Figure 5.6, the reconstructed edge contours in the scaled image in Figures 5.6(b) and (d) are not sufficiently smooth. This lower level of smoothness of the reconstructed edge contours in the scaled image degrades the subjective quality of the image.

Careful analyses of the various scaled images containing the above problem revealed that the root cause lies in the polyline representation of the image edges as follows. In the MISMG$_1$ method, the detected edges are approximated using a set of polylines that will form a set of edge constraints in the triangulation. Since a polyline is composed of a limited number of line segments, during image scaling, these line segments in the polyline will also be magnified. Consequently, the edge contours that are approximated by the magnified polylines will show low level of smoothness (as the examples shown in Figures 5.6(b) and (d)). Therefore, to have more smoothed edge

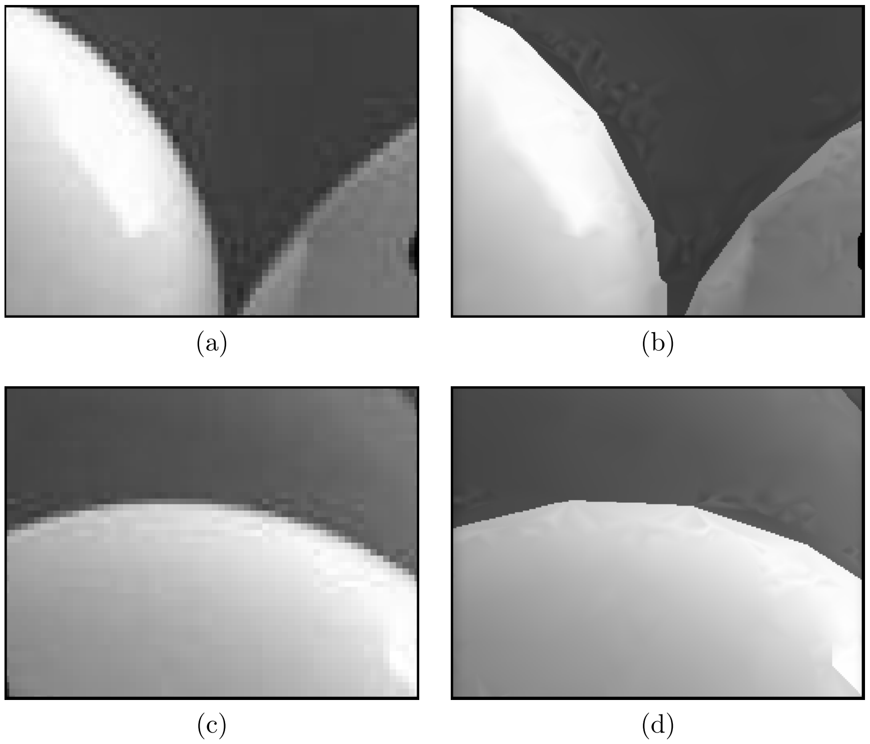

Figure 5.6: Two examples showing the edge contours with low level of smoothness from the scaled image obtained with the MISMG$_1$ method using the bull image with scaling factor of $k = 4$. The (a) and (c) parts of the input low-resolution image. The (b) and (d) corresponding parts from the scaled image obtained with the MISMG$_1$ method. The scaled image was produced with no antialiasing.

contours after the scaling process, one possible solution would be to use polylines with many more points from the first place in the model. Although this approach could potentially create smoother edge contours after scaling, it definitely increases the number of vertices in the mesh, which is not desirable from a practical point of view. Another possible approach is to use a technique, called **mesh subdivision**, which creates a refined mesh from a coarser one. As a result of this process, coarser polylines in the mesh are also refined to generate finer polyline (with more points), without actually increasing the number of points in the original polyline. This approach is practically more desirable and can be performed through different mesh subdivision schemes, of which examples can be found in [60] and [102]. Therefore, to address the problem of edge contours with low level of smoothness in scaled images, in what follows, we propose to use an additional step of mesh refinement using the subdivision scheme in [60].

5.2.6 Subdivision-Based Mesh Refinement

In the subdivision-based mesh refinement, an ERD model is iteratively refined through a process called subdivision. In particular, the mesh-subdivision process is applied to the coarser ERD mesh to produce a more refined mesh. As a result, in the refined mesh, finer polylines with more points and line segments are used for producing smoother image-edge contours. Furthermore, benefiting from more triangles in the refined mesh, a smoother image function is also reconstructed. For this purpose, a variation of the Loop subdivision scheme proposed in [60] is employed. This variation of Loop subdivision was chosen as it is able to selectively smooth only certain parts of the mesh, allowing the discontinuities in our ERD mesh model to be maintained (i.e., not smoothed). In each iteration of subdivision, each triangle face is split into four sub-triangles. Then, the vertex positions and wedge values in the refined mesh are computed as weighted averages of the nearby vertex positions and wedge values in the unrefined mesh as described in [60]. The subdivision process is repeated ℓ times iteratively, resulting in a refined mesh. In order to apply the subdivision scheme of [60], each vertex must be labeled as one of *smooth*, *tear*, or *corner*, and each edge must be labeled as one of *smooth* or *tear*. To use this subdivision scheme with our ERD model, a correspondence between the vertices/edges in our mesh model and the preceding vertex/edge labels in the subdivision scheme is established as follows:

1. A vertex with no incident constrained edges is deemed to be a smooth vertex.
2. A vertex with exactly two incident constrained edges is treated as a tear vertex.
3. A vertex with either one or three or more incident constrained edges is deemed to be a corner vertex.
4. Unconstrained and constrained edges are deemed to be smooth and tear edges, respectively.

With the preceding correspondence between the vertices and edges in our mesh model and the labels in the subdivision scheme having been established, the subdivision scheme from [60] can be applied to our ERD model. For this purpose, subdivision is applied three times (i.e., $l = 3$) to produce a sufficiently-smooth edge contours. An example of the subdivision-based mesh refinement introduced above for the bull image from Appendix A is illustrated in Figure 5.7, where the constrained edges are denoted by thick lines. As this figure shows, the part of the mesh shown in Figure 5.7(a) is

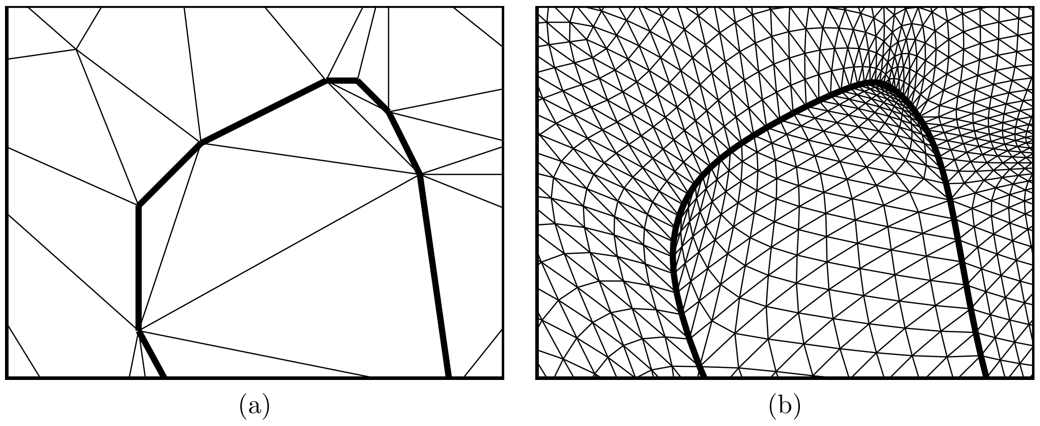

Figure 5.7: An example of the subdivision-based mesh refinement using the bull image. The part of the mesh generated at a sampling density of 1% using the MISMG$_1$ method (a) before subdivision and (b) after three levels of subdivision.

subdivided three times to produce the refined mesh shown in Figure 5.7(b). As the refined mesh in Figure 5.7(b) shows, constrained edges are now much smoother which result in smoother image-edge contours in the scaled image.

To compare the subjective qualities of the scaled images obtained with and without the subdivision-based mesh refinement, two examples of the same edge contours from the bull image previously used in Figure 5.6 are again used in Figure 5.8. In this figure, two parts of the original bull image containing some edge contours are shown in Figures 5.8(a) and (d). The corresponding edge contours from the scaled image obtained with the MISMG$_1$ method with a scaling factor of 4 without the subdivision-based mesh refinement are shown in Figures 5.8(b) and (e). Similarly, the corresponding parts in the scaled image obtained with the subdivision-based mesh refinement are shown in Figures 5.8(c) and (f). As can be seen in Figure 5.8, the parts from the scaled image obtained after subdivision in Figures 5.8(c) and (f) clearly display much smoother edge contours than those obtained without subdivision as shown in Figures 5.8(b) and (e).

As the above comparison shows, employing the subdivision-based mesh-refinement approach in model rasterization, effectively increases the smoothness of the polylines by using more points and line segments to approximate an image-edge contour. Consequently, edge contours in the scale images look more natural and smoother (e.g., in Figures 5.8(c) and (f)). Therefore, the subdivision-based image-refinement approach will be used later to form the proposed MIS method in addition to the previously

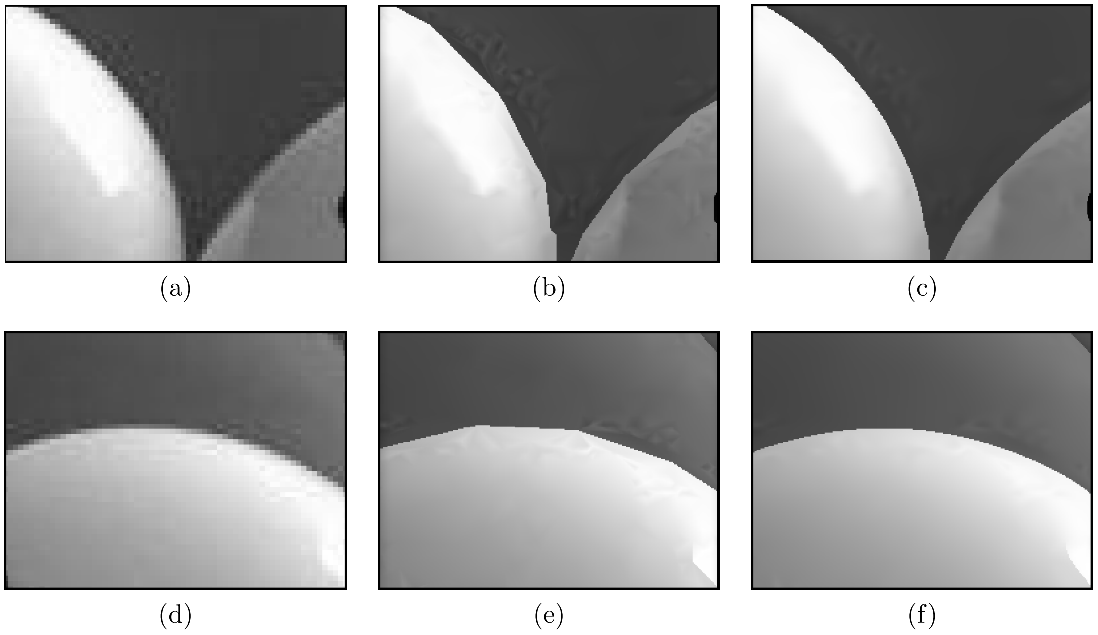

Figure 5.8: Subjective quality comparison of the scale images obtained before and after using the subdivision-based mesh refinement using the bull image with scaling factor of $k = 4$. The (a) and (d) parts of the input low-resolution image. The (b) and (e) corresponding parts from the scaled image obtained by the MISMG$_1$ method without subdivision. The (c) and (f) corresponding parts from the scaled image obtained by the MISMG$_1$ method after applying subdivision. The scaled images were produced with no antialiasing.

proposed techniques (i.e., the backfilling-based and modified centroid-based point-selection approaches). In what follows, the MISMG$_1$ method combined with the proposed subdivision-based mesh refinement is studied for detecting further areas for improvements in image scaling.

5.2.7 Polyline Simplification Revisited

The fourth and final approach that is revisited here is the approach used for polyline simplification. For this purpose, the MISMG$_1$ method with the subdivision-based mesh refinement was used to generate several scaled images. Our investigations on the scaled images showed that, in some areas of the image, edge contours are excessively smoothed so that they do not look good. To better describe the problem of excessively smoothed edge contours, two examples using the bull image (from Appendix A) are presented in Figure 5.9. In this figure, two parts of the original bull image are shown

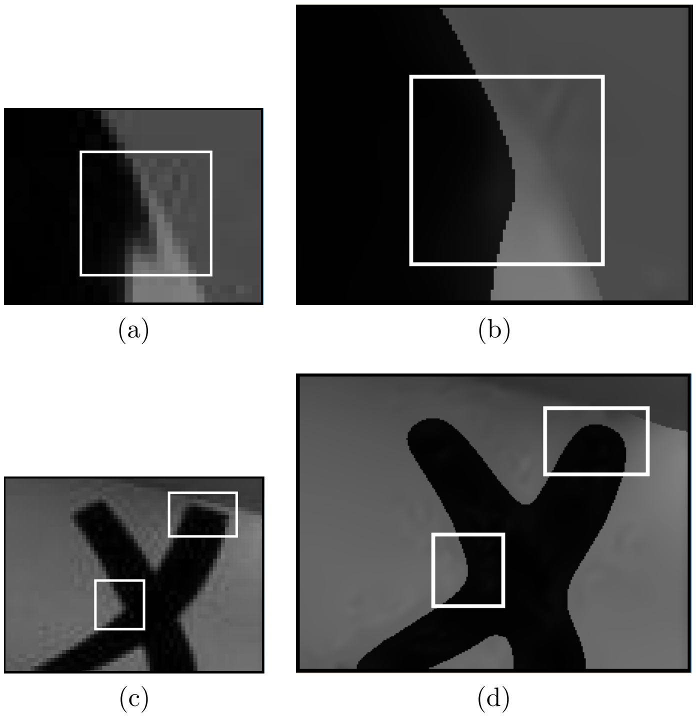

Figure 5.9: Visual examples of the excessively-smoothed edge contours obtained by the MISMG$_1$ method after subdivision in image scaling for the bull image with a scaling factor of $k = 4$. The (a) and (c) parts of the input low-resolution image. The (b) and (d) corresponding parts in the scaled image obtained by the MISMG$_1$ method with subdivision. The regions of interest with high curvatures are marked with rectangles. The high-resolution images were produced with no antialiasing.

in Figures 5.9(a) and (c), where the regions of interest are marked with rectangles. The corresponding parts from the scaled image obtained by the MISMG$_1$ method with the subdivision-based mesh refinement with a scaling factor of 4 are shown in Figures 5.9(b) and (d), with regions of interest marked by rectangles. As can be seen in Figure 5.9, the parts of the scaled image shown in Figures 5.9(b) and (d) display edge contours that are excessively smoothed. This over-smoothing of the edge contours in the scaled image is more distinguishable in the areas that contain edge contours with higher degrees of curvatures, such as the areas marked with rectangles in Figures 5.9(b) and (d). In what follows, the root cause of such problem is first identified and then a solution is proposed.

Many investigations on several scaled images obtained by the MISMG$_1$ method with subdivision reveled that the root cause of the problem of over-smoothed edge contours is related to the polyline-simplification approach used by the MISMG$_1$ method.

More specifically, edge contours that are excessively smoothed in the scaled images often correspond to the image edges that are poorly approximated with the polylines because of using a polyline-simplification approach that is not suitable for image scaling. This can be elaborated as follows. Since the subdivision scheme of [60] that is used for the purpose of mesh refinement is approximating, the subdivided (smoother) polyline is not guaranteed to pass through the points of the control (coarser) polyline. On one hand, using an approximating subdivision scheme results in smoother edge curves after subdivision that look more natural and pleasant to the human observer. On the other hand, since the resulting subdivided polyline does not necessarily pass through the points in the control polyline, the subdivided polyline can, in some places, deviate too much from its control polyline. Many experiments on different test cases showed that this excessive shifting of the subdivided polyline from its corresponding control polyline occurs wherever both of the following conditions are satisfied:

1. the control polyline corresponds to an edge contour with high degree of curvature in the low-resolution image, and

2. the control polyline does not contain a sufficient number of control points to accurately approximate that high-curvature part of the edge contour.

When above two conditions are satisfied, the subdivided polyline will most probably shift too much away from its corresponding control polyline near the high-curvature parts of the edge contour. Consequently, the edge contours in the scaled image, which are reconstructed based the subdivided polylines, also deviate too much from their original edge curves in the low-resolution image, resulting in over-smoothed edge contours (as previously shown in Figures 5.9(b) and (d)).

Since the subdivision-based mesh refinement is applied as a post processing step after mesh generation, the polyline-simplification approach, in the MISMG$_1$ method, is blind to the subdivided polylines. Therefore, polylines are simplified as if there will be no subdivision later. Consequently, they most probably are simplified too much at high-curvature edge contours so that, after subdivision, the subdivided polyline deviates too much from the simplified polyline. In what follows, a solution to address this problem is proposed.

5.2.8 Adaptive Polyline Simplification

Having identified the root cause of the problem of excessively-smoothed edge contours to be in the polyline-simplification approach of the MISMG$_1$ method, we now propose an adaptive polyline-simplification (APS) approach to address the problem as follows. The input to our APS method is an original polyline P of N consecutively-connected points (i.e., $P = \{p_0, p_1, ..., p_{N-1}\}$) and the output is the simplified polyline $\tilde{P}$. The proposed APS approach is comprised of the following steps (in order):

1. Apply the simplification method of DP [34] to P, as explained in Section 2.3, to generate the simplified polyline P', with the tolerance $\epsilon = 0.75$ (i.e., $P' \subset P$).

2. Compute the subdivided polyline P'' from P' using the subdivision scheme of [60], with ℓ level of iterations, where $l = 3$.

3. Find a set Q of high-error points in P' whose distances from P'' is greater than a shifting threshold τ (to be explained later).

4. For each point $p'_i \in P'$, if p'_i is a high-error point (i.e., $p'_i \in Q$), find a point $p_j \in P$, where $p_j = p'_i$, then insert two extra points p_{j-1} and p_{j+1} from P into P' as the new points p'_{i-1} and p'_{i+1}, respectively.

5. Finally, select $\tilde{P} = P'$.

Selection of τ. In step 3 of the APS approach explained above, threshold τ is selected adaptive to the local curvature profile of the polyline P' at each point. To achieve this, for a point $p'_i \in P'$, first, the angle α between the line segments $\overline{p'_i p'_{i-1}}$ and $\overline{p'_i p'_{i+1}}$ is computed which is in the range $0° \leq \alpha \leq 180°$. Then, τ is determined as

$$\tau = \begin{cases} 0.5, & \alpha \leq 135° \\ 1.0, & 135° < \alpha < 160° \\ 1.4, & \alpha \geq 160°. \end{cases} \tag{5.3}$$

The α in (5.3) indicates an estimation of the local curvature level of the polyline P' at p'_i. In particular, a smaller (i.e., sharper) and larger (i.e., wider) angle α represents a higher and lower degree of curvature at p'_i, respectively. Our analyses on several scaled images showed that the problem of the excessively-shifted polylines is more annoying (and evident) when it occurs at the edge contours with a higher degree of curvature. Therefore, through several experiments with the above thresholding technique, a smaller τ was found to be more beneficial in regions with a higher degree of curvature to keep the subdivided polyline P'' closer to its control polyline P' near p'_i. On the other hand, a more relaxed (i.e., larger) τ was found to perform better in regions with a lower degree of curvature to avoid the insertion of unnecessary extra points, where the shifting problem is not much evident. Consequently, no single threshold value works perfectly for all types of edge curvatures in all images. Therefore, the values of τ and upper/lower bounds of α, in (5.3), were determined heuristically through a series of experiments as follows. For this purpose, different threshold values of τ within a range of $[0.5, 2]$ with various angles of α were tested on several test images. Then, the scaled images were visually inspected around edge contours with different degrees of curvatures to see whether the shape of the original curvatures are maintained well in the scaled images. As a result, the values of τ and upper/lower bounds of α, in (5.3), were selected. Although (as will be seen later in results chapter) these values are not optimal for all edge curvatures in all images, they were selected to work well overall in most cases.

Using the new proposed APS technique as explained above instead of the old polyline-simplification approach in the MISMG$_1$ method, the third and final intermediate method, called the MISMG$_2$ method, is introduced. To evaluate the performance of the APS approach, several scaled images were generated using both the MISMG$_1$ and MISMG$_2$ methods and the edge contours generated by each method compared visually. For the purpose of subjective comparison here, two examples from the bull image previously used in Figure 5.9 are again used in Figure 5.10, where high-curvature edge contours are marked with rectangles. In this figure, two parts of the original bull image containing some high-curvature edge contours are shown in Figures 5.10(a) and (d). The corresponding edge contours from the scaled image obtained with the MISMG$_1$ method with the subdivision-based mesh refinement and a scaling factor of 4 are shown in Figures 5.10(b) and (e). Similarly, the corresponding parts in the scaled image obtained by the MISMG$_2$ method using the subdivision-based mesh refinement are shown in Figures 5.10(c) and (f). As can be seen in Figure 5.10, the high-curvature parts in the scaled image obtained with the MISMG$_2$ method in Figures 5.10(c) and (f) were reconstructed much more accurately than those in the scaled image obtained with the MISMG$_1$ method in Figures 5.10(b) and (e). More specifically, the excessive shifting in the edge contours in Figures 5.10(b) and (e) are effective reduced in the edge contours of Figures 5.10(c) and (f), using the APS approach in the MISMG$_2$ method.

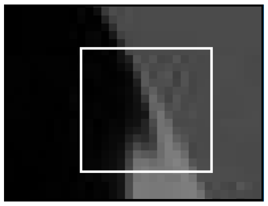
(a)

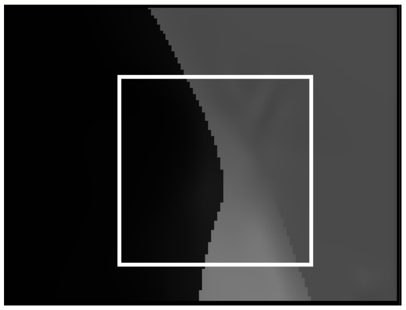
(b)

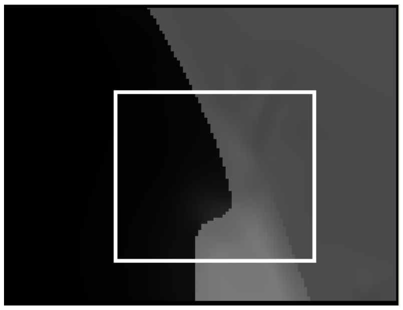
(c)

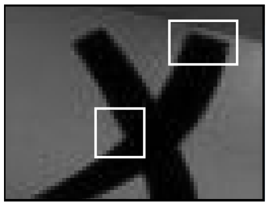
(d)

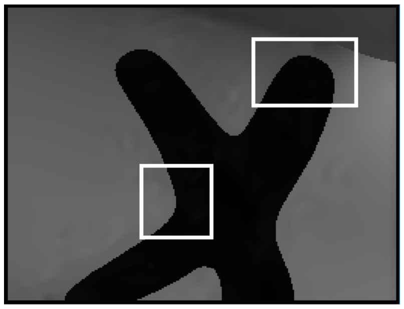
(e)

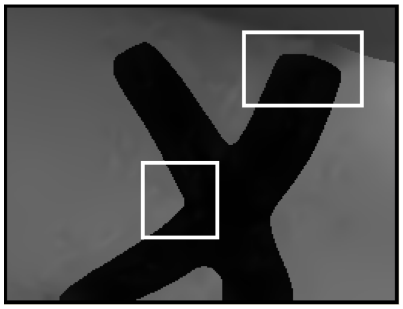
(f)

Figure 5.10: Subjective quality comparison between the scaled images obtained by the MISMG$_1$ and MISMG$_2$ methods both with the subdivision-based mesh refinement using the bull image with a scaling factor of $k = 4$. The (a) and (d) parts of the input low-resolution image. The (b) and (e) corresponding parts in the scaled image obtained by the MISMG$_1$ method. The (c) and (f) corresponding parts in the scaled image obtained by the MISMG$_2$ method. The regions of interest with high curvatures are marked with rectangles and the high-resolution images were produced with no antialiasing.

As the above comparison indicates, the proposed APS approach effectively addresses the problem of excessively-smoothed edge contours in high-curvature regions. Therefore, the APS approach is the fourth modification that is used later to form the proposed MIS method, in addition to the modified wedge-value calculation, point selection, and subdivision-based mesh refinement presented in previous sections. In what follows, the new MIS method is proposed that integrates all the above four main modifications into a unified framework.

5.3 Proposed MIS Method

In the preceding sections, the performances of various approaches in different steps of mesh generation and model rasterization for image scaling were studied. As a result of this study, several problematic areas that have negative effects on the quality of the resulting scaled images were identified. Moreover, for each problematic case, a specific modification proposed to further adapt the processes of mesh generation and model rasterization for image scaling. With the insight from those analyses, we are now ready to introduce our proposed method for mesh-based image scaling (MIS).

The MIS method is based on the ERD models (introduced in Section 2.9) and, as stated earlier, is designed to solve the problem of image scaling, for grayscale raster images that are approximately piecewise-smooth, with no (or minimal) textures or patterns. More specifically, the inputs to the MIS method are a low-resolution raster image ϕ_l defined on an integer lattice of width W and height H and an integer scaling factor of $k > 1$. The output of the MIS method is a high-resolution raster image ϕ_h defined on an integer lattice of width kW and height kH. The proposed MIS method is comprised of the following three stages (in order):

1. mesh generation,
2. mesh transformation, and
3. model rasterization.

In stage 1, an ERD mesh model from ϕ_l is generated. Then, in stage 2, the mesh vertices are transformed using a scaling operation. Finally, in stage 3, the scaled ERD model obtained from stage 2 is rasterized using a subdivision-based approach to produce the scaled image ϕ_h. In what follows, each stage will be described in detail.

5.3.1 Mesh Generation

As mentioned earlier, in the first stage of our MIS method, an ERD mesh model is generated from the input low-resolution image ϕ_l. For this purpose, the mesh-based image-scaling mesh-generation (MISMG) method is designed to generate the ERD models that are effective in image scaling. The MISMG method is the ultimate version of the intermediate methods (i.e., the MISMG$_0$, MISMG$_1$, and MISMG$_2$ methods) previously introduced in the development process. In particular, the MISMG method integrates all the modifications used by those intermediate methods, including modified approaches for wedge-value calculation, polyline simplification, and point selection. In what follows, we explain how the MISMG method works.

For a low-resolution image function ϕ_l defined on the rectangular region $\Gamma = [0, W-1] \times [0, H-1]$, an ERD triangle mesh model of ϕ_l (as introduced in Section 2.9) consists of: 1) a set $P = \{p_i\} \subset \Gamma$ of sample points, 2) a set E of edge constraints, and 3) a set Z of integer wedge values. The proposed MISMG method selects the parameters of the ERD model (i.e., P, E, and Z) that is effective in image scaling. The input to the MISMG algorithm is the low-resolution image function ϕ_l that is known only at the points in $\Lambda = \{0, 1, ..., W-1\} \times \{0, 1, ..., H-1\}$ (i.e., a truncated integer lattice of width W and height H). The outputs of the MISMG method are the ERD model parameters, including P (i.e., $P \subset \Lambda \subset \Gamma$), E, and Z. In what follows, we first introduce the general algorithmic framework for the MISMG method. Then, the specifics of the method are explained. The general algorithmic framework of the MISMG method consists of the following steps (in order):

1. *Initial triangulation selection.* Select the values for the initial set P_0 of sample points and E. Then, the initial mesh associated with the preferred triangulation $\operatorname{pcdt}(P_0, E)$ is constructed.

2. *Wedge-value initialization.* For each vertex $v \in P_0$, compute the initial wedge values using the backfilling-based technique proposed in Section 5.2.2.

3. *Point selection.* Select a new sample point $q \in \Lambda$ to add to the mesh using the modified centroid-based approach proposed in Section 5.2.4.

4. *Point insertion.* Insert q in the triangulation. Calculate the wedge values of the affected wedges in the mesh using the same backfilling-based approach proposed in Section 5.2.2 and select the set P_{i+1} of sample points for the next iteration as $P_i \cup \{q\}$.

5. *Stopping criterion.* If $|P_{i+1}| < 0.04|\Lambda|$, go to step 3. Otherwise, set the output parameter $P = P_{i+1}$ and stop.

The steps 1 and 2, in the framework above, choose an initial coarse mesh of size $|P_0|$. Then, in steps 3 to 5, the initial mesh is iteratively refined by adding more sample points to achieve the mesh of size $0.04|\Lambda|$ (i.e., with a sampling density of 4%).

Selection of P_0 and E. In step 1 of the above framework, the procedure to select the initial set P_0 and E is same as the one introduced in Section 3.3 for the SEMMG method, except that the new APS method proposed in Section 5.2.8 is used to simplify the polylines, instead of the DP method used in the SEMMG method.

5.3.2 Mesh Transformation

Once the ERD mesh model is generated in stage 1, in stage 2 of the MIS method, the vertices of the model are scaled with any scale factor of interest. While the MIS method specifically focuses on the scaling operation, the mesh model that is generated from stage 1 can be stored and used anytime later for different purposes, such as mesh editing or applying any combination of affine transformations like scaling, translation, and rotation. Indeed, such properties of the MIS method simply allow for producing image models that are portable, editable, and reusable, which may not be easily (or ever) achievable with other state-of-the-art raster-based scaling methods.

5.3.3 Model Rasterization

Having introduced the MISMG method and mesh transformation used in stages 1 and 2 of the MIS method, respectively, we now describe the third stage, which is model rasterization. The model rasterization, in the MIS method, consists of two steps (in order):

1. mesh refinement and
2. mesh rasterization.

In step 1, the ERD mesh model of ϕ_l obtained using the MISMG method from the mesh-generation stage (introduced in Section 5.3.1) is refined. For this purpose, the subdivision-based mesh-refinement approach previously proposed in Section 5.2.6 is used. Although, in principle, we could simply rasterize the mesh obtained from the mesh-generation and mesh-transformation stages (i.e., omit the mesh-refinement step), this would lead to an image reconstruction with artifacts. In particular, the image discontinuity contours in the scaled image (as studied in Section 5.2.5) would lack a desirable level of smoothness as well as the image function itself. By employing the subdivision-based mesh refinement, however, we are able to obtain a mesh with better smoothness.

In step 2 of the above model rasterization approach, the refined (i.e., subdivided) ERD mesh model is rasterized to a high-resolution lattice grid to produce the scaled image. For this purpose, with a raster low-resolution image ϕ_l of width W and height H and a scaling factor of $k > 1$, the scaled and refined ERD model is rasterized to a high-resolution lattice grid of width kW and height kH. To achieve this, the piecewise-linear interpolating function associated with the ERD model (as described in Section 2.9) is used to produce the high-resolution image ϕ_h as a scaled version of ϕ_l. Since the ERD model explicitly represents discontinuities, edges in the reconstructed image could generate undesirable aliasing effects. Thus, a supersampling technique based on the 3$\times$3 grid algorithm (introduced in Section 2.6) is used during rasterization to avoid such aliasing effects at the edges.

Chapter 6

Evaluation and Analysis of the MIS Method

6.1 Overview

Having introduced the proposed MIS method, we now compare it with other image scaling methods. Different categories of image scaling methods (as introduced in Section 1.4) have been proposed to date, of which two important ones are those based on raster-based and mesh-based interpolation techniques. Regarding the the raster-based methods, many implementations are readily available which make the comparison with them practically easy to perform. Therefore, the comparison between the MIS and raster-based methods here is performed through various experimental comparisons, including subjective and objective evaluations. Regarding the mesh-based image-scaling methods, since the MIS method is based on a mesh-based technique, a comparison between the MIS and those methods is also desirable. This type of comparison, however, is not straightforward due to the difficulties mentioned previously in Section 4 and also reminded as follows. Firstly, due to the high complexity of the mesh-based methods, implementing them often requires at least several months of work, including coding, testing, and debugging. Secondly, since so much effort is involved in implementing mesh-based methods, researchers often do not want to make their code freely available. Thus, finding implementations of other competing mesh-based methods is often impossible. Because of such reasons, for evaluating our MIS method, no implementations of any other mesh-based approaches could be obtained. One approach for comparing to methods, where no implementation was available, would be to compare to the results reported in other researcher's publications (as it was done previously in Section 4.3 for evaluating the SEMMG method). For this purpose, however, the same test data that was used to produce the results in other publications should be accessible and also has to be a valid input for the method under evaluation. Otherwise, there is no basis for comparison. Because of the reasons explained above, performing an experimental comparison between the MIS and other mesh-based scaling methods became impractical. In such cases, however, a conceptual comparison is provided through presenting the theoretical differences and similarities between the methods. In what follows, first, the experimental comparisons between the MIS and several raster-based methods are presented, including both the subjective and objective evaluations, followed by some supplementary discussions. Finally, a conceptual comparison between the MIS method and two other relevant mesh-based methods is performed. Some of the results presented in this chapter have also been published in the author's paper [67].

6.2 Experimental Comparisons

Among the numerous raster-based image-scaling methods that have been proposed over the years, the MIS method is compared to the following five well-known approaches:

1. bilinear interpolation,
2. bicubic interpolation of Keys [51],
3. the DCCI method of Zhou et al. [101],
4. the NEDI method of Li and Orchard [59], and
5. the SRCNN method of Dong et al. [33].

These methods were selected in a way to include two methods from the classical and convolutional techniques (i.e., bilinear and bicubic methods), two methods from the edge-directed class (i.e, the DCCI and NEDI methods), and one from the most recent class of methods based on deep learning (i.e., the SRCNN method). Due to the availability of implementations of the above methods, a comparison between the MIS method and each of the above techniques is made through experimental results, including both subjective and objective evaluations.

The software implementations of the MIS method were developed by the author of this thesis and written in C++. The details of the software implementation are presented in Appendix D. In the case of bilinear and bicubic methods, their corresponding built-in functions from MATLAB were used. Moreover, for the DCCI, NEDI, and SRCNN methods, their MATLAB implementations from [2], [3], and [4], respectively, were used to generate results.

In what follows, the test data used for the experimental comparisons is first introduced. Then, the subjective evaluation is presented, including its methodology, results, and analysis. Next, the objective evaluation is presented as well as its methodology, results, and analysis. Finally, some supplementary discussions are presented to highlight the benefits and drawbacks of the methods under comparison.

6.2.1 Test Data

For test data we use a set of 20 low-resolution images listed in Appendix B. In our experimental comparisons, the evaluation is performed in terms of multiple metrics. In particular, we consider a subjective and several objective measures. The objective measures require a ground-truth image as a reference, whereas the subjective measure does not. Therefore, our test data must have be chosen in a way to, first, accommodate the ground-truth image for the objective measures, and second, be consistent across the subjective and objective evaluations. For these reasons, all of the 20 test images that are used here were generated from their high-resolution counterparts using a downscaling process. In our work, such a reduction in resolution, was performed using a simple pixel-averaging (also called pixel-mixing) technique, provided as the default resizing method by the Netpbm toolkit [5], with a factor of $k = 4$. Therefore, the same set of 20 test images can be used for both subjective and objective evaluations. Furthermore, the high-resolution image corresponding to each test image can be used as a ground truth for computing the metric of interest in the objective evaluation.

Regarding the test images for image scaling, two considerations need to be taken into account as follows. One consideration is that, as explained earlier, a downscaling process is involved to, first, obtain a low-resolution test image ϕ_l from its high-resolution ground-truth counterpart ϕ_h. Then, the test image ϕ_l is used as the input to the scaling methods under comparison. In the case of the proposed MIS method (as we recall from Section 5.3), the MISMG approach, used by the MIS method, initially detects the edges in the input image (i.e., ϕ_l herein). Moreover, the accuracy of the edge localization is critically important to the performance of the MIS method because the constrained edges (as one of the critical parameters) in the mesh model are selected directly based on the detected edges. Although a more advanced edge detector with sub-pixel accuracy could potentially have been used in the MISMG method for more accurate edge localization, a Canny edge detector (with one pixel accuracy) was used in order to avoid unnecessarily increasing computational complexity. Also, with the recent increase in the resolutions of today's typical images, such an edge detector with one-pixel accuracy works reasonably well with them. Later, in the evaluation process, however, the downscaling-based procedure was found to produce too small low-resolution images if applied to some standard test images, such as those used in Chapter 3. For example, in the case of the commonly-used test images, such as lena and peppers, the ground-truth image ϕ_h is of size 512 by 512 pixels. Thus, with a typical scaling factor of $k = 4$, the low-resolution test image ϕ_l will be of size 128 by 128. For such a small test image, however, a more advance edge detector is needed to locate edges with sub-pixel accuracy. Therefore, due to such a usability limitation in the MIS method, the ground-truth image ϕ_h itself cannot be too small so that the low-resolution test image ϕ_l can still be handled by an edge detector with one-pixel accuracy.

The other consideration when selecting the test data for image scaling is the fact that our MIS method (as introduced in Section 5.3) is not intended to work with textured images, where the image is not approximately piecewise smooth. The two previously mentioned considerations for selecting the test data in evaluating the MIS method, however, were not much necessary in the case of the SEMMG method proposed in Chapter 3. This is because (as we recall from Chapter 3) the SEMMG method was designed to solve a completely different problem, where it could handle images with smaller sizes and with small to moderate textures. Thus, the set of test data that was used for evaluating the SEMMG method in Chapter 3 cannot be fully utilized for evaluating the MIS method too. Consequently, the new set of 20 test images, as introduced earlier and listed in Appendix B, was collected by the author to contain images with larger resolutions and with approximately piecewise-smooth functions (such as cartoon images). This test data was chosen to include images with low, medium, and high levels of detail. Moreover, some natural photographic images with low amount of texture (e.g., frangipani, dahlia, balloons, and rose) are also included to facilitate the analysis.

6.2.2 Subjective Evaluation

Having introduced the test data for experimental comparisons, we now focus on the subjective evaluation. Since our ultimate goal is to generate scaled images of better quality with respect to the human visual system, the most accurate and also reliable way of assessing the quality of scaled images is through a subjective evaluation. In this evaluation, a group of people are asked to give their opinion about the scaled images obtained from different methods. In what follows, the methodology used for performing the subjective evaluation is first explained. Then, the results of the subjective evaluation are presented followed by their analysis.

6.2.2.1 Methodology for Subjective Evaluation

Since several methodologies can be used to perform a subjective evaluation, the specific method used here is explained. A rigorous industrial-scale subjective evaluation requires having a complete control over many factors, including lighting conditions, display devices, viewing distances/angles, subjects vision ability, and subjects mood. Several international standards have been proposed (e.g., ITU-R BT.500-13 [50]) on how to control and set the aforementioned factors for various applications, such as (high-definition) television images and video quality assessments. An extensive survey on different standardized subjective methods can be found in [65]. In the case of our subjective evaluation, providing such an industrial-scale environment to satisfy all the standards was impractical due to the limited laboratory facilities. The subjective evaluation, however, was performed in the most rigorous way possible, given our limited laboratory facilities. In what follows, the details of this subjective evaluation are explained.

The subjective evaluation was performed in the Digital Signal Processing laboratory in the University of Victoria using two monitors of the same models. The ambient lighting conditions, monitors resolutions, brightnesses, and contrasts were all kept the same during the test for all participants. For our subjective evaluation, a methodology based on ordering by force-choice pairwise comparison in [65] and a voting platform similar to the one developed by [89], were used. For this purpose, the test set of 20 low-resolution images (as introduced in Section 6.2.1) and the scaling factor of $k = 4$ were given to each of the six scaling methods under comparison to produce the scaled images. Thus, six different high-resolution images were generated from each low-resolution image. In our subjective assessment, first, each participant

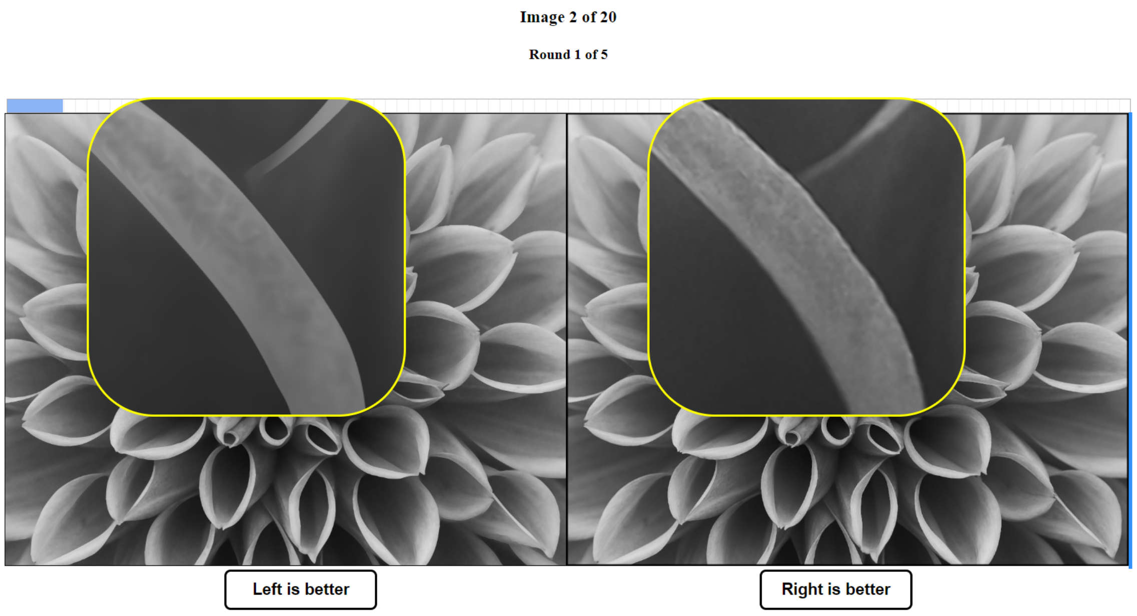

Figure 6.1: A screenshot of the survey software developed and used for the subjective evaluation. The magnifier tool can be moved around the two images.

in the survey was shown a pair of randomly selected scaled (high-resolution) images obtained using two different methods from the same low-resolution image. Using a magnifier tool, the participant would inspect different parts of the images and decide which one is better than the other in terms of perceptual quality. Next, the winning image was kept and the losing image was replaced with a scaled image obtained with another randomly selected method under competition. This process would continue until the (first) best scaled image was found and removed from the dataset. Then, the whole procedure was repeated in multiple rounds to find the second, third, fourth, fifth, and sixth best scaled images. Consequently, for each test image, the six competing scaling methods were ranked from the first (i.e, best) to sixth (i.e., worst) methods. A screenshot of the survey software developed and used for the subjective evaluation is illustrated in Figure 6.1. In what follows, the results of the subjective evaluation are presented.

6.2.2.2 Subjective Evaluation Results

Using the methodology explained above, the subjective evaluation was performed with a total of 19 participants who were given 300 pairwise comparisons, over 20 test images, leading to a total of 380 rankings. The obtained ranking results for the six

Table 6.1: Statistical properties of the ranks collected during the subjective evaluation, with the lower rank corresponding to the better method

	Bilinear	Bicubic	DCCI	NEDI	SRCNN	MIS
Mean Rank	5.28	4.78	3.27	3.23	2.44	2.00
Median Rank	6	5	3	3	2	1
Standard Deviation	0.97	1.02	1.06	1.19	1.26	1.75

scaling methods under comparison (i.e., the bilinear, bicubic, DCCI, NEDI, SRCNN, and MIS methods) are summarized in Tables 6.1, with the lower rank corresponding to the better method. More specifically, Table 6.1 shows mean, median, and standard deviation of the ranks collected for each method. As can be seen in Table 6.1, the proposed MIS method has the best average rank of 2 followed by the SRCNN method with the second best average rank of 2.44. Moreover, Table 6.1 shows that the NEDI and DCCI methods performs fairly similarly by having the average ranks of 3.23 and 3.27, gaining the third and fourth best ranks, respectively. Lastly, the bicubic and bilinear methods are ranked as fifth and sixth with average ranks of 4.78 and 5.28, respectively.

In order to have a better understanding of how the votes are distributed among the six ranks over the collected 380 rankings, Figure 6.2 shows the histograms of collected votes for all methods. In this figure, the histograms of the votes for the bilinear, bicubic, DCCI, NEDI, SRCNN, and MIS methods are illustrated in Figures 6.2(a) to (f), respectively. As the histogram in Figure 6.2)(f) shows, the proposed MIS method is the ultimate winner overall because it was ranked as the first method among all in almost 67% of cases. Similarly, comparing the other histograms in Figure 6.2 show that the SRCNN, NEDI, DCCI, bicubic, and bilinear methods performed best to worst in order.

6.2.2.3 Analysis of Subjective Evaluation Results

Having presented an overview of the subjective evaluation results, we now analyze them in more detail. As shown in Figure 6.2(f), the MIS method was ranked as the best method among all other methods, in approximately 67% of cases. The analysis made on the results collected from the subjective evaluation shows that the MIS method performs the best with cartoon (or graphical) images, by producing much sharper edges with the lowest distortions. For example, in the case of the images, like monster, fish, rooster, and shadow2, the MIS method was ranked as the best

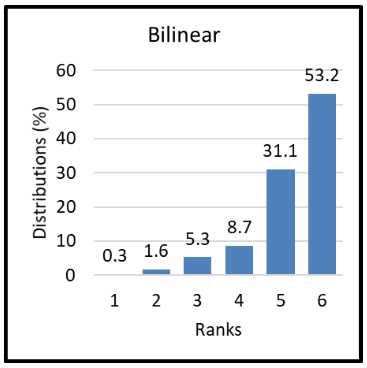

(a)

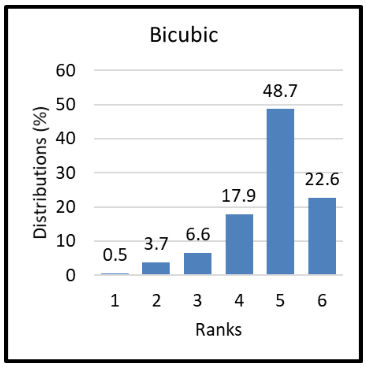

(b)

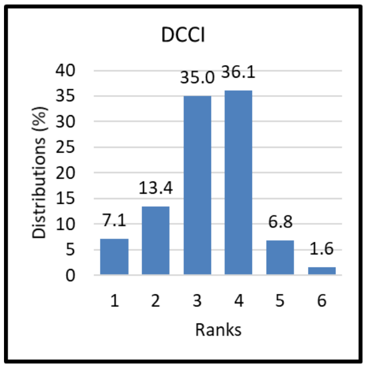

(c)

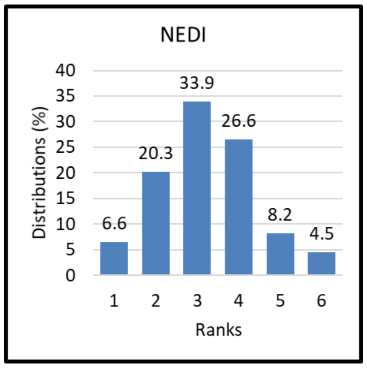

(d)

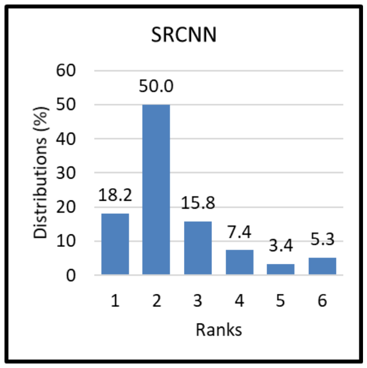

(e)

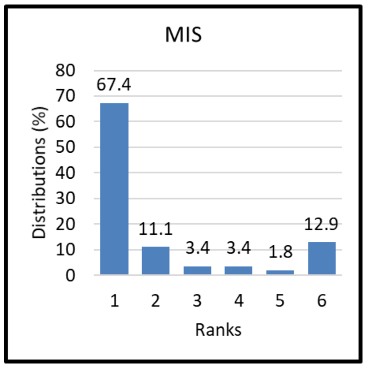

(f)

Figure 6.2: The distributions of the votes collected during the subjective evaluation among six ranks in percentage for the (a) bilinear, (b) bicubic, (c) DCCI, (d) NEDI, (e) SRCNN, and (f) MIS methods.

method in approximately 74% to 95% of the cases and was never ranked as the sixth method. In what follows, to illustrate the better performance of the MIS method, four examples with the monster, fish, rooster, and shadow2 images (from Appendix B) are shown in Figures 6.3, 6.4, 6.5, and 6.6, respectively. For the purpose of analysis here, in each example, the ground-truth image along with each test image is also considered to show the region of interest. Each of Figures 6.3 to 6.6 contains a part of the ground-truth image with the region of interest being marked by a rectangle, the magnified view of the region of interest in the ground-truth and (downscaled) test images, and the same parts in the scaled images obtained with the bilinear, bicubic, DCCI, NEDI, SRCNN, and MIS methods.

In Figure 6.3, the part of the ground-truth image in Figure 6.3(a) shows a region of interest marked by a rectangle which is magnified in Figure 6.3(b). The corresponding part from the downscaled test image is also shown in Figure 6.3(c). As Figure 6.3

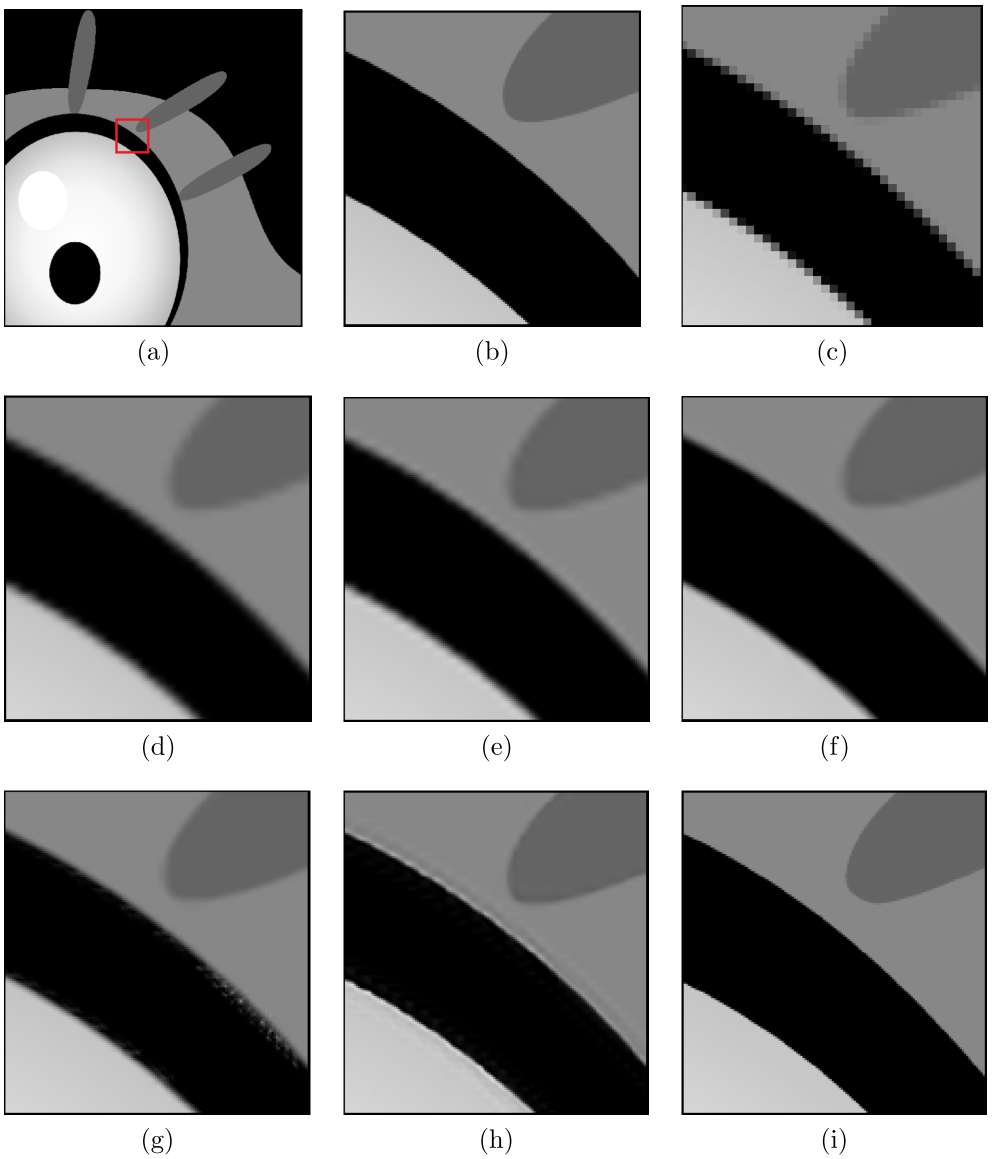

Figure 6.3: Scaling results obtained by the bilinear, bicubic, DCCI, NEDI, SRCNN, and MIS methods for the monster image with $k = 4$. (a) A part of the ground-truth high-resolution image with the area of interest marked by a rectangle. The magnified region of interest in the (b) ground-truth and (c) test images. The same region in the scaled image obtained from the (d) bilinear, (e) bicubic, (f) DCCI, (g) NEDI, (h) SRCNN, and (i) MIS methods.

shows, the corresponding parts in the scaled images obtained from the bilinear method in Figure 6.3(d), bicubic method in Figure 6.3(e), DCCI method in Figure 6.3(f), and NEDI method in Figure 6.3(g) all illustrate severely-blurred and distorted edges. Moreover, although the corresponding part in the scaled image obtained from the SRCNN method in Figure 6.3(h) shows sharper edges than the previous methods, it contains another type of artifacts near the edges of the black strip. With a closer look at the top and bottom edges of the black strip in the scaled image obtained from the SRCNN method in Figure 6.3(h), we can see some ringing artifacts both along the edge contours and in the image function near edges. The result obtained from the proposed MIS method shown in Figure 6.3(i), however, shows a much more accurate and sharper reconstruction of edges compared to all the other methods under comparison. As a result, in the case of the monster image in the subjective evaluation, the MIS method achieved the best rank in approximately 74% of cases, followed by the SRCNN method in only 16% of cases.

Also, in another example in Figure 6.4, the part of the ground-truth image in Figure 6.4(a) shows a region of interest which is magnified in Figure 6.4(b). The corresponding part from the downscaled test image is also shown in Figure 6.4(c). As Figure 6.4 shows, the corresponding parts in the scaled images obtained from the bilinear method in Figure 6.4(d), bicubic method in Figure 6.4(e), DCCI method in Figure 6.4(f), and NEDI method in Figure 6.4(g) all illustrate severely-blurred edges. Moreover, the corresponding part in the scaled image obtained from the SRCNN method shown in Figure 6.4(h) shows sharper edges than the previous methods, but it shows some ringing artifacts along all three edge contours in the image. The image obtained from the proposed MIS method shown in Figure 6.4(i), however, contains a much more accurate and sharper reconstruction of edges compared to all the other competing methods. As a result, in the case of the fish image in subjective evaluation, the best rank was assigned to the MIS method in approximately 84% of cases, followed by the DCCI method in approximately 10% of cases.

Similarly, in other two examples shown in Figures 6.5 and 6.6, we observe that the results obtained from the MIS method in Figures 6.5(i) and 6.6(i), respectively, have better subjective quality with sharper edges and less artifacts compared to the results obtained from each of the other five competing methods shown in Figures 6.5(d) to (h) and Figures 6.6(d) to (h). Similar to the results shown in previous examples, the scaled images obtained from the bilinear, bicubic, DCCI, and NEDI methods shown in Figures 6.5(d) to (g) and Figures 6.6(d) to (g) are all blurred at the edges. More-

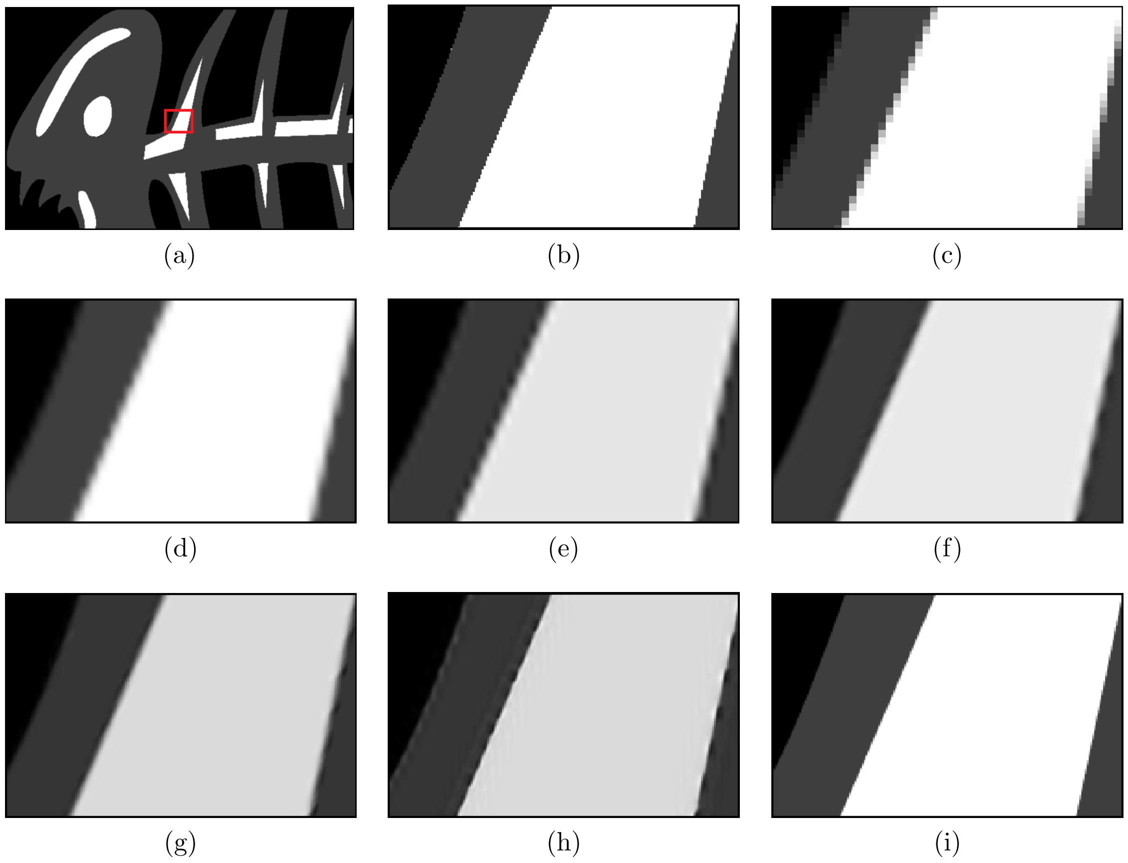

Figure 6.4: Scaling results obtained by the bilinear, bicubic, DCCI, NEDI, SRCNN, and MIS methods for the fish image with $k = 4$. (a) A part of the ground-truth high-resolution image with the area of interest marked by a rectangle. The magnified region of interest in the (b) ground-truth and (c) test image. The same region in the scaled image obtained from the (d) bilinear, (e) bicubic, (f) DCCI, (g) NEDI, (h) SRCNN, and (i) MIS methods.

over, the scaled images obtained from the SRCNN method shown in Figures 6.5(h) and 6.6(h) illustrate ringing artifacts at the edges. As a result, in the cases of both the rooster and shadow2 images in the subjective evaluation, the MIS method was ranked as the best method in approximately 95% of cases, followed by the DCCI method in only 5% of cases.

In the preceding discussion, the MIS method was shown to produce superior results by generating more accurate and sharper edges compared to all other competing methods and achieving the best rank in up to 95% of cases. Although the MIS method has shown the best overall performance in the subjective evaluation, it was also found to have some weaknesses that affect the subjective quality to some extent.

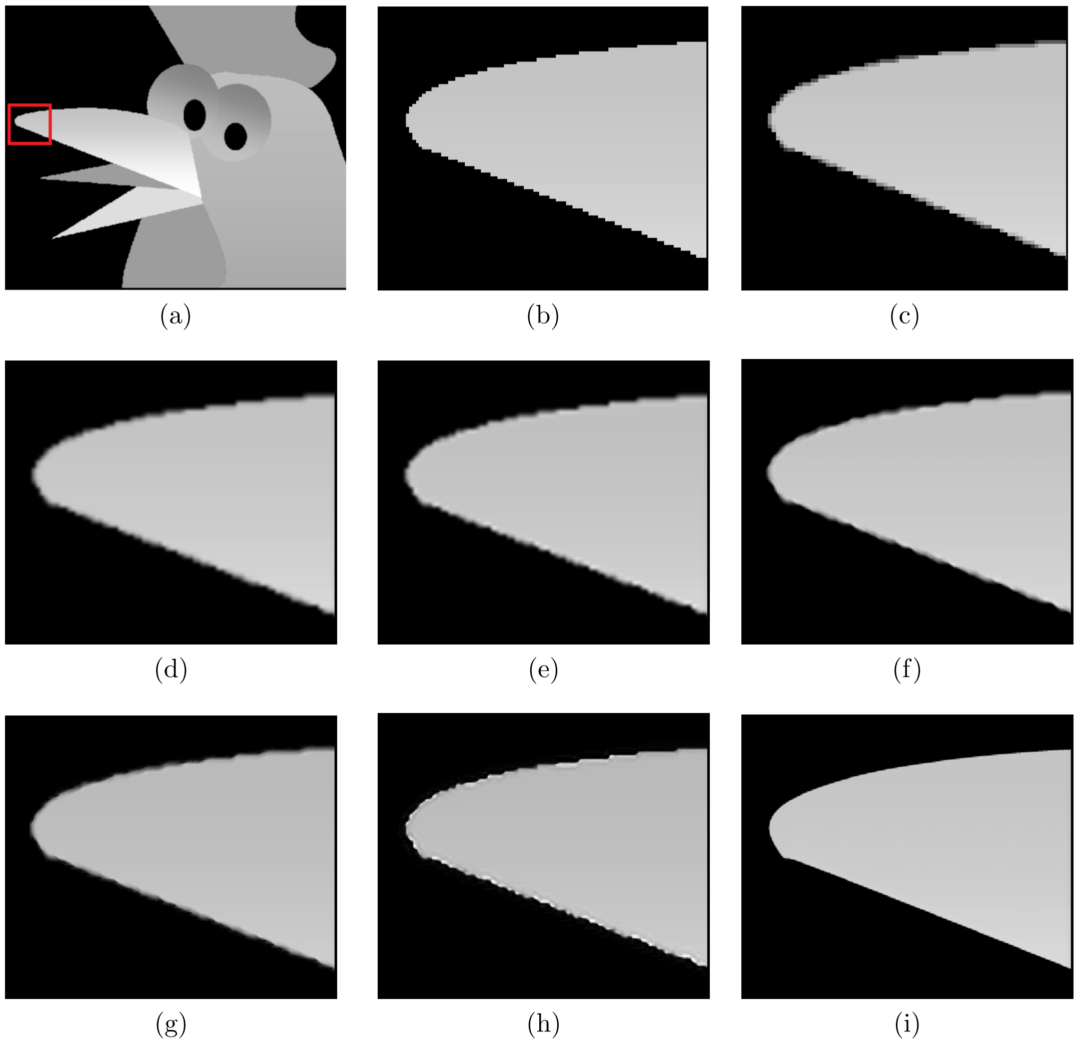

Figure 6.5: Scaling results obtained by the bilinear, bicubic, DCCI, NEDI, SRCNN, and MIS methods for the rooster image with $k = 4$. (a) A part of the ground-truth high-resolution image with the area of interest marked by a rectangle. The magnified region of interest in the (b) ground-truth and (c) test images. The same region in the scaled image obtained from the (d) bilinear, (e) bicubic, (f) DCCI, (g) NEDI, (h) SRCNN, and (i) MIS methods.

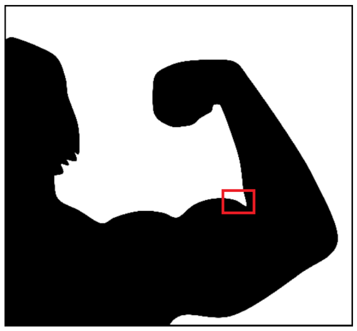
(a)

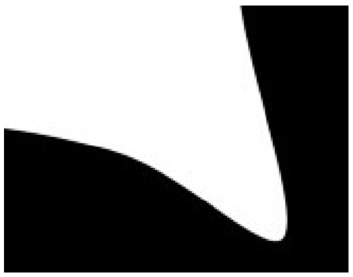
(b)

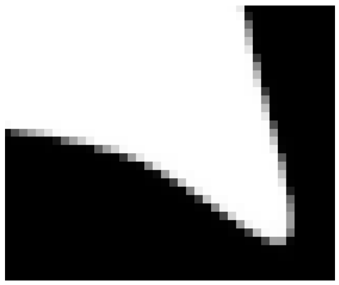
(c)

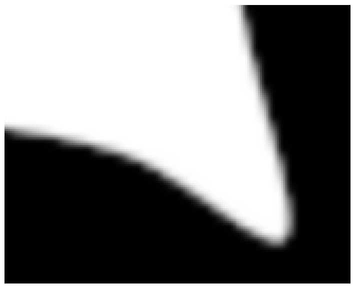
(d)

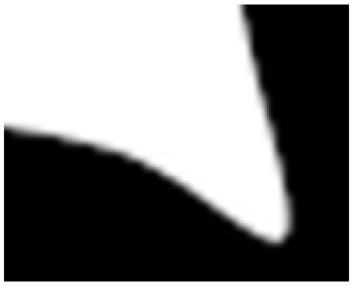
(e)

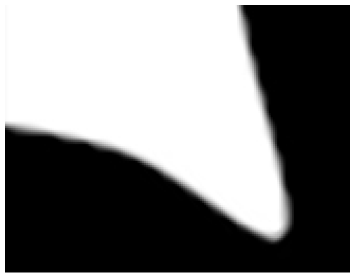
(f)

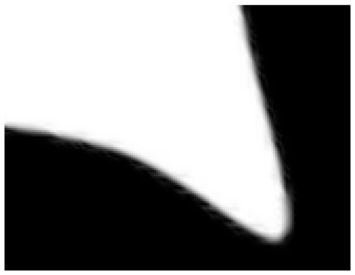
(g)

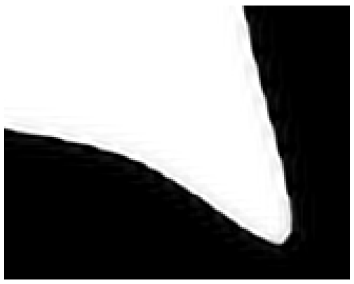
(h)

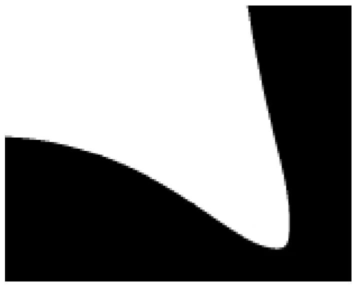
(i)

Figure 6.6: Scaling results obtained by the bilinear, bicubic, DCCI, NEDI, SRCNN, and MIS methods for the shadow2 image with $k = 4$. (a) A part of the ground-truth high-resolution image with the area of interest marked by a rectangle. The magnified region of interest in the (b) ground-truth and (c) test images. The same region in the scaled image obtained from the (d) bilinear, (e) bicubic, (f) DCCI, (g) NEDI, (h) SRCNN, and (i) MIS methods.

In order to find those weaknesses, several investigations were performed on different cases where the MIS method gained poor rankings during the subjective evaluation. As a results, the MIS was found to be ranked worst in the case of the scaled images with obvious geometric distortions. These cases are explained more below.

Based on the analysis made on the subjective evaluation results, the image quality perceived by the participants was found to be very drawn to the geometry of the edge contours in the image even more than the edge sharpness. More specifically, if an image has even some minor, but obvious, geometric distortions in some of its edge contours the image will be recognized as a low-quality image by the participant and will not be selected as the best image in the first round of pairwise comparisons. Similarly, when the same image is shown in later rounds of comparisons, it will be quickly identified again by its geometric distortions and will not be selected as the better-looking image. This process continues until the image is ranked worst, even if it has much better edge reconstructions in other places. An example of such geometric distortions is shown in Figure 6.7 using the dragon image from Appendix B. In this figure, a part of the ground-truth high-resolution image is shown in Figure 6.7(a), where the region of interest is marked with a rectangle. The magnified regions of interest from the ground-truth and test images are shown in Figures 6.7(b) and (c), respectively. The corresponding parts from the scaled images obtained with the bilinear, bicubic, DCCI, NEDI, SRCNN, and MIS methods are shown in Figures 6.7(d) to (i), respectively. As can be seen in Figure 6.7, the three circular shapes in the region of interest obtained from the MIS method in Figure 6.7(i) are affected by some geometric distortions. These types of geometric distortions are easily caught by human observers and lead to achieving poor ranks in the subjective evaluation. Although the scaled images obtained from other competing methods in Figures 6.7(d) to (h) contain blurring and ringing distortions, they gained better subjective ranks. Such geometric distortions in the scaled image obtained by the MIS method were found to be related to the APS algorithm proposed earlier in Section 5.2.8. As we recall, the threshold selection approach in (5.3) was achieved heuristically to work well overall but not necessarily in all cases. Therefore, in some cases, depending on the local curvature profile of the edge contour, the thresholding algorithm in (5.3) cannot produce desirable results, leading to such geometric distortions of which as example shown in Figure 6.7(i).

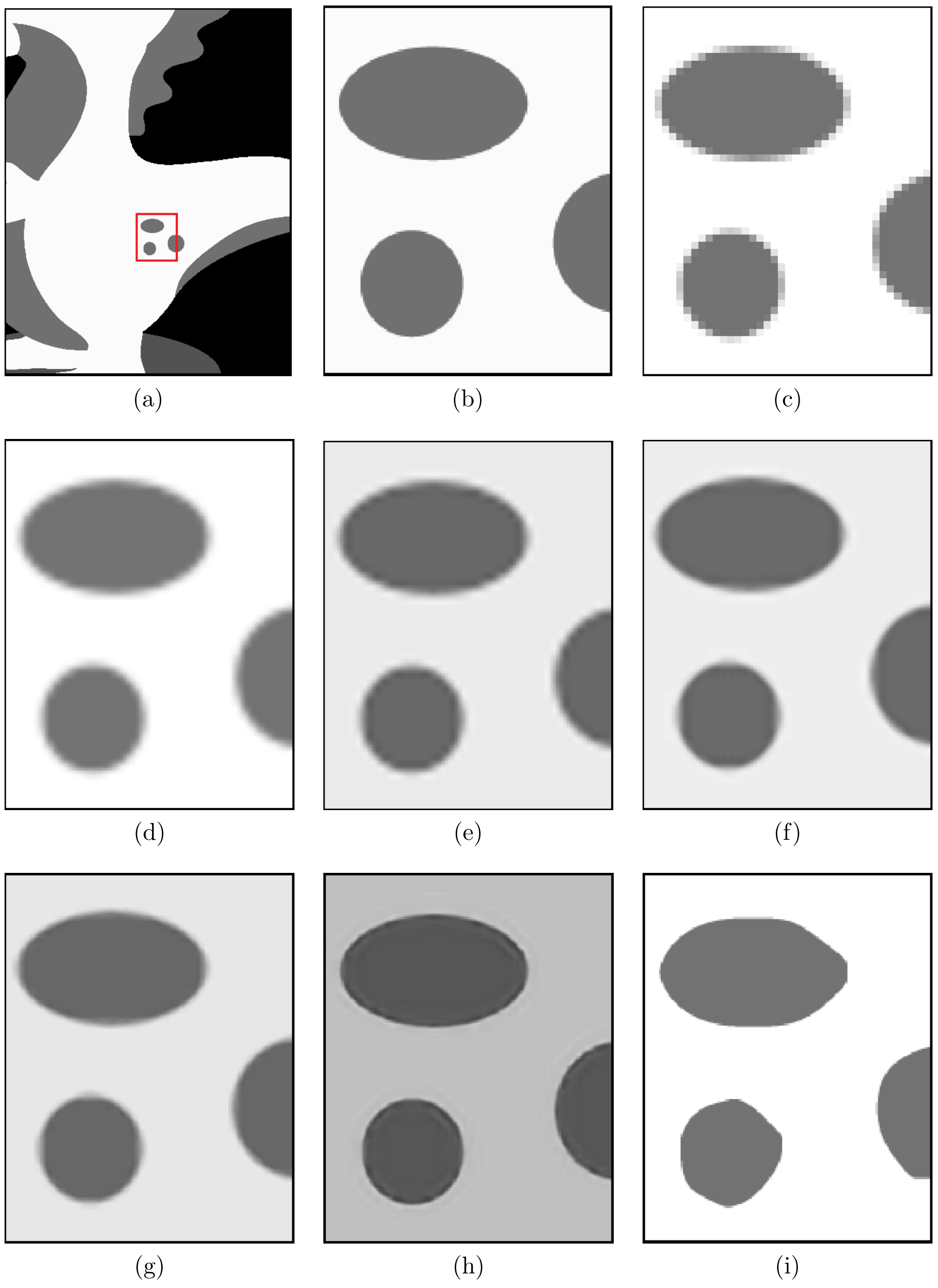

Figure 6.7: An example of a geometric distortion produced by the MIS method for the dragon image at $k = 4$. (a) A part of the ground-truth high-resolution image with the area of interest marked by a rectangle. The magnified region of interest in the (b) ground-truth and (c) test images. The same region in the scaled images obtained from the (d) bilinear, (e) bicubic, (f) DCCI, (g) NEDI, (h) SRCNN, and (i) MIS methods.

6.2.3 Objective Evaluation

As part of our experimental comparisons, in addition to the subjective evaluation, an objective evaluation is performed to quantitatively compare the quality of the scaled images obtained with the proposed MIS and those produced by the competing methods. In what follows, the methodology used for the objective evaluation is explained followed by presenting and analyzing the results.

6.2.3.1 Methodology for Objective Evaluation

One of the most well-known objective metrics that is often used for assessing image quality is the PSNR (as introduced in Section 2.11.1). Although the PSNR does not always reflect the human visual perception of image quality (as studied in [87]), it is still widely used in many applications. Many other metrics based on image perceptual quality have also been introduced (e.g., [76, 56, 97, 47]), of which the SSIM [88] (as introduced in Section 2.11.2) has gained much attention and has been widely used. Thus, for our objective evaluation, both the PSNR and SSIM are used. Moreover, since our main goal is to reduce the blurring artifacts in scaled images, the PEE metric (as introduced in Section 2.11.3) is also used to measure the sharpness of edges in scaled images because neither PSNR or SSIM is designed to perform that.

For the objective evaluation, we proceeded as follows. In order to be consistent with the subjective evaluation, the same set of 20 low-resolution test images and the sampling factor $k = 4$, which were used previously for the subjective evaluation, were given to each of the six scaling methods under comparison. Then, the resulting scaled image obtained from each method was compared with its ground-truth high-resolution counterpart to compute the PSNR, SSIM, and PEE metrics.

6.2.3.2 Objective Evaluation Results and Analysis

Using the methodology explained above, the computed PSNR, SSIM, and PEE results with the bilinear, bicubic, DCCI, NEDI, SRCNN, and MIS methods, for a representative subset of 10 images, are summarized in Table 6.2. As will be seen shortly, the objective results are not necessarily consistent with the subjective results and results of different metrics are not even consistent well with each other either. Such inconsistencies in the objective results are because of the fact that devising objective metrics that always match well with subjective image quality, as it is perceived by humans, is extremely difficult. Therefore, all objective metrics, including the ones

		Bilinear	Bicubic	DCCI	NEDI	SRCNN	MIS
frangipani	PSNR	45.60	46.91	40.49	40.46	47.15	35.61
	SSIM	0.9884	0.9894	0.9860	0.9859	0.9891	0.9748
	PEE	15.83	13.44	14.96	13.10	2.66	-2.49
balloons	PSNR	42.36	43.26	39.30	39.25	44.28	36.16
	SSIM	0.9675	0.9689	0.9629	0.9626	0.9702	0.9518
	PEE	15.82	8.67	10.22	11.43	3.54	-7.28
dragon	PSNR	36.35	37.07	33.68	33.57	39.70	33.17
	SSIM	0.9873	0.9888	0.9863	0.9858	0.9915	0.9860
	PEE	29.61	20.04	27.59	27.80	0.56	0.51
ammo	PSNR	37.87	38.96	35.18	35.03	41.78	36.16
	SSIM	0.9930	0.9940	0.9936	0.9922	0.9957	0.9935
	PEE	26.48	17.23	20.72	21.60	-0.60	1.55
apple	PSNR	37.42	38.37	35.06	34.95	42.50	33.96
	SSIM	0.9916	0.9924	0.9917	0.9910	0.9962	0.9913
	PEE	26.88	18.07	20.21	20.02	0.36	1.43
bird	PSNR	37.45	38.43	34.36	34.32	41.50	34.04
	SSIM	0.9905	0.9914	0.9888	0.9887	0.9938	0.9911
	PEE	27.58	18.00	23.47	24.33	1.47	1.37
fish	PSNR	35.91	36.65	32.91	32.67	39.47	33.25
	SSIM	0.9852	0.9868	0.9837	0.9834	0.9899	0.9867
	PEE	29.49	19.69	27.23	26.02	0.73	2.02
monster	PSNR	34.44	35.24	31.84	31.69	37.70	31.14
	SSIM	0.9822	0.9844	0.9800	0.9797	0.9867	0.9812
	PEE	31.45	22.09	27.86	28.12	1.38	1.67
rooster	PSNR	35.80	36.28	33.19	33.09	36.94	32.91
	SSIM	0.9908	0.9917	0.9900	0.9898	0.9908	0.9919
	PEE	28.03	20.06	24.96	28.09	4.90	1.56
shadow2	PSNR	34.09	34.93	31.48	31.40	37.11	31.10
	SSIM	0.9929	0.9943	0.9936	0.9930	0.9930	0.9947
	PEE	24.18	17.11	21.67	22.62	4.78	0.45

Table 6.2: Comparison between the quality of the scaled images obtained at scaling factor of $k = 4$ from the bilinear, bicubic, DCCI, NEDI, SRCNN, and MIS methods, using the PSNR, SSIM, and PEE metrics.

used in our evaluation, sometimes fail to accurately reflect the image quality that is actually perceived by humans. Therefore, due to this limitation, multiple objective metrics sometimes result in different image quality measurements that are inconsistent not only with themselves, but also with the actual perceived image quality. Despite the above shortcomings, such objective measures are still used in many applications, where performing a subjective evaluation is not practical, but they leave much to be desired. Therefore, analyzing such results needs more careful considerations which is presented below.

Starting with the PSNR results in Table 6.2, we realize that the bicubic method always performs better than the bilinear method, which is consistent with the subjective results. Similarly, comparing the PSNR results between the DCCI and NEDI methods shows that they perform fairly close, with the DCCI method being slightly better than the NEDI method, which also is consistent with the subjective results. Between the bicubic and DCCI methods, however, the PSNR results in Table 6.2 show that the bicubic method is always better than the DCCI method, with a PSNR margin of approximately 3 dB (for rooster image) to 6 dB (for frangipani image). Similarly, the PSNR results in Table 6.2 show that even the bilinear method performs better than the DCCI method in all the cases with a PSNR margin of over 2 dB (for apple image) to 5 dB (for frangipani image). Thus, based on the PSNR results, the bilinear/bicubic methods perform much better than the DCCI/NEDI methods, by a considerable margin. According to the subjective evaluation, however, the DCCI/NEDI methods achieved better ranks than the bilinear/bicubic methods overall. Therefore, the better performance of the bilinear/bicubic methods compared to the DCCI/NEDI methods, based on Table 6.2, fully contradicts the subjective results previously presented in Table 6.1 and Figure 6.2. In the case of the SRCNN method, however, the PSNR results in Table 6.2 show that it performs better than the bilinear, bicubic, DCCI, and NEDI methods, which is consistent with the subjective results. In the case of the proposed MIS method, the PSNR results in Table 6.2 show that it produces the lowest PSNRs in almost all cases, except for the ammo and fish images, where the MIS method outperforms the DCCI and NEDI methods with an average margin of 0.66 dB and 0.85 dB, respectively. The lower performance of the MIS method in terms of PSNR again contradicts the subjective results, where the MIS method ranked best overall in approximately 67% of the cases. As explained earlier, such inconsistencies that are observed between the PSNR and subjective results are due to the significant limitations of PSNR in accurately measuring the error as perceived by the human visual system.

The lower PSNRs obtained by the MIS method, in Table 6.2, can be justified as follows. Firstly, as shown previously through subjective evaluation results, two strengths of the MIS method are producing sharper edges and smoother edge contours. Secondly, the image functions at points on the opposite sides of image edges often differ by a large amount. Consequently, even minor changes in the image function near edges (made by edge sharpening) and minor shifting in the location of the edges (made by edge-contour smoothing) can drastically affect the PSNR. Such edge sharpening and edge-contour smoothness in the MIS method may not necessarily generate a poor image reconstruction as proved through the subjective evaluation, but they can definitely reduce the PSNR. Another factor that can negatively affect the PSNR is the deficiency of the edge detector at junctions points, where three (or more) edges meet. In some junctions areas, where the edge detector fails to detect the junction point and its nearby edges, a reconstruction error will happen which has a negative effect on the PSNR. An example of such a missed junction point is shown in Figure 6.8, using a junction area in the dragon image from Appendix B. In this figure, a magnified area of the ground-truth high-resolution image containing a junction point, its corresponding part from the downscaled test image, and the corresponding part from the resulting edge map are shown in Figures 6.8(a), (b), and (c), respectively. The corresponding junction areas from the scaled images obtained using the bilinear, bicubic, DCCI, NEDI, SRCNN, and MIS methods are shown in Figures 6.8(d) to (i), respectively. As can be seen in Figure 6.8, the three edges approaching the junction point in Figure 6.8(b) were not fully detected in the edge map shown in Figure 6.8(c). Thus, the edge map contains a gap near the junction area. Consequently, the corresponding junction area in the scaled image obtained from the MIS method shown in Figure 6.8(i) shows some reconstruction error in that region, which can decrease the PSNR. Moreover, although the scaled images obtained from other methods, such as the bicubic and SRCNN methods in Figures 6.8(e) and (h), have higher PSNRs, they all have other types of artifacts like blurring and ringing near the edges, which reduce the perceptual image quality.

Having studied the PSNR results in Table 6.2, we now focus on the SSIM results. Similar to PSNR, the SSIM results, in Table 6.2, show that the bicubic and DCCI methods perform better that the bilinear and NEDI methods, respectively, in all the test cases. These improvements in SSIM, however, are very marginal (unlike the improvements in PSNR) and reasonably consistent with the subjective results.

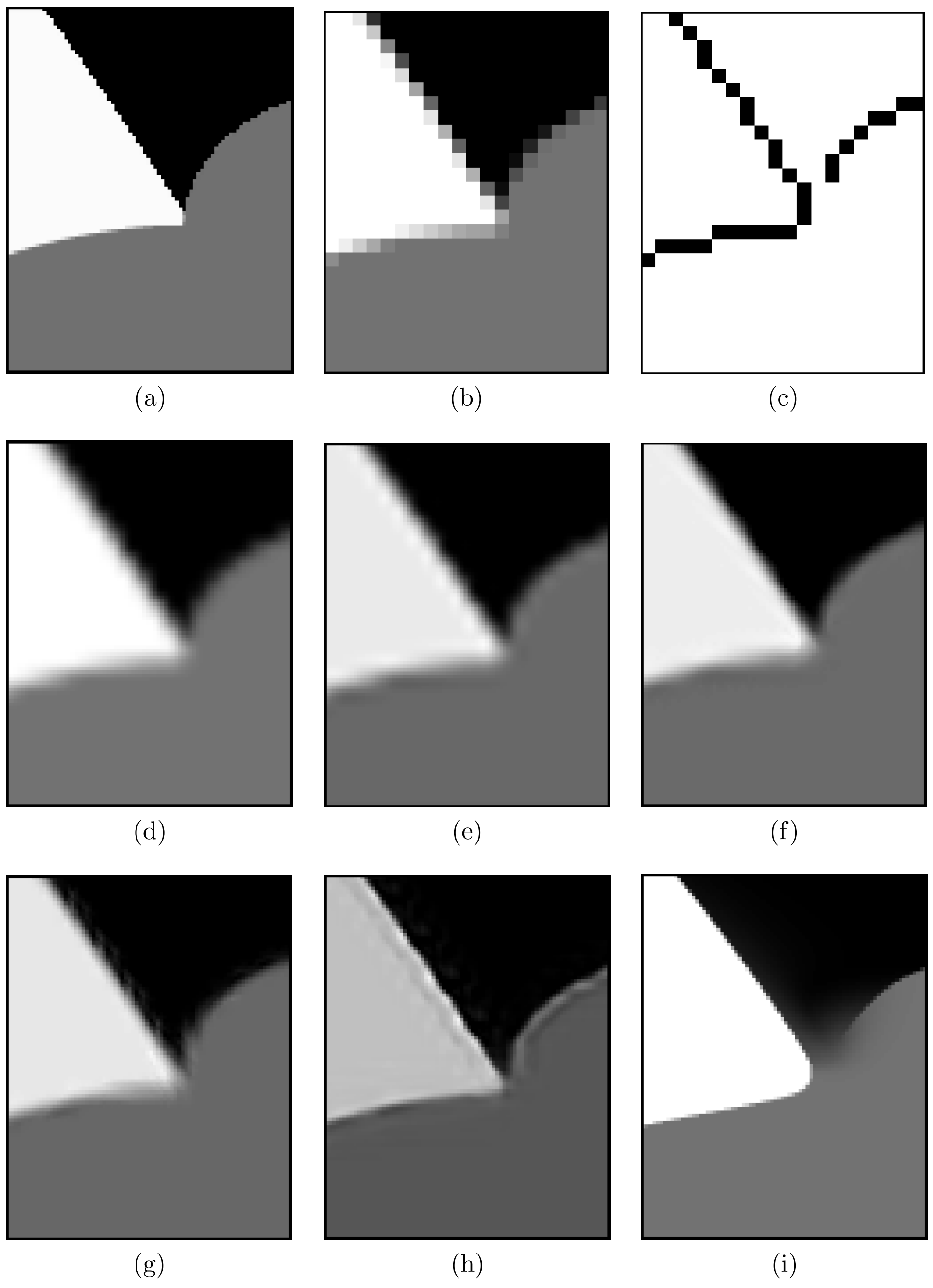

Figure 6.8: An example showing how a missed junction point can affect the scaled image obtained from the MIS method using the dragon image at $k = 4$. (a) A magnified area of the ground-truth high-resolution image containing a junction point. The corresponding part from the (b) downscaled test image and (c) resulting edge map. The same junction region in the scaled images obtained with the (d) bilinear, (e) bicubic, (f) DCCI, (g) NEDI, (h) SRCNN, and (i) MIS methods.

Between the bicubic and DCCI methods, however, the SSIM results in Table 6.2 indicate that the bicubic method still performs better that the DCCI method, with a margin of 0.0003 (for ammo image) to 0.0060 (for balloons image). It is worth mentioning that although the SSIM results for the bicubic and DCCI methods are not completely consistent with the subjective evaluation, the differences in the SSIM values are not as significant as they are in the PSNR results. For example, for images like ammo, apple, and shadow2 from Table 6.2, the bilinear method outperforms the DCCI method with an average PSNR margin of 3.5 dB, but with an average SSIM margin of only 0.0005. Consequently, in this example, the average of 3.5 dB difference is considered reasonably high for PSNR, whereas the 0.0005 difference is not that large for SSIM and indicates a very comparable perceptual quality between the images under comparison and also a better consistency with the subjective results.

In the case of the SRCNN and bicubic methods in Table 6.2, the SSIM results show that bicubic method outperforms the SRCNN method in the frangipani, rooster, and shadow2 images. In terms of PSNR, however, the SRCNN method was shown to perform better than the bicubic method in all cases in Table 6.2, indicating the inconsistency between the PSNR and SSIM metrics. Finally, regarding the MIS method, the SSIM results collected from all 20 test images shows that, unlike the PSNR results, in the case of the cartoon/graphical images, the MIS method produces comparable or even better results compared to the bilinear, bicubic, DCCI, and NEDI methods. For example, in the case of the eight cartoon/graphical images in the representative results shown in Table 6.2 (i.e., all excluding the frangipani and balloons images), the MIS method outperforms the NEDI method in 8/8 of cases with an average SSIM margin of 0.0016. Similarly, the MIS method outperforms the DCCI method in 5/8 of cases by an average SSIM margin of 0.0019. In the remaining 3/8 of cases, however, the MIS method performs fairly comparable with an average SSIM of only 0.0003 smaller. Between the SRCNN and SIM method, the MIS method outperforms the SRCNN method in 2/8 of cases, for the rooster and shadow2 images, with an average SSIM margin of 0.0014. With respect to PSNR, however, the MIS method falls behind the SRCNN method with a average PSNR margin of approximately 5 dB, which is another example of inconsistency between the PSNR and SSIM metrics. As explained before, such inconsistencies between different objective metrics, such as PSNR and SSIM, is due to the limitations of each of them in accurately capturing the perceived image quality. In the case of the two natural photographic and moderately textured images in Table 6.2, such as frangipani and balloons, the MIS method performs weaker than other competitors with an average SSIM margin of 0.0130 and 0.0146, respectively. In summary, the inconsistencies between different objective metrics makes the comparison difficult without having a subjective evaluation. In the case of the SSIM results, the stronger performance of the MIS method for the cartoon images and its weaker performance for the natural photographic and textured images show a better consistency with the subjective results.

The last metric that is considered from Table 6.2 is PEE. Since one of our main initial motivations for proposing the MIS method is to produce scaled images with sharper edges, the PEE metric is useful to measure the sharpness of the edges. As the PEE results in Table 6.2 show, the bilinear, bicubic, DCCI, and NEDI methods all produce much higher levels of blurring (i.e., larger PEE) at the image edges than the SRCNN and MIS methods. More specifically, for the subset in Table 6.2, the bilinear, bicubic, DCCI, and NEDI methods produced scaled images with an average PEE of approximately 26%, 17%, 22%, and 22%, respectively. The SRCNN and MIS methods, however, produced much lower PEE with an average of approximately 2% and 0.10%, respectively. Moreover, based on the subjective results, the MIS and SRCNN methods also achieved better ranks than other methods. Thus, a reduction in PEE can be an indication of higher perceptual image quality. Furthermore, the PEE results in Table 6.2 show that the SRCNN method in some cases (e.g., the dragon, ammo, apple, and bird images) achieves better (i.e., lower) or similar PEE results compared to the MIS method. Visual inspections on the scaled images obtained by the SRCNN and MIS methods, however, reveals that the SRCNN method adds some undesirable ringing artifacts around the edges which can result in lower PEE values. In order to show such artifacts, an example using the dragon image is displayed in Figure 6.9. In this figure, the magnified parts of the same edge from the ground-truth (high-resolution) and downscaled test images are shown in Figures 6.9(a) and (b), respectively. The corresponding parts in the scaled images obtained from the bilinear, bicubic, DCCI, NEDI, SRCNN, and MIS methods are displayed in Figures 6.9(c) to (h), respectively. As can be seen in Figure 6.9, the edges in the scaled images obtained with the bilinear, bicubic, DCCI, and NEDI methods show more blurring, all with the overall PEE of above 20%, compared to the SRCNN and MIS methods with the overall PEE of approximately 0.5%. Although the PEE results for the SRCNN and MIS methods are very similar, the edge produced by the MIS method in Figure 6.9(h) looks sharper and more accurate than the one generated by the SRCNN method in Figure 6.9(g). Indeed, the edge produced by the SRCNN method

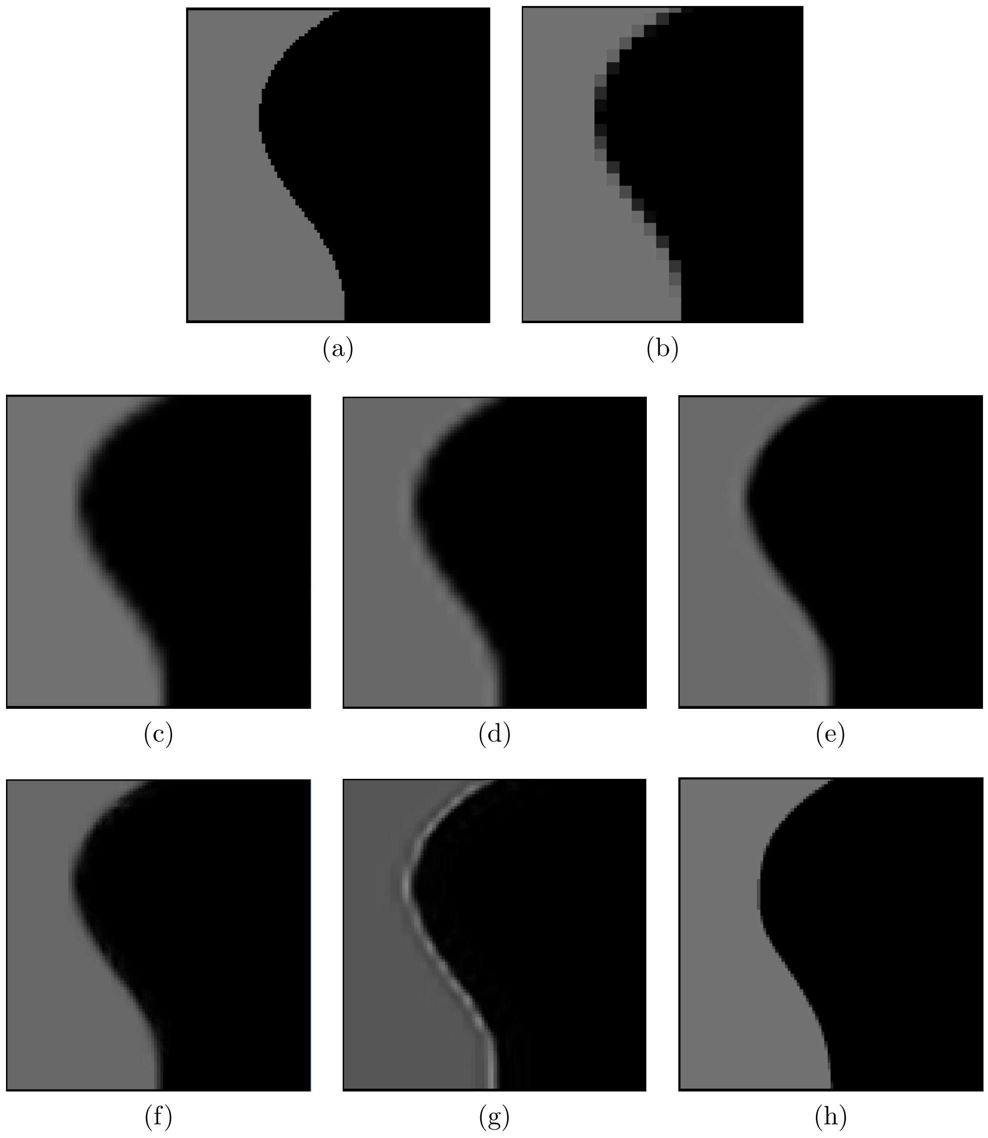

Figure 6.9: Scaling results obtained by the bilinear, bicubic, DCCI, NEDI, SRCNN, and MIS methods for the dragon image with $k = 4$. Magnified regions containing the same edge in the (a) ground-truth and (b) low-resolution test image. The same region in the scaled images obtained from the (c) bilinear (PEE 29.61%), (d) bicubic (PEE 20.04%), (e) DCCI (PEE 27.59%), (f) NEDI (PEE 27.80%), (g) SRCNN (PEE 0.56%), and (h) MIS (PEE 0.51%) methods.

in Figure 6.9(g) shows an undesirable bright strip along the edge contour which can undesirably produce large gradients, leading to a small overall PEE value.

The negative PEE values, in some cases in Table 6.2, such as the frangipani and balloons images obtained by the MIS method, show that the scaled image contains edges that are sharper than those in its ground-truth counterpart. Thus, the negative PEE values do not necessary indicate a weak edge reproduction, as long as the general structure of the image and edge contours are maintained well and the absolute value of the PEE is close enough to zero. The collected PEE results show that, with natural photographic images, the MIS method more often produces scaled images with negative PEE values. This behavior can be justified as follows. In photographic images, some (parts of) objects almost always fall outside of the lens depth of field, where the objects are supposed to appear acceptably sharp. As a result, those parts that intentionally/unintentionally fall outside of the lens depth of field look much more blurred. Moreover, objects that fall inside the depth of field themselves do not have absolute sharp edges, due to lens optics limitations and maybe because of some post processing that is applied by some cameras internally. Therefore, when such photographic images are used with the MIS method, all those intentionally/unintentionally blurred edges are sharpened during the the scaling process because the MIS method has originally been designed to produce sharp edges. Consequently, the scaled images obtained with the MIS method most often contain sharper edges than the ground-truth image, leading to negative PEE results. Whether such sharpening is desirable is very subjective, but the overall results from our subjective evaluation seem to suggest that, for the average/typical person, sharpening is usually preferred over blurring or ringing.

In order to illustrate the sharpening effect that often exists in the case of the natural photographic images as explained above, an example using the frangipani image from Appendix B is shown Figure 6.10. In this figure, a part of the ground-truth image, with the region of interest being marked by a rectangle is shown in Figure 6.10(a). As can be seen from the magnified views of the region of interest in the ground-truth and test images shown in Figures 6.10(b) and (c), respectively, they themselves show some level of blurriness due to the reasons explained earlier. Therefore, the blurring/ringing artifacts that happen by the the bilinear, bicubic, DCCI, NEDI, and SRCNN methods are not much visually recognizable in the scaled images shown in Figures 6.10(d) to (h) because the original images themselves are already blurred. The corresponding part in the scaled image obtained by the MIS

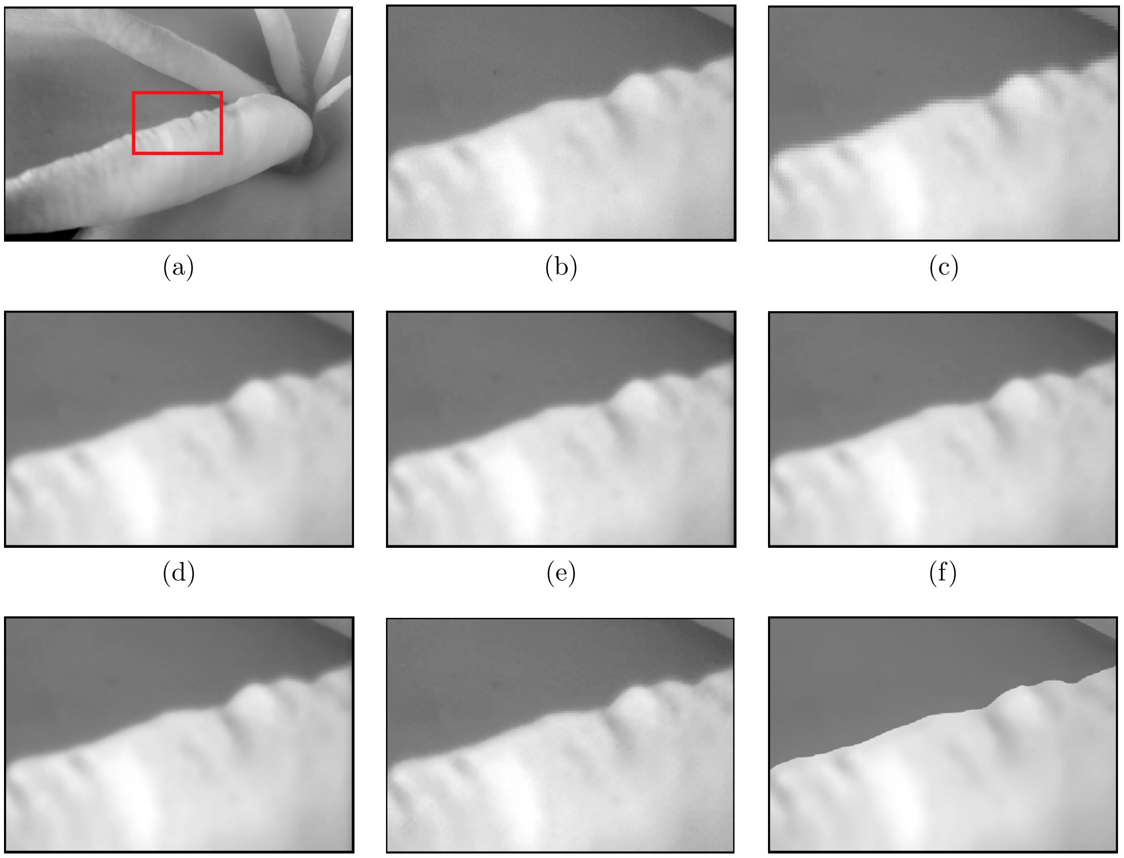

Figure 6.10: Scaling results obtained by the bilinear, bicubic, DCCI, NEDI, SRCNN, and MIS methods using the frangipani image at $k = 4$. (a) A part of the ground-truth high-resolution image, with a region of interest being marked by a rectangle. The magnified region of interest from the (b) ground-truth and (c) test images. The same part in the scaled images obtained with the (d) bilinear (PEE 15.83%), (e) bicubic (PEE 13.44%), (f) DCCI (PEE 14.96%), (g) NEDI (PEE 13.10%), (h) SRCNN (PEE 2.66%), and (i) MIS (PEE -2.49%) methods.

method shown in Figure 6.10(i), however, shows considerably sharper edges than all other images (including the ground-truth image), leading to a negative PEE of -2.49%. Such an observation, of which as example shown in Figure 6.10, is often valid in the case of the natural photographic images, where many edges are usually blurred either intentionally (by the photographer) or unintentionally.

In summary, as the analysis of the objective results shows, the PSNR, SSIM, and PEE metrics all performed differently, with the PSNR and PEE metrics being shown to have the lowest and highest consistency with the subjective results, respectively. Moreover, some objective metrics, such as PSNR and SSIM, were shown not to represent consistent results due to their limitations. Therefore, for evaluating complicated imaging systems, such as image scaling, objective metrics along with a subjective evaluation should be taken into consideration, as objective measures by themselves often cannot accurately reflect perceptual image quality.

6.2.4 Supplementary Discussions

With the insights obtained through the experimental comparisons between the MIS and other relevant scaling methods, we now provide some supplementary discussions on the advantages and disadvantages of each method. As the results of the experimental comparisons in previous sections showed, no single scaling method is yet able to perform perfectly well with all types of images in all aspects.

The classical convolution-based interpolation techniques, such as bilinear and bicubic methods, were shown to produce scaled images with weaker perceptual qualities and significantly blurred edges. Given all their weaknesses, these methods have been still being used as the main upscaling techniques in many commercial software, such as Adobe Photoshop for many years, due to their simplicity, fast speed, and ease of implementation. Other edge-directed approaches, such as the NEDI and DCCI methods, however, have shown to be capable of handling the edge-blurring problem to some extent. The improvements in the perceptual quality of the scaled images obtained by these methods, however, are too marginal to justify the added computational complexity.

The SRCNN method, as a representative of the most recent and advanced methods based on deep learning, showed a reasonably better performance compared to other raster-based methods in our comparisons. Using a deep convolutional neural network, the SRCNN method is able to reduce the edge-blurring that can happen during image scaling. As shown in our experiments, however, the scaled images obtained with the SRCNN method often contain some undesirable ringing artifacts which reduce the subjective quality. Such deep-learning based scaling methods have recently become very advanced and probably been known as the best general-purpose image scaling methods. These methods, however, have some serious drawbacks that should be taken into consideration as follows. First of all, deep-learning based scaling methods are known to be computationally very expensive and require a huge training dataset to perform reasonably well. Therefore, often graphics processing units (GPUs) with multiple cores are used to perform the training stage. Because of such a large training data and high computational cost, the SRCNN method can take up to several days to train its network. Moreover, such methods have a very high memory cost. For example, in our experiment, to generate a scaled image with a high resolution of approximately 6000×6000, the SRCNN method would require more than 20 gigabytes (GB) of RAM which is too much with respect to the typical RAM sizes in today's personal computers. Lastly, almost all deep-learning based scaling methods, including the SRCNN method, are trained for a single scale factor and are only guaranteed to work well only with that specified scale. Thus, for a new scale factor, a new model has to be trained. One may intuitively think that if a network is trained for a larger scale factor it may then work well with smaller factors too, but that is not true (as will be shown shortly).

Regarding the proposed MIS method, although it has higher computational complexity than the convolution-based scaling methods, the subjective evaluation has shown that the MIS method obtained the best rank among all. Compared to the SRCNN method, however, the MIS method has lower computational complexity mainly because no training stage is involved to take several days long. Moreover, in our experiment, the MIS method could generate scaled images with large resolutions of up to 9000×9000 with a moderate CPU and typical RAM of 4 GB, which is much lower than the RAM needed by the SRCNN method. Furthermore, one of the most beneficial advantages of the MIS method is the fact that, once an image mesh model is generated, it can be used with almost any scale factor (unlike the SRCNN method). Figure 6.11 shows an example, where the same mesh model from the MIS method and the same trained model with the SRCNN method, used in the previous experiments for a scale factor of $k = 4$, tested with a new factor of $k = 2$ on the dragon image. In Figure 6.11, a magnified part of the low-resolution test image is shown in Figure 6.11(a). The corresponding part in the scaled image obtained with the

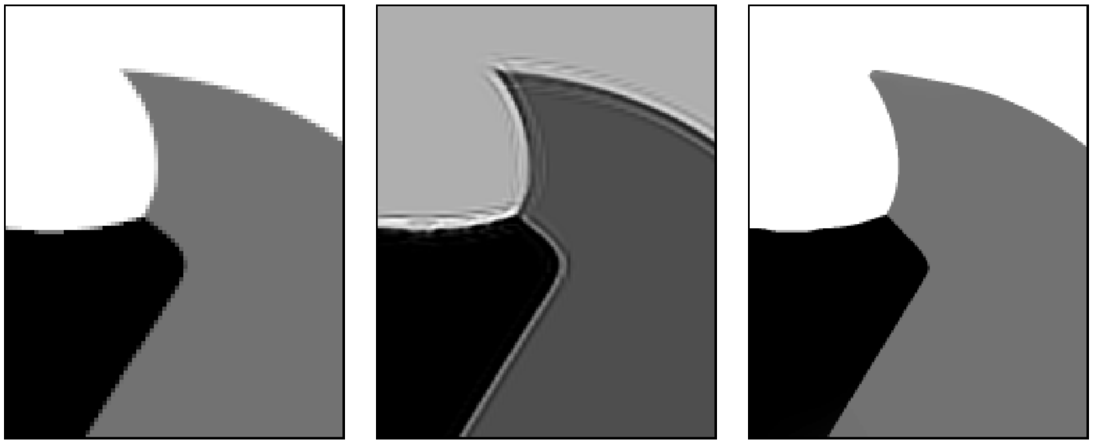
(a) (b) (c)

Figure 6.11: An example of the scaled images obtained with the SRCNN and MIS methods with the scaling factor of $k = 2$, with the dragon image. (a) A magnified part of the test image. (b) The same part from the the scaled image obtained with the SRCNN method with a model that is trained for $k = 4$. (c) The same part from the scaled image obtained with the MIS method with the same model previously used with $k = 4$.

SRCNN method using a model that is trained for $k = 4$ is shown in Figure 6.11(b). Similarly, the corresponding part in the scaled image obtained from the MIS method with the same model used previously for $k = 4$ is shown in Figure 6.11(c). Both scaled images, however, obtained at a new scale factor of $k = 2$. As can be seen in Figure 6.11, the part of the scaled image obtained with the SRCNN method shown in Figure 6.11(b) shows obvious distortions and undesirable artifacts near the edges. The corresponding part in the scaled image obtained with the MIS method shown in Figure 6.11(c), however, clearly has better subjective quality with more accurate edges.

As the example in Figure 6.11 shows, such a drop in the scale factor from $k = 4$ to $k = 2$ significantly affects the performance of the SRCNN method if a model that is trained for a different (even larger) factor is used. Thus, a new model has to be trained again for the new factor. In contrast, as the same example shows, such a change in scale factor from $k = 4$ to $k = 2$ does not destroy the performance of the MIS method. In other words, the same mesh model that is generated once can be directly used for the new scale factor too. Another advantage of the MIS method, as a mesh-based approach, is the fact the mesh-model that is generated once in the first stage of the MIS method can be stored as an image model for future usages. For example, the same image model can also be used for mesh editing or any combination of other affine transformation, such as translation, rotation, and shearing. Such flexible functionalities of the MIS method, which allow for image models that are portable, editable, and reusable, however, are not (easily) provided with other raster-based methods, including the SRCNN method.

6.3 Conceptual Comparison

Due to the difficulties of comparing with the mesh-based methods as explained before, an experimental comparison between the MIS method and other mesh-based image-scaling methods was not feasible. In what follows, however, a conceptual comparison through theoretical analysis is made between the MIS method and the following two relevant mesh-based image scaling methods:

1. the subdivision-based image-representation (SBIR) method of Liao et al. [60], and
2. the curvilinear feature driven image-representation (CFDIR) method of Zhou et al. [102].

Like our MIS method, the SBIR and CFDIR methods are based on triangle-mesh models and employ a subdivision-based technique to create smoother edge contours. Moreover, both of them are edge preserving, but each method employs a different technique for preserving the image edges. Furthermore, both of the SBIR and CFDIR methods employ a function that approximates the original image function at sample points, unlike the MIS method where an interpolating function is used. In what follows, other specific similarities and differences between our MIS method and each of the above methods are discussed.

Comparison with the SBIR method. The SBIR method, like our MIS method, employs an approximating function that allows for discontinuities. Moreover, the SBIR method applies subdivision to a mesh model that is associated with an approximating function with discontinuities. In our MIS method, the subdivision scheme of the SBIR method is adapted and applied to the ERD mesh model. When mesh generation is considered, the SBIR method employs a technique that is fundamentally different from the one employed by the MIS method. More specifically, the mesh-generation technique of the SBIR method is based on mesh simplification, where a mesh is initially generated using all sample points in the input image as the vertices in the mesh. Then, the initial mesh is iteratively simplified to achieve a desired number of vertices. Such mesh-generation schemes typically have a very high computational and memory cost because of generating meshes with a very large number of sample points at early stages of the simplification process. In our MIS method, however, a mesh-generation approach based on mesh refinement is used to reduce the complexity, where a very coarse mesh is initially generated and then iteratively refined by point insertion. The mesh-refinement scheme used by the MIS method potentially has lower computational complexity and also is believed to have much lower memory cost than the mesh-simplification scheme of the SBIR method in comparable conditions.

Comparison with the CFDIR method. The CFDIR method, like our MIS method, employs a mesh-generation scheme that is based on mesh refinement and a constrained Delaunay triangulation. The CFDIR method, however, uses a completely different model that is associated with a continuous approximating function. Therefore, in the CFDIR method, image discontinuities are modeled differently by enclosing each image-edge feature with a pair of parallel polylines (similar to the GVS method as illustrated previously in Figure 4.5). The MIS method, however, employs a model that is associated with an approximating function that allows for discontinuities. Thus, each image-edge feature is modeled with only one polyline, which potentially results in meshes with many fewer vertices. Furthermore, because the CFDIR method uses a continuous function everywhere, it will still create inevitable blurring artifacts during image scaling. To address this issue, in our MIS method, however, a function with selected discontinuities is used to effectively reduce (if not eliminate) edge blurring during image scaling (as previously shown through the experimental comparisons in Section 6.2).

Chapter 7

Conclusions and Future Work

7.1 Conclusions

In this thesis, we have addressed two problems: 1) mesh generation, where mesh models of images are generated to minimize squared error, and 2) image scaling, where raster images are scaled using mesh models. To solve the mesh-generation problem, the SEMMG method was proposed to generate triangle-mesh models that are effective for representing grayscale images. To solve the image-scaling problem, the MIS method was proposed for scaling grayscale raster images that are approximately piecewise-smooth, using triangle-mesh models.

The SEMMG method, which was proposed for solving the mesh-generation problem, was developed by analyzing and modifying two existing schemes for generating ERD triangle-mesh models, namely, the ERDED and ERDGPI methods. Through this analysis, potential areas for improvement in different steps of the methods were identified. Then, different techniques were developed to select more effective parameters for the ERD model, by applying several key modifications. Finally, all the modifications were integrated into a unified framework to yield the new SEMMG method. For evaluating the SEMMG method, it was compared with eight competing methods. Through experimental results, we demonstrated that the reconstructed images obtained by the SEMMG method have higher quality than those obtained by the competing methods, in terms of PSNR. Moreover, in the case of the competing methods whose implementations are available, the subjective quality was compared in addition to the PSNR. Evaluation results showed that the reconstructed images obtained from the SEMMG method are better than those obtained by the competing methods in terms of both PSNR and subjective quality. More specifically, in cases where an implementation of the competing method was available, our experimental results collected from 350 test cases show that the SEMMG method outperforms the ED, MGH, ERDED, and ERDGPI schemes in approximately 100%, 89%, 99%, and 85% of cases, respectively. Furthermore, in the case of the methods without implementations, the results that are reported in their publications were used for comparison. Through this comparison, we showed that the PSNR of the reconstructed images produced by the SEMMG method are on average 3.85, 0.75, 2.00, and 1.10 dB higher than those obtained by the GVS, HWT, BSP, and ATM methods, as reported in their publications, respectively. Moreover, for a given PSNR, the SEMMG method was shown to produce much smaller meshes compared to those obtained by the GVS and BSP methods, with approximately 65% to 80% fewer vertices and 10% to 60% fewer triangles, respectively. The better performance of the SEMMG method is due to employing the advantageous ERD mesh model and, more importantly, effective techniques used to select parameters of the model. More specifically, with the Otsu threshold-selection approach, a more useful set of edge constraints is found. Furthermore, the optimization-based technique selects more effective wedge values for the ERD model. Moreover, the centroid-based approach selects more accurate set of sample points, by reducing the chance of selecting noisy pixels. Finally, with the help of the ERD model, image discontinuities can be explicitly represented in the mesh using fewer sample points. Therefore, as our experimental results show, the SEMMG method is capable of producing triangular meshes of higher quality and smaller sizes (i.e., number of vertices or triangles) which can be effectively used for image representation.

For addressing the image-scaling problem, the MIS method was proposed which produces scaled images of higher subjective quality with minimal edge blurring. The MIS method was developed based on triangle-mesh modeling techniques. For evaluating the MIS method, it was compared with five well-known raster-based image-scaling approaches called bilinear, bicubic, DCCI, NEDI, and SRCNN, using a subjective evaluation followed by objective evaluations. The results of the subjective evaluation show that the proposed MIS method was ranked best overall in almost 67% of the cases, with the best average rank of 2 out of 6, among 380 collected rankings with 20 images and 19 participants. Moreover, visual inspections on the scaled images obtained with different methods show that the proposed MIS method produces scaled images of better quality with more accurate and sharper edges. Furthermore, in the case of two other mesh-based scaling methods, named SBIR and CFDIR, where an experimental comparison was impractical, a conceptual comparison was made between the MIS method and them. The comparison showed that, unlike the SBIR and CFDIR methods, where either a continuous approximating function or a mesh-simplification approach is used, the MIS method employs both a mesh-refinement technique and an approximating function that allows for selected discontinuities. Therefore, the MIS method is capable of producing sharper scaled images with smaller meshes and potentially lower memory cost. The better performance of the proposed MIS method observed in our subjective evaluation is, first, because of employing the ERD model, which can explicitly represent discontinuities in the image, resulting in a great reduction in the blurring artifacts. Second, and more importantly, with the help an improved mesh generator, an ERD mesh model with the parameters that are effectively selected for image scaling is generated. In particular, the backfilling-based technique used in the MIs method selects a more effective set of wedge values for the ERD model. Moreover, the modified centroid-based approach selects a more useful set of sample points, resulting in distortion-free edges. Furthermore, the proposed APS method effectively selects the set of edge constraints to preserve curvatures of the edge contours in the scaled image. Finally, using a subdivision-based model rasterization, the MIS method produces scaled images with edge contours and image functions that are sufficiently smooth. Therefore, as our experimental comparisons show, the MIS method is capable of producing scaled images with overall higher subjective quality, with more accurate and sharper edges, than some well-known methods that are often used for image scaling. Aside from the improvements in subjective quality of the scaled images, the MIS method allows for other practical functionalities that may not easily (or ever) provided by state-of-the-art raster-based methods. For example, most of the image scaling methods based on deep learning are guaranteed to work well with the only specific scale factor for which they are trained. Using the MIS method, however, the image mesh model that is generated in the first stage of the method works well with almost any scaling factor of interest to produce the high-resolution image. Moreover, the same image model can be stored by its own and reused anytime later for other purposes like image editing or any combination of affine transformations (other than just scaling), such as translation, rotation, and shearing. Such flexible functionalities of the MIS method, which allow for image models that are portable, editable, and reusable, when combined with the improvements it makes in the subjective quality of the scaled images, makes the MIS method very practical and beneficial to many image processing applications.

7.2 Future Work

In this thesis, triangle-mesh models of images, their generation, and their application in image scaling were studied, which lead to the proposal of a new mesh-generation method and a mesh-based image-scaling method. Throughout this work, various aspects of generating mesh models that are effective for image representation and image scaling were analyzed and new methods were proposed to improve the quality of the meshes and scaled images. Although our proposed mesh-generation and image-scaling methods work fairly well, further research on certain areas may still be potentially beneficial. In what follows, these areas are briefly described.

As discussed earlier, in our proposed mesh-generation methods, which employ image edge information, edge detection is a crucial step to find the constrained edges for the ERD mesh model. Therefore, the consistency and accuracy of the detected edges are critically important in selecting more effective edge constraints. In our methods, to keep the computational complexity lower, a Canny edge detector (with one-pixel accuracy) is employed, which was shown to work well with images with today's typical resolutions. Our experiments on different test images, however, showed that in case of the smaller images, an edge localization with only one-pixel accuracy is not good enough. As a future work, one might consider employing a more advanced edge detector to detect edges with subpixel accuracy, if input images with very low resolutions are considered. In this case, using a more accurate edge detector could be quite beneficial to image representation, and also to image scaling, by selecting more accurate set of edge constraints.

Another important aspect of our proposed methods is the selection of wedge values for an ERD model. As mentioned earlier, wedge values are one of the most significant parameters of an ERD model. In this work, two different techniques for computing the wedge values were introduced, for generating mesh models that are effective for image representation and image scaling. For example, in our optimization-based technique, first, corner z-values associated with the corners inside the wedge are optimized and then the wedge value is computed as the weighted average of them. Although the weighted averaging reduces the negative effects of the less-reliable corner z-values, they still can affect the final computed wedge value. Therefore, another future work could be finding a more effective way to select the wedge values. For example, using a technique which directly optimizes the wedge values themselves may be more beneficial, instead of optimizing the corner z-values and averaging them.

Another potential area for future work is to find a better way to employ mesh subdivision for image scaling. In our proposed method of image scaling, the mesh subdivision is applied as a post-processing step after the mesh is completely generated. Although, in the process of the polyline simplification, the effect of subdivision on each polyline is considered, the effect of subdivision on other parts of the mesh, such as faces, is not taken into account. Thus, as a future research, one might consider embedding the mesh subdivision into the mesh generation, instead of applying it only after the mesh is generated. This may potentially increase the mesh quality for the following two reasons. Firstly, by applying the mesh subdivision in each iteration of the mesh generation process, the candidate face for point insertion can be selected as the face that, if it were subdivided, it would still have the highest squared error. This procedure efficiently insert points into the faces that after subdivision still have the highest squared error, not before the subdivision. Secondly, in our proposed method of image scaling, because the subdivision is applied after the mesh generation, the wedge values associated with the new vertices produced by subdivision are computed based on specific rules dictated by the subdivision scheme. The actual image function, however, may not necessarily follow the pattern of the subdivision scheme. Thus, applying subdivision at the time of mesh generation would allow us to select the new wedge values produced by subdivision based on the actual image function (not just based on subdivision rules), using techniques such as the optimization-based or backfilling-based approaches.

Another potential future work would be to extend the proposed SEMMG and MIS methods for color images. Since the experimental results showed that our methods perform well in the case of the grayscale images, one potential future work would be to extend these methods to work with color images too. Although such an extension may sound trivial, some aspects need to be considered more carefully. For example, the most trivial way would be to generate an ERD mesh model with the same triangulation for all color channels in the image. For this purpose, the intensity value at each vertex in the mesh is simply extended from a single grayscale value of z to a 3-tuple of (r, g, b), to represent the intensity values of Red, Green, and Blue channels in the image. Also, the face squared errors that are required during the mesh generation for point insertion, can be easily computed based on the new 3-tuples. Consequently, an image model is achieved where the same triangulation will be used for all three color channels. In this approach, a single edge map that has to reflect the image edges from all color channels should have also been obtained to start. More effective approach to model a color image, however, would be to construct an image model that has a separate triangulation for each color channel. This is mainly due to the fact that the face with highest squared error with respect to one color channel (e.g., red) may not necessarily be the same as the face with highest squared error with respect to another color channel (e.g., blue). Therefore, a different face must be selected with respect to each color channel for point insertion, leading to the insertion of different points too. Consequently, such process may result in an image model where a different triangulation is used per each color channel. In this approach, a separate edge map per each color channel should also be obtained which may be more reasonable than merging all edges in one edge map.

Another potential future work would be to develop a more effective means of measuring the sharpness of the scaled images. The PEE metric, which was used herein for measuring the sharpness of the scaled images, is blind to the location of the edges in the ground-truth and scaled images. As a result, based on the PEE definition in Section 2.11.3, a scaled image can have a lower PEE value (i.e., sharper edges) but contain edges that are placed in different locations than the edges in the ground-truth image. Consequently, the PEE metric, as defined in Section 2.11.3, cannot be alone considered if it is not accompanied by a proper subjective evaluation or other objective metrics such as PSNR and SSIM. Therefore, developing a modified PEE metric that considers the location of the edges in the ground-truth and scaled images as well as the sharpness of edges would be potentially beneficial.

Last, but not least, another potential future work would be to employ a more detailed statistical analysis to compare the scaling methods based on the collected ranks in the subjective evaluation. One potential approach would be to use a t-test [81], which is a type of inferential statistic often employed to determine if the means of two groups differ significantly. The t-test is mostly used when the datasets follow a normal distribution. Using the t-statistic, t-distribution values, and degrees of freedom, a t-test determines the probability of difference between two groups of datasets. For our purpose, a t-test could be performed on the ranks of any pair of scaling methods for which the means are presented in Table 6.1 to determine how likely the difference between the means occurred by chance, or whether the datasets really have intrinsic differences.

Appendix A

Test Images For Mesh Generation

The test images used for different purposes in Chapters 2 to 5 of this thesis are summarized in Table A.1. In this table, for each test image, the name and resolution of the image are given. All the test images in Table A.1 are grayscale and have the bit-depth of 8 bits/pixel, except `ct` image which has 12 bits/pixel. Also, thumbnails of all the images in Table A.1 are given in Figure A.1.

Table A.1: List of the test images used in Chapters 2 to 5 of this thesis

Image	Size	Image	Size
lena	512 × 512	bull	1024 × 768
peppers	512 × 512	bowling	1200 × 1400
wheel	512 × 512	pepper	2200 × 1800
ct	512 × 512	cherry	1920 × 1920
elaine	512 × 512	fruits	2560 × 1980
teddy	450 × 375	doll	3000 × 3000
house	256 × 256	pig2	3000 × 3000

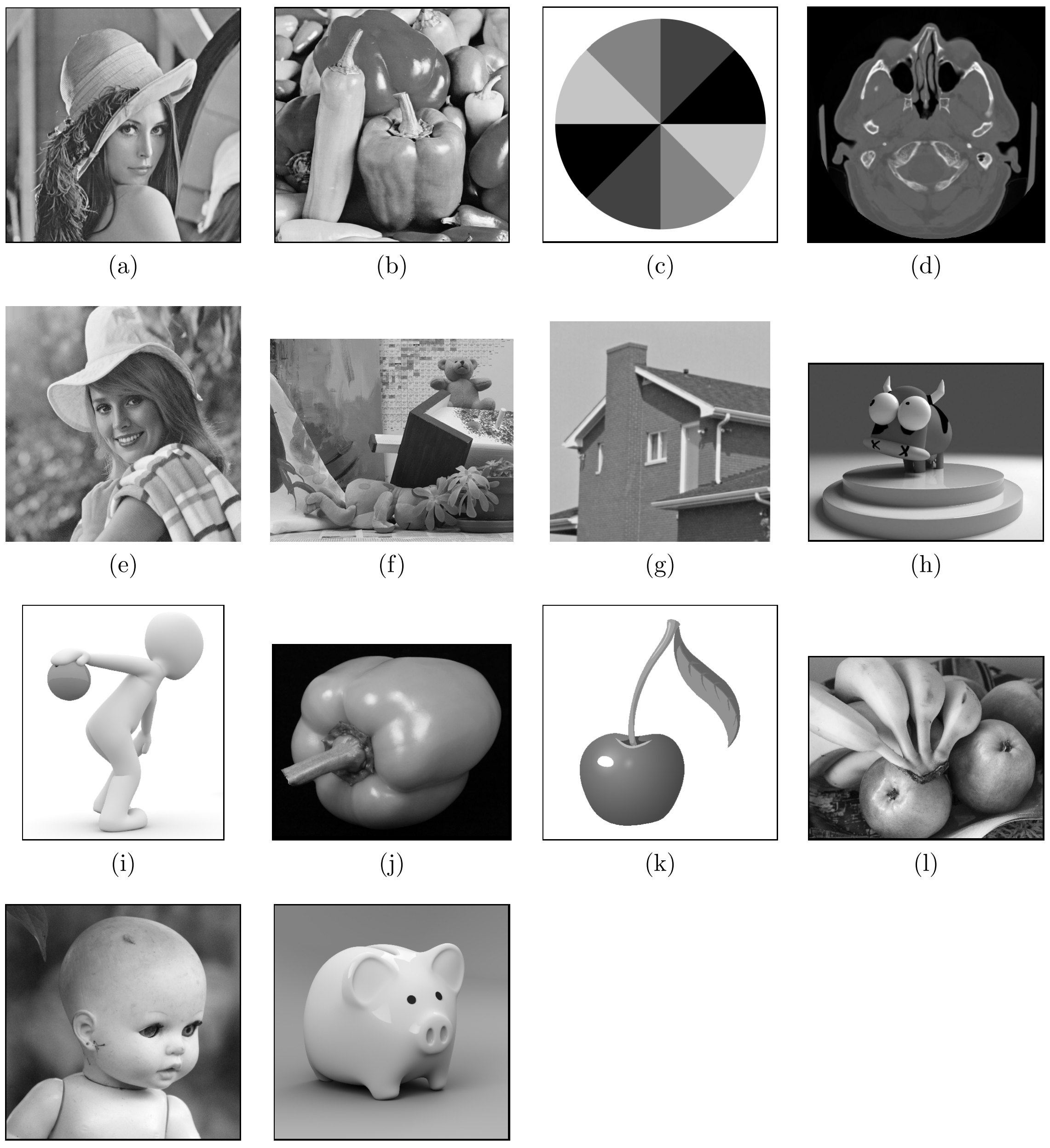

Figure A.1: Thumbnails of the test images used in Chapters 2 to 5 of this thesis. The (a) lena, (b) peppers, (c) wheel, (d) ct, (e) elaine, (f) teddy, (g) house, (h) bull, (i) bowling, (j) pepper, (k) cherry, (l) fruits, (m) doll, and (n) pig2 images.

Appendix B

Test Images For Image Scaling

For evaluating the MIS method proposed in this thesis, 20 test images were used. These 20 test images are summarized in Table B.1. In this table, for each test image, the name and resolution of the image are given. All the test images in Table B.1 are grayscale and 8 bits/pixel. Also, thumbnails of all the images in Table B.1 are given in Figures B.1 and B.2.

Table B.1: List of the 20 test images used for evaluating the MIS method in Chapter 6.

Image	Size	Image	Size
frangipani	1500 × 1000	bird	1240 × 975
dahlia	1105 × 890	fish	1500 × 950
balloons	1250 × 830	monster	1125 × 1200
rose	1500 × 1000	owl	1250 × 1050
candle	1425 × 935	potato	875 × 950
pig1	750 × 750	rooster	1325 × 1000
pig2	750 × 750	shadow1	1250 × 1000
dragon	625 × 800	shadow2	1250 × 1150
ammo	690 × 540	shadow3	1500 × 1000
apple	750 × 750	shadow4	1500 × 1000

(a)

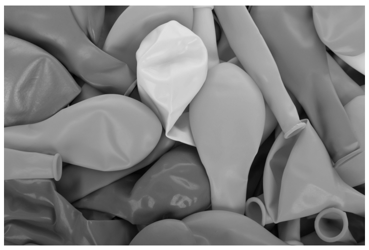
(b)

(c)

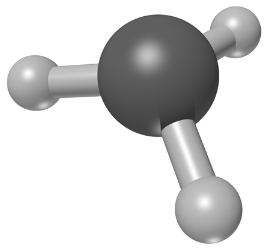
(d)

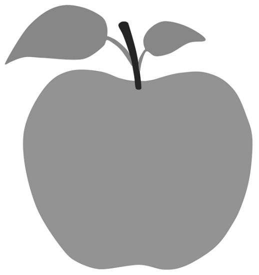
(e)

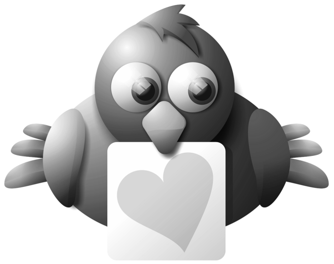
(f)

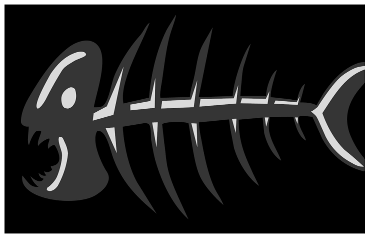
(g)

(h)

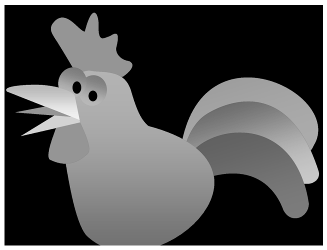
(i)

(j)

(k)

(l)

Figure B.1: Thumbnails of the test images used for evaluating the MIS method in Chapter 6 (Part 1 of 2). The (a) frangipani, (b) balloons, (c) dragon, (d) ammo, (e) apple, (f) bird, (g) fish, (h) monster, (i) rooster, (j) pig1, (k) pig2, and (l) candle images.

(a)

(b)

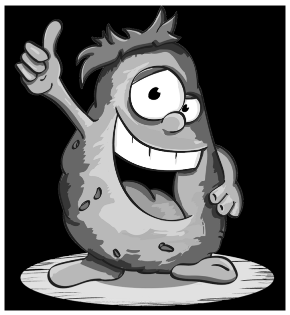
(c)

(d)

(e)

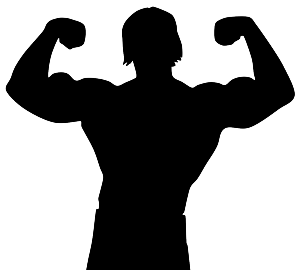
(f)

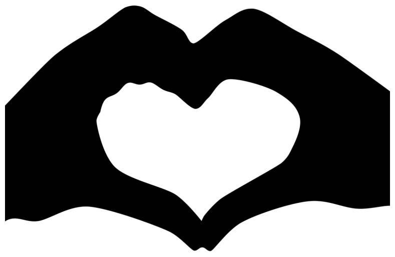
(g)

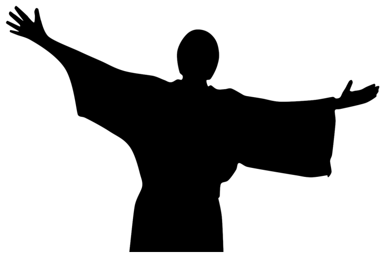
(h)

Figure B.2: Thumbnails of the test images used for evaluating the MIS method in Chapter 6 (Part 2 of 2). The (a) dahlia, (b) owl, (c) potato, (d) rose, (e) shadow1, (f) shadow2, (g) shadow3, and (h) shadow4 images.

Appendix C

Supplementary Experimental Results

The full set of 350 test cases collected for comparing the proposed SEMMG method with the ED, MGH, ERDED, and ERDGPI methods is presented in Tables C.1 to C.7.

Table C.1: Comparison of the mesh quality obtained with the ED, MGH, ERDED, ERDGPI, and SEMMG methods.

			PSNR (dB)				
Images	Size	Sampling Density (%)	ED	MGH	ERDED	ERDGPI	SEMMG
lena	512 x 512	0.0078125	14.08	12.25	14.16	12.84	14.94
		0.015625	13.93	13.40	13.17	12.41	16.18
		0.03125	14.01	14.76	12.97	14.40	17.22
		0.0625	12.81	16.60	15.27	17.47	18.43
		0.125	13.78	19.01	15.89	19.59	20.43
		0.25	14.49	21.66	17.96	22.77	23.08
		0.5	17.17	24.25	20.55	25.58	25.75
		1	21.13	26.87	25.81	28.35	28.29
		2	25.83	29.75	29.28	30.80	30.39
		3	28.06	31.33	31.31	32.31	31.54
peppers	512 x 512	0.0078125	10.63	11.13	11.12	10.61	12.01
		0.015625	10.61	12.69	11.13	11.39	13.13
		0.03125	10.67	13.93	11.22	13.24	14.63
		0.0625	9.93	15.42	14.28	16.22	16.48
		0.125	11.71	18.47	15.76	19.28	19.39
		0.25	13.88	21.39	17.66	22.81	23.00
		0.5	16.03	24.68	22.14	25.99	26.30
		1	21.35	27.52	25.97	28.40	28.67
		2	26.09	29.85	29.00	30.42	30.49
		3	28.17	31.13	30.17	31.50	31.47
bull	1024 x 768	0.0078125	13.51	15.72	15.14	16.57	16.02
		0.015625	11.85	18.59	15.12	18.25	18.65
		0.03125	10.11	21.22	14.89	22.64	21.79
		0.0625	15.57	25.83	15.52	29.25	29.49
		0.125	15.54	30.74	24.68	35.47	34.10
		0.25	20.59	35.29	28.86	38.33	35.91
		0.5	25.89	38.76	35.15	40.17	38.47
		1	33.34	41.07	39.02	41.39	41.04
		2	37.56	43.07	40.55	42.55	43.43
		3	40.36	44.54	41.05	43.35	44.80
maple_low	1000 x 1000	0.0078125	11.09	17.29	13.53	15.82	19.82
		0.015625	13.40	18.85	13.52	18.40	22.19
		0.03125	13.96	20.89	16.18	21.40	24.63
		0.0625	13.40	23.43	20.51	24.20	27.26
		0.125	15.66	25.57	25.19	26.19	28.61
		0.25	17.50	27.89	27.55	28.47	30.14
		0.5	17.95	30.17	29.26	30.67	31.53
		1	24.50	32.61	31.43	33.09	33.03
		2	32.11	35.11	32.95	35.46	34.83
		3	34.14	36.66	33.37	36.92	36.10
face3	1200 x 1200	0.0078125	8.81	18.76	11.46	18.68	18.06
		0.015625	8.55	20.25	12.87	20.25	20.29
		0.03125	10.68	22.26	14.80	22.13	23.14
		0.0625	14.84	24.39	15.18	23.69	24.95
		0.125	17.91	25.91	22.59	26.45	27.83
		0.25	20.45	27.59	24.51	28.41	29.53
		0.5	23.80	29.31	27.95	30.48	31.65
		1	26.84	31.57	31.17	32.95	33.63
		2	30.68	34.39	33.74	35.30	35.23
		3	32.84	36.26	35.30	37.00	36.26

Table C.2: Comparison of the mesh quality obtained with the ED, MGH, ERDED, ERDGPI, and SEMMG methods.

			PSNR (dB)				
Images	Size	Sampling Density (%)	ED	MGH	ERDED	ERDGPI	SEMMG
bowling	1200 x 1400	0.0078125	16.27	22.84	19.70	23.68	27.27
		0.015625	16.28	26.64	21.29	33.51	33.63
		0.03125	16.96	32.16	26.95	38.70	38.86
		0.0625	16.34	37.89	33.89	42.09	41.45
		0.125	22.47	43.21	36.35	45.24	43.26
		0.25	26.76	47.07	38.71	47.22	46.01
		0.5	31.70	49.96	44.06	48.54	49.29
		1	32.91	52.50	45.36	48.94	52.45
		2	41.29	55.08	46.44	48.85	55.47
		3	45.08	56.86	46.76	49.56	57.26
puppet1	1980 x 1320	0.0078125	14.25	22.89	15.83	22.81	23.94
		0.015625	15.94	26.28	18.66	24.44	27.57
		0.03125	17.45	29.68	20.05	28.89	32.56
		0.0625	18.89	31.83	23.54	31.56	35.10
		0.125	23.92	33.49	30.53	33.24	36.94
		0.25	26.88	34.75	34.51	34.93	37.94
		0.5	29.80	35.92	36.85	36.06	38.89
		1	35.39	37.07	38.06	37.06	39.68
		2	37.91	38.44	38.58	38.58	40.44
		3	38.86	39.36	38.94	39.52	40.92
bird	1940 x 1430	0.0078125	10.64	26.55	13.98	24.91	27.14
		0.015625	13.67	28.24	17.10	27.64	30.12
		0.03125	17.05	30.42	20.91	29.91	33.64
		0.0625	21.17	32.07	24.78	31.42	35.63
		0.125	23.83	33.26	30.59	33.12	36.79
		0.25	27.05	34.17	34.09	34.04	37.64
		0.5	32.34	35.06	36.50	35.14	38.22
		1	35.78	36.04	37.48	36.20	38.70
		2	37.25	37.18	38.29	37.71	39.16
		3	37.85	37.98	38.78	38.47	39.49
veggie	1920 x 1469	0.0078125	10.08	21.04	13.30	21.13	21.47
		0.015625	14.87	24.54	17.75	23.85	25.33
		0.03125	16.10	27.44	19.57	27.91	29.49
		0.0625	15.82	30.05	21.33	30.91	32.39
		0.125	16.77	32.49	27.65	33.43	34.73
		0.25	24.52	34.86	33.00	36.04	36.63
		0.5	20.68	37.48	36.04	38.10	38.08
		1	24.13	40.06	38.74	40.01	39.99
		2	36.12	42.92	40.54	42.30	42.36
		3	40.55	44.73	41.32	43.39	44.00
girl1	1860 x 1860	0.0078125	9.58	20.08	8.04	20.97	21.53
		0.015625	9.69	22.95	10.89	21.97	23.83
		0.03125	12.23	25.30	16.87	25.35	26.59
		0.0625	13.46	27.09	20.78	27.01	28.96
		0.125	16.45	28.69	23.86	28.83	30.66
		0.25	20.20	30.51	26.37	31.13	32.63
		0.5	25.08	32.60	29.43	33.38	34.57
		1	30.06	35.17	31.82	35.87	36.27
		2	34.60	38.14	34.65	38.31	38.12
		3	36.94	40.08	37.54	39.96	39.40

Table C.3: Comparison of the mesh quality obtained with the ED, MGH, ERDED, ERDGPI, and SEMMG methods.

			PSNR (dB)				
Images	Size	Sampling Density (%)	ED	MGH	ERDED	ERDGPI	SEMMG
cherry	1920 x 1920	0.0078125	11.76	16.31	11.91	17.01	34.52
		0.015625	13.28	17.56	12.10	19.20	37.77
		0.03125	13.39	28.10	26.89	31.59	38.78
		0.0625	13.92	37.56	41.32	43.47	39.87
		0.125	29.24	43.57	41.87	44.46	42.25
		0.25	23.07	55.71	41.71	44.28	49.52
		0.5	37.16	61.18	42.99	44.75	57.89
		1	39.69	65.10	43.35	44.94	63.05
		2	47.48	70.75	43.37	44.95	67.47
		3	53.57	inf	43.36	44.94	69.67
pepper	2200 x 1800	0.0078125	8.23	27.88	11.68	28.00	28.52
		0.015625	13.41	30.99	13.36	29.52	31.53
		0.03125	17.85	32.86	18.06	32.54	33.49
		0.0625	22.10	35.26	27.10	34.76	36.33
		0.125	25.77	36.57	31.67	36.49	39.32
		0.25	31.91	37.77	34.34	37.57	40.70
		0.5	37.34	39.00	36.99	38.80	41.77
		1	39.73	40.25	40.13	40.42	42.61
		2	41.36	41.64	41.41	41.55	43.45
		3	42.15	42.55	40.71	42.66	44.01
fruits	2560 x 1980	0.0078125	12.11	20.35	11.56	20.18	20.59
		0.015625	13.21	22.31	11.71	20.75	21.72
		0.03125	16.26	24.21	13.63	23.57	24.62
		0.0625	18.47	26.15	22.79	25.81	27.59
		0.125	21.07	27.69	25.45	27.33	29.67
		0.25	23.95	28.80	27.85	28.58	31.14
		0.5	27.00	29.83	29.52	29.71	32.67
		1	29.99	30.83	31.80	31.03	33.42
		2	31.81	31.88	32.78	32.29	33.99
		3	32.57	32.57	33.11	33.06	34.32
rose	3000 x 2250	0.0078125	12.21	22.76	15.30	23.07	24.07
		0.015625	13.41	27.22	17.50	28.14	27.31
		0.03125	13.17	31.27	19.96	33.05	32.17
		0.0625	14.64	35.48	27.93	36.94	36.74
		0.125	22.12	39.07	32.26	39.38	39.52
		0.25	30.32	42.99	36.76	42.40	42.26
		0.5	37.86	45.29	39.88	44.95	45.14
		1	42.54	47.35	41.39	45.95	47.75
		2	46.61	49.45	43.61	47.28	49.99
		3	48.23	50.76	44.15	47.82	51.17
doll	3000 x 3000	0.0078125	13.60	26.50	14.80	25.13	26.30
		0.015625	16.57	27.93	16.77	27.57	28.92
		0.03125	16.64	29.11	25.24	28.96	32.71
		0.0625	20.25	30.17	28.64	29.51	34.47
		0.125	23.78	31.22	31.44	30.92	36.07
		0.25	28.43	32.33	34.08	32.19	37.11
		0.5	33.33	33.50	35.40	33.47	37.66
		1	35.22	34.87	36.55	35.11	38.11
		2	36.46	36.50	37.61	36.81	38.68
		3	37.27	37.63	38.10	37.93	39.15

Table C.4: Comparison of the mesh quality obtained with the ED, MGH, ERDED, ERDGPI, and SEMMG methods.

			PSNR (dB)				
Images	Size	Sampling Density (%)	ED	MGH	ERDED	ERDGPI	SEMMG
dahlia	4420 x 3560	0.0078125	14.74	15.15	9.38	15.55	19.50
		0.015625	14.68	18.23	12.32	17.68	22.01
		0.03125	15.10	20.41	17.24	20.11	24.97
		0.0625	16.48	22.14	20.88	22.08	27.01
		0.125	17.87	23.40	23.83	23.79	28.19
		0.25	20.35	24.44	26.33	24.88	28.70
		0.5	23.37	25.42	27.72	25.78	29.10
		1	25.65	26.41	28.48	26.77	29.48
		2	27.20	27.48	28.98	27.96	29.86
		3	28.07	28.21	29.26	28.72	30.13
puppet2	3456 x 4608	0.0078125	19.01	30.37	16.42	28.67	28.92
		0.015625	20.42	33.00	23.85	32.58	32.41
		0.03125	23.29	34.62	28.19	34.13	35.57
		0.0625	26.42	35.87	30.44	35.02	38.50
		0.125	29.88	36.81	35.66	36.69	40.82
		0.25	33.76	37.70	38.55	37.58	41.76
		0.5	38.49	38.65	40.24	38.58	42.26
		1	40.25	39.74	40.84	39.91	42.69
		2	41.21	40.99	41.49	41.38	43.17
		3	41.74	41.85	41.85	42.24	43.52
pig1	3000 x 3000	0.0078125	14.76	27.75	14.14	25.42	25.59
		0.015625	16.86	31.69	16.52	29.08	29.91
		0.03125	20.26	34.95	22.85	34.13	33.66
		0.0625	23.30	36.82	26.04	36.34	38.69
		0.125	26.72	38.07	30.43	37.72	40.91
		0.25	31.05	38.98	34.46	38.69	42.09
		0.5	37.13	39.80	38.46	39.62	42.75
		1	40.72	40.68	40.81	40.89	43.16
		2	42.00	41.73	41.81	42.15	43.60
		3	42.42	42.50	41.94	42.76	43.95
pig2	3000 x 3000	0.0078125	17.35	38.48	18.22	36.54	37.56
		0.015625	16.43	42.44	19.31	39.33	42.22
		0.03125	23.05	44.71	30.93	44.03	46.22
		0.0625	27.65	46.08	37.36	45.92	48.78
		0.125	35.42	47.02	42.89	46.98	50.32
		0.25	42.86	47.97	45.52	47.53	51.19
		0.5	47.22	49.08	48.16	49.04	51.70
		1	49.43	50.34	48.29	49.27	52.16
		2	50.39	51.83	49.37	51.40	52.74
		3	50.84	52.86	49.70	52.12	53.18
frangipani	6000 x 4000	0.0078125	11.98	34.70	13.23	32.54	31.62
		0.015625	14.73	36.92	17.05	34.78	35.11
		0.03125	16.00	38.99	19.28	38.41	39.66
		0.0625	16.87	40.69	23.01	40.05	42.29
		0.125	17.91	42.27	25.39	41.65	44.18
		0.25	20.52	43.68	28.76	43.14	45.67
		0.5	26.29	45.01	35.85	44.48	46.86
		1	31.03	46.38	43.06	46.45	47.85
		2	44.87	48.05	45.17	48.11	48.90
		3	45.78	49.36	45.76	49.17	49.69

Table C.5: Comparison of the mesh quality obtained with the ED, MGH, ERDED, ERDGPI, and SEMMG methods.

			PSNR (dB)				
Images	Size	Sampling Density (%)	ED	MGH	ERDED	ERDGPI	SEMMG
cartoon	1600 x 1200	0.0078125	14.16	19.59	17.73	21.25	19.82
		0.015625	11.75	22.54	20.22	27.85	25.16
		0.03125	14.67	29.40	21.24	32.88	31.52
		0.0625	14.79	34.27	23.94	36.35	35.58
		0.125	18.94	37.09	28.44	37.66	37.91
		0.25	27.22	39.22	34.69	39.09	39.92
		0.5	33.32	41.14	37.30	40.70	41.76
		1	37.64	43.18	37.57	42.03	43.69
		2	41.80	45.54	40.63	43.96	45.68
		3	43.45	47.23	41.11	44.70	47.14
kodim03	768 x 512	0.0078125	11.94	14.55	16.24	15.10	16.29
		0.015625	11.94	16.47	16.24	15.77	17.51
		0.03125	12.20	18.28	18.08	20.12	20.19
		0.0625	13.54	20.23	18.40	21.93	22.09
		0.125	14.94	22.37	20.45	23.98	24.66
		0.25	17.74	24.58	22.99	26.50	27.78
		0.5	20.45	26.65	26.96	28.17	29.29
		1	23.70	28.83	28.96	30.11	30.66
		2	28.01	31.14	31.32	32.53	31.82
		3	29.30	32.79	32.60	33.71	32.74
kodim09	512 x 768	0.0078125	10.96	11.95	10.76	11.50	14.88
		0.015625	10.97	12.68	10.98	14.60	16.78
		0.03125	10.61	16.16	10.63	16.16	18.02
		0.0625	11.53	18.00	14.75	19.64	20.40
		0.125	15.16	19.78	17.71	22.01	23.02
		0.25	16.96	22.02	21.45	24.01	25.70
		0.5	19.09	24.53	24.02	25.67	27.42
		1	22.71	26.92	26.58	28.42	28.80
		2	25.77	29.55	29.73	30.99	30.18
		3	27.54	31.18	31.15	32.34	31.32
kodim11	768 x 512	0.0078125	11.33	12.14	15.26	11.60	14.22
		0.015625	11.33	13.51	15.26	13.24	16.76
		0.03125	11.33	14.32	15.26	14.74	17.92
		0.0625	11.46	16.24	15.92	16.86	19.07
		0.125	12.02	17.24	18.24	18.75	20.92
		0.25	14.00	18.79	19.61	20.43	22.40
		0.5	16.18	20.71	21.56	22.38	24.21
		1	18.58	22.71	23.46	24.32	25.63
		2	21.99	24.86	25.82	26.28	26.97
		3	23.74	26.26	27.07	27.67	27.65
kodim15	768 x 512	0.0078125	7.62	11.85	10.33	12.87	13.72
		0.015625	7.62	13.73	11.77	15.25	16.50
		0.03125	7.99	16.46	11.46	17.25	18.45
		0.0625	8.76	18.88	14.26	20.02	21.91
		0.125	11.40	21.79	18.90	22.62	23.86
		0.25	14.62	23.98	21.09	24.42	25.97
		0.5	18.36	25.81	24.67	26.15	27.76
		1	23.25	27.35	26.36	27.81	29.02
		2	26.24	29.38	29.10	29.88	30.42
		3	27.66	30.69	29.97	31.14	31.25

Table C.6: Comparison of the mesh quality obtained with the ED, MGH, ERDED, ERDGPI, and SEMMG methods.

			PSNR (dB)				
Images	Size	Sampling Density (%)	ED	MGH	ERDED	ERDGPI	SEMMG
kodim17	512 x 768	0.0078125	13.65	12.26	13.72	13.31	15.48
		0.015625	13.65	14.08	13.72	13.79	15.88
		0.03125	12.98	15.67	14.38	16.63	17.77
		0.0625	12.37	17.38	17.50	17.57	19.40
		0.125	14.25	18.87	18.36	20.08	21.32
		0.25	16.08	20.90	20.34	22.28	23.43
		0.5	18.03	22.80	22.52	24.39	25.58
		1	21.13	25.40	25.38	27.01	27.81
		2	24.54	28.37	28.15	29.73	29.81
		3	26.92	30.20	29.61	31.36	30.90
kodim19	512 x 768	0.0078125	13.76	12.24	12.93	12.85	16.12
		0.015625	13.75	13.58	14.91	14.29	17.01
		0.03125	15.99	14.75	14.99	14.49	17.36
		0.0625	14.85	16.27	14.71	16.93	18.89
		0.125	14.13	17.32	16.59	18.39	20.47
		0.25	15.97	18.46	19.76	20.39	21.98
		0.5	17.27	19.76	21.86	22.11	23.84
		1	18.43	21.39	23.80	24.50	25.41
		2	21.36	23.80	26.27	26.80	26.52
		3	22.99	25.50	27.11	28.12	27.37
kodim20	768 x 512	0.0078125	6.02	12.69	9.89	12.25	13.53
		0.015625	5.89	14.28	9.89	13.68	16.01
		0.03125	6.09	15.81	7.26	17.07	18.04
		0.0625	9.77	17.83	7.82	19.16	20.16
		0.125	11.31	20.34	10.43	21.63	22.35
		0.25	16.04	22.38	17.32	24.30	25.80
		0.5	18.46	24.59	24.32	26.33	27.58
		1	22.66	27.05	27.89	28.43	28.72
		2	26.11	29.63	29.49	30.40	30.42
		3	28.09	31.26	30.43	31.69	31.51
kodim04	768 x 512	0.0078125	13.12	11.67	15.17	14.01	14.54
		0.015625	13.14	15.57	14.33	15.97	17.36
		0.03125	13.08	17.43	14.35	16.48	18.96
		0.0625	15.09	19.66	16.57	19.23	20.66
		0.125	15.30	21.39	19.99	21.83	23.64
		0.25	18.10	23.27	22.06	24.10	25.31
		0.5	19.60	24.86	23.96	25.65	27.25
		1	22.11	26.66	25.92	27.61	28.79
		2	25.82	28.87	28.32	29.33	30.42
		3	27.65	30.31	29.58	30.76	31.22
kodim07	512 x 768	0.0078125	10.45	13.42	15.50	14.14	15.29
		0.015625	10.45	13.81	14.08	14.66	17.47
		0.03125	10.45	15.00	14.20	15.58	17.97
		0.0625	12.26	16.53	15.45	16.39	18.77
		0.125	13.28	18.10	15.88	19.03	20.48
		0.25	15.28	19.82	19.13	20.95	21.87
		0.5	16.80	21.52	21.17	22.99	24.34
		1	19.70	24.95	24.12	26.69	27.74
		2	23.84	29.14	27.68	30.83	29.95
		3	26.56	31.47	30.49	32.63	31.25

Table C.7: Comparison of the mesh quality obtained with the ED, MGH, ERDED, ERDGPI, and SEMMG methods.

			PSNR (dB)				
Image	Size	Sampling Density (%)	ED	MGH	ERDED	ERDGPI	SEMMG
kodim10	768 x 512	0.0078125	11.66	13.23	12.44	14.24	16.24
		0.015625	11.67	14.41	14.30	16.19	17.96
		0.03125	13.97	16.80	13.64	17.36	19.66
		0.0625	14.03	18.48	16.03	19.94	21.15
		0.125	16.15	20.22	19.84	21.71	22.96
		0.25	17.07	22.14	21.78	23.32	25.05
		0.5	19.47	23.98	24.13	25.66	27.09
		1	21.69	26.44	26.14	28.24	29.11
		2	25.13	29.28	29.21	30.95	30.60
		3	27.13	31.06	30.71	32.47	31.60
kodim12	512 x 768	0.0078125	6.23	14.42	7.39	13.99	12.66
		0.015625	6.23	16.02	8.03	16.74	17.12
		0.03125	6.23	18.36	8.05	18.66	19.62
		0.0625	9.47	19.96	14.00	21.84	22.14
		0.125	9.16	22.27	15.03	23.23	24.38
		0.25	13.31	24.11	22.45	25.23	27.28
		0.5	16.66	25.93	24.77	26.66	28.75
		1	22.66	27.76	27.30	28.49	29.69
		2	26.87	29.76	29.77	30.83	30.70
		3	28.04	31.08	30.67	31.97	31.51
kodim18	768 x 512	0.0078125	15.05	12.57	13.52	11.67	16.43
		0.015625	15.09	13.52	14.20	13.98	17.18
		0.03125	14.67	13.78	14.46	14.23	18.25
		0.0625	14.64	14.90	15.54	14.86	18.80
		0.125	15.73	15.90	17.39	15.92	19.71
		0.25	15.69	17.30	18.90	17.62	20.73
		0.5	17.16	18.70	19.99	19.14	21.72
		1	18.68	20.34	21.24	21.16	22.82
		2	20.64	22.37	23.03	23.34	24.29
		3	22.01	23.68	23.87	24.65	25.38
blonde	512 x 512	0.0078125	15.21	12.92	9.34	11.80	15.55
		0.015625	15.19	13.37	13.78	14.35	16.29
		0.03125	15.25	14.37	13.46	14.62	16.21
		0.0625	15.28	16.15	13.47	15.59	18.10
		0.125	14.99	18.42	15.16	18.86	19.59
		0.25	13.64	20.58	17.10	21.40	22.06
		0.5	17.50	22.74	21.54	24.09	24.74
		1	20.07	24.87	24.47	26.54	27.02
		2	23.70	26.82	26.91	28.32	28.51
		3	25.34	28.03	28.24	29.51	29.31
pirate	512 x 512	0.0078125	13.79	13.39	13.78	13.07	14.83
		0.015625	13.81	15.31	13.51	14.29	15.92
		0.03125	13.78	14.92	13.73	15.24	17.05
		0.0625	14.52	16.24	15.82	16.44	18.17
		0.125	14.92	17.61	17.31	18.42	19.46
		0.25	14.87	19.39	19.13	20.10	21.55
		0.5	16.30	21.16	20.29	22.39	23.75
		1	19.12	23.39	23.32	24.85	25.68
		2	22.23	25.86	25.66	27.04	27.57
		3	24.35	27.36	27.31	28.61	28.58

Appendix D

Software User Manual

D.1 Introduction

As part of the work presented in this thesis, a software implementation of the mesh-generation and image-scaling methods proposed herein was developed. The software was all implemented in C++ by the author of this thesis, with significant help from his supervisor, Dr. Michael Adams. The software implementation consists of over 14000 lines of code and involves quite complicated algorithms and data structures. For the implementation of this software, various C++ libraries were utilized, including the Computational Geometry Algorithms Library (CGAL) [6], the Open Source Computer Vision Library (OpenCV) [7], the Signal Processing Library (SPL) [8] and its extension library (SPLEL), and the Boost library [9].

The software implements all the methods proposed and developed in this thesis, including the SEMMG, MISMG, and MIS methods. Moreover, the software includes different image quality assessment measures used in this thesis, such as the PSNR, MSSIM, and PEE metrics. The software package contains the following four executable programs:

1. `mesh_generation`: generates an ERD mesh model using either the SEMMG or MISMG method from an input grayscale raster image.

2. `mesh_subdivision`: subdivides an input ERD mesh with a given number of subdivision levels.

3. `mesh_rasterization`: rasterizes an ERD model to a raster image with a given scaling factor $k > 1$.

4. `img_cmp`: computes the PSNR, MSSIM, or PEE image quality assessments metrics between two input images.

The remainder of this appendix provides details on how to build the software, followed by complete descriptions of each of the above programs. Also, specific examples are provided to illustrate how to use the software.

D.2 Building the Software

For the purpose of building the software, the Make tool is used. Since the programs in the software utilize several features from C++17 features, the compiler which is used needs to be compatible with C++17. As mentioned earlier, our software utilizes several libraries such as CGAL, SPL, SPLEL, OpenCV, and Boost. Therefore, before building the software, users need to ensure that these libraries are installed. The versions of the libraries used by the author and known to work are as below:

- CGAL version 4.2
- SPL version 2.0.3
- SPLEL version 2.0.5
- OpenCV version 3.0
- Boost version 1.53

In order to compile all of the source files and link the object files, one should set the directory to the top-level directory for the software, which contains the `Makefile` file, and run the following commands:

```
make clean
make
```

The command `make clean` is optional and deletes all the object files and executable files that may have been generated during the previous building process.

D.3 File Formats

As mentioned earlier, the inputs to the `mesh_generation` and `img_cmp` programs and the output of the `mesh_rasterization` program are grayscale raster images.

Moreover, the output of the `mesh_generation` program and input/output for the `mesh_subdivision` program is a ERD mesh model. Therefore, in total, two different file formats are required to represent: 1) grayscale images and 2) ERD mesh models. The format of grayscale images recognized by the software package herein is a specific type of the portable gray-map (PGM) format called the **plain PGM** format defined by the Netpbm project [10]. The plain PGM format used herein is associated with `.pnm` file extension. In what follows, the specifics of the other file format used for mesh models are explained.

The ERD mesh models that are generated and used by different programs of the software package herein have a special format associated with the "`.model`" extension. The `.model` format has been specially designed to contain different attributes of the mesh, such as the corner z-values and constrained edges. In general, the `.model` file has the following entries (in order):

```
WIDTH HEIGHT
MAX_VAL
NUM_VERTICES NUM_FACES NUM_CONSTRAINED_EDGES NUM_CORNERS
VERTICES_DATA
FACES_DATA
CONSTRAINED_EDGES_DATA
CORNERS_DATA
```

In the above format, the first entries are the width and height of the input image to which the model belongs. The next entry is the maximum graylevel that a pixel in the image can have (i.e., `MAX_VAL`$= 2^n - 1$, for a n-bit image). The next entries in the above format are the number of vertices, number of faces, number of constrained edges, and number of corners in the ERD mesh. In what follows, the other fields used in the `.model` format above, such as `VERTICES_DATA`, `FACES_DATA`, `CONSTRAINED_EDGES_DATA`, and `CORNERS_DATA`, are described.

The `VERTICES_DATA` field in the `.model` format holds the information of all the vertices in the mesh. In particular, for each vertex in the mesh, the following information is provided (in order) separated by whitespace: the x and y coordinates of the vertex and the gray value g of the original image at the point (x, y), followed by a newline character. Using this configuration, any vertex in the `.model` format, can be realized as a triplet of (x, y, g).

The `FACES_DATA` field in the `.model` format contains the information of all the

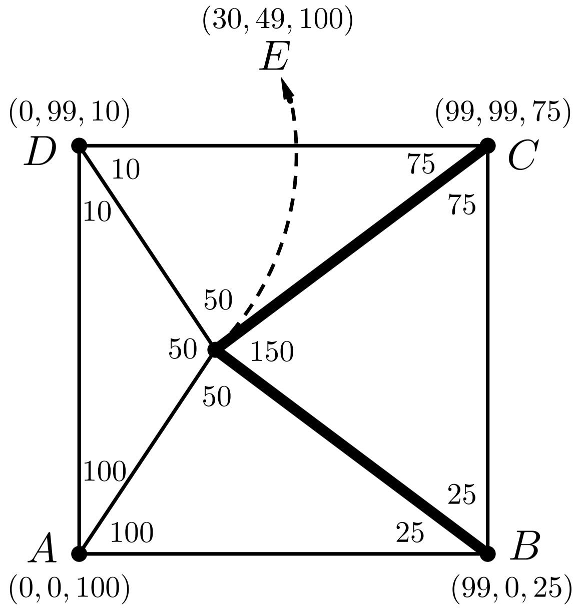

Figure D.1: An example of a ERD model, where constrained edges are denoted by thick lines and corner z values are written inside each triangle corner.

faces in the mesh. In particular, for each face in the mesh, the following information is given separated by whitespace: for each vertex in the face (in CCW order), the index of the vertex is given and the last (i.e., third) index is followed by a newline character. Note that vertices are indexed starting from zero.

The `CONSTRAINED_EDGES_DATA` field in the `.model` format contains the information of all the constrained edges in the mesh. In particular, for each constrained edge in the mesh, the indices of its two end vertices are given separated by whitespace and then followed by a newline character. The smaller index must be given first.

The `CORNERS_DATA` field in the `.model` format contains the information of all the (triangle) corners in the mesh. In particular, for each corner in the mesh, the following information is provided (in order) separated by whitespace: the index of the vertex to which the corner is incident, the index of the triangle face to which the corner belongs, and the corresponding corner z-value, followed by a newline character. Note that, like the vertices, the faces are also indexed from zero.

For the benefit of the reader, we provide an example illustrating the `.model` format. Suppose that we have an image with the width, height, and maximum value of 100, 100, and 255, respectively. Moreover, assume that the mesh model of the image is the one illustrated in Figure D.1. As this figure shows, the model is associated with a triangulation consisting of four triangles, namely $\triangle ABE$, $\triangle BCE$, $\triangle CDE$, and $\triangle DAE$, and two constrained edges $\overline{EB}$ and $\overline{EC}$. In the model shown in Figure D.1, vertices A, B, C, D, and E have xy-coordinates (0,0), (99,0), (99,99), (0,99), and (30,49), respectively. Furthermore, the gray values at A, B, C, D, and E are 100, 25, 75, 10, and 100, respectively. Also, the z-values associated with the face corners are the ones written inside each corner in Figure D.1. Therefore, the `.model` file of the above mesh model (shown in Figure D.1) is shown in Figure D.2.

D.4 Detailed Program Descriptions

In the following sections, a detailed description of the command line interface for each program is provided.

D.4.1 The `mesh_generation` Program

SYNOPSIS

```
mesh_generation [OPTIONS] < input_image
```

DESCRIPTION

This program reads a grayscale image of either PGM or plain PGM format (which is associated with `.pnm` extension) from standard input and generates the ERD mesh model with respect to the mesh-generation method and sampling density specified by the user. This program can write different types of data, such as the edge map, triangulation, polylines, and mesh model, to a file specified by the command line options. Any of the two mesh-generation methods used in this thesis, namely, the proposed SEMMG method and the MISMG method that is used by the MIS method can be selected through the options provided for this program. Although, in theory, either of these methods can be selected for mesh generation, the SEMMG method was mainly designed for the purpose of image representation where no image scaling is involved, whereas the MISMG method was primarily designed to be used for image scaling.

OPTIONS

`-d $samplDensity` Sets the mesh sampling density in percent to `$samplDensity`.

```
100 100
255
5 4 2 12

0 0 100
99 0 25
99 99 75
0 99 10
30 49 100

0 1 4
1 2 4
2 3 4
3 0 4

1 4
2 4

0 0 100
0 3 100
1 0 25
1 1 25
2 1 75
2 2 75
3 2 10
3 3 10
4 0 50
4 1 150
4 2 50
4 3 50
```

Figure D.2: The `.model` file of the mesh model shown in Figure D.1.

`-n $methodFlag`	Specifies the mesh-generation method to be used. In particular, if `$methodFlag` is set to 0 the SEMMG method and if it is set to 1 the MISMG method is selected.
`-b $modelFile`	Sets the output `.model` file name to `$modelFile` in which the generated mesh model is stored.
`-p $polyFile`	Sets the output polyline file name to `$polyFile` in which the generated set of polylines is stored in the format used by iviewer software.
`-t $triFile`	Sets the output triangulation file name to `$triFile` in which the triangulation data is stored in a format similar to the one used by the iviewer software. Note that, in the generated triangulation file, the entry of the number of edges must be deleted, before using the iviewer.
`-e $edgeFile`	Sets the name of the binary edge map obtained by the edge detector to `$edgeFile` in the plain PGM format.
`-s $edgeDetector`	Specifies the edge-detection method to be used. If `$edgeDetector` is set to `susan` the SUSAN method and if it is set to `canny` the Canny method is selected for generating edge maps. If this option is not specified, the default is the Canny method.
`-v $tol`	Specifies the tolerance parameter used in the DP polyline-simplification method to be `$tol`, which is a positive real number.

D.4.2 The `mesh_subdivision` Program

SYNOPSIS

```
mesh_subdivision [OPTIONS] < input_mesh
```

DESCRIPTION

This program reads an input ERD mesh in `.model` format from standard input and subdivides the mesh with respect to the number of subdivision steps specified by the user. This program can write different types of data, such as the subdivided triangulation mesh, subdivided polylines, and subdivided mesh model, to a file specified by the command line options. For the subdivision scheme, a variation of the Loop method proposed in [60] was implemented.

OPTIONS

`-s $subStep`	Sets the number of subdivision steps to `$subStep`.
`-o $modelFile`	Sets the output subdivided mesh-model file name to `$modelFile` in which the subdivided mesh is stored in `.model` format.
`-p $polyFile`	Sets the subdivided polyline file name to `$polyFile` in which the subdivided polyline is stored in the format used by the iviewer software.
`-t $triFile`	Sets the subdivided triangulation file name to `$triFile` in which the subdivided triangulation mesh is stored in the format used by the iviewer software.

D.4.3 The `mesh_rasterization` Program

SYNOPSIS

```
mesh_rasterization [OPTIONS] < input_mesh
```

DESCRIPTION

This program reads an input ERD mesh in `.model` format from standard input and rasterizes it to obtain the reconstructed image with respect to a scaling factor specified by the user.

OPTIONS

`-k $scaleFactor`	Sets the scaling factor to `$scaleFactor`, which is a positive integer.
`-a $superSamplingFactor`	Specifies the supersampling factor used during the rasterization process to be `$superSamplingFactor`, which

is a positive integer number (for antialiasing). For example, if `$superSamplingFactor` is set to 3, the program applies a 3×3 grid algorithm (introduced in Section 2.6) for supersampling. If this option is not specified, the rasterization process is performed with no supersampling.

`-r $reconstImg`	Sets the output raster-image file name to `$reconstImg` in the plain PGM format.

D.4.4 The `img_cmp` Program

SYNOPSIS

```
img_cmp origImg reconstImg [$errorMetric]
```

DESCRIPTION

This program takes the original and reconstructed images as inputs specified by `$origImg` and `$reconstImg`, respectively, in PGM (or plain PGM) format and computes the error between them in terms of the optional error metric specified by `$errorMetric`. The computed answer is written to standard output. Valid entries for `$errorMetric` are `psnr`, `mssim`, and `pee` which compute PSNR, MSSIM, and PEE, respectively. If no error metric is specified, the program only computes the PSNR by default.

D.5 Examples of Software Usage

Having introduced all the programs in the software package implemented for this thesis, we provide some examples to show how to use the software for different purposes in what follows.

Example 1. Suppose that, for the image `peppers.pnm`, we want to use the SEMMG method to generate the ERD mesh model with a sampling density of 2% and tolerance parameter of 1.0. We also want to save the resulted edge map, polylines, triangulation, and mesh model to the files `peppers_edgeMap.pnm`, `peppers_semmg_d2%.poly`, `peppers_semmg_d2%.tri`, and `peppers_semmg_d2%.model`, respectively. For this purpose, the following command can be used:

```
./mesh_generation -n 0 -d 2 -v 1.0 -e peppers_edgeMap.pnm
   -p peppers_semmg_d2%.poly -t peppers_semmg_d2%.tri -b
   peppers_semmg_d2%.model < peppers.pnm
```

Once the mesh model is generated, we may then want to rasterize it with a 3×3 grid algorithm for supersampling and store the reconstructed image (with the same resolution) to the file `peppers_semmg_d2%.pnm`. This can be done using the following command:

```
./mesh_rasterization -k 1 -a 3 -r peppers_semmg_d2%.pnm <
   peppers_semmg_d2%.model
```

Then, for the purpose of measuring the error between the original image `peppers.pnm` and the reconstructed image `peppers_semmg_d2%.pnm` in terms of the PSNR, the following command can be used:

```
./img_cmp peppers.pnm peppers_semmg_d2%.pnm psnr
```

Example 2. For this example, suppose that we want to use the MIS method to scale the input image `dahlia.pnm` with a scaling factor of 4 and a sampling density of 2% and store the scaled image to `dahlia_mis_k4_d2%.pnm`. As we recall from Section 5.3, the MIS method comprised of three distinct stages, including mesh generation, mesh transformation, and mesh rasterization. The mesh-rasterization stage itself contains two steps of mesh subdivision and model rasterization. In stage 1 of the MIS method, the MISMG method is used to generate the ERD mesh model with tolerance parameter of 0.75. Suppose that we want to save the resulting edge map, polylines, triangulation, and mesh model to the files `dahlia_edgeMap.pnm`, `dahlia_mismg_d2%.poly`, `dahlia_mismg_d2%.tri`, and `dahlia_mismg_d2%.model`, respectively. For this purpose, the following command can be used:

```
./mesh_generation -n 1 -d 2 -v 0.75 -e dahlia_edgeMap.pnm
   -p dahlia_mismg_d2%.poly -t dahlia_mismg_d2%.tri -b
   dahlia_mismg_d2%.model < dahlia.pnm
```

Then, the generated mesh is subdivided with three steps of subdivision. Suppose that we want to save the subdivided polylines, subdivided triangulation, and subdivided mesh model to the files `dahlia_mismg_d2%_s3.poly`, `dahlia_mismg_d2%_s3.tri`, and `dahlia_mismg_d2%_s3.model`, respectively. For this purpose, the following command can be used:

```
./mesh_subdivision -s 3 -p dahlia_mismg_d2%_s3.poly -t
   dahlia_mismg_d2%_s3.tri -o dahlia_mismg_d2%_s3.model <
   dahlia_mismg_d2%.model
```

Finally, the scaled image `dahlia_mis_k4_d2%.pnm` is obtained using the following command:

```
./mesh_rasterization -k 4 -a 3 -r dahlia_mis_k4_d2%.pnm <
   dahlia_mismg_d2%_s3.model
```

It is worth mentioning that the MIS method was implemented in the way that the mesh transformation in stage 2, which is scaling operation, was implemented as part of the model rasterization in stage 3 of the MIS method. So, no separate program is needed to apply the scaling operation. Also, note that in the above example, the scaled image (i.e., `dahlia_mis_k4_d2%.pnm`) is four times larger than the original image (i.e., `dahlia.pnm`) in each dimension. Therefore, the `img_cmp` program cannot be used to compute the error between them because they do not have the same resolution. For the purpose of evaluation, however, a low-resolution version of the `dahlia.pnm`, for example `dahlia_LR4.pnm`, which is four times smaller in each dimension, should be used instead of the `dahlia.pnm`. Then, using the similar commands as above, the same steps of mesh generation, mesh subdivision, and mesh rasterization are applied to `dahlia_LR4.pnm` to obtain the scaled image named as `dahlia_LR4_mis_k4_d2%.pnm`. Now, since the ground-truth image (i.e., `dahlia.pnm`) and the scaled image (i.e., `dahlia_LR4_mis_k4_d2%.pnm`) have the same resolution, the PEE between them can be computed using the following command:

```
./img_cmp dahlia.pnm dahlia_LR4_mis_k4_d2%.pnm pee
```

Bibliography

[1] C11 language standard: ISO/IEC 9899:2011. https://www.iso.org/standard/57853.html, 2018.

[2] The MATLAB implementation of the DCCI method: https://www.mathworks.com/matlabcentral/fileexchange/38570-image-zooming-using-directional-cubic-convolution-interpolation, 2018.

[3] The MATLAB implementation of the NEDI method: https://www.mathworks.com/matlabcentral/fileexchange/49900-image-interpolation, 2018.

[4] The MATLAB implementation of the SRCNN method: http://mmlab.ie.cuhk.edu.hk/projects/SRCNN.html, 2018.

[5] Netpbm homepage. http://netpbm.sourceforge.net/, 2018.

[6] Computational Geometry Algorithms Library. http://www.cgal.org, 2018.

[7] Open Source Computer Vision Library. http://www.opencv.org, 2018.

[8] Signal Processing Library. http://www.ece.uvic.ca/ frodo/SPL, 2018.

[9] Boost C++ Library. http://www.boost.org, 2018.

[10] PGM grayscale image format. http://netpbm.sourceforge.net/doc/pgm.html, 2018.

[11] M. D. Adams. An efficient progressive coding method for arbitrarily-sampled image data. *Signal Processing Letters, IEEE*, 15:629–632, 2008.

[12] M. D. Adams. An evaluation of several mesh-generation methods using a simple mesh-based image coder. In *15th IEEE International Conference on Image Processing*, pages 1041–1044, Oct. 2008.

[13] M. D. Adams. A flexible content-adaptive mesh-generation strategy for image representation. *IEEE Transactions on Image Processing*, 20(9):2414–2427, Sep. 2011.

[14] M. D. Adams. An incremental/decremental Delaunay mesh-generation framework for image representation. In *2011 18th IEEE International Conference on Image Processing*, pages 189–192, Sep. 2011.

[15] M. D. Adams. A highly-effective incremental/decremental Delaunay mesh-generation strategy for image representation. *Signal Processing*, 93(4):749 – 764, 2013.

[16] A. S. Al-Fohoum and A. M. Reza. Combined edge crispiness and statistical differencing for deblocking JPEG compressed images. *IEEE Transactions on Image Processing*, 10(9):1288–1298, Sep. 2001.

[17] N. Asuni and A. Giachetti. Accuracy improvements and artifacts removal in edge based image interpolation. In *2008 3rd International Conference on Computer Vision Theory and Applications (VISAPP)*, pages 58–65, 2008.

[18] M. Basu. Gaussian-based edge-detection methods-a survey. *IEEE Transactions on Systems, Man, and Cybernetics, Part C (Applications and Reviews)*, 32(3):252–260, Aug. 2002.

[19] F. Bergholm. Edge focusing. *IEEE Transactions on Pattern Analysis and Machine Intelligence*, PAMI-9(6):726–741, Nov. 1987.

[20] M. J. Black, G. Sapiro, D. H. Marimont, and D. Heeger. Robust anisotropic diffusion. *IEEE Transactions on Image Processing*, 7(3):421–432, Mar. 1998.

[21] J. G. Brankov, Y. Yang, and N. P. Galatsanos. Image restoration using content-adaptive mesh modeling. In *2003 International Conference on Image Processing (ICIP)*, volume 2, pages 997–1000, Sep. 2003.

[22] J. G. Brankov, Y. Yang, and M. N. Wernick. Tomographic image reconstruction based on a content-adaptive mesh model. *IEEE Transactions on Medical Imaging*, 23(2):202–212, Feb. 2004.

[23] J. Canny. A computational approach to edge detection. *IEEE Transactions on Pattern Analysis and Machine Intelligence*, PAMI-8(6):679–698, Nov. 1986.

[24] G. Casciola, L. B. Montefusco, and S. Morigi. Edge-driven image interpolation using adaptive anisotropic radial basis functions. *Journal of Mathematical Imaging and Vision*, 36(2):125–139, 2010.

[25] P. Çivicioğlu and M. Alçı. Impulsive noise suppression from highly distorted images with triangular interpolants. *International Journal of Electronics and Communications*, 58(5):311–318, 2004.

[26] L. P. Chew. Constrained Delaunay triangulations. In *3rd Annual Symposium on Computational Geometry (SCG)*, pages 215–222. ACM, 1987.

[27] S. A. Coleman, B. W. Scotney, and M. G. Herron. Image feature detection on content-based meshes. In *2002 International Conference on Image Processing*, volume 1, pages 844–847, 2002.

[28] M. de Berg, O. Cheong, M. Kreveld, and M. Overmars. *Computational Geometry Algorithms and Applications*. Springer, 3rd edition, 2008.

[29] B. Delaunay. Sur la sphère vide. a la mémoire de georges voronoi. *Bulletin de l'Académie des Sciences de l'URSS, Classe des sciences mathématiques et naturelles*, (6):793–800, 1934.

[30] L. Demaret and A. Iske. Advances in digital image compression by adaptive thinning. *Annals of the Marie-Curie Fellowship Association*, 3:105–109, 2004.

[31] O. Devillers and M. Teillaud. Perturbations and vertex removal in a 3D Delaunay triangulation. In *Proceedings of the 14th Annual Symposium on Discrete Algorithms (SODA)*, pages 313–319, ACM-SIAM, Philadelphia, PA, USA, 2003.

[32] L. Ding and A. Goshtasby. On the canny edge detector. *Pattern Recognition*, 34:721–725, 2001.

[33] C. Dong, C. C. Loy, K. He, and X. Tang. Image super-resolution using deep convolutional networks. *IEEE Transactions on Pattern Analysis and Machine Intelligence*, 38(2):295–307, Feb. 2016.

[34] D. H. Douglas and T. K. Peucker. Algorithms for the reduction of the number of points required to represent a digitized line or its caricature. *Cartographica: The International Journal for Geographic Information and Geovisualization*, 10(2):112–122, 1973.

[35] C. Dyken and M. S. Floater. Preferred directions for resolving the non-uniqueness of Delaunay triangulations. *Computational Geometry*, 34(2):96–101, 2006.

[36] N. Dyn, M. S. Floater, and A. Iske. Adaptive thinning for bivariate scattered data. *Journal of Computational and Applied Mathematics*, 145(2):505–517, Aug. 2002.

[37] R. W. Floyd and L. Steinberg. An adaptive algorithm for spatial greyscale. *Proceedings of the Society of Information Display*, 17(2):75–77, 1976.

[38] G. Freedman and R. Fattal. Image and video upscaling from local self-examples. *ACM Trans. Graph.*, 30(2):12:1–12:11, Apr. 2011.

[39] W. T. Freeman, T. R. Jones, and E. C. Pasztor. Example-based super-resolution. *IEEE Computer Graphics and Applications*, 22(2):56–65, Mar. 2002.

[40] M. A. Garcia and A. D. Sappa. Efficient generation of discontinuity-preserving adaptive triangulations from range images. *IEEE Transactions on Systems, Man, and Cybernetics, Part B (Cybernetics)*, 34(5):2003–2014, Oct. 2004.

[41] M. A. Garcia and B. X. Vintimilla. Acceleration of filtering and enhancement operations through geometric processing of gray-level images. In *2000 International Conference on Image Processing (ICIP)*, volume 1, pages 97–100, 2000.

[42] M. A. Garcia, B. X. Vintimilla, and A. D. Sappa. Approximation and processing of intensity images with discontinuity-preserving adaptive triangular meshes. In *European Conference on Computer Vision (ECCV) - Lecture Notes in Computer Science*, volume 1842, pages 844–855. Springer, Berlin, Heidelberg, 2000.

[43] M. Garland and P. S. Heckbert. Fast polygonal approximation of terrains and height fields. Tech. Rep. CMU-CS-95-181. School of Computer Science, Carnegie Mellon University, Pittsburgh, PA, USA, Sep. 1995.

[44] A. Giachetti and N. Asuni. Real-time artifact-free image upscaling. *IEEE Transactions on Image Processing*, 20(10):2760–2768, Oct. 2011.

[45] D. Glasner, S. Bagon, and M. Irani. Super-resolution from a single image. In *2009 IEEE 12th International Conference on Computer Vision*, pages 349–356, Sep. 2009.

[46] M. Grundland, C. Gibbs, and N. A. Dogson. Stylized multiresolution image representation. *Journal of Electronic Imaging*, 17(1):013009.1–17, 2008.

[47] H. Hadizadeh and I. V. Bajic. Full-reference objective quality assessment of tone-mapped images. *IEEE Transactions on Multimedia*, 20(2):392–404, Feb. 2018.

[48] H. Hou and H. Andrews. Cubic splines for image interpolation and digital filtering. *IEEE Transactions on Acoustics, Speech, and Signal Processing*, 26(6):508–517, Dec. 1978.

[49] M. Hugentobler and B. Schneider. Breaklines in coons surfaces over triangles for the use in terrain modelling. *Computers and Geosciences*, 31(1):45–54, 2005.

[50] ITU-R Recommendation BT.500-13. Methodology for the subjective assessment of the quality of television pictures. International Telecommunication Union (ITU), Geneva, Switzerland, 2012.

[51] R. Keys. Cubic convolution interpolation for digital image processing. *IEEE Transactions on Acoustics, Speech, and Signal Processing*, 29(6):1153–1160, Dec. 1981.

[52] J. Kim, J. K. Lee, and K. M. Lee. Accurate image super-resolution using very deep convolutional networks. In *2016 IEEE Conference on Computer Vision and Pattern Recognition (CVPR)*, pages 1646–1654, Jun. 2016.

[53] K. I. Kim and Y. Kwon. Single-image super-resolution using sparse regression and natural image prior. *IEEE Transactions on Pattern Analysis and Machine Intelligence*, 32(6):1127–1133, Jun. 2010.

[54] P. Kocharoen, K. M. Ahmed, R. M. A. P. Rajatheva, and W. A. C. Fernando. Adaptive mesh generation for mesh-based image coding using node elimination approach. In *2005 IEEE International Conference on Communications (ICC)*, volume 3, pages 2052–2056 Vol. 3, May 2005.

[55] V. Lacroix. The primary raster: a multiresolution image description. In *10th International Conference on Pattern Recognition*, volume i, pages 903–907 vol.1, Jun. 1990.

[56] E. C. Larson and D. M. Chandler. Most apparent distortion: full-reference image quality assessment and the role of strategy. *Journal of Electronic Imaging*, 19:19–21, 2010.

[57] C. Ledig, L. Theis, F. Huszr, J. Caballero, A. Cunningham, A. Acosta, A. Aitken, A. Tejani, J. Totz, Z. Wang, and W. Shi. Photo-realistic single image super-resolution using a generative adversarial network. In *2017 IEEE Conference on Computer Vision and Pattern Recognition (CVPR)*, pages 105–114, Jul. 2017.

[58] X. Li. Anisotropic mesh adaptation for image representation. *EURASIP Journal on Image and Video Processing*, 2016(1):26, Sep. 2016.

[59] X. Li and M. T. Orchard. New edge-directed interpolation. *IEEE Transactions on Image Processing*, 10(10):1521–1527, Oct. 2001.

[60] Z. Liao, H. Hoppe, D. Forsyth, and Y. Yu. A subdivision-based representation for vector image editing. *IEEE Transactions on Visualization and Computer Graphics*, 18(11):1858–1867, Nov. 2012.

[61] C. Liu, H. Pang, L. Ren, Z. Zhao, and S. Zhang. An image interpolation method based on weighted subdivision. *International Journal of Pattern Recognition and Artificial Intelligence*, 32(04):1854009, 2018.

[62] D. Liu, Z. Wang, B. Wen, J. Yang, W. Han, and T. S. Huang. Robust single image super-resolution via deep networks with sparse prior. *IEEE Transactions on Image Processing*, 25(7):3194–3207, Jul. 2016.

[63] K. Liu, M. Xu, and Z. Yu. Feature-preserving image restoration from adaptive triangular meshes. In *Computer Vision - ACCV 2014 Workshops*, pages 31–46. Springer International Publishing, Cham, 2015.

[64] B. E. E. Marzouki and M. D. Adams. An improved incremental/decremental Delaunay mesh-generation strategy for image representation. In *2017 IEEE Pacific Rim Conference on Communications, Computers and Signal Processing (PACRIM)*, pages 1–6, Aug. 2017.

[65] P. Mohammadi, A. Ebrahimi-Moghadam, and S. Shirani. Subjective and objective quality assessment of image: A survey. *CoRR*, abs/1406.7799, 2014.

[66] S. Mostafavian and M. D. Adams. An optimization-based mesh-generation method for image representation. In *2015 IEEE Pacific Rim Conference on Communications, Computers and Signal Processing*, pages 234–239, Aug. 2015.

[67] S. Mostafavian and M. D. Adams. A novel edge-preserving mesh-based method for image scaling. In *2017 IEEE Pacific Rim Conference on Communications, Computers and Signal Processing (PACRIM)*, pages 1–6, Aug. 2017.

[68] N. Otsu. A threshold selection method from gray-level histograms. *IEEE Transactions on Systems, Man, and Cybernetics*, 9(1):62–66, Jan. 1979.

[69] V. Patel and K. Mistree. A review on different image interpolation techniques for image enhancement. *International Journal of Emerging Technology and Advanced Engineering*, 3:129–133, Dec. 2013.

[70] P. Perona and J. Malik. Scale-space and edge detection using anisotropic diffusion. *IEEE Transactions on Pattern Analysis and Machine Intelligence*, 12(7):629–639, Jul. 1990.

[71] M. Petrou, R. Piroddi, and A. Talebpour. Texture recognition from sparsely and irregularly sampled data. *Computer Vision and Image Understanding*, 102(1):95 – 104, 2006.

[72] D. Salesin, D. Lischinski, and T. DeRose. Reconstructing illumination functions with selected discontinuities. In *3rd Eurographics Workshop on Rendering*, pages 99–112, 1992.

[73] M. Sarkis and K. Diepold. A fast solution to the approximation of 3D scattered point data from stereo images using triangular meshes. In *7th IEEE-RAS International Conference on Humanoid Robots*, pages 235–241, Nov. 2007.

[74] M. Sarkis and K. Diepold. Content adaptive mesh representation of images using binary space partitions. *IEEE Transactions on Image Processing*, 18(5):1069–1079, May 2009.

[75] W. Shao, P. Shen, X. Xiao, L. Zhang, M. W. Z. Li, C. Qin, and X. Zhang. Advanced edge-preserving pixel-level mesh data-dependent interpolation technique

by triangulation. In *2011 IEEE International Conference on Signal Processing, Communications and Computing (ICSPCC)*, pages 1–6, Sep. 2011.

[76] H. R. Sheikh and A. C. Bovik. Image information and visual quality. *IEEE Transactions on Image Processing*, 15(2):430–444, Feb. 2006.

[77] X. Shen, G. Zeng, and Z. Wei. Nonuniform sampling and reconstruction for high resolution satellite images. In *International Conference on Image Analysis and Signal Processing (IASP)*, pages 187–191, Oct. 2011.

[78] W. Shi, J. Caballero, F. Huszár, J. Totz, A. P. Aitken, R. Bishop, D. Rueckert, and Z. Wang. Real-time single image and video super-resolution using an efficient sub-pixel convolutional neural network. *CoRR*, abs/1609.05158, 2016.

[79] S. M. Smith and J. M. Brady. SUSAN-A new approach to low level image processing. *International Journal of Computer Vision*, 23(1):45–78, 1997.

[80] A. Sood, M. Kaul, and R. Siddavatam. Fast novel image reconstruction algorithm using adaptive R-tree based segmentation and linear bivariate splines. In *Proceedings of the Second International Conference on Computational Science, Engineering and Information Technology*, CCSEIT '12, pages 676–682, ACM, New York, NY, USA, 2012.

[81] Student. The probable error of a mean. *Biometrika*, 6(1):1–25, Mar. 1908.

[82] D. Su and P. Willis. Image interpolation by pixel-level data-dependent triangulation. *Computer Graphics Forum*, 23(2):189–201, 2004.

[83] P. Trisiripisal, S. M. Lee, and A. L. Abbott. Iterative image coding using hybrid wavelet-based triangulation. In *Advances in Multimedia Modeling*, pages 309–321. Springer, Berlin, Heidelberg, 2006.

[84] X. Tu and M. D. Adams. Improved mesh models of images through the explicit representation of discontinuities. *Canadian Journal of Electrical and Computer Engineering*, 36(2):78–86, Spring 2013.

[85] R. Verma, R. Mahrishi, G. K. Srivastava, and S. Rajesh. A fast image reconstruction algorithm using significant sample point selection and linear bivariate splines. In *TENCON 2009 - 2009 IEEE Region 10 Conference*, pages 1–6, Jan. 2009.

[86] L. Wang, Z. Huang, Y. Gong, and C. Pan. Ensemble based deep networks for image super-resolution. *Pattern Recogn.*, 68(C):191–198, Aug. 2017.

[87] Z. Wang and A. C. Bovik. Mean squared error: Love it or leave it? A new look at signal fidelity measures. *IEEE Signal Processing Magazine*, 26(1):98–117, Jan. 2009.

[88] Z. Wang, A. C. Bovik, H. R. Sheikh, and E. P. Simoncelli. Image quality assessment: from error visibility to structural similarity. *IEEE Transactions on Image Processing*, 13(4):600–612, Apr. 2004.

[89] Z. Wang, Y. Yang, Z. Wang, S. Chang, J. Yang, and T. S. Huang. Learning super-resolution jointly from external and internal examples. *IEEE Transactions on Image Processing*, 24(11):4359–4371, Nov. 2015.

[90] T. Xia, B. Liao, and Y. Yu. Patch-based image vectorization with automatic curvilinear feature alignment. *ACM Transactions on Graphics (TOG)*, 28(5):115:1–115:10, Dec. 2009.

[91] H. Xie and R. Tong. Image meshing via hierarchical optimization. *Frontiers of Information Technology & Electronic Engineering*, 17(1):32–40, Jan. 2016.

[92] H. Xie, R. Tong, and Y. Zhang. Image meshing via alternative optimization. 10:82098217, Oct. 2014.

[93] C. Yang, J. Huang, and M. Yang. Exploiting self-similarities for single frame super-resolution. In Ron Kimmel, Reinhard Klette, and Akihiro Sugimoto, editors, *Computer Vision – ACCV 2010*, pages 497–510, Springer, Berlin, Heidelberg, 2011.

[94] J. Yang, J. Wright, T. S. Huang, and Y. Ma. Image super-resolution via sparse representation. *IEEE Transactions on Image Processing*, 19(11):2861–2873, Nov. 2010.

[95] X. Yang and J. Pei. 3D interpolation of image elastic deformation using Delaunay triangulation. In *2009 3rd International Conference on Bioinformatics and Biomedical Engineering (ICBBE)*, pages 1–4, Jun. 2009.

[96] Y. Yang, M. N. Wernick, and J. G. Brankov. A fast approach for accurate content-adaptive mesh generation. *IEEE Transactions on Image Processing*, 12(8):866–881, Aug. 2003.

[97] H. Yeganeh and Z. Wang. Objective quality assessment of tone-mapped images. *IEEE Transactions on Image Processing*, 22(2):657–667, Feb. 2013.

[98] K. Zhang, B. Wang, W. Zuo, H. Zhang, and L. Zhang. Joint learning of multiple regressors for single image super-resolution. *IEEE Signal Processing Letters*, 23(1):102–106, Jan. 2016.

[99] X. Zhang and X. Wu. Image interpolation by adaptive 2-D autoregressive modeling and soft-decision estimation. *IEEE Transactions on Image Processing*, 17(6):887–896, Jun. 2008.

[100] H. Zhenjie, X. Fei, and Y. Dezheng. Fast algorithm for image interpolation based on data dependent triangulation. *Bio Technology An Indian Journal*, 10(23):14238–14243, 2014.

[101] D. Zhou, X. Shen, and W. Dong. Image zooming using directional cubic convolution interpolation. *IET Image Processing*, 6(6):627–634, Aug. 2012.

[102] H. Zhou, J. Zheng, and L. Wei. Representing images using curvilinear feature driven subdivision surfaces. *IEEE Transactions on Image Processing*, 23(8):3268–3280, Aug. 2014.

[103] D. Ziou and S. Tabbone. A multi-scale edge detector. *Pattern Recognition*, 26(9):1305–1314, 1993.

[104] D. Ziou and S. Tabbone. Edge detection techniques - an overview. *International Journal of Pattern Recognition and Image Analysis*, 8:537–559, 1998.